Using mechanosynthesis to produce possible cathodes with a disordered rock-salt phase

Submitted for the Degree of Doctor of Philosophy

Xuan Zhi

Supervisor: Professor Anthony R West

The Department of Materials Science and Engineering

The University of Sheffield

11/2018 – 9/2022

Declaration

This synthesis is submitted in consideration for the award of Doctor of Philosophy. It is believed to be completely original, except where references have been made.

Xuan Zhi

04/09/22

Acknowledge

I would like to express my greatest gratitude to Professor Anthony R. West for his continuous support and guidance through my PhD study. His patience and support encouraged me to go through these four years. His dedication to work and insight to science will benefit me all my life.

I would like to thank Dr. Nik Reeves-McLaren and Dr. Robert Moorehead for sharing their knowledge on X-ray. Thank you to Dr. Oday Hussein for training on TG and DSC. Thank you to Dr. Le Ma for training on SEM. Thank you to Dr. Kirstie S McCombie for training on battery tests. Thank you to Dr. Laura Wheatcroft for performing TEM, Dr Samuel Booth for performing XANES, and Miss Shania Laming and Mr. Joseph Smith for performing ICP and CHNS. Thank you to Dr. Han Wu for performing and discussing on TG-MS. Special thanks to Professor Alan V. Chadwick for his support in XANES.

I would like to acknowledge FutureCat for funding to do characterisations.

Thanks to all members and former members in Tony's group, Dr. Bo Dong, Dr. Yun Dang, Dr. Laurence A Middlemiss, Dr. Julia Ramirez Gonzalez, Dr. Wan Fareen, Meshari M Alotaibi, Fawaz Almutairi, Xiaoyuan Zhu for useful help and suggestions. Thanks to all staff and students in the functional ceramic group, especially Dr Linhao Li, Dr. Zhilun Lu, Dr. Ge Wang, Dr. Fan Yang, Dr. Dawei and Miss Kerry McLaughlin for all discussion and assistance they gave for four years.

Finally, I would like to thank my parents, Mr. Yongwen Zhi and Mrs. Yanjie Liu, my parents in law, Mr. Zhao Sun and Mrs. Ping Xu and my husband, Yanqing Sun, for their love, understanding and support throughout highs and lows of my PhD journey.

Abstract

The use of mechanosynthesis methods to prepare a wide range of single phase materials with a disordered rock salt structure, and their subsequent characterisation using a range of techniques, is reported. Phase studies by X-ray diffraction, thermal stability by thermogravimetry, evolved gas analysis by mass spectrometry MS and differential scanning calorimetry, chemical analysis by inductively coupled plasma MS and X-ray fluorescence, were carried out to analyse the products and confirm successful synthesis.

Contamination caused by ball-milling reactants and products using three milling media, stainless steel, tungsten carbide and zirconia and choice of suitable reactants to obtain the target products, have been studied systematically and results are summarised. All three milling media introduced corresponding contamination, i.e. Fe, W and Zr. Transition metal oxides were highly contaminated (10-40 wt%) when separately ball-milled. However, the products using suitable reactant mixtures usually contained little contamination (2-3 wt%). Li_2O and Li_2O_2 were possible Li sources to produce Li_2MnO_2 when milled with suitable manganese oxides.

Products of mechanosynthesis showed high hygroscopicity. They may absorb water and probably CO_2 during synthesis and storage. The loss and absorption of water, CO_2 and oxygen was studied by thermogravimetry profiles with evolved gas analysis on heat/cool cycles.

A wide range of Li-Mn-O compositions were prepared by mechanosynthesis and many of the products had a disordered rock-salt structure. Compositions with a fixed Li/Mn ratio but different oxygen stoichiometry, such as Li_2MnO_δ and $Li_4Mn_5O_\delta$, and with a varied Li/Mn ratio, but a fixed cation/anion ratio, such as $Li_xMn_{1-x}O$ and $Li_xMn_{3-x}O_4$, were prepared and characterised. Some had a rock-salt stoichiometry and structure whereas others had spinel stoichiometry.

The doping of Li_2MnO_δ by partially substituting O for F was studied. Four possible charge compensation mechanisms and the extent of doping for each was determined. Some F doped solid solutions which cannot be produced by high temperature synthesis were successfully produced by mechanosynthesis and their thermal stability studied. Ball-milled products were often metastable and underwent phase transformation or decomposition during heating.

A wide range Li-TM-O (TM=Nb, Ti, Al, Fe, Co, V, and Ni) compositions was prepared by mechanosynthesis and obtained with disordered rock-salt structure, such as Li_3NbO_4, $LiTiO_2$, Li_2TiO_3, $LiAlO_2$, $LiFeO_2$, $LiNiO_2$, Li_2NbO_3 and Li_2NbO_2F. However, their thermal stabilities were poor. During heating, phase transformation from disordered to ordered structures often

occurred. Li loss might also occur, as for example, disordered Li_3NbO_4 which transformed to a mixture of ordered Li_3NbO_4 and $LiNbO_3$ during heating.

The F doped solid solution, $Li_2MnO_{3-x}F_x$, is attractive as a possible cathode, in which fluorine replaces oxygen, accompanied by reduction of Mn^{4+} to Mn^{3+} to form the redox couple Mn^{4+}/Mn^{3+}. Ball-milled $Li_2MnO_{3-x}F_x$ martials were nanosize and had an initial charge capacity of 215 mAh/g, much higher than that of undoped Li_2MnO_3.

Most ball-milled rock-salt phases were metastable but several F doped solid solutions on the Li-TM-O-LiF join had a good thermal stability, where Li-TM-O was Li_2MnO_3, Li_3NbO_4 and Li_2TiO_3. No structure change or F loss from those compositions occurred up to 800 °C.

Contents

Chapter 1 Literature review

1.1 Introduction

Methods for large-scale energy storage have become essential since nuclear energy and solar/wind energy have been developed well as alternatives to fossils fuels. The applications for electric vehicles also require batteries with higher capacity and higher energy density. Rechargeable lithium ion batteries (LIBs) provide possible solutions to these challenges. In 1980, $LiCoO_2$ was used as the first commercial cathode material by the SONY corporation of Japan. As cobalt is expensive and toxic, $LiMn_2O_4$ and $LiFePO_4$ were then developed to replace it, but their usage was limited by bad cyclability and low energy density, respectively. After 40 years' research, three cathode structures, the layered $LiMO_2$, the spinel LiM_2O_4 and the olivine $MM'XO_4$, have been amply studied, but the energy density of LIBs is still limited by their relatively low capacities. Recently, a new and promising cathode structure, disordered rock-salt, has started to be explored as a new research direction. It has been successfully formed for several lithium transition metal oxides, such as Li_2VO_2F, Li_2MnO_2F, $LiTiO_2$, Li-Mo-Cr-O, Li_3NbO_4 and so on. It appears that disordered rock-salt materials offer the possibility of significant increases in capacity and energy density, and operation at high voltages.

Manganese is a very cheap and non-toxic element, so it is attractive as a possible source of cathode materials. $LiMn_2O_4$ was the first Li-Mn-O compound to be used in commercial cathodes, but a structural distortion related to Mn^{3+} formation yielded a poor cyclability. $LiMnO_2$ is difficult to synthesise as a fully ordered orthorhombic structure and it does not present as good electrochemical properties as rhombohedral $LiCoO_2$. Li_2MnO_3 has a very high theoretical capacity (458 mAh/g) which is almost double that of $LiMnO_2$ (285 mAh/g). But it is considered to be electrochemically inactive because Mn^{4+} is difficult to oxidise to, for instance, Mn^{5+}. However, active electrochemical properties of Li_2MnO_3 due to oxygen redox were observed but were still very poor. Studies on doping into lithium and transition metal sites have been widely reported but doping into oxygen sites still requires more research. Fluorine dopants have been tried on some $LiMO_2$ materials and showed a significant improvement in cyclability and conductivity, but it was found difficult to keep fluorine homogeneous using traditional solid-state synthesis.

Mechanosynthesis as a new synthesis method that can introduce disorder and dopants into samples and produce nanoparticles. Plus, reactions by mechanosynthesis can occur at room

temperature so metastable compounds are possible to produce by this method, which gives an extended compositional space to explore existing and new materials. As yet, mechanosynthesis is not widely used for the synthesis of cathode materials and the reaction mechanisms are not well understood.

1.2 Cathodes in Lithium ion batteries

1.2.1 History of cathode development and three types of cathode structure

1.2.1.1 History cathode development

The first cathode used in lithium ion batteries, reported by the Bell Telephone Laboratories in the early 1970s, was the layered material, TiS_2 [1], where Li^+ is inserted to form Li_xTiS_2. In 1976, the FeS_2/LiAl system was commercialised, but sulphides are not stable at high voltages [2]. Oxides are more stable at high voltages, such as CuO and MnO, but a layered structure is not formed in most MO_x compounds [3]. Oxides became competitive later when three framework structures were found to be good intercalation hosts, which are layered $LiMO_2$, spinels $Li[M_2]O_4$ and olivines $LiMPO_4$, where M is a transition metal [3].

1.2.1.2 Layered structure

Although most MO_x structures are not layered, many $LiMO_2$ phases consist of well-ordered Li^+ and M^{3+} layers and became promising cathode materials [3]. In 1980, $LiCoO_2$ [4] and $LiNiO_2$ [5] were first reported as cathodes and in the 1990s, the SONY Corporation of Japan was the first to use $Li_{1-x}Ni_{1-y}Co_yO_2$ in cell phones as a cathode with a high energy density, which launched the portable electronic revolution. However, both $Li_{1-x}CoO_2$ and $Li_{1-x}NiO_2$ were observed to lose oxygen above ~180 ℃ and 250 ℃, respectively [6]. $LiCoO_2$, as the cathode for the first generation of lithium ion batteries, has two drawbacks: first, cobalt is expensive and toxic; second, when more than half of the lithium is extracted, the oxides begin to lose oxygen and/or to oxidise the electrolyte, which decreases the capacity and cyclability and also creates a severe safety issue. Since then, it has drawn much attention on exploring the possibility to remove cobalt and synthesise new materials with higher theoretical capacities.

In 2001, $LiMn_{0.5}Ni_{0.5}O_2$ was reported as a possible alternative to $LiCoO_2$, but it was difficult to prepare with a well-ordered structure [7]. It was subsequently realised that the size of the Mn^{4+} ion in $LiMn_{0.5}Ni_{0.5}O_2$ was probably too large to form the desired structure [8]. In 2006, $Li_{1-x}Ni_{0.56}Mn_{0.44}O_2$, containing more Ni^{2+} and less Mn^{4+}, was reported to have a well-ordered, layered structure and a capacity as high as that of $LiCoO_2$ but without containing any cobalt [9]. Today, layered lithium nickel manganese cobalt oxide (NMC) and lithium nickel cobalt aluminium oxide (NCA) have become two of the standard cathode materials in hybrid electric vehicles (HEV) and battery electric vehicles (BEV) [10].

1.2.1.3 Spinel structure

The spinel structure, with formula $Li[M_2]O_4$, has a close-packed oxygen array. Li ions occupy the 8a tetrahedral sites and transition metal ions occupy the 16c octahedral sites. This 3D framework is strongly bonded and interconnected and appears to be stable during cycling [3]. It exhibits a high operating voltage (4.1 V) and a good rate capacity [11]–[16]. However, $LiMn_2O_4$ has a low specific capacity of 110 mAh/g. Although it is possible to enhance the capacity by discharging $LiMn_2O_4$ to $Li_2Mn_2O_4$, a significant structural change, associated with a so-called Jahn-Teller distortion on Mn^{3+}, has been observed during this process and the capacity fades quickly on cycling [17]. (See more about $LiMn_2O_4$ in section 1.2.2.1)

1.2.1.4 Olivine structure

The olivine framework is a hexagonal analog of cubic spinel. Similar to $Li[M_2]O_4$, the olivine framework, with formula as M_2XO_4, is also a 3D framework. M atoms occupy in half of the octahedral sites and X atoms are in 1/8 of the tetrahedral sites of the hexagonal close-packed oxygen array. Unlike the spinel, the two octahedral sites, M and M' in olivine $MM'XO_4$, are distinct and different in size and charge, which favours ordering. In 1997, it was reported that Li^+ ions in $LiFePO_4$ can be extracted to form $FePO_4$. These two phases have the same space group and a small difference in lattice parameter, which reduces the volumetric change during cycling. Also, Fe is cheap, abundant in the earth's crust and non-toxic to the environment, which makes $LiFePO_4$ a good cathode for low-power applications and scale-up to produce larger-size batteries, in spite of its low electronic conductivity and low energy density. In 2001, Ravet et al. reported that less than 1 wt% of an electronic conductor added into $LiFePO_4$ led to

very conductive $LiFePO_4$ particles and outstanding electrochemical performance, where it delivered almost the full theoretical capacity [18]. Then it was proposed [19] that in order to optimise the electrochemical performance of $LiFePO_4$, two key strategies were applied: one was to increase the conductivity, which was achieved by coating particles with a conducting phase, such as carbon black, to increase the overall conductivity, [20] and by doping to increase the intrinsic conductivity, such as doping Nb and Zr [21], [22]; a third strategy was to decrease the particle size by low temperature synthesis, and therefore, to partially avoid particle coalescence [23].

Disordered rock-salt materials have been considered as possible cathodes in recent years, as they were reported to have high operation voltages and high energy densities. See the review on disordered rock-salt materials in section 1.5.

1.2.2 The Li-Mn-O family of cathode materials

1.2.2.1 $LiMn_2O_4$

Manganese, as a cheap, non-toxic and abundant element, is attractive and possible to replace cobalt and nickel. But historically, few phases in the Li-Mn-O family have been considered as flexible cathode materials [24]. $LiMn_2O_4$ was the first to be used as a cathode material in 1983 [25] and later was used in commercial rechargeable lithium batteries in 1996 [26]. Compared with $LiCoO_2$, $LiMn_2O_4$ is easily prepared and has a high operating voltage. The $Li_xMn_2O_4$ cathode ($0 < x < 1$) provides a specific capacity of 110 mAh/g [27]–[29] at 4 V and maintains 98% of initial capacity for over 100 cycles [30]. The reason that it has a good cyclability with x=0.0-1.0 is that Mn_2O_4 and $LiMn_2O_4$ both have cubic symmetry. This allows the unit cell to expand and contract isotropically and only the Li ions occupying the 8a tetrahedral sites are extracted and inserted during cycling [31]. $Li_xMn_2O_4$ with x=1.0-2.0 provides a higher discharge capacity at 3 V, but 60% of the capacity fades quickly. During this process, it experiences a large volume expansion as some Li ions are inserted into the 16c octahedral sites. The c/a ratio of the spinel unit cell increases by 16% [25].

Although the 4 V $Li_xMn_2O_4$ electrode is relatively stable, a slow capacity fade still occurs in its high-voltage range, where the electrode starts to dissolve into the electrolyte solution [32], [33]. It is also reported that the dissolution of $LiMn_2O_4$ is aggravated with elevated temperature [30]. Strategies to improve the cyclability, such as increasing the average manganese oxidation

state slightly above 3.5 and doping Li, Zn and Mg, have been carried out, but at the expense of losing initial capacity [33]. The Jahn Teller effect of Mn^{3+} causes the structural change. Unequal occupancy of the e_g 3d orbitals in Mn^{3+} leads to distorted MnO_6 octahedra, which causes the overall cubic structure tends to be distorted to tetragonal [14], [30], [34], [35]. To balance the change of lattice parameter and stabilise the structure, Al substitution [36] and F^- and Ni^+ co-doping [37] were introduced into $LiMn_2O_4$. Ball-milling was also reported to effectively mitigate the structural change of $LiMn_2O_4$ during cycling by introducing stacking faults and microdomains [17].

1.2.2.2 $LiMnO_2$

$LiMnO_2$ has a higher lithium content that other lithium manganese oxide compounds. Therefore, it has a high theoretical capacity of 285 mAh/g, but its cyclability is quite poor [38], [39]. It was reported that nanosized spinel domains have been observed in discharged $LiMnO_2$, indicating a structural transformation from layered rock salt to spinel during charge/discharge [40]. Unlike $LiCoO_2$, in $LiMnO_2$, Mn ions first migrate into the Li layers and then Mn and Li ions tend to rearrange to form spinel [41]. $LiMnO_2$ has an orthorhombic structure when it is synthesised at high temperature. It has been prepared with the $LiCoO_2$-like rhombohedral structure by aqueous ion exchange method under nitrogen gas. However, the products were air unstable [42]. Recently, the disordered rock-salt $LiMnO_2$ was reported. A metastable rock-salt phase with nanoparticles was formed by ball-milling. Compared with the orthorhombic-polymorph, disordered $LiMnO_2$ had an increased rate capacity and doubled specific capacity [40].

1.2.2.3 Li_2MnO_3

Li_2MnO_3 possesses a ABO_2 layered structure with formula $Li[Li_{1/3}Mn_{2/3}]O_2$. Li layers and Li, Mn mixed layers with the ratio Li/Mn of 1:2 are arranged alternately in the close packed oxygen layers. It has a very high theoretical capacity of 460 mAh/g, and promises to be a high capacity cathode material.

Theoretically, Li_2MnO_3 is not expected to be electrochemically active because the tetravalent state manganese in a tetrahedral site is difficult to oxidise to pentavalent state manganese which usually exists in an octahedral environment [43]. However, electrochemical activity of

Li_2MnO_3 was often observed. It was first reported in 1999 [44] with a moderately high specific capacity (150 mAh/g) [45]. In 2001, it was found that in a Li-rich NMC compound, Li_2MnO_3, as a coating on NMC particles, not only stabilised the structure, but also provided a capacity even larger than that of the main component (over 250 mAh/g) [46]. At the time, some people suggested that the tetravalent state Mn was oxidised to pentavalent state [44], while other researchers believed that lithium deintercalation was not due to the oxidation of Mn^{4+} but oxygen loss and the exchange of lithium ions by hydrogen ions. The proton redox has been reported to occur at elevated temperature and to be minimal at room temperature [47]. Oxygen redox was also observed in $Li_4Mn_5O_{12}$ and a Na-Mn-O compound which contain tetravalent manganese too [48], [49], where oxygen loss occurred during cycling and oxygen holes were created [50], [51].

In Li-excess cation disordered Li-TM-O materials, oxygen redox has been often observed. Those materials tend to have higher capacities because their capacities derive from both the transition metal redox and oxygen redox [42]. In 2005, oxygen redox was first proved experimentally in Li_2MnO_3 [52]. Mn^{4+} was partially reduced to Mn^{3+} in order to balance the charge associated with oxygen loss. This may not only activate its electrochemical behaviour, but also significantly increase the electronic conductivity by electron hopping between Mn^{4+} and Mn^{3+}. Oxygen loss occurred when Li_2MnO_3 is synthesised by the solid-state reaction. It was believed to be impossible to produce samples free of oxygen deficiency and Mn^{3+} tended to form at the surface of particles [53].

A study [54] on a series of Li_2MnO_3 samples with different amount of Mn^{3+} demonstrated that the sample with the largest amount of Mn^{3+} (9.7%), produced by ball-milling and subsequent quenching, had the highest initial discharge specific capacity and the highest electrochemical activation. However, Mn^{3+} tends to activate and accelerate the structure transformation from layered rock salt to spinel. In addition, the formation of holes on oxygen during cycling was reported to be irreversible and the structure eventually faded [55]. A study by Delai Ye et al. [56] using in situ X-ray diffraction in the synchrotron observed the irreversible oxygen redox processes. It showed that oxygen redox occurred in the first cycle and stopped after 5 cycles, but the capacity still increased for many cycles, perhaps due to TM redox. Armstrong et al. [57] demonstrated this as an ‘activation’ process of Mn^{4+}: during cycling, oxygen loss first occurred at the surface and oxide ions could diffuse from the bulk to the surface; then oxygen vacancies were formed in the bulk, which might reduce Mn^{4+} and form Mn^{4+}/Mn^{3+} redox couple; this ‘activation’ process was sustained by continuous oxygen loss from the surface. Yabuuchi et al. [58] explained the oxygen redox by ‘ the formation of peroxo-like species’, which has been experimentally [50] and theoretically [59] studied.

1.2.2.4 New Li-Mn-O cathodes

Some new lithium manganese oxide phases have been studied as cathodes. $Li_4Mn_2O_5$ is a Li-excess disordered rock-salt cathode material and was considered to be electrochemically active with Mn^{3+}/Mn^{5+} and O^{2-}/O^- redox couples during charge/discharge. It was shown by XANES that Mn^{3+}/Mn^{5+} redox was achieved but Mn^{5+} had a poor reversibility due to a large barrier to migration between adjacent octahedral and tetrahedral sites [60]–[62]. Li_3MnO_4, with a theoretical capacity of 698 mAh/g, was synthesised by hydrothermal reaction under O_2 atmosphere. Based on computational studies, Li may be extracted from Li_3MnO_4 to form $LiMnO_4$ at ~3.4 V and inserted from Li_3MnO_4 to form Li_5MnO_4 at ~1.9 V. However, practically, it yielded much lower capacities and exhibited severe irreversibility, possibly due to the presence of several polymorphs [63].

1.3 Electrolytes and anodes in lithium ion batteries

1.3.1 Electrolyte

Electrolytes are the key factor of safety and performance of LIBs. Good electrolytes have to meet the demands for low vapour pressure, low melting points and high boiling points, fast transport of Li^+, and good chemical and electrochemical stability [64]. Classic electrolytes, lithium hexafluorophosphate ($LiPF_6$), usually work in organic solvents with poor thermal stability and high flammability. Overheating causes the thermal dissociation of $LiPF_6$, and finally leads to thermal runaway, giving combustion and explosion.

The flammability has been one of the biggest concerns for LIBs to be used widely as power sources for portable devices and electric vehicles. Therefore, non-flammable electrolytes were extensively studied. One of the strategies is to incorporate flame-retardant additives or non-flammable solvents into $LiPF_6$ [65]. Electrolytes derived from ionic liquids (IL-based electrolytes) have good thermal and electrochemical stability, flame retardant performance and negligible vapour pressure [66]. Another strategy is to use solid electrolytes, such as ceramic and polymetric solid electrolytes, which eliminates the use of liquid electrolyte to improve safety and simply the cell design. Several types of ceramics are suitable for LIBs, including sulfides, such as so-called thio-LiSiCON, Li-Ge-P-S , oxides, such (La, Li)TiO_3 (LLTO) [67] and phosphates, such as $Li_{1+x}Al_xGe_{2-x}(PO_4)_3$ (LAGP) [68]. Polymer electrodes can be classified

as solid polymer electrodes and gelled solid polymer electrolytes, such as poly(ethylene oxide) (PEO), the most commonly used one, and poly(vinylidene fluoride) (PVdF). By comparison, polymers are more flexible for battery design, and ceramics are more suitable for more aggressive environments, such as high temperature. Also, ceramics have a higher ionic conductivity and high Li^+ mobility than polymer electrolytes [69]. Solid electrolytes have drawbacks however: they generally have lower conductivity than liquid electrolytes; strength and electrode compatibility need to be considered. Selecting the most suitable solid electrolytes for a particular LIB is essential.

1.3.2 Anode

1.3.2.1 Graphite and Li metal

Graphite is the most used anode in LIBs. It has presented a good electrochemical performance, such as long cycle life and high energy density, and its price is cheap, with a dominating market share of 98% (leaving 2% for $Li_4Ti_5O_{12}$) [70]. But in graphite, the intercalation of one Li^+ requires six carbons, leading to a low power density. Its rate performance is relatively low and cannot achieve fast charging [71]. Li metal was widely used in rechargeable Li metal batteries in 1980s, but it forms dendrites at the anode/electrolyte interface, which causes short circuit and therefore a safety issue [72].

1.3.2.2 Carbon anodes

Recent studies of anodes can be classified as carbon and non-carbon. Carbon materials are attractive as they are abundant, environmentally friendly, chemically and electrochemically stable. Carbon nanotubes (CNTs), an allotrope of graphite, have high conductivity, low density and high rigidity, due to their unique structure. Single walled CNTs achieve reversible capacities of 300-600 mAh/g [73]. The challenge is their production methods are currently not refined enough to produce the desirable structures [74]. Carbon nanofibers were also successfully produced by the electrospinning technique, where fibres were extruded from a solution by electrostatic forces. Nanofibres present high surface areas, thin web morphologies [75]. Graphene was reported first in 2004, with a 2D sheet structure, consisting of a monolayer

of carbon atoms [76]. It is the strongest material ever measured with a high intrinsic strength (~130 GPa) and Young's modulus (~1.0 TPa). It also has a high surface area, a high conductivity. Unfortunately, it requires complex fabrication techniques and high production costs which makes the scalable production of graphene challenging.

1.3.2.3 Non-carbon anodes

For non-carbon anodes, some alloys and oxides have been widely studied. Silicon, with a high theoretical capacity of 4200 mAh/g [77], is one of the most attractive anode materials for LIBs. It is cheap, abundant, and environmentally friendly. The discharging potential is only ~0.2 V [78] with respect to Li/Li^+. Lithiated silicon is more stable than graphite [79]. But it suffers from fast capacity fading. It achieved an initial discharging capacity of 3260 mAh/g but faded immediately to 1170 mAh/g in the first charge. After 10 cycles, only ~200 mAh/g of capacity were retained [80]. Compared with alloys, oxides are easier to handle and process. Group IV oxides, SiO and SiO_2, GeO_2 and germanates, and SnO_2 have been studied as anodes. Commercial SiO is a mixture of amorphous Si and amorphous SiO_2, where the active species is the Si. During the first lithiation, Li_xSi, Li-Si-O and Li_2O are formed but only Li_xSi is reversible during charge/discharge [81]. Germanate anodes show high specific capacities too. However, they have large volume change during charge/discharge, which leads to poor cycling performance [82]. Compared with silicon and germanium, tin-based compounds (TBCs) do not have the highest theoretical capacity, but are easier to synthesis and more abundant. The drawbacks of TBCs are that: 1. the huge volume expansion of tin causes the pulverisation of TBCs and 2. the irreversible reaction with solid electrolyte interface and formation of Li_2O or Li_2S leads to a relatively low Coulombic efficiency [83]. $Li_4Ti_5O_{12}$ (LTO) has a spinel phase with the Ti^{4+}/Ti^{3+} redox couple. It is a zero strain insertion material, so it has a good reversibility with no structural change during charge and discharge. It offers a stable operating voltage of ~1.55 V with respect to Li/Li^+ [84]. However, its insulating nature makes its intrinsic electronic conductivity very low. Many experiments working on improving its electronic conductivity have been carried out, including new synthesis method, doping on Li, Ti and O sites and incorporation of second phase with high electronic conductivity [85].

1.4 Synthesis methods of solids

1.4.1 Solid state reaction

Solid state reaction is the most traditional and simplest synthesis method. It is the most widely used method to produce inorganic solids. Reactants initially are mixed at the particle level, and are inhomogeneous at the atomic level. The synthesis process takes relatively long time, when atoms diffuse to form the desired product, driven by high temperature. An obvious drawback of solid state reaction is that the reactants are not mixed at the atomic level, so that the product is inhomogeneous to some degree. Also, solids that are not thermodynamically stable require low temperature synthesis methods [86].

1.4.2 Low temperature synthesis

Many low temperature synthesis methods achieve atomic level mixing of reactants. The final synthesis temperature may be still high, especially for ceramic products. Those products obtained by low temperature synthesis have higher chemical homogeneity and usually improved properties or provide a platform to study properties with less effect of impurities. Compared with solid state reaction, low temperature synthesis methods are more costly and more difficult to be industrialised [86].

1.4.2.1 Sol-gel synthesis

The starting material is usually a homogeneous solution. It is gradually dried and transformed to a viscous sol, and finally to a homogeneous amorphous solid gel. This gel is then fired at a relatively high temperature to remove volatile and organic components and finally forms a crystallised desired product. Sol forming is a key step in sol-gel synthesis. Sols can be classified into alkoxide sols and inorganic sols by different reagents they dissolve with. The final firing temperature of sol-gel synthesis is usually much lower than that of solid state reaction [86]. For example, by solid state reaction, $MgAl_2O_4$ is produced by heating at ~1500 ℃ for days, whilst by sol-gel method, it was finally fired at only 280 ℃ for 3 h [87].

1.4.2.2 Hydrothermal/solvothermal synthesis

Hydrothermal synthesis uses water or steam (supercritical solvents, in the case of solvothermal synthesis) to dissolve reactants and the solvent is heated under high pressure and temperature. The solubility of the reactants is *P*, *T* dependent. When the solvent is sealed and heated in the supercritical condition in a temperature gradient, the reactants dissolve at the hot end, and the product crystallises at the cool end. This method is suitable for materials that require extremely high reaction temperature [86].

1.4.3 Mechanosynthesis

1.4.3.1 History of mechanochemistry

Mechanochemistry has been used since Stone Age times to process building materials such as clay or to grind seeds and wheat. Today, a set consisting of a mortar and pestle is widely used as modern mechanochemistry tools. In the early 20th century, automated ball mills were invented. They were used in laboratories in order to make the grinding reproducible and labour-saving and also widely used in industrial production to meet the demand for large-scale milling.

Different from those vibration ball mills, planetary ball mills, invented by the Fritsch company in 1961, not only grind and mix raw materials but directly cause raw materials to react. Planetary ball mills have been used to produce samples with desired properties by changing parameters such as ball size, rotating speed, milling time and milling media [88]. Temperature, pressure and atmosphere also could be monitored when milling. A small temperature increase has been observed during ball-milling, which may influence the reaction kinetics and change temperature-sensitive samples [89]. Common milling media used in a planetary ball mill are steel, zirconia and tungsten carbide. Stainless hardened steel is mostly used as it is cheap. Tungsten carbide has been reported to provide higher kinetic energy [90] and introduce less metal contamination [91]. The choice of milling media depends on the density of samples. Milling materials should always have higher density than the samples.

1.4.3.2 Mechanosynthesis by ball-milling of inorganic materials

For inorganic materials, mechanochemistry was mainly applied to solid systems and has been developed to improve reactivity by introducing solid-state defects, producing nanoparticles and making processes eco-friendly and waste-free [92]. Recently, it started to be used to synthesise new materials or known materials with new structures. Using mechanosynthesis, it is possible to synthesise materials at low temperatures, for instance, room temperature. Compared with multiple-step solid-state reactions, ball-milling is always one-step. Moreover, as a novel synthesis method, it may permit access to products which are inaccessible by traditional high-temperature methods.

Mechanosynthesis frequently extends the compositional range of solid solutions. Ball-milled $M_{1-x}Pb_xF_2$ (M=Ca, Sr and Ba) formed solid solution over the whole compositional range in all three systems and also had better stability and higher ionic conductivity, which could not be achieved by high temperature solid-state reaction. [93]. $Li_{4+x}Si_{1-x}Fe_xO_4$ was used as CO_2 capture material and CO_2 chemisorption is largely improved by Fe doping. Ball-milling was reported to be an efficient way to synthesise and extend the solid solution of $Li_{4+x}Si_{1-x}Fe_xO_4$. The ball-milled sample had smaller crystal size and higher surface area, which facilitates CO_2 chemisorption [94].

Mechanochemistry also can be used in liquid and gaseous systems since ball-milling creates more interfaces and improves reactivity. As an alternative to solution-based synthesis, using ball-milling can avoid the large amount of waste which is generated by solution-based reactions. Insoluble reagents become usable in mechanosynthesis [95]. A successful example in a solid-gas system is GaN, which was produced in a pressurised planetary ball mill starting from Ga_2O_3 and Li_3N [96]. Graphene nanoplates were reported to be successfully produced in the planetary ball mill under CO_2 atmosphere. It has been considered as a facile strategy for the low-cost and large-scale production of graphene nanoplatelets [95]. Noticeably, in gas-related ball-milling, temperature and pressure are crucial from a safety perspective.

1.4.3.3 Mechanosynthesis by ball-milling cathodes in LIBs

As mechanosynthesis has been demonstrated to be a powerful technique to synthesise oxides, research on synthesis of possible cathode materials by mechanosynthesis has extensively drawn attention.

$LiCoO_2$ was produced by ball-milling using LiOH and $Co(OH)_2$ in agate jars and ordered $LiCoO_2$ was directly formed after 10 h milling. After prolonged milling, 40 h, impurities of

Co_3O_4 appeared and lithia and oxygen loss occurred [97]. A series of $Li_xMn_{1-x}O$ ($0 < x < 0.5$) was successfully produced by ball-milling Li_2O and MnO. They formed a disordered α-$LiFeO_2$ structure which showed a poor electrochemical performance. To study $LiMO_2$ materials, $LiCoO_2$, $LiNiO_2$ and $LiTiO_2$ were prepared by the same method and all formed an α-$LiFeO_2$ structure. A large amount of lithia and oxygen loss was again observed after prolonged milling time. It was concluded that $LiMO_2$ (M=Fe, Co, Ni and Ti) with α-$LiFeO_2$ structure tended to have a poor electrochemical performance. However, $LiMnO_2$ which was produced by the same process kept some short-range cation order and showed a moderate electrochemical performance. Iron contamination was observed in ball-milled $LiTiO_2$, which might be from the milling medium [98]. Single phase β-$LiFeO_2$, with a tetragonal structure, proved to be difficult to produce by solid-state reaction, so mechanosynthesis was considered. Li_2O and Fe_2O_3 were ball-milled under argon atmosphere and single phase β-$LiFeO_2$ was directly produced. Ball-milled β-$LiFeO_2$ gave a long and stable plateau in the discharge/charge voltage profile [99].

$LiMn_2O_4$ was prepared by mechanosynthesis with raw materials of LiOH and three manganese oxides, MnO_2, Mn_2O_3 and MnO [100]. However, only with MnO_2, $LiMn_2O_4$ was formed. According to XRD patterns, Mn_2O_3 remained unchanged during milling. MnO transformed to Mn_3O_4 after milling and no $LiMn_2O_4$ was formed. The Jahn-Teller effect still existed in ball-milled $LiMn_2O_4$, but electrochemical cyclability was improved. It might have resulted from the presence of nanoparticles which can tolerate distortions and accommodate strains. But nanoparticles that mechanosynthesis produces are not always good. It has been reported that higher surface areas of nanoparticles accelerated the dissolution of Mn^{3+} in the electrolyte [30]. As for reactants, they mentioned that Li_2CO_3, the most common lithium source in solid state reaction, was not reactive in mechanosynthesis whereas LiOH and Li_2O was. It is possible that LiOH and Li_2O had a good plasticity but Li_2CO_3 was a typical ionic compound and very brittle [101].

The disordered rock-salt structure is promising for cathode material as reported by Ceder in 2014 and mechanosynthesis has become a standard synthesis method. (See the review on disordered rock salt structure in section 1.5.) However, a full systematic study into the optimum condition for mechanosynthesis has not been reported.

Besides oxides, other types of cathode material have also been made by mechanosynthesis. Metal sulphide and metal fluoride cathodes showed high capacities and voltages, but large structural changes during cycling limited their reversibility. Several lithium metal sulphides with rock-salt structure were successfully fabricated by mechanosynthesis, such as Li_2TiS_3 and Li_3NbS_4 with high capacities of 273 mAh/g and 386 mAh/g, respectively [102], [103].

Mechanosynthesis is a relatively new method. Currently, it still lacks standardised

protocols, making it more difficult for large-scale industrial production [104].

1.5 Disordered rock-salt structure

The layered rock salt, spinel and olivine structures have been widely studied and used as cathodes based on classic 3d metal redox couples of Co, Ni, Mn and Fe. The current commercial lithium ion cathodes using $LiCoO_2$, $LiNi_{0.5}Mn_{0.5}O_2$, $LiMn_2O_4$ and $LiFePO_4$, generally have low energy densities and capacities and cannot be used for large-scale applications in electrical vehicles. Therefore, a new direction to design cathode materials, based on lithium transition metal oxides with disordered rock-salt structure, has attracted much attention.

1.5.1 Disorder in ordered layered structures and the disordered rock-salt structure

Disordered materials used to be neglected as possible electrode materials. In the 1990s, when layered rock salt structure materials were first studied as cathodes, cation disordered arrangements were often observed. It was observed that cation disorder in layered $LiCoO_2$ [105] and $LiNiO_2$ [106], [107] led to the degradation of cyclability and lithium diffusion. α-$LiFeO_2$ and $LiTiO_2$ tend to become disordered at high temperature, and lithium could not be intercalated/de-intercalated. $Li_{0.9}Ni_{0.45}Ti_{0.55}O_2$ was reported to contain some cation disorder after high temperature synthesis, and this disorder was considered as the root cause of its severe, first cycle capacity loss [108]. $Li_{0.86}V_{0.8}O_2$ with disordered vanadium ion arrangements was reported to have a worse reversibility compared with ordered $LiVO_2$ [109]. Before the 2010s, it was generally believed that a cation disorder in layered rock salt structure reduced the Li slab distance and Li diffusion path, which was the key factor to reduce lithium diffusivity. Plus, the disorder was often irreversible so cyclability faded fast [110]–[112].

Recently, however, some ordered layered lithium transition metal oxides have been reported to form disordered structure during cycling. The resulting disordered phases present good electrochemical properties. In 2012, disordered rock-salt Li_2VO_3 was formed after the first discharge of layered $LiVO_3$. This disordered phase was very stable with a good cyclability and delivered a high specific energy density (632 Wh/kg) [113]. Similarly, $Li_{1.211}Mo_{0.467}Cr_{0.3}O_2$ transformed to a disordered rock-salt structure after 10 cycles. It had a high capacity of 265 mAh/g and good reversibility. In 2015, a disordered rock-salt $Li_{1.3}Nb_{0.3}Mn_{0.4}O_2$ was

synthesised by ball-milling and showed a high cyclability. It may be due to the introduction of Nb^{5+} which stabilised the oxygen redox [114]. Similarly, F doping was introduced to mitigate the oxygen redox in Li_2VO_3. Li_2VO_2F was successfully synthesised by ball-milling with a more stable structure and a higher rate capacity [115]. In 2017, monoclinic Li_2MnO_3 formed a disordered rock-salt structure after high-energy ball-milling. This disordered phase had a reversible capacity of 250 mAh/g at the voltage of 3V [42]. Mechanosynthesis, such as ball-milling, started to be considered as a routine synthesis to obtain disordered electrode materials. In this structure, Li and TM ions locate randomly in cubic close-packed cation sites. It can stabilise the framework because after Li ions are extracted from random cation sites, TM ions may remain in the remaining cation sites [116].

1.5.2 Lithium excess strategy

Many groups have offered their understandings on disorder in cathode materials. Ceder et al. [110], [111] believed that a so-called 0-TM environment was important for lithium ion diffusion in disordered rock-salt structure. They have first modelled the effect of disorder in ordered layered structure. In close packed oxides, ions in one octahedral site diffuse to another octahedral site via an intermediate tetrahedral site, so called o-t-o diffusion. Lithium diffusion largely depends on the height of the tetrahedron, which are face-sharing with four octahedral sites which act as gates for lithium ion transport. In layered materials, all Li^+ tetrahedral sites are interconnected by 3 Li^+ octahedral sites and 1 TM ion octahedral sites, which was named as 1-TM channel, Figure 1.1 [117]. When a tetrahedral site is interconnected by x of TM ion octahedral sites and 4-x of Li ion tetrahedral sites, this site was named as x-TM channel site. So-called 0-TM channel site is directly adjacent to no TM ion and 4 Li ions. In layered structures, lithium diffusion depends on the effect of different transition metals on the size of tetrahedral sites. For example, transition metals with higher valence have smaller tetrahedral sites, therefore, larger barriers to lithium ion hopping. In this case, disorder inhibits or even blocks the ion diffusion pathway through tetrahedral sites. According to their modelling results, the tetrahedron height in disordered structures for Li-TM-O (TM=Ni, Co, V and Mo) was generally smaller than the slab distances in ordered structures [55], therefore, disorder results in a reduced diffusion path, and a large energy barrier.

In disordered rock-salt structure, 0-TM, 1-TM and 2-TM sites are all possible to exist. 2-TM and 1-TM channels are generally inactive to transport lithium ions, so only 0-TM can support lithium migration. Creating more 0-TM channels by lithium excess has been proved to

effectively enhance the rate capacity and reversibility. Li diffusing from a 0-TM channel had an even higher hopping rate than diffusing in ordered layered structures with 1-TM channels [117]. When lithium excess was more than 10% in a completely or partially disordered rock-salt structure, an effective percolation network of 0-TM channels was created [55], [113], [114], [116], [117].

Li excess, however, it is widely accepted to aggravate the oxygen loss and reduce the amount of active transition metal redox. In a lithium-rich environment, oxygen ions are more easily oxidised and react with the electrolyte [47], [118]–[123]. The lithium excess also reduces the available cation sites for transition metal and further reduces the transition metal redox. This not only generally occurs in layered structure, but also disordered rock-salt structure. The rate capacity was enhanced by the existence of 0-TM at the expense of the theoretical capacity. To compensate the effect of Li excess, high valence metal, such as Nb^{+5}, was used [114], [124]. F-doping was also applied and effectively reduced oxygen redox [125]–[127].

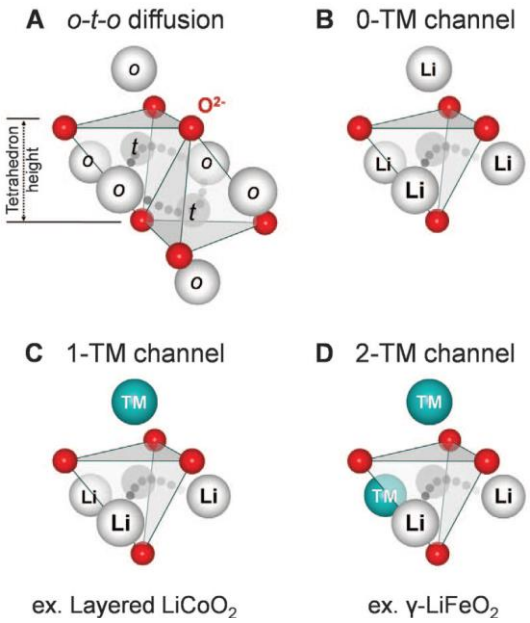

Figure 1.1 Possible environments for an o-t-o Li hop in rocksalt-like Li-TM-Os.

1.5.3 Doping strategy

Cation doping as an effective strategy to modify LIB performance has been widely used on $LiCoO_2$. To replace Co, two cathode families, NMC and NCA, have been developed and successfully used in commercial batteries, with higher energy density and capacity [57], [128].

Much research on cation doping has been done on Li_2MnO_3, such as doping Ni^{2+}, Co^{2+}, Al^{3+} and Fe^{3+} to change its electrical properties [129]–[131] and doping Zr^{4+} and Al^{3+} to alleviate the phase transition to spinel [132].

Anion doping, on the other hand, has been rarely studied. One of the reasons is that the candidates to act as possible dopants on oxygen sites are very limited, essentially to phosphorus, nitrogen and fluorine. In this thesis, F doping is studied in Chapter 4. The possible charge compensation mechanisms on replacing O^{2-} by F^- involve three possibilities: i. cation vacancies, ii. interstitial F^- ions or iii. hole creation, leading, for instance, to Mn^{3+} in $Li_2MnO_{3-x}F_x$. The latter mechanism would yield mixed valence Mn and increased electronic conductivity but the Jahn-Teller distortion related to the presence of Mn^{3+} is aggravated. F doping was first used in NMC and NCA, because in the low electrical conductivities are unfavourable to fast intercalation/de-intercalation [133]. In 2003, F substitution was studied in the $Li_{1+x}(Ni_yMn_yCo_{1-2y})_{1-x}O_2$ system synthesised by hydrothermal reaction and showed an improvement in cycling performance and thermal stability [134]. F-doped in $LiMn_2O_4$ was reported to effectively enhance the thermal stability and alleviate the structural instability caused by the Jahn-Teller effect [135], [136]. In a disordered structure, F-doping effectively reduces the irreversible oxygen redox and allows charge/discharge at higher voltage [137]

Some researchers still doubted the success of F doping. F has a high M-F bond energy, which leads to unfavourable incorporation.[138] Although the cell parameters were changed with F substitution, XPS and NMR showed F was present only on the surface layer and not in the bulk. They believed F homogeneity was difficult to achieve by high temperature synthesis [139]. However, the integration of F into the bulk DRX lattice has been confirmed using ^{19}F NMR spectroscopy [140]. AlF_3 surface modification on Li_2VO_2F formed an inactive surface layer, which protects the bulk materials and results in a more stable electrochemical cycling [141].

Mechanosynthesis is a useful method to introduce anion dopants into disordered rock-salt structures. Disordered rock-salt Li_2VO_2F was successfully produced by mechanosynthesis with a high capacity of 420 mAh/g and good electrical properties. This framework allowed 60% of cation sites to be vacant with only 3% lattice volume change during cycling [116], [142]. N-doping has been reported to enhance the lithium ion conductivity of Li_3VO_4 [143]. P-doping in Li_2MnO_3 restrained the oxygen loss and enhanced the structural stability. It created four polaron states for one P atom and has less trapping of polaron states [144].

1.5.4 Disordered structures in the Li-Mn-O family

Mn based compounds with disordered structures have received attention as Mn is abundant and cheap. In 2017, monoclinic Li_2MnO_3 was found to transform to a disordered rock-salt structure after high-energy ball-milling. This disordered phase had reversible capacity of 250 mAh/g at 3V [42]. Later, it was determined that the average structure of nano-Li_2MnO_3 is cubic but with short-range layered ordering in space group $R\bar{3}m$ [145]. Disordered $Li_4Mn_2O_5$, produced by mechanosynthesis, was shown by XANES to have Mn^{3+}/Mn^{5+} and O^{2-}/O^- redox couples and achieve a discharge capacity of 355 mAh/g. Its poor cyclability was presumably due to a large barrier of Mn^{5+} migrating from octahedral to adjacent tetrahedral sites [61], [62]. A family of Li_2O:$Li_{2/3}Mn_{1/3}O_{5/6}$ composites was also produced by mechanosynthesis, where Li_2O was as a prelithiation additive. With 7 mol% excess Li_2O, the capacity of $Li_4Mn_2O_5$ increased from 200 mAh/g to 370 mAh/g . The extraordinary but irreversible capacity was attributed to the active Li_2O, which was trapped in vacancy clusters on the cathode surface [146].

One of the difficulties to study disordered rock-salt materials is to characterise their local structure and understand their charge compensation mechanisms. Some characterisation techniques, such as Rietveld refinement of X-ray and neutron diffraction patterns, scanning electron microscopy (SEM) and X-ray absorption spectroscopy (XAS), were not suitable in disordered rock-salt materials, especially for fluorine-doped manganese-based ones. Both X-ray and neutron diffraction cannot distinguish oxygen and fluorine. In the rock-salt structure, with a varied ratio of lithium and transition metal cation site occupancy, as well as possible cation vacancies, and indistinguishable oxygen and fluorine anion sites, Rietveld refinement is not suitable. Also, ball-milled powders often have nano-sized particles. Their diffraction patterns show broadened peaks, which makes peak fitting more difficult. An ordering phase transformation may occur because the disordered phase is probably metastable but easily forms a short-range order domain, which is possible to be detected by SEM. XAS is often used to observe the oxidation states and local structures. However, in Mn based materials, the peak fitting of XANES depends highly on the manganese local environment. Also, the different degrees of local disorder makes the analysis of EXAFS in terms of on local structure tricky.

1.6 References

[1] S. Sinha and D. W. Murphy, "Lithium intercalation in cubic TiS2," *Solid State Ionics*, vol. 20, no. 1, pp. 81–84, 1986, doi: 10.1016/0167-2738(86)90038-X.

[2] M. S. Whittingham, "Electrical Energy Storage and Intercalation Chemistry," *Science (80-.).*, vol. 192, pp. 1126–1127, 1976, [Online]. Available: Exxon research and engineering company.

[3] J. B. Goodenough, "Cathode materials: A personal perspective," *J. Power Sources*, vol. 174, no. 2, pp. 996–1000, 2007, doi: 10.1016/j.jpowsour.2007.06.217.

[4] K. Mizushima, P. C. Jones, P. J. Wiseman, and J. B. Goodenough, "LixCoO2 (0<x≤1): A new cathode material for batteries of high energy density," *Mat. Res. Bull.*, vol. 15, pp. 783–789, 1980, doi: 10.1016/0167-2738(81)90077-1.

[5] J. B. Goodenough, K. Mizushima, and T. Takeda, "Related content Solid-Solution Oxides for Storage-Battery Electrodes," *Jpn. J. Appl. Phys.*, vol. 19, no. 3, pp. 305–313, 1980.

[6] J. R. Dahn and E. W. Fuller, "Thermal stability of LixCoO2, LixNiO2 and 2-MnO2 and consequences for the safety of Li-ion cells," *Solid state Ion.*, vol. 69, pp. 265–270, 1994.

[7] O. Tsutomu and M. Yoshinari, "Layered Lithium Insertion Material of LiNi1/2Mn1/2O2 : A Possible Alternative to LiCoO2 for Advanced Lithium-Ion Batteries," *Chem. Lett.*, vol. 30, no. 8, pp. 744–745, 2001, doi: 10.1246/cl.2010.1118.

[8] K. Kang, Y. S. Meng, C. P. G. Julien Bréger, and G. Ceder, "Electrodes with High Power and High Capacity for Rechargeable Lithium Batteries," *Science (80-.).*, vol. 311, no. 5763, pp. 977–980, 2006, doi: 10.1210/jcem-10-10-1361.

[9] S. B. Schougaard, J. Bréger, M. Jiang, C. P. Grey, and J. B. Goodenough, "LiNi0.5+δMn0.5-δO2-a high-rate, high-capacity cathode for lithium rechargeable batteries," *Adv. Mater.*, vol. 18, no. 7, pp. 905–909, 2006, doi: 10.1002/adma.200500113.

[10] D. Andre *et al.*, "Future generations of cathode materials: An automotive industry perspective," *J. Mater. Chem. A*, vol. 3, no. 13, pp. 6709–6732, 2015, doi: 10.1039/c5ta00361j.

[11] G. Amatucci and J. M. Tarascon, "Optimization of insertion compounds such as LiMn2O4 for Li-Ion batteries," *J. Electrochem. Soc.*, vol. 149, no. 12, 2002, doi: 10.1149/1.1516778.

[12] M. M. Thackeray *et al.*, "Structural fatigue in spinel electrodes in high voltage (4 V) Li/LixMn2O4 cells," *Electrochem. Solid-State Lett.*, vol. 1, no. 1, pp. 7–9, 1998.

[13] D. H. Jang and S. M. Oh, "Electrolyte effects on spinel dissolution and cathodic capacity losses in 4 V Li/LixMn2O4 rechargeable cells," *J. Electrochem. Soc.*, vol. 144, no. 10, pp. 3342–3348, 1997, doi: 10.1149/1.1838016.

[14] H. Huang, C. A. Vincent, and P. G. Bruce, "Correlating capacity loss of stoichiometric

and nonstoichiometric lithium manganese oxide spinel electrodes with their structural integrity," *J. Electrochem. Soc.*, vol. 146, no. 10, pp. 3649–3654, 1999, doi: 10.1149/1.1392528.

[15] Y. Shin and A. Manthiram, "Factors Influencing the Capacity Fade of Spinel Lithium Manganese Oxides," *J. Electrochem. Soc.*, vol. 151, no. 2, pp. 204–208, 2004, doi: 10.1149/1.1634274.

[16] B. Deng, H. Nakamura, and M. Yoshio, "Capacity fading with oxygen loss for manganese spinels upon cycling at elevated temperatures," *J. Power Sources*, vol. 180, no. 2, pp. 864–868, 2008, doi: 10.1016/j.jpowsour.2008.02.071.

[17] S. H. Kang, J. B. Goodenough, and L. K. Rabenberg, "Effect of ball-milling on 3-V capacity of lithium-manganese oxospinel cathodes," *Chem. Mater.*, vol. 13, no. 5, pp. 1758–1764, 2001, doi: 10.1021/cm000920g.

[18] P. P. Prosini, D. Zane, and M. Pasquali, "Improved electrochemical performance of a LiFePO4-based composite cathode," *Electrochim. Acta*, vol. 46, no. 23, pp. 3517–3523, 2001, doi: 10.1016/S0013-4686(01)00631-4.

[19] C. Delacourt, C. Wurm, L. Laffont, J. B. Leriche, and C. Masquelier, "Electrochemical and electrical properties of Nb- and/or C-containing LiFePO4 composites," *Solid State Ionics*, vol. 177, no. 3–4, pp. 333–341, 2006, doi: 10.1016/j.ssi.2005.11.003.

[20] P. S. Herle, B. Ellis, N. Coombs, and L. F. Nazar, "Nano-network electronic conduction in iron and nickel olivine phosphates," *Nat. Mater.*, vol. 3, no. 3, pp. 147–152, 2004, doi: 10.1038/nmat1063.

[21] S. Y. Chung, J. T. Bloking, and Y. M. Chiang, "Electronically conductive phospho-olivines as lithium storage electrodes," *Nat. Mater.*, vol. 1, no. 2, pp. 123–128, 2002, doi: 10.1038/nmat732.

[22] S. Y. Chung and Y. M. Chiang, "Microscale Measurements of the Electrical Conductivity of Doped LiFePO 4," *Electrochemical and Solid-State Letters*, vol. 6, no. 12. 2003, doi: 10.1149/1.1621289.

[23] S. Franger, F. Le Cras, C. Bourbon, and H. Rouault, "LiFePO4 synthesis routes for enhanced electrochemical performance," *Electrochemical and Solid-State Letters*, vol. 5, no. 10. 2002, doi: 10.1149/1.1506962.

[24] P. G. Bruce, "Solid-state chemistry of lithium power sources," *Chem. Commun.*, no. 19, pp. 1817–1824, 1997.

[25] M. M. Thackeray, W. I. F. David, P. G. Bruce, and J. B. Goodenough, "Lithium Insertion into Magnesium Spinels," *Mater. Res. Bull.*, vol. 18, pp. 461–472, 1983.

[26] Y. Xia and M. Yoshio, "An investigation of lithium ion insertion into spinel structure Li-Mn-O compounds," *J. Electrochem. Soc.*, vol. 143, no. 3, pp. 825–833, 1996, doi: 10.1149/1.1836544.

[27] J. M. Tarascon, F. Coowar, G. Amatuci, F. K. Shokoohi, and D. G. Guyomard, "The Li1+xMn2O4C system Materials and electrochemical aspects," *J. Power Sources*, vol. 54, no. 1, pp. 103–108, 1995, doi: 10.1016/0378-7753(94)02048-8.

[28] H. Huang and P. G. Bruce, “3V and 4V lithium manganesee oxide cathodes for rechargeable lithium batteries,” *J. Power Sources*, vol. 3, pp. 52–57, 1995.

[29] H. Huang and P. Bruce, “A 4 V Lithium Manganese Oxide Cathode for Rocking-Chair Lithium-Ion Cells,” *J. Electrochem. Soc.*, vol. 141, no. 9, pp. L106–L107, 1994, doi: 10.1149/1.2055168.

[30] T. Inoue and M. Sano, “An investigation of capacity fading of manganese spinels stored at elevated temperature,” *J. Electrochem. Soc.*, vol. 145, no. 11, pp. 3704–3707, 1998, doi: 10.1149/1.1838862.

[31] M. M. Thackeray, P. J. Johnson, P. G. Bruce, and J. B. Goodenough, “Electrochemical extraction of lithium from LiMn2O4,” *Mat.Res.Bull*, vol. 19, pp. 179–187, 1984.

[32] J. M. and D. G. Tarascon, “Li Metal-Free Rechargeable Batteries Based on Li1 + xMn2 O 4 Cathodes ($0 \leq x \leq 1$) and Carbon Anodes,” *J. Electrochem. soc*, vol. 138, no. 10, pp. 2864–2868, 1992.

[33] R. J. Gummow, A. de Kock, and M. M. Thackeray, “Improved capacity retention in rechargeable 4 V lithium/lithium-manganese oxide (spinel) cells,” *Solid State Ionics*, vol. 69, no. 1, pp. 59–67, 1994, doi: 10.1016/0167-2738(94)90450-2.

[34] D. H. Jang, Y. J. Shin, and S. M. Oh, “Dissolution of spinel oxides and capacity losses in 4 V Li/LixMn2O4 cells,” *J. Electrochem. Soc.*, vol. 143, no. 7, pp. 2204–2211, 1996, doi: 10.1149/1.1836981.

[35] H. Yamane, T. Inoue, M. Fujita, and M. Sano, “A causal study of the capacity fading of Li1.01Mn1.99O4 cathode at 80°C, and the suppressing substances of its fading,” *J. Power Sources*, vol. 99, no. 1–2, pp. 60–65, 2001, doi: 10.1016/S0378-7753(01)00479-7.

[36] Y. Xia, Q. Zhang, H. Wang, H. Nakamura, H. Noguchi, and M. Yoshio, “Improved cycling performance of oxygen-stoichiometric spinel Li1+xAlyMn2-x-yO4+δ at elevated temperature,” *Electrochim. Acta*, vol. 52, no. 14, pp. 4708–4714, 2007, doi: 10.1016/j.electacta.2007.01.004.

[37] W. Choi and A. Manthiram, “Superior capacity retention spinel oxyfluoride cathodes for lithium-ion batteries,” *Electrochem. Solid-State Lett.*, vol. 9, no. 5, pp. 1–5, 2006, doi: 10.1149/1.2186022.

[38] L. Croguennec, P. Deniard, R. Brec, and A. Lecerf, “Nature of the stacking faults in orthorhombic LiMnO2,” *J. Mater. Chem.*, vol. 7, no. 3, pp. 511–516, 1997, doi: 10.1039/a604947h.

[39] Z. X. Shu, I. J. Davidson, R. S. McMillan, and J. J. Murray, “Electrochemistry of LiMnO2 over an extended potential range,” *J. Power Sources*, vol. 68, no. 2, pp. 618–622, 1997, doi: 10.1016/S0378-7753(96)02571-2.

[40] T. Sato, K. Sato, W. Zhao, Y. Kajiya, and N. Yabuuchi, “Metastable and nanosize cation-disordered rocksalt-type oxides: revisit of stoichiometric LiMnO2 and NaMnO2,” *J. Mater. Chem. A*, pp. 13943–13951, 2018, doi: 10.1039/C8TA03667E.

[41] J. Reed, G. Ceder, and A. Van Der Ven, “Layered-to-spinel phase transition in LixMnO2,” *Electrochem. Solid-State Lett.*, vol. 4, no. 6, pp. 78–81, 2001, doi:

10.1149/1.1368896.

[42] M. Freire, O. I. Lebedev, A. Maignan, C. Jordy, and V. Pralong, “Nanostructured Li2MnO3: A disordered rock salt type structure for high energy density Li ion batteries,” *J. Mater. Chem. A*, vol. 5, no. 41, pp. 21898–21902, 2017, doi: 10.1039/c7ta07476j.

[43] B. B. Ammundsen and J. Paulsen, “Novel Lithium-Ion Cathode Materials Based on Layered Manganese Oxides,” no. 12, pp. 943–956, 2001.

[44] P. Kalyani, S. Chitra, T. Mohan, and S. Gopukumar, “Lithium metal rechargeable cells using Li2MnO3 as the positive electrode,” *J. Power Sources*, vol. 80, no. November 1998, pp. 103–106, 1999.

[45] A. D. Robertson and P. G. Bruce, “The origin of electrochemical activity in Li2MnO3,” *Chem. Commun.*, vol. 2, no. 23, pp. 2790–2791, 2002, doi: 10.1039/b207945c.

[46] T. Ohzuku, M. Nagayama, K. Tsuji, and K. Ariyoshi, “High-capacity lithium insertion materials of lithium nickel manganese oxides for advanced lithium-ion batteries: Toward rechargeable capacity more than 300 mA h g-1,” *J. Mater. Chem.*, vol. 21, no. 27, pp. 10179–10188, 2011, doi: 10.1039/c0jm04325g.

[47] N. Yabuuchi, K. Yoshii, S. T. Myung, I. Nakai, and S. Komaba, “Detailed studies of a high-capacity electrode material for rechargeable batteries, Li2MnO3-LiCo1/3Ni 1/3Mn1/3O2,” *J. Am. Chem. Soc.*, vol. 133, no. 12, pp. 4404–4419, 2011, doi: 10.1021/ja108588y.

[48] J. R. D. Monique N. Richard, E.W. Fuller, “The effect of ammonia reduction on the spinel electrode materials, LiMn204 and Li (Lil/3Mns/3)O4,” vol. 73, pp. 81–91, 1994.

[49] Z. Lu and J. R. Dahn, “Understanding the anomalous capacity of Li/Li[Ni xLi (1/3-2x/3)Mn (2/3-x/3)]O 2 cells using in situ X-ray diffraction and electrochemical studies,” *J. Electrochem. Soc.*, vol. 149, no. 7, pp. 815–822, 2002, doi: 10.1149/1.1480014.

[50] K. Luo *et al.*, “Charge-compensation in 3d-transition-metal-oxide intercalation cathodes through the generation of localized electron holes on oxygen,” *Nat. Chem.*, vol. 8, no. 7, pp. 684–691, 2016, doi: 10.1038/nchem.2471.

[51] K. Du, J. Zhu, G. Hu, H. Gao, Y. Li, and J. B. Goodenough, “Exploring reversible oxidation of oxygen in a manganese oxide,” *Energy Environ. Sci.*, vol. 9, no. 8, pp. 2575–2577, 2016, doi: 10.1039/c6ee01367h.

[52] D. Pasero, V. McLaren, S. De Souza, and A. R. West, “Oxygen nonstoichiometry in Li2MnO3: An alternative explanation for its anomalous electrochemical activity,” *Chem. Mater.*, vol. 17, no. 2, pp. 345–348, 2005, doi: 10.1021/cm040186r.

[53] A. Boulineau, L. Croguennec, C. Delmas, and F. Weill, “Structure of Li2MnO 3 with different degrees of defects,” *Solid State Ionics*, vol. 180, no. 40, pp. 1652–1659, 2010, doi: 10.1016/j.ssi.2009.10.020.

[54] L. Xiao *et al.*, “Effects of structural defects on the electrochemical activation of Li2MnO3,” *Nano Energy*, vol. 16, pp. 143–151, 2015, doi: 10.1016/j.nanoen.2015.06.011.

[55] A. Urban, J. Lee, and G. Ceder, “The configurational space of rocksalt-type oxides for

high-capacity lithium battery electrodes," *Adv. Energy Mater.*, vol. 4, no. 13, pp. 1–9, 2014, doi: 10.1002/aenm.201400478.

[56] D. Ye *et al.*, "Understanding the Origin of Li2MnO3 Activation in Li-Rich Cathode Materials for Lithium-Ion Batteries," *Adv. Funct. Mater.*, vol. 25, no. 48, pp. 7488–7496, 2015, doi: 10.1002/adfm.201503276.

[57] A. R. Armstrong *et al.*, "Demonstrating Oxygen Loss and Associated Structural Reorganization in the Lithium Battery Cathode Li[Ni 0.2 Li 0.2 Mn 0.6]O 2 (Li2MnO3-like structure)," *J. Am. Chem. Soc.*, vol. 128, no. 26, pp. 8694–8698, 2006, doi: 10.1021/ja062027+.

[58] N. Yabuuchi *et al.*, "Origin of stabilization and destabilization in solid-state redox reaction of oxide ions for lithium-ion batteries," *Nat. Commun.*, vol. 7, no. May, pp. 1–10, 2016, doi: 10.1038/ncomms13814.

[59] D. H. Seo, J. Lee, A. Urban, R. Malik, S. Kang, and G. Ceder, "The structural and chemical origin of the oxygen redox activity in layered and cation-disordered Li-excess cathode materials," *Nat. Chem.*, vol. 8, no. 7, pp. 692–697, 2016, doi: 10.1038/nchem.2524.

[60] M. Diaz-Lopez *et al.*, "Interplay of cation and anion redox in Li4Mn2O5 cathode material and prediction of improved Li4(Mn,M)2O5 electrodes for Li-ion batteries," *J. Phys. Chem. C*, vol. 122, no. 51, pp. 29586–29597, 2018, doi: 10.1021/acs.jpcc.8b09397.

[61] M. Diaz-Lopez *et al.*, "Local Structure and Lithium Diffusion Pathways in Li4Mn2O5High Capacity Cathode Probed by Total Scattering and XANES," *Chem. Mater.*, vol. 30, no. 9, pp. 3060–3070, 2018, doi: 10.1021/acs.chemmater.8b00827.

[62] M. Freire *et al.*, "A new active Li-Mn-O compound for high energy density Li-ion batteries," *Nat. Mater.*, vol. 15, no. 2, pp. 173–177, 2016, doi: 10.1038/nmat4479.

[63] S. Juliette.A, D. Marcia M., and R. John, "Synthesis and electrochemistry of Li3MnO4: Mn in the 5+ oxidation state," no. July, pp. 35–43, 2010.

[64] M. Pigłowska, B. Kurc, and M. Galinski, "Challenges for Safe Electrolytes Applied in Lithium-Ion," pp. 1–52, 2021.

[65] Y. E. Hyung, D. R. Vissers, and K. Amine, "Flame-retardant additives for lithium-ion batteries," vol. 121, pp. 383–387, 2003, doi: 10.1016/S0378-7753(03)00225-8.

[66] E. Bolimowska, T. Gutel, and S. M. He, "Ionic liquid-based electrolytes for lithium-ion batteries : review of performances of various electrode systems," pp. 149–155, 2016, doi: 10.1007/s10800-015-0905-1.

[67] S. Stramare, V. Thangadurai, and W. Weppner, "Lithium Lanthanum Titanates : A Review," pp. 3974–3990, 2003.

[68] B. Kumar, J. Electrochem, A. Soc, B. Kumar, D. Thomas, and J. Kumar, "Space-Charge-Mediated Superionic Transport in Lithium Ion Conducting Glass – Ceramics Space-Charge-Mediated Superionic Transport in Lithium Ion Conducting Glass – Ceramics," 2009, doi: 10.1149/1.3122903.

[69] J. W. Fergus, “Ceramic and polymeric solid electrolytes for lithium-ion batteries,” *J. Power Sources*, vol. 195, no. 15, pp. 4554–4569, 2010, doi: 10.1016/j.jpowsour.2010.01.076.

[70] J. S. Weaving *et al.*, “Development of high energy density Li-ion batteries based on,” vol. 98, pp. 733–735, 2001.

[71] H. Zhang, Y. Yang, D. Ren, L. Wang, and X. He, “Graphite as anode materials : Fundamental mechanism , recent progress and advances,” *Energy Storage Mater.*, vol. 36, no. October 2020, pp. 147–170, 2021, doi: 10.1016/j.ensm.2020.12.027.

[72] F. Orsini, “In situ SEM study of the interfaces in plastic lithium cells,” pp. 918–921, 1999.

[73] C. De Casas and W. Li, “A review of application of carbon nanotubes for lithium ion battery anode material,” *J. Power Sources*, vol. 208, pp. 74–85, 2012, doi: 10.1016/j.jpowsour.2012.02.013.

[74] S. Iijima, “Helical microtubules of graphitic carbon.”

[75] B. C. Kim, K. S. Yang, M. Kojima, K. Yoshida, Y. J. Kim, and Y. A. Kim, “Fabrication of Electrospinning-Derived Carbon Nanofiber Webs for the Anode Material of Lithium-Ion Secondary Batteries **,” pp. 2393–2397, 2006, doi: 10.1002/adfm.200500911.

[76] J. M. Raimond, M. Brune, Q. Computation, F. De Martini, and C. Monroe, “Electric Field Effect in Atomically Thin Carbon Films,” vol. 306, no. October, pp. 666–670, 2004.

[77] C. Park, J. Kim, H. Sohn, C. Park, and J. Kim, “Li-alloy based anode materials for Li secondary batteries,” pp. 3115–3141, 2010, doi: 10.1039/b919877f.

[78] X. Su *et al.*, “Silicon-Based Nanomaterials for Lithium-Ion Batteries : A Review,” pp. 1–23, 2014, doi: 10.1002/aenm.201300882.

[79] Y. I. N. Yaxia, W. A. N. Lijun, and G. U. O. Yuguo, “Silicon-based nanomaterials for lithium-ion batteries,” vol. 57, no. 32, pp. 4104–4110, 2012, doi: 10.1007/s11434-012-5017-2.

[80] J. H. Ryu, J. W. Kim, Y. E. Sung, and S. M. Oh, “Failure modes of silicon powder negative electrode in lithium secondary batteries,” *Electrochemical and Solid-State Letters*, vol. 7, no. 10. 2004, doi: 10.1149/1.1792242.

[81] Z. Liu *et al.*, “Silicon oxides: a promising family of anode materials for lithium-ion batteries,” *Chem Soc Rev*, vol. 48, pp. 285–309, 2019, doi: 10.1039/c8cs00441b.

[82] W. Wei, J. Xu, M. Xu, S. Zhang, and L. Guo, “Recent progress on Ge oxide anode materials for lithium-ion batteries,” vol. 61, no. 5, pp. 515–525, 2018.

[83] M. Zhang, T. Wang, and G. Cao, “Promises and challenges of tin-based compounds as anode materials for lithium-ion batteries,” *Int. Mater. Rev.*, vol. 60, no. 6, pp. 330–352, 2015, doi: 10.1179/1743280415Y.0000000004.

[84] T. Ohzuku, A. Ueda, and N. Yamamoto, “Zero-Strain Insertion Material of Li [Li1 / 3Ti5 / 3] O 4 for Rechargeable Lithium Cells,” *J. Electrochem. Soc.*, vol. 142, no. 5,

pp. 1431–1435, 1995, doi: 10.1149/1.2048592.

[85] T. F. Yi, L. J. Jiang, J. Shu, C. B. Yue, R. S. Zhu, and H. Bin Qiao, "Recent development and application of Li4Ti5O 12 as anode material of lithium ion battery," *J. Phys. Chem. Solids*, vol. 71, no. 9, pp. 1236–1242, 2010, doi: 10.1016/j.jpcs.2010.05.001.

[86] A. R. West, "Solid state chemistry and its applications." https://www.vlebooks.com/Product/Index/327871?page=0 (accessed Aug. 05, 2022).

[87] P. G. Koutsoukos, "Progress in Colloid and Polymer Science: Trends in Colloid and Interface Science XV," vol. 118, p. 309, 2001, [Online]. Available: https://linkinghub.elsevier.com/retrieve/pii/S152500161632679X.

[88] S. G. Intasa-ard, K. Imwiset, S. Bureekaew, and M. Ogawa, "Mechanochemical way for the preparation of intercalation compounds," *Dalt. Trans.*, vol. 47, pp. 2896–2916, 2018, doi: 10.1039/C7DT03736H.

[89] H. Kulla, M. Wilke, F. Fischer, M. Röllig, C. Maierhofer, and F. Emmerling, "Warming up for mechanosynthesis - temperature development in ball mills during synthesis," *Chem. Commun.*, vol. 53, no. 10, pp. 1664–1667, 2017, doi: 10.1039/c6cc08950j.

[90] A. Perejón *et al.*, "Direct mechanosynthesis of pure BiFeO3 perovskite nanoparticles: reaction mechanism," *J. Mater. Chem. C*, vol. 1, no. 22, p. 3551, 2013, doi: 10.1039/c3tc30446a.

[91] J. De, A. M. Umarji, and K. Chattopadhyay, "Origin of contamination and role of mechanochemistry during mechanical alloying: the case of Ag-Te alloys," *Mater. Sci. Eng. A*, vol. 448–451, pp. 1062–1066, 2007, doi: 10.1016/j.msea.2006.02.268.

[92] P. Baláž *et al.*, "Hallmarks of mechanochemistry: from nanoparticles to technology," *Chem. Soc. Rev.*, vol. 42, no. 18, p. 7571, 2013, doi: 10.1039/c3cs35468g.

[93] A. Düvel, "Ionic conductivity and structure of M1−xPbxF2 (M = Ca, Sr, Ba) solid solutions prepared by ball milling," *Dalt. Trans.*, vol. 48, no. 3, pp. 859–871, 2019, doi: 10.1039/c8dt03759k.

[94] H. A. Lara-García, O. Ovalle-Encinia, J. Ortiz-Landeros, E. Lima, and H. Pfeiffer, "Synthesis of Li 4+: X Si 1- x Fe x O 4 solid solution by dry ball milling and its highly efficient CO 2 chemisorption in a wide temperature range and low CO 2 concentrations," *J. Mater. Chem. A*, vol. 7, no. 8, pp. 4153–4164, 2019, doi: 10.1039/c8ta12359d.

[95] C. Bolm and J. G. Hernández, "Mechanochemistry of Gaseous Reactants," *Angew. Chemie - Int. Ed.*, vol. 58, no. 11, pp. 3285–3299, 2019, doi: 10.1002/anie.201810902.

[96] J. Kano, E. Kobayashi, W. Tongamp, and F. Saito, "Preparation of GaN powder by mechanochemical reaction between Ga2O3 and Li3N," *J. Alloys Compd.*, vol. 464, no. 1–2, pp. 337–339, 2008, doi: 10.1016/j.jallcom.2007.09.120.

[97] J. M. F. Rodríguez, J. Morales, and J. L. Tirado, "Mechanochemical preparation and degradation of LiCoO2," *React. Solids*, vol. 4, no. 1–2, pp. 163–171, 1987, doi: 10.1016/0168-7336(87)80095-5.

[98] M. Obrovac, "Structure and electrochemistry of LiMO2 (M=Ti, Mn, Fe, Co, Ni) prepared by mechanochemical synthesis," *Solid State Ionics*, vol. 112, no. 1–2, pp. 9–

19, 1998, doi: 10.1016/S0167-2738(98)00225-2.

[99] M. N. Obrovac, R. A. Dunlap, R. J. Sanderson, and J. R. Dahn, "The Electrochemical Displacement Reaction of Lithium with Metal Oxides," *J. Electrochem. Soc.*, vol. 148, no. 6, p. A576, 2001, doi: 10.1149/1.1370962.

[100] N. Kosova and E. Devyatkina, "Soft mechanochemical synthesis: Preparation of cathode materials for rechargeable lithium batteries," *Ann. Chim. Sci. des Mater.*, vol. 27, no. 6, pp. 77–90, 2002, doi: 10.1016/S0151-9107(02)90016-4.

[101] N. Kosova, E. Devyatkina, and D. Osintsev, "Dispersed materials for rechargeable lithium batteries: Reactive and non-reactive grinding," *J. Mater. Sci.*, vol. 39, no. 16–17, pp. 5031–5036, 2004, doi: 10.1023/B:JMSC.0000039181.03644.b0.

[102] F. Badway, F. Cosandey, N. Pereira, and G. G. Amatucci, "Carbon Metal Fluoride Nanocomposites: High-Capacity Reversible Metal Fluoride Conversion Materials as Rechargeable Positive Electrodes for Li Batteries," *J. Electrochem. Soc.*, vol. 150, no. 10, pp. 1318–1327, 2003, doi: 10.1149/1.1602454.

[103] A. Sakuda *et al.*, "Rock-salt-type lithium metal sulphides as novel positive-electrode materials," *Sci. Rep.*, vol. 4, pp. 2–6, 2014, doi: 10.1038/srep04883.

[104] L. Takacs, "The historical development of mechanochemistry," *Chem. Soc. Rev.*, vol. 42, no. 18, p. 7649, 2013, doi: 10.1039/c2cs35442j.

[105] A. Rougier, I. Saadoune, P. Gravereau, P. Willmann, and C. Delmas, "Effect of cobalt substitution on cationic distribution in LiNi1-yCoyO2 electrode materials," *Solid State Ionics*, vol. 90, no. 1–4, pp. 83–90, 1996.

[106] J. P. Peres *et al.*, "The relationship between the composition of lithium nickel oxide and the loss of reversibility during the first cycle," *J. Phys. Chem. Solids*, vol. 57, no. d, pp. 1057–1060, 1995.

[107] A. Rougier, P. Gravereau, and C. Delmas, "Optimization of the Composition of the Li1-xNi1+xO2 Electrode Materials: Sfructural, Magnetic, and Electrochemical Studies," *Electrochem. Soc. Proc. Ser. Pennington, NJ*, vol. 143, no. 4, pp. 1168–1175, 1996.

[108] K. Kang *et al.*, "Synthesis and Electrochemical Properties of Layered Li0. 9Ni0. 45Ti0. 55O2," *Chem. Mater*, vol. 15, no. 23, pp. 4503–4507, 2003, doi: 10.1021/cm034455+.

[109] K. Ozawa *et al.*, "Structural modifications caused by electrochemical lithium extraction for two types of layered LiVO2(R-3m)," *J. Power Sources*, vol. 174, no. 2, pp. 469–472, 2007, doi: 10.1016/j.jpowsour.2007.06.100.

[110] A. Van der Ven and G. Ceder, "Lithium diffusion mechanisms in layered intercalation compounds," *J. Power Sources*, vol. 97–98, no. June 2000, pp. 529–531, 2001, doi: 10.1016/S0378-7753(01)00638-3.

[111] K. Kang and G. Ceder, "Factors that affect Li mobility in layered lithium transition metal oxides," *Phys. Rev. B - Condens. Matter Mater. Phys.*, vol. 74, no. 9, pp. 1–7, 2006, doi: 10.1103/PhysRevB.74.094105.

[112] A. Van Der Ven, J. Bhattacharya, and A. A. Belak, "Understanding Li diffusion in Li-intercalation compounds," *Acc. Chem. Res.*, vol. 46, no. 5, pp. 1216–1225, 2013, doi:

10.1021/ar200329r.

[113] V. Pralong, V. Gopal, V. Caignaert, V. Duffort, and B. Raveau, “Lithium-rich rock-salt-type vanadate as energy storage cathode: Li 2-xVO3,” *Chem. Mater.*, vol. 24, no. 1, pp. 12–14, 2012, doi: 10.1021/cm203281q.

[114] N. Yabuuchi *et al.*, “High-capacity electrode materials for rechargeable lithium batteries: Li3NbO4-based system with cation-disordered rocksalt structure.,” *Proc. Natl. Acad. Sci. U. S. A.*, vol. 112, no. 25, pp. 7650–5, 2015, doi: 10.1073/pnas.1504901112.

[115] R. Chen *et al.*, “Li+ intercalation in isostructural Li2VO3 and Li2VO2F with O2- and mixed O2-/F- anions,” *Phys. Chem. Chem. Phys.*, vol. 17, no. 26, pp. 17288–17295, 2015, doi: 10.1039/c5cp02505b.

[116] R. Chen *et al.*, “disordered lithium-rich oxyfluoride as a stable host for enhanced Li+ intercalation storage,” *Adv. Energy Mater.*, vol. 5, no. 9, pp. 1–7, 2015, doi: 10.1002/aenm.201401814.

[117] J. Lee, A. Urban, X. Li, D. Su, G. Hautier, and G. Ceder, “Unlocking the potential of cation-disordered oxides for rechargeable lithium batteries,” *Science (80-.).*, vol. 343, no. 6170, pp. 519–522, 2014, doi: 10.1126/science.1246432.

[118] C. S. Johnson, J. S. Kim, C. Lefief, N. Li, J. T. Vaughey, and M. M. Thackeray, “The significance of the Li2MnO3 component in ‘composite’ xLi 2MnO3·(1 - x)Lin0.5Ni0.5O2 electrodes,” *Electrochem. commun.*, vol. 6, no. 10, pp. 1085–1091, 2004, doi: 10.1016/j.elecom.2004.08.002.

[119] R. Wang *et al.*, “Atomic structure of Li2MnO3 after partial delithiation and re-lithiation,” *Adv. Energy Mater.*, vol. 3, no. 10, pp. 1358–1367, 2013, doi: 10.1002/aenm.201200842.

[120] Z. Lu, L. Y. Beaulieu, R. A. Donaberger, C. L. Thomas, and J. R. Dahn, “Synthesis structure, and electrochemical behavior of Li[Ni xLi 1/3-2x/3Mn 2/3-x/3]O 2,” *J. Electrochem. Soc.*, vol. 149, no. 6, pp. 778–791, 2002, doi: 10.1149/1.1471541.

[121] A. Ito, Y. Sato, T. Sanada, M. Hatano, H. Horie, and Y. Ohsawa, “In situ X-ray absorption spectroscopic study of Li-rich layered cathode material Li[Ni0.17Li0.2Co0.07Mn 0.56]O2,” *J. Power Sources*, vol. 196, no. 16, pp. 6828–6834, 2011, doi: 10.1016/j.jpowsour.2010.09.105.

[122] B. Xu, C. R. Fell, M. Chi, and Y. S. Meng, “Identifying surface structural changes in layered Li-excess nickel manganese oxides in high voltage lithium ion batteries: A joint experimental and theoretical study,” *Energy Environ. Sci.*, vol. 4, no. 6, pp. 2223–2233, 2011, doi: 10.1039/c1ee01131f.

[123] M. Sathiya *et al.*, “Reversible anionic redox chemistry in high-capacity layered-oxide electrodes,” *Nat. Mater.*, vol. 12, no. 9, pp. 827–835, 2013, doi: 10.1038/nmat3699.

[124] N. Twu *et al.*, “Designing new lithium-excess cathode materials from percolation theory: Nanohighways in LixNi2-4x/3Sbx/3O2,” *Nano Lett.*, vol. 15, no. 1, pp. 596–602, 2015, doi: 10.1021/nl5040754.

[125] A. Kapylou *et al.*, “Improved Thermal Stability of Lithium-Rich Layered Oxide by Fluorine Doping,” *ChemPhysChem*, vol. 19, no. 1, pp. 116–122, 2018, doi:

10.1002/cphc.201700927.

[126] J. Lee *et al.*, "Mitigating oxygen loss to improve the cycling performance of high capacity cation-disordered cathode materials," *Nat. Commun.*, vol. 8, no. 1, 2017, doi: 10.1038/s41467-017-01115-0.

[127] M. A. Jones, P. J. Reeves, I. D. Seymour, M. J. Cliffe, S. E. Dutton, and C. P. Grey, "Short-range ordering in a battery electrode, the 'cation-disordered' rocksalt Li1.25Nb0.25Mn0.5O2," *Chem. Commun.*, vol. 55, no. 61, pp. 9027–9030, 2019, doi: 10.1039/c9cc04250d.

[128] D. Mohanty *et al.*, "Modification of Ni-Rich FCG NMC and NCA Cathodes by Atomic Layer Deposition: Preventing Surface Phase Transitions for High-Voltage Lithium-Ion Batteries," *Sci. Rep.*, vol. 6, no. February, pp. 1–16, 2016, doi: 10.1038/srep26532.

[129] M. Tabuchi *et al.*, "Preparation of lithium manganese oxides containing iron," *J. Power Sources*, vol. 97–98, pp. 415–419, 2001, doi: 10.1016/S0378-7753(01)00684-X.

[130] M. Tabuchi *et al.*, "Synthesis, cation distribution, and electrochemical properties of Fe-substituted Li2MnO3 as a novel 4 V positive electrode material," *J. Electrochem. Soc.*, vol. 149, no. 5, 2002, doi: 10.1149/1.1462791.

[131] S. H. Kang, J. Kim, M. E. Stoll, D. Abraham, Y. K. Sun, and K. Amine, "Layered Li(Ni0.5-xMn0.5-xM′2x)O2 (M′ = Co, Al, Ti; x = 0, 0.025) cathode materials for Li-ion rechargeable batteries," *J. Power Sources*, vol. 112, no. 1, pp. 41–48, 2002, doi: 10.1016/S0378-7753(02)00360-9.

[132] C. S. Johnson *et al.*, "Structural and electrochemical analysis of layered compounds from Li2MnO3," *J. Power Sources*, vol. 81–82, pp. 491–495, 1999, doi: 10.1016/S0378-7753(99)00248-7.

[133] Z. Q. Wang, Y. C. Chen, and C. Y. Ouyang, "Polaron states and migration in F-doped Li2MnO3," *Phys. Lett. Sect. A Gen. At. Solid State Phys.*, vol. 378, no. 32–33, pp. 2449–2452, 2014, doi: 10.1016/j.physleta.2014.06.025.

[134] S. Jouanneau and J. R. Dahn, "Preparation, structure, and thermal stability of new NixCo1-2xMnx(OH)2 ($0 \leq x \leq 1/2$) phases," *Chem. Mater.*, vol. 15, no. 2, pp. 495–499, 2003, doi: 10.1021/cm020818e.

[135] Y. Luo *et al.*, "Fluorine gradient-doped LiNi0.5Mn1.5O4 spinel with improved high voltage stability for Li-ion batteries," *Electrochim. Acta*, vol. 238, pp. 237–245, 2017, doi: 10.1016/j.electacta.2017.04.043.

[136] H. R. Lee, B. Lee, K. Y. Chung, B. W. Cho, K. Y. Lee, and S. H. Oh, "Scalable synthesis and electrochemical investigations of fluorine-doped lithium manganese spinel oxide," *Electrochim. Acta*, vol. 136, pp. 396–403, 2014, doi: 10.1016/j.electacta.2014.05.106.

[137] Z. Lun *et al.*, "Improved Cycling Performance of Li-Excess Cation-Disordered Cathode Materials upon Fluorine Substitution," *Adv. Energy Mater.*, vol. 9, no. 2, pp. 1–11, 2019, doi: 10.1002/aenm.201802959.

[138] W. D. Richards, S. T. Dacek, D. A. Kitchaev, and G. Ceder, "Fluorination of Lithium-Excess Transition Metal Oxide Cathode Materials," *Adv. Energy Mater.*, vol. 8, no. 5, pp. 1–7, 2018, doi: 10.1002/aenm.201701533.

[139] M. Ménétrier *et al.*, "NMR evidence of LiF coating rather than fluorine substitution in Li(Ni0.425Mn0.425Co0.15)O2," *J. Solid State Chem.*, vol. 181, no. 12, pp. 3303–3307, 2008, doi: 10.1016/j.jssc.2008.09.002.

[140] R. J. Clément, D. Kitchaev, J. Lee, and Gerbrand Ceder, "Short-Range Order and Unusual Modes of Nickel Redox in a Fluorine-Substituted Disordered Rocksalt Oxide Lithium-Ion Cathode," *Chem. Mater.*, vol. 30, no. 19, pp. 6945–6956, 2018, doi: 10.1021/acs.chemmater.8b03794.

[141] A. J. Naylor *et al.*, "Stabilization of Li-Rich Disordered Rocksalt Oxyfluoride Cathodes by Particle Surface Modification," *ACS Appl. Energy Mater.*, vol. 3, no. 6, pp. 5937–5948, 2020, doi: 10.1021/acsaem.0c00839.

[142] R. Chen *et al.*, "Li^{+} intercalation in isostructural Li<inf>2</inf>VO<inf>3</inf> and Li<inf>2</inf>VO<inf>2</inf>F with O^{2-} and mixed O^{2-}/F^{-} anions," *Phys. Chem. Chem. Phys.*, vol. 17, no. 26, pp. 17288–17295, 2015, doi: 10.1039/c5cp02505b.

[143] B. Dong, R. Jarkaneh, S. Hull, N. Reeves-McLaren, J. J. Biendicho, and A. R. West, "Synthesis, structure and electrical properties of N-doped Li3VO4," *J. Mater. Chem. A*, vol. 4, no. 4, pp. 1408–1413, 2016, doi: 10.1039/C5TA07823G.

[144] Z. Q. Wang, M. S. Wu, B. Xu, and C. Y. Ouyang, "Improving the electrical conductivity and structural stability of the Li2MnO3 cathode via P doping," *J. Alloys Compd.*, vol. 658, pp. 818–823, 2016, doi: 10.1016/j.jallcom.2015.11.013.

[145] M. Diaz-lopez, P. A. Chater, Y. Joly, O. Proux, J. Hazemann, and V. Pralong, "Reversible densification in nano-Li2MnO3 cation disordered rock-salt Li-ion battery cathodes," vol. 2, pp. 10998–11010, 2020, doi: 10.1039/d0ta03372c.

[146] M. Diaz-Lopez *et al.*, "Li2O:Li–Mn–O Disordered Rock-Salt Nanocomposites as Cathode Prelithiation Additives for High-Energy Density Li-Ion Batteries," *Adv. Energy Mater.*, vol. 10, no. 7, pp. 1–6, 2020, doi: 10.1002/aenm.201902788.

[147] A. H. Simon, "Sputter Processing," *Handb. Thin Film Depos. Tech. Process. Technol. Third Ed.*, pp. 55–88, Jan. 2012, doi: 10.1016/B978-1-4377-7873-1.00004-8.

[148] X. Bu, T. Wang, and G. Hall, "Determination of halogens in organic compounds by high resolution inductively coupled plasma mass spectrometry (HR-ICP-MS)," *J. Anal. At. Spectrom.*, vol. 18, no. 12, pp. 1443–1451, 2003, doi: 10.1039/b306570g.

Chapter 2 Experimental

2.1 Sample processing procedures

2.1.1 Solid state reaction

All reactants used in this thesis are listed in Table 2.1. They were dried first at 180 ℃ (except: Mn_3O_4, 600 ℃; Mn_2O_3, 600-650 ℃; Nb_2O_5, 900 ℃; TiO_2, 900 ℃; Al_2O_3, 900 ℃; Fe_2O_3, 600 ℃; Co_3O_4, 600 ℃; and NiO, 800 ℃) overnight and were then weighed in their stoichiometric amounts with a precision of ± 0.001g.The reactants were mixed in acetone and ground with an agate mortar and pestle for 20 minutes to prepare the precursor powders. The powders were heated in muffle furnaces in air except those where the reactions were in another atmosphere, such as N_2 or O_2, which were heated in a tube furnace. As all samples contained lithium which reacts with Al_2O_3, powders were placed in alumina crucibles lined with gold foil during heating. The solid-state synthesis programs were set as two separate programs. In the first program, powders were heated at 150 ℃ for 2 hours to remove the organic solvents and then heated at 600℃ for 6 hours to decompose Li_2CO_3 and initiate reaction. The powders were cooled to room temperature, ground for 30 minutes and heated at specific conditions for the final synthesis and then cooled to room temperature. All the heating and cooling rates were 5 ℃/min.

2.1.2 Mechanosynthesis

The reactants were ball-milled by planetary ball mill, Pulverisette 6 (Fritsch) in three different milling media: i. an 80-mL stainless hardened steel jar with 10 of 15-mm-diameter steel balls; ii. an 80-mL tungsten carbide jar with 25 of 10-mm-diameter tungsten carbide balls; iii. an 80-mL zirconia jar with 25 of 10-mm-diameter zirconia balls. The mixtures were milled at 350 rpm in air for different times.

Table 2.1 Reagents, purity, supplier and drying temperature

Reagent	**Purity**	**Supplier**	**Drying temperature (°C)**
Li_2O_2	90%	Alfa Aesar	80 (in vacuum)
Li_2O	95%	Aldrich	80 (in vacuum)
Li_2CO_3	99%	Aldrich	180
$LiOH·H_2O$	99.95%	Aldrich	80
$LiCH_3COO·2H_2O$	99%	Aldrich	80
LiF	99.9%	Fluka	180
MnO	99%	Aldrich	180
Mn_2O_3	99%	Aldrich	600-650
Mn_3O_4	97%	Aldrich	600
MnO_2	99%	Aldrich	180
Nb_2O_5	99%	Aldrich	180
TiO	99.9%	Aldrich	-
Ti_2O_3	99.9%	Alfa	-
TiO_2	99.9%	Aldrich	900
Al_2O_3	99%	Aldrich	900
Fe_2O_3	99%	Aldrich	600
CoO	99%	Aldrich	180
Co_3O_4	99%	Aldrich	600
V_2O_5	99.9%	Aldrich	180
V_2O_3	99.6%	Aldrich	-
NiO	99%	Aldrich	800

Note: '-' means the reactants were not dried before use due to the concern on their thermal stability.

Table 2.2 Milling materials data

Material	Main component	Density g/cm^3
Hardened, stainless steel	Fe-Cr	7.65
Tungsten carbide	WC	14.3
Zirconia	ZrO_2	5.7

The choice of different size of balls depends on the size of feed materials. Feed materials with smaller size require smaller grinding balls and give corresponding smaller final products. For a 80-ml jar, it is recommended that the amount of filling powders is 10-30 ml, with 10 pcs of 15-mm-diameter or 25 pcs of 10-mm-diameter balls. However, the size of samples in this thesis is relatively small, usually 1-2 g, but for an 80-ml-jar, it requires at least 40 g of powders to meet the minimum filling amount. Considering the factors with an impact on including grinding time, speed, and number and size of balls, the size of samples in this thesis was kept as 1-2 g, but the powder-to-ball mass ratio was fixed at 1: 40, so the number of balls were largely reduced and the grinding speed was relatively low. However, this may cause extended contamination to samples. Future work for high quality characterisations, such as long-cycle battery test, Rietveld refinement, and pair distribution function (PDF), samples need to be re-prepared with large sample or small jars and higher milling speed to reduce contamination. Details of parameters associated with the milling media are listed in Table 2.2.

2.1.3 Pellet preparation for XRF, battery test and impedance measurements

The powders of products that were used for XRF, battery tests and impedance measurements were pressed uniaxially into pellets under ~1 tonne of pressure, using a 5-mm-diameter or 10-mm-diameter die. Pellets for impedance measurements were then sintered on Au foil at different temperatures: i. pellets produced by solid state reaction were sintered at the synthesis temperature + 10-20 ℃; ii. pellets produced by mechanosynthesis were sintered at 500 ℃. Specifically, in section 3.1.3.3, pellets of Li_2MnO_3 produced by five different synthesis and sintering procedures were studied by impedance measurements, and details are shown in section 3.1.3.3. XANES measurements used pellets too and details are shown in section 2.8.

2.2 X-ray diffraction

2.2.1 Instrumentation

X-Ray Diffraction (XRD) is a fingerprinting technique that can identify the phase(s) present, establish phase purity and calculate lattice parameters of single phase products. X-rays are waves of electromagnetic radiation. They can be scattered by crystalline to solids to produce a

regular array of spherical waves, which cancel each other out through destructive interference but add constructively in specific directions, and produce diffraction patterns.

All compositions were measured by XRD using a Bruker D2 Phaser, with Cu K_α radiation (λ=1.5406 Å) at following stages: i. raw materials before use; ii. products after synthesis and heat treatment; iii. products after TG measurement. For phase identification, the reference data were obtained from the inorganic crystal structure database (ICSD). Lattice parameter measurements were carried out by measuring the powders with Si internal standard for peak position calibration, using a high resolution STOE-Stadi PSD with Mo $K_{\alpha 1}$ radiation (λ=0.7093 Å). The data were analysed with WinX^{pow} software.

2.2.2 Line broadening

When crystal size is below ~2000Å diameter, extra line-broadening of X-ray powders diffraction peaks occurs. A common formula used to calculate the particle size from the extra broadening is the Scherrer equation, as follows:

$$t = \frac{0.9\lambda}{B\cos\theta_B}$$

where:

t is the thickness of crystal (in angstroms),

λ is the wavelength of X-ray,

θ_B is the Bragg angle,

B is the extra line broadening, which is measured from full width at half maximum (FWHM) and obtained from the Warren formula:

$$B^2 = B_M^2 - B_S^2$$

where:

B_M is FWHM (in radians) of a sample broad peak,

B_S is FWHM (in radians) of the peak that is at a similar 2θ position to the sample peak(s) of a standard material with grain size > 2000 Å.

2.2.3 Fluorescence phenomenon

Scattering of X-rays can occur in elastic and inelastic ways. In elastic scattering, the X-ray is diffracted by the electron it hits. The electron emits an electromagnetic wave of its own, which has the same wavelength as the incident beam and therefore contributes to the diffractogram. In inelastic scattering, the X-ray is also diffracted by the electron it hits, but the X-ray knocks one of the electrons out of the inner shell of an atom and the atom emits a characteristic fluorescent radiation. It is the basis of the technique of XRF (section 2.4) but an undesirable phenomenon in XRD. A large part of the energy of an incident beam may be absorbed so that the intensity of beam that reaches the detector is low. Fluorescent radiation is also detected, which leads to a high background. In this thesis, Mn (Z=25) compounds in Chapter 3-5, Co (Z=27) compounds in Chapter 6 and Fe (Z=26) contamination caused by steel jars are likely to show fluorescence in XRD using Cu K_α radiation, leading to XRD patterns that have peaks with low intensity and noisy background.

2.3 Thermal analysis: Thermogravimetry (TG) and Differential scanning calorimetry (DSC)

2.3.1 Thermogravimetry (TG)

Thermogravimetry measures the mass change in samples as a function of temperature or time. The sample is heated at a specific rate and under a specific atmosphere. Decomposition or absorption occurs over a range of temperatures. The mass difference can be used for quantitative calculations of compositional changes. The thermal stability and properties of chemicals under different atmospheres is observed.

TG measurements were carried out with a Perkin Elmer Pyris TGA. The calibration was carried out regularly using 10 mg calibration weights. The initial samples' weight was ~150 mg. The sample holder was made of Al_2O_3. The heating and cooling rates were set to 5 °C/min, except some experiments for study of the heating rate in section 3.1.2.3. Three different atmospheres were applied, air, N_2 and O_2 to study the effect of different atmospheres in sections 3.1.2.3 and 4.2.6.1.

2.3.2 Differential scanning calorimetry (DSC)

Differential scanning calorimetry is similar to differential thermal analysis (DTA), which measures the difference in temperature between the sample and a reference material to observe the thermal behaviours, exothermic and endothermic reactions. DSC is more accurate than DTA, as it gives a calorimetric response; it measures directly the heat flows into/out of the sample. DSC measurements were carried out with a Perkin Elmer Diamond DSC. The sample holder was made of Al_2O_3. An Ar flow was applied during measurement and heating and cooling rates were set to 5 ℃/min. Calibration was carried out with an empty sample holder under the same conditions before measurement of the sample.

2.4 Chemical analysis: X-ray fluorescence (XRF) and inductively coupled plasma (ICP)

X-ray fluorescence and inductively coupled plasma are both widely used chemical analysis methods but with different signal collection mechanisms. In XRF, each element in samples gives a characteristic X-ray emission spectrum. Qualitative and quantitative analysis is achieved by measuring peak positions which depends on atomic number and peak intensities. However, XRF has a limitation to measure the light elements ($Z< 11$) [147]. Lithium ($Z=3$) is unable to be detected. Data on oxygen and fluorine, which have atomic numbers 8 and 9, respectively, have large errors, due to weak fluorescence from them; therefore, quantitative analysis of oxygen and fluorine may be not reliable. The accuracy of XRF is largely affected by sample preparation; fused glass beads are usually produced at a high temperature. Unfortunately, ball-milled samples are not suitable for making glass beads due to the poor thermal stability. Instead, samples are prepared as pellets by cold pressing.

ICP measurement is one of the most accurate chemical analyses and can detect lithium. Sample preparation may be challenging as samples need to dissolve in suitable solvents. In sections 3.1.1.5 and 4.2.6.1, samples produced using tungsten carbide and zirconia milling media were not fully dissolved by aqua regia. Oxygen and fluorine cannot be measured by ICP as the solvents contain oxygen and F has low ionisation efficiency, resulting in low sensitivity [148].

XRF was measured by a PANalytical Zetium. ICP measurements were carried out by Miss Shania Laming in the Department of Chemistry.

2.5 Impedance spectroscopy (IS)

Impedance spectroscopy is an ideal technique to measure the electrical properties of ceramic materials where it may be possible to determine the nature of conducting species and detect inhomogeneities in samples. It can separate different regions of materials, such as bulk, surface layers, grain boundary, second phases and sample electrode contacts, as different regions respond to the ac signal at different frequencies. Impedance measurements were carried out using a Solartron SI 1260 impedance analyser, typically over a range of frequency of 10^{-2} to 10^{7} Hz, with a temperature range from room temperature to ~560 ℃ for solid-state samples and up to ~360 ℃ for ball-milled samples. The software "ZView2" was used to analyse data. Au-coated pellets were placed into a jig and placed in a tube furnace. In this thesis, the measurements were performed using temperature, oxygen partial pressure and heating time as variables. Typical capacitance values for possible regions of ceramics are shown in Table 2.3.

2.6 Electrochemical measurements

To prepare samples for battery testing, a ratio of 80:10:10 wt% of active cathode material, carbon black and PVdF (binder) was mixed as the cathode. Unfortunately, preparation of slurry failed as they did not form a slurry with N-ethyl-2-Pyrrolidone but formed a jellylike wet solid and so that the cathodes cannot be calendered to pellets. Instead of calendaring, the mixtures were ground in a mortar and pestle, and directly pressed into pellets and then soaked in electrolyte. Glass fibre separators and Li metal counter electrodes were put with pellets and made into a Swagelok cell. Cells were cycled with galvanostatic charge-discharge using a BioLogic potentiostat. The whole operation was assembled in an Ar glove box. Cells were run within the voltage window 2.0V to 4.8V and the rate of C/10, except in section 3.1.3.1, where disordered Li_2MnO_3 run within the voltage window 3.0V to 4.8V.

Table 2.3 Capacitance values and their possible interpretation

Capacitance (Y)	Possible interpretation
10^{-12}	Bulk
10^{-11}	Secondary phases
10^{-11}-10^{-8}	Grain boundary
10^{-10}-10^{-9}	Bulk ferroelectric
10^{-9}-10^{-7}	Surface layers
10^{-7}-10^{-5}	Sample-electrode interface
10^{-4}	Electrochemical reactions

2.7 SEM/TEM

SEM and TEM are used to collect morphological information on carbon-coated powders and pellets. Elemental information is obtained using energy-dispersive X-ray spectroscopy (EDS) and electron energy loss spectroscopy (EELS). High-angle annular dark field, HAADF, collects scattered electrons from interactions with high Z-number components.

Scanning electron microscopy (SEM) images were acquired using FEI inspect F50 (Sorby Centre, UK). Transmission electron microscopy (TEM) images were acquired using a JEOL JEM F200 (Sorby Centre, UK), and electron energy loss spectra (EELS) were acquired using a Gatan Quantum GIF with a 200 kV beam voltage. Data collection and analysis of TEM were carried out by Dr. Laura J Wheatcroft.

2.8 XANES

The X-ray absorption spectrum is a characteristic emission spectrum for different atoms. The main techniques are X-ray absorption near edge structure (XANES) and extended X-ray absorption fine structure (EXAFS) to detect the local structure and bond distances.

Samples were prepared by mixing powders with powdered cellulose, which will not absorb the usual range of X-rays and pressing into 13-mm-diameter pellets. The X-ray absorption near edge structure spectra (XANES) were collected on beamline I18 at the Diamond Lightsource (Oxfordshire, U.K.) and the Advanced Photon Source (APS) at Argonne National Laboratory (in Argonne, Illinois, USA). Data collection was carried out by Dr. Samual Booth and Dr. David Pickup.

2.9 Density measurements

Density measurements were carried out using a Micromeritics AccuPyc 1340 gas displacement pycnometer on powdered samples.

Chapter 3 Li_2MnO_3

3.1 Results and discussion

3.1.1 Synthesis conditions

To study the response to ball milling using steel, tungsten carbide and zirconia milling media, raw materials were first ball-milled separately under the same conditions for 20 h. In order to determine the most suitable Li and Mn sources for mechanosynthesis, mixtures of different Li sources and Mn sources were then ball-milled with a Li:Mn ratio of 2:1 for 20 h with steel jars and the results compared.

3.1.1.1 Ball-milling of Li reactants in steel jars

XRD and XRF results of ball-milled Li reactants are shown in Figure 3.1 and Table 3.1, respectively. The XRD patterns of (a) Li_2O_2, (b) Li_2O, (c) LiF and (e) Li_2CO_3 correspond to their standard XRD patterns and show no difference of phase before and after milling. After milling, however, peaks were much broader and the background was noisy, indicating a reduction in particle size. Li_2O and Li_2O_2 contained a small amount of Li_2CO_3 before milling, which may be due to impurity in the chemicals or atmospheric attack during storage. The peaks of (f) $LiOH{\cdot}H_2O$ remained sharp, indicating that particle size did not change, but peak intensities changed after milling and were more similar to those reported in the ICSD File. Similar effects were observed with $LiCH_3COO{\cdot}2H_2O$: there was no XRD line broadening but XRD intensities were different before and after milling. The $LiOH{\cdot}H_2O$ and $LiCH_3COO{\cdot}2H_2O$ particles probably showed preferred orientation either before or after milling, therefore; further analysis of the XRD data, together with SEM, is required. Measurements on particle size of reactants before and after milling is required.

XRF was not able to detect elements which have smaller atomic number than O; Li, C and H could not be detected. The apparent contents of all Li sources were expected to be 100 wt% therefore, except LiF, which should show 100 wt% F. Results in Table 3.1 show that all Li

sources had ≤ 3 wt% contamination, which consisted mainly of Fe and small amounts of Zn, Mn, Cr. These were attributed to contamination from the steel milling media with the possibility of some impurities in the chemicals. As lithium sources have relatively low purities (Li_2O, 95%; Li_2O_2, 90%) and the impurities may contain carbon and hydrogen, quantitative analysis of raw materials before and after milling is needed to study contamination obtained during milling and any subsequent hygroscopicity or atmospheric sensitivity of the ball-milled products.

3.1.1.2 Ball-milling of Mn-O reactants in steel, ZrO_2 and tungsten carbide jars

XRD and XRF results of ball-milled manganese oxides using steel jars are shown in Figure 3.2 and Table 3.2. After 20 h milling, (a) MnO and (c) Mn_2O_3 showed no phase change but presented much broader peaks and noisy background. On the other hand, (b) Mn_3O_4 and (d) MnO_2 formed a large amount of Mn_2O_3 on milling and very little of the original phases remained. Mn_3O_4 also formed a small amount of a spinel of unknown composition. XRF data show that Mn_3O_4, Mn_2O_3 and MnO_2 were highly contaminated by Fe with a small amount of Cr, especially Mn_3O_4 which had 52.1 wt% Fe. It is concluded that, under these conditions, ball-milling of manganese oxides effectively took place in an open environment, where Fe contamination from the milling media occurred and oxygen content of the products was variable, especially for MnO_2 containing Mn^{4+} that reduced to Mn^{3+}, accompanied by loss of oxygen.

Figure 3.3 and Table 3.3 show XRD and XRF results of ball-milled manganese oxides using tungsten carbide jars. After 20 h milling, they showed no obvious phase change, but noisy XRD background, indicating that some amorphous phases may have formed in ball-milled Mn_2O_3 and MnO_2 (red boxes of Figures 3.3 (b, c)). Although the ball-milling did not lead to phase changes or any apparent loss of oxygen, it introduced a high W (more than 12 wt%) and slight Co, Zr contamination, based on XRF analysis.

Figure 3.4 and Table 3.4 show XRD and XRF results of ball-milled manganese oxides using zirconia jars. Ball-milled (a) MnO formed a spinel, possibly $ZnMn_2O_4$, which relates to the incorporation of milling media, while (b) Mn_2O_3 and (c) MnO_2 showed no phase change after ball-milling. However, the XRD background was high, especially for Mn_2O_3, indicating that amorphous material may have formed. XRF data showed high levels of Zr (>20 wt%) and slight Y, Hf contamination.

In summary, all manganese oxides were contaminated by the three different milling media and in some cases, there was evidence of phase or compositional changes. Ball-milling manganese oxides with tungsten carbide jars retained the original phases but some amorphous structure may be created as well as W contamination. Using zirconia and especially, steel jars, oxides containing Mn^{4+} were reduced and therefore lost oxygen; in some cases, a spinel phase formed. Tungsten carbide is the hardest material among the three milling media. It may be the least reactive towards the reactants but is the most abrasive, which may relate to the formation of amorphous material. On the other hand, the steel and zirconia milling media contain elements and oxides that are structurally and chemically similar to manganese oxides, leading to direct reaction between the media and manganese oxides that includes both reduction of Mn^{4+} and oxidation of Fe. This illustrates that potential reactions involving the milling media must be taken into consideration, as well as contamination caused by ablation.

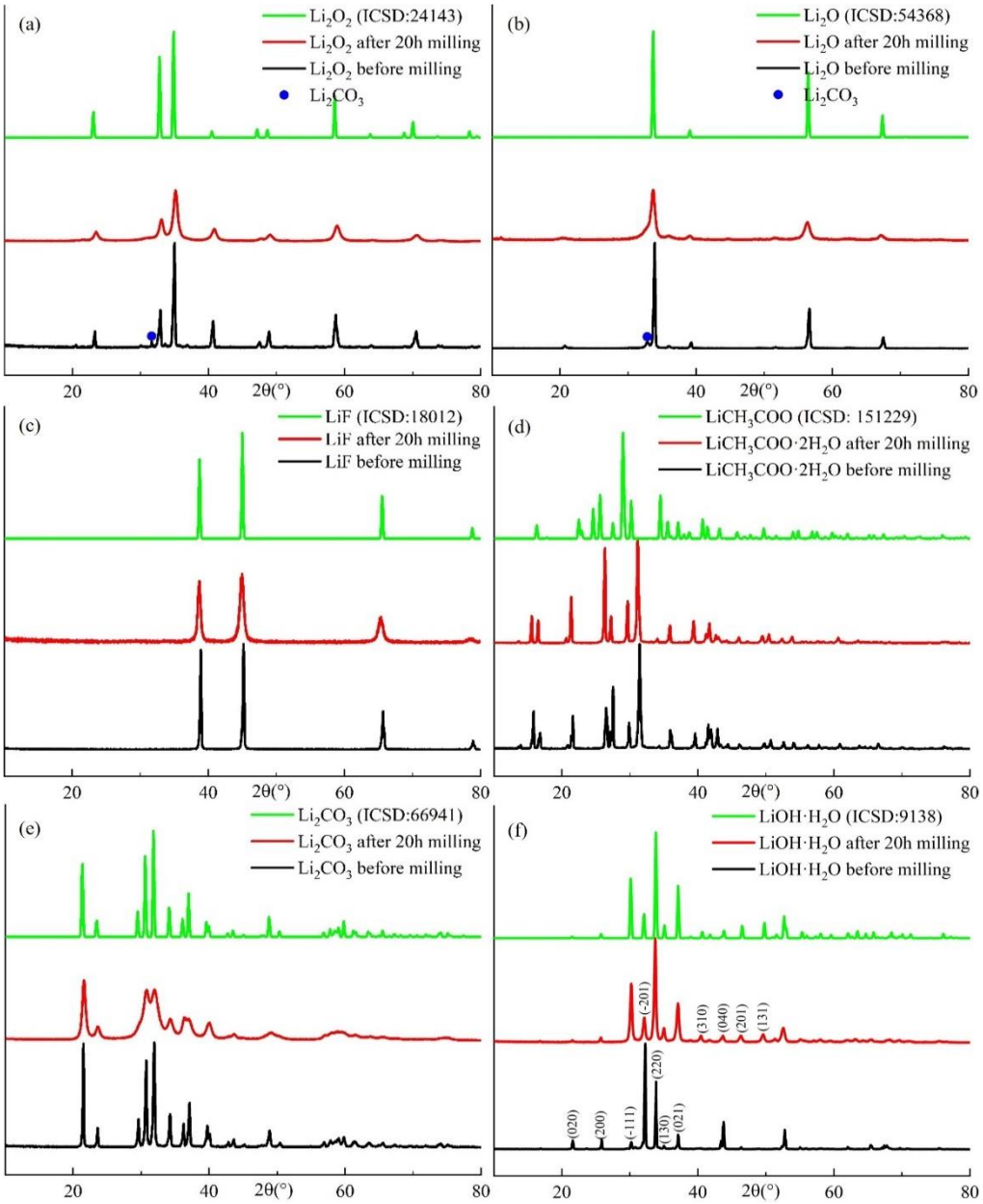

Figure 3.1 the XRD patterns of (a) Li_2O_2, (b) Li_2O, (c) LiF, (d) CH_3COOLi, (e) Li_2CO_3, and (f) $LiOH·H_2O$ with steel jars

Table 3.1 XRF of Li reactants ball-milled with steel jars

Ball-milled Li_2O_2 for 20h	**Measured wt%**			**Expected wt%**
O	96.4	95.5	95.5	100.0
Zn	2.3	2.8	2.8	0.0
Fe	1.2	1.6	1.6	0.0
Mn	0.1	0.1	0.1	0.0
Ball-milled Li_2O for 20h	**Measured wt%**			**Expected wt%**
O	96.9	95.7	96.4	100.0
Fe	2.3	3.2	2.8	0.0
Mn	0.8	0.8	0.7	0.0
Cr	0.1	0.1	0.1	0.0
Ball-milled LiF for 20h	**Measured wt%**			**Expected wt%**
F	91.1	93.5	92.7	100.0
Fe	3.8	4.4	5.2	0.0
Mn	0.6	2.0	2.0	0.0
Cr	0.1	0.1	0.1	0.0
Ball-milled $LiCH_3COO$	**Measured wt%**			**Expected wt%**
O	98.4	97.0	-	100.0
Fe	1.0	1.4	-	0.0
Zn	0.3	1.3	-	0.0
Mn	0.2	0.2	-	0.0
Cr	0.2	-	-	0.0
Ball-milled Li_2CO_3	**Measured wt%**			**Expected wt%**
O	99.5	99.7	99.7	100.0
Fe	0.1	0.1	0.1	0.0
Mn	0.0	0.0	0.0	0.0
Zn	0.4	0.2	0.2	0.0
Ball-milled $LiOHH_2O$	**Measured wt%**			**Expected wt%**
O	99.0	97.9	98.6	100.0
Fe	0.7	1.4	1.0	0.0
Mn	0.0	0.0	0.0	0.0
Zn	0.2	0.4	-	0.0

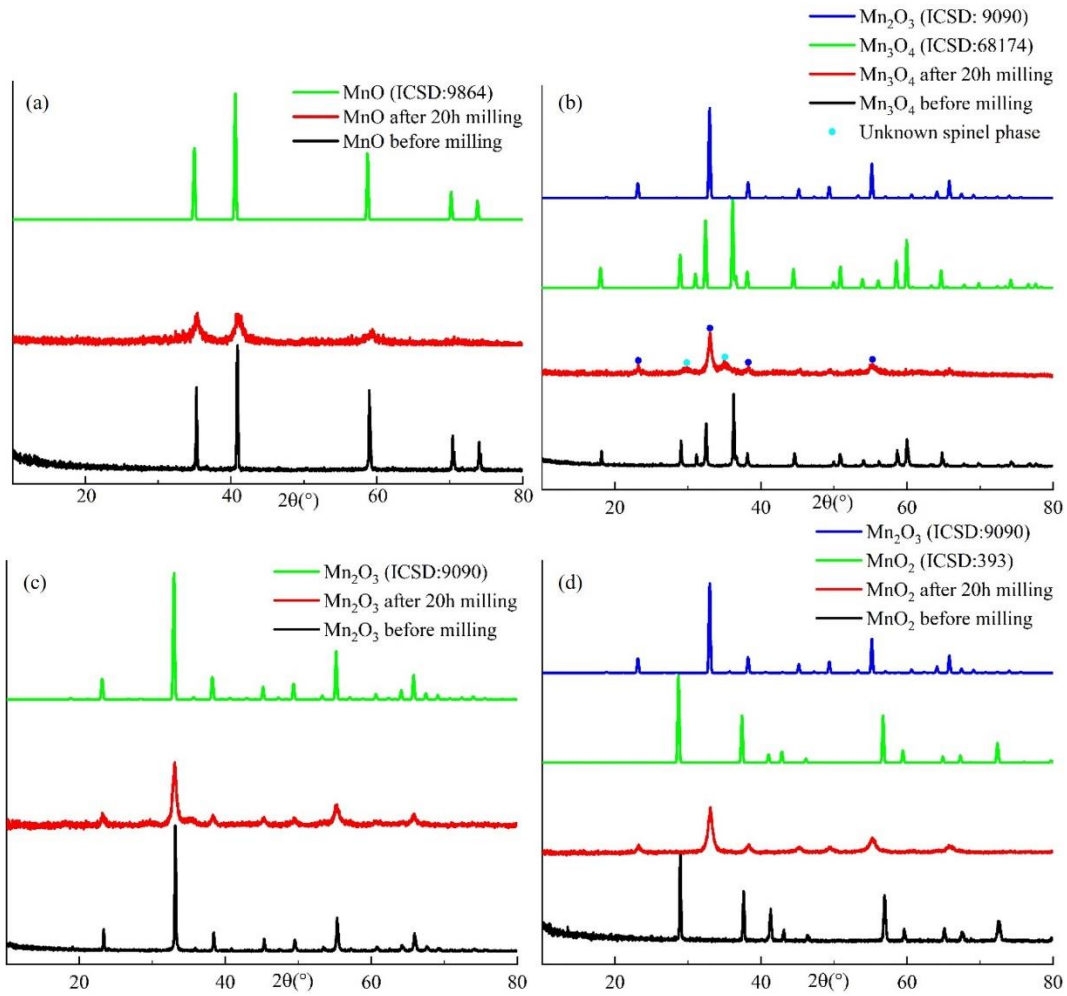

Figure 3.2 the XRD patterns of (a) MnO, (b) Mn_3O_4, (c) Mn_2O_3 and (d) MnO_2 with steel jars

Table 3.2 XRF of Mn-O ball-milled with steel jars

MnO ball-milled for 20h	**Measured wt%**			**Expected wt%**
Mn	49.5	44.1	49.7	77.4
O	30.1	42.4	33.0	22.6
Fe	8.3	7.9	8.6	0.0
Cr	0.1	0.3	0.4	0.0
Mn_3O_4 ball-milled for 20h	**Measured wt%**			**Expected wt%**
Mn	13.6	14.4	14.1	72.0
O	35.4	36.8	40.2	28.0
Fe	52.1	53.4	51.1	0.0
Cr	1.5	2.0	1.6	0.0
Mn_2O_3 ball-milled for 20h	**Measured wt%**			**Expected wt%**
Mn	33.9	32.4	35.0	69.6
O	29.8	32.4	29.7	30.4
Fe	30.0	29.1	31.6	0.0
Cr	0.7	0.8	0.8	0.0
MnO_2 ball-milled for 20h	**Measured wt%**			**Expected wt%**
Mn	42.1	37.8	41.4	63.2
O	30.5	40.8	26.0	36.8
Fe	20.7	18.5	19.6	0.0
Cr	0.6	0.5	0.5	0.0

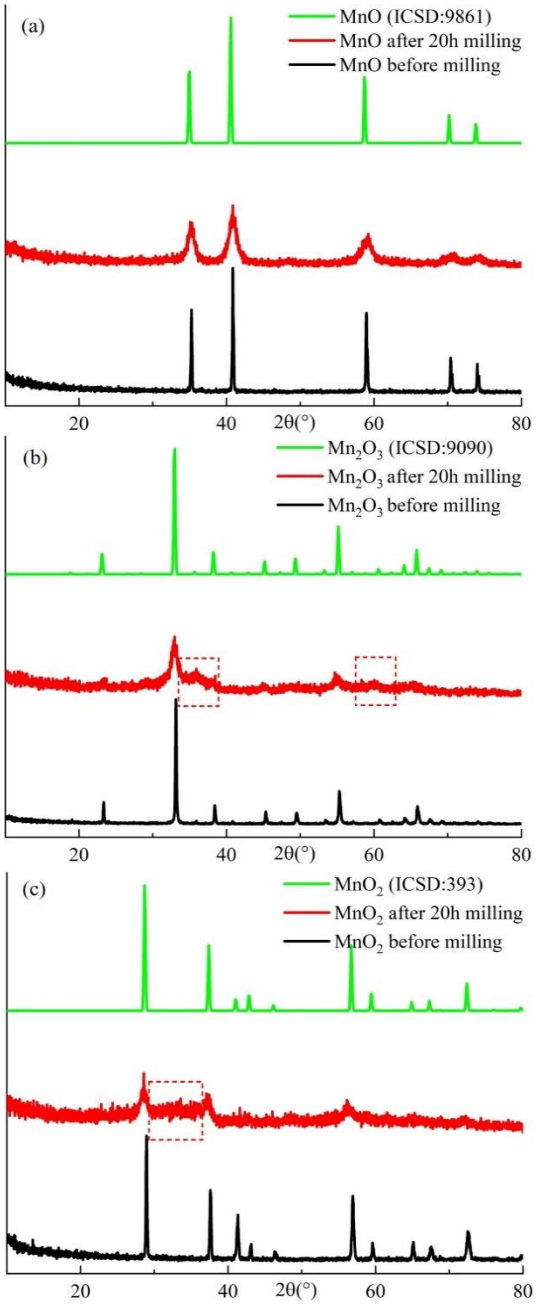

Figure 3.3 the XRD patterns of (a) MnO, (b) Mn_2O_3 and (c) MnO_2 with tungsten carbide jars

Table 3.3 XRF of Mn-O ball-milled with tungsten carbide jars

MnO ball-milled for 20h	**Measured wt%**			**Expected wt%**
Mn	-	-	-	77.4
O	-	-	-	22.6
W	-	-	-	0.0
Co	-	-	-	0.0
Zr	-	-	-	0.0
Mn_2O_3 ball-milled for 20h	**Measured wt%**			**Expected wt%**
Mn	64.9	64.7	64.9	69.6
O	29.8	22.3	22.3	30.4
W	11.4	12.1	11.9	0.0
Co	1.0	0.9	0.9	0.0
Zr	-	-	-	0.0
MnO_2 ball-milled for 20h	**Measured wt%**			**Expected wt%**
Mn	48.8	49.5	49.0	63.2
O	22.0	22.1	22.1	36.8
W	25.3	26.0	25.5	0.0
Co	2.0	1.9	2.7	0.0
Zr	0.6	0.6	0.6	0.0

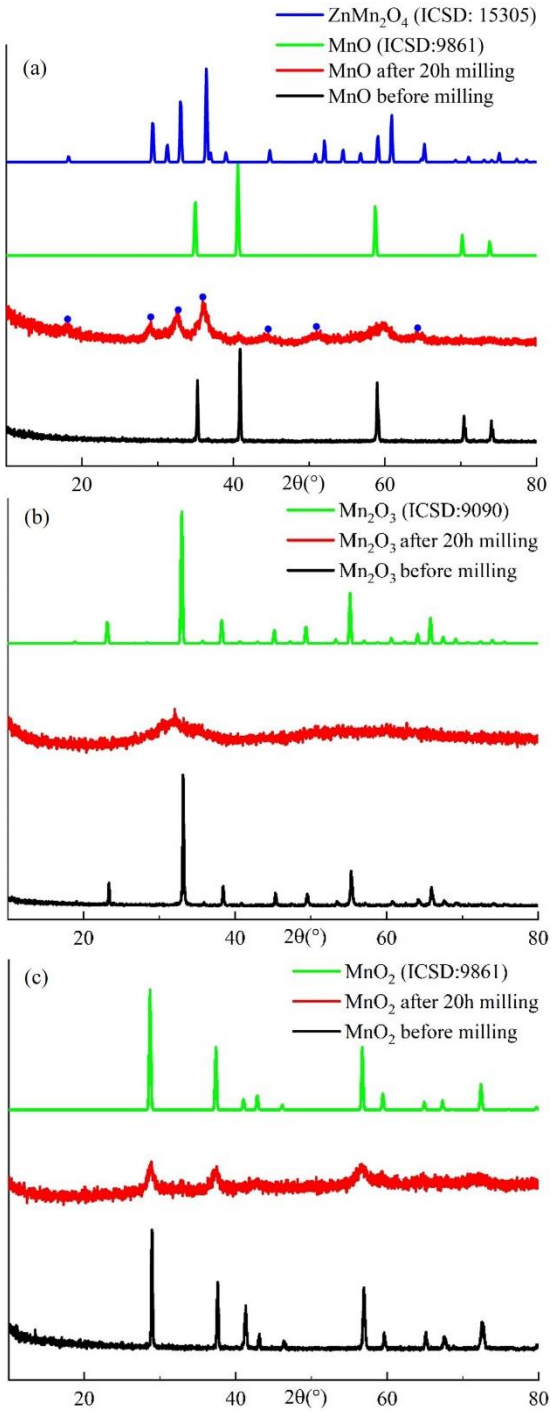

Figure 3.4 the XRD patterns of (a) MnO, (b) Mn_2O_3 and (c) MnO_2 with zirconia jars

Table 3.4 XRF of Mn-O ball-milled by zirconia jars

MnO ball-milled for 20h	**Measured wt%**			**Expected wt%**
Mn	-	-	-	77.4
O	-	-	-	22.6
Zr	-	-	-	0.0
Y	-	-	-	0.0
Hf	-	-	-	0.0
Mn_2O_3 ball-milled for 20h	**Measured wt%**			**Expected wt%**
Mn	55.6	53.7	54.9	69.6
O	23.5	23.4	23.5	30.4
Zr	19.9	20.7	20.8	0.0
Y	0.9	0.9	0.8	0.0
Hf	-	0.5	-	0.0
MnO_2 ball-milled for 20h	**Measured wt%**			**Expected wt%**
Mn	48.1	47.8	48.3	63.2
O	23.8	23.7	23.7	36.8
Zr	27.1	26.5	25.9	0.0
Y	0.9	1.0	0.9	0.0
Hf	-	0.8	0.6	0.0

3.1.1.3 Reactivity of Li_2O_2 and Li_2O with different Mn sources for Li_2MnO_δ synthesis

Two lithium oxides, Li_2O_2 and Li_2O were used as lithium sources and were ball-milled with three different manganese oxides, MnO, Mn_2O_3 and MnO_2 for 20 h in steel jars, Figure 3.5. Although the Li:Mn ratio was 2:1, the combined oxygen contents of the reagents was not constrained to value 3 at the outset in some of these experiments.

Using Li_2O_2 (a), a disordered rock-salt phase formed with all three manganese oxides; expected oxygen contents δ in the formula Li_2MnO_δ were δ=3 (using MnO), 3.5 (Mn_2O_3) and 4 (MnO_2). However, using Li_2O (b), a disordered rock-salt phase formed only with Mn_2O_3 (δ=2.5) and MnO_2 (δ=3). Li_2O and MnO (δ=2) did not react during ball-milling, although the reactant particle size was reduced, as shown in (c). The implication from these results is that excess oxygen can be released readily, using Li_2O_2, but the milling equipment and procedure is not sufficiently open for oxygen-deficient samples to pick up atmospheric oxygen. However, a second implication is the possibility of forming oxygen-deficient products with a disordered rock salt structure and reduced Mn valence, as with δ=2.5.

The above considerations focus on Li:Mn:O ratios. There are several ways that the valence state of Mn either may be targeted to a specific value or changes spontaneously during milling. First, a combination of Mn oxide starting materials may be used to give the desired stoichiometry and Mn valence without change in overall oxygen content. Second, oxygen may be lost during milling. Third, oxygen may be gained slowly from the atmosphere during milling. Fourth, reactions involving peroxides, in particular Li_2O_2, have several possible outcomes, as discussed next.

The peroxide ion may (1) act as an oxidising agent, (2) undergo internal redox or disproportionation or (3) act as a reducing agent, depending on the experimental conditions and other reactants present:

$$O_2^{2-} = 2O^{2-} + 2h^{\bullet} \quad (3.1)$$

$$O_2^{2-} = O^{2-} + \frac{1}{2}O_2 \quad (3.2)$$

$$O_2^{2-} = O_2 + 2e^- \quad (3.3)$$

We do not know for certain the mode of operation of Li_2O_2 in our samples at present, but may make some observations. Assuming the product is oxygen stoichiometric Li_2MnO_3, Li_2O_2 appears to react as (1) using MnO, as follows:

$$Li_2O_2 + Mn^{2+}O = Li_2Mn^{4+}O_3 \quad (3.4)$$

Using Mn_2O_3, a combination of (1) and (2) is required:

$$2Li_2O_2 + Mn_2^{3+}O_3 = 2Li_2Mn^{4+}O_3 + \frac{1}{2}O_2 \quad (3.5)$$

Using MnO_2, (2) alone is needed:

$$Li_2O_2 + Mn^{4+}O_2 = Li_2Mn^{4+}O_3 + \frac{1}{2}O_2 \quad (3.6)$$

In contrast to these reactions involving Li_2O_2, Li_2O cannot influence significantly the Mn valence. On reacting Li_2O and MnO, where the initial Mn valence was as 2+, the oxygen content was insufficient, oxygen uptake from the external atmosphere did not occur and Li_2MnO_3 did not form. The disordered rock salt phase was, however, produced using Mn_2O_3. It could be either oxygen-deficient:

$$2Li_2O + Mn_2^{3+}O_3 = 2Li_2Mn^{3+}O_{2.5} \quad (3.7)$$

Or, enough oxygen may be picked up from the atmosphere during milling:

$$2Li_2O + Mn_2^{3+}O_3 + \frac{\delta}{2}O_2 = 2Li_2Mn_{1-\delta}^{3+}Mn_{\delta}^{4+}O_{2.5+\delta} \quad (3.8)$$

Reaction of Li_2O with MnO_2 gives stoichiometric Li_2MnO_3 without change in oxygen content:

$$Li_2O + Mn^{4+}O_2 = Li_2Mn^{4+}O_3 \quad (3.9)$$

3.1.1.4 Reactivity of other Li sources for Li_2MnO_3 synthesis

$LiCH_3COO$, Li_2CO_3 and $LiOH{\cdot}H_2O$, with MnO and MnO_2 were respectively ball-milled in steel jars for 20 h in a Li/Mn ratio of 2:1, Figure 3.6, 3.7 and 3.8.

Using $LiCH_3COO$, Figure 3.6, no reaction occurred and the products were a mixture of $LiCH_3COO$ and manganese oxides. Ball-milling Li_2CO_3 and MnO had very little reaction and formed a small amount of a disordered rock-salt phase, Figure 3.7. Some Li_2CO_3 remained and unknown spinel was also formed. Milling Li_2CO_3 and MnO_2 gave no reaction and the products were a mixture of Li_2CO_3 and MnO_2.

Using $LiOH{\cdot}H_2O$ with (a)MnO and (b)MnO_2, Figure 3.8, a disordered rock-salt phase formed (red boxes) but the reactions did not complete and some $LiOH{\cdot}H_2O$ and manganese oxides remained. Noticeably, after milling, the $LiOH{\cdot}H_2O$ phase corresponds to the reagent measured in the lab in (a) and standard ICSD card in (b).

In summary, using $LiCH_3COO$, Li_2CO_3 and $LiOH \cdot H_2O$ as the lithium source did not successfully form single phase disordered rock-salt Li_2MnO_3. $LiCH_3COO$ and Li_2CO_3 may not have reacted because it is difficult to lose carbon during milling. $LiOH \cdot H_2O$ may be reactive once its dehydration is first triggered.

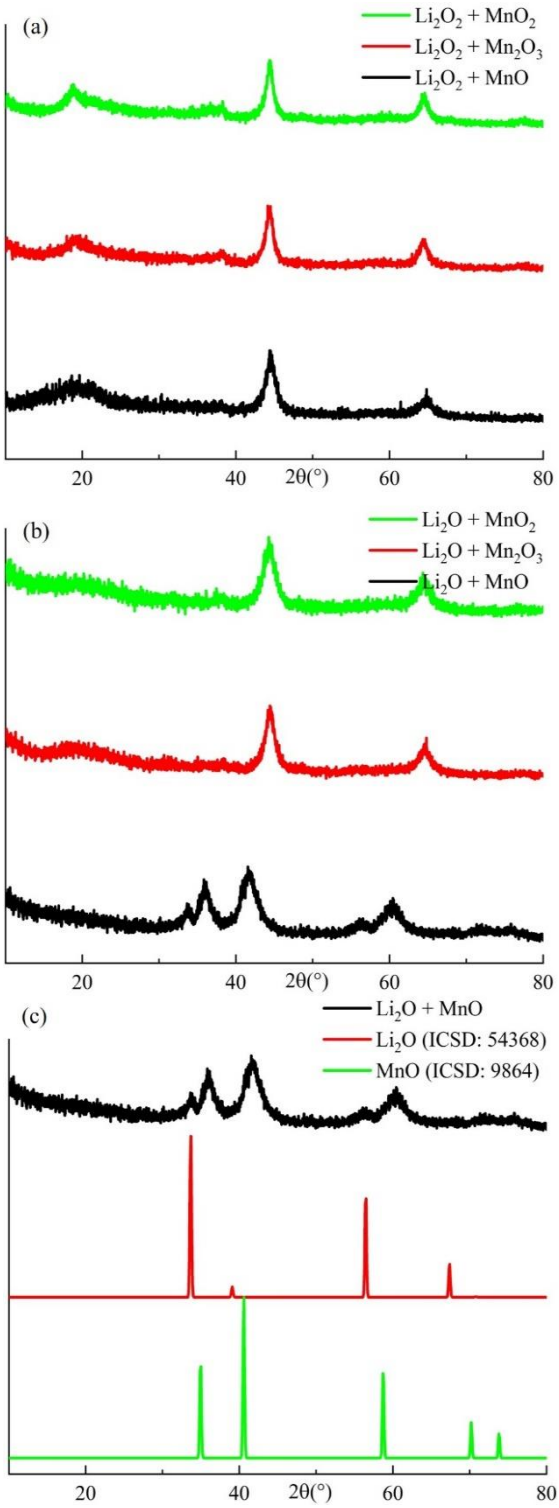

Figure 3.5 the XRD patterns of (a) Li_2O_2 ball-milled with different Mn sources; and (b) Li_2O ball-milled with different Mn sources, with the ratio of Li : Mn was 2:1. (c) is the phase analysis of ball-milled Li_2O and MnO.

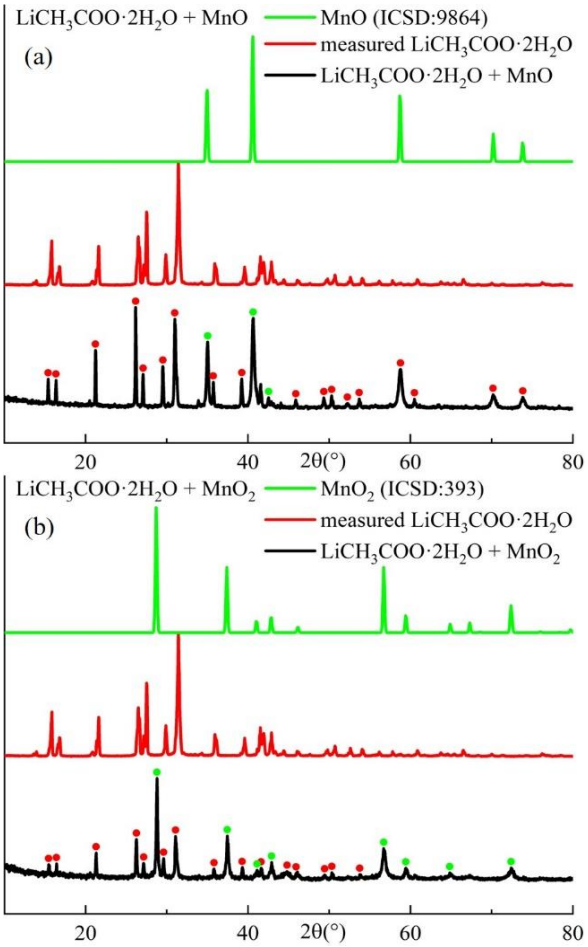

Figure 3.6 the XRD patterns of $LiCH_3COO$ ball-milled with MnO and MnO_2 with the ratio of Li : Mn was 2:1.

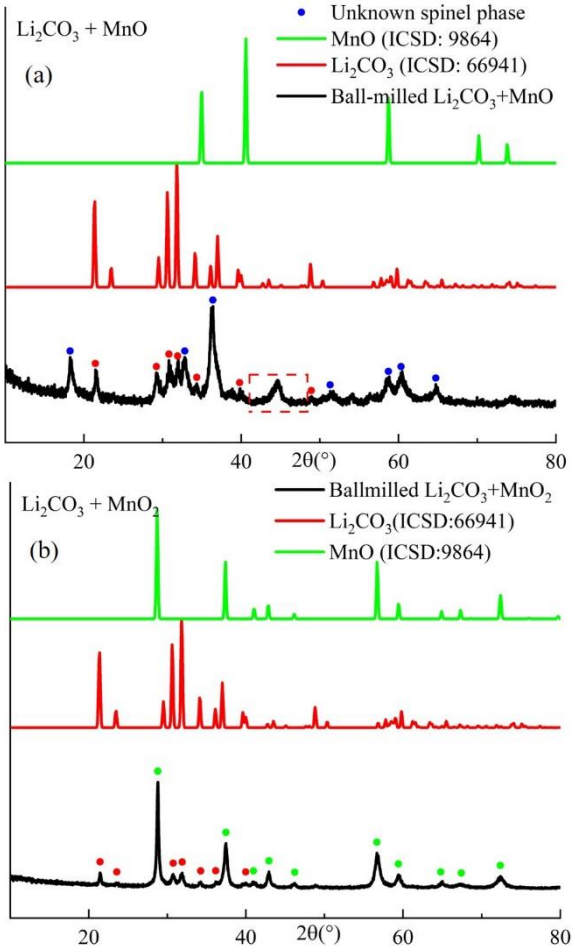

Figure 3.7 the XRD patterns of Li_2CO_3 ball-milled with MnO and MnO_2 with the ratio of Li : Mn was 2:1.

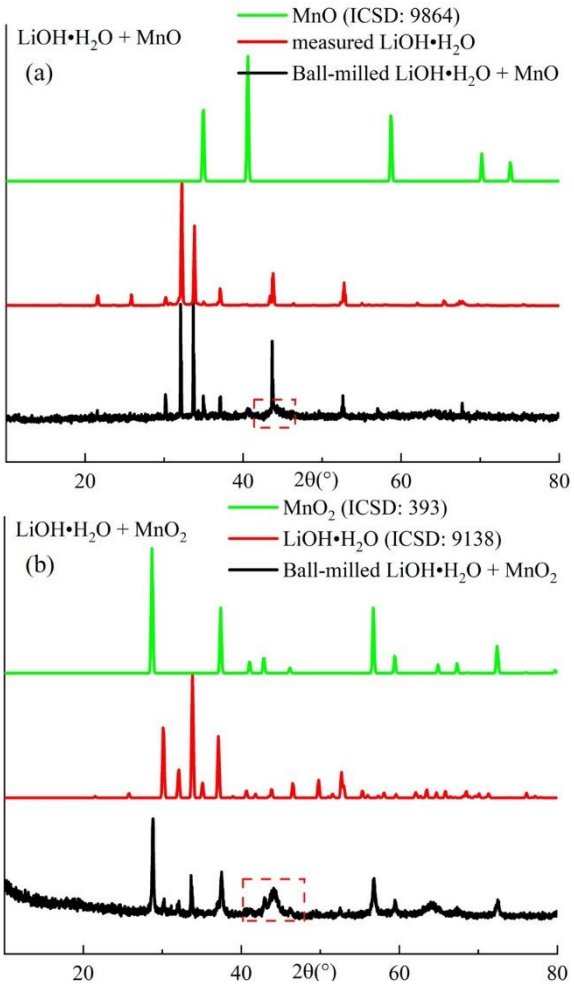

Figure 3.8 the XRD patterns of $LiOH{\cdot}H_2O$ ball-milled with (a) MnO and (b) MnO_2 with the ratio of Li : Mn was 2:1.

3.1.1.5 Chemical analysis of Li_2MnO_3 prepared using zirconia, steel and tungsten carbide jars

Disordered rock-salt Li_2MnO_3 was produced using Li_2O and MnO_2 for 20 h in three milling media and chemical analysis was collected. Tables 5 and 6 show the combined ICP, CHNS and XRF analysis results. For ICP, samples were dissolved in aqua regia, but the ones milled with tungsten carbide and zirconia did not fully dissolve. Results show the Li/Mn ratio was 2.01, 2.20 and 1.70 for samples using steel, WC and zirconia, respectively. These samples contained 1.6 wt% of Fe, 0.03 wt% of W, and 0.5 wt% of Zr.

XRF is unable to measure quantitatively light elements, such as oxygen and fluorine and therefore, any results may have large errors. In addition, due to their low thermal stability, preparing samples as fused beads is not suitable; instead, pellets were prepared by cold pressing. Each sample was measured on three different regions of the pellet surface and averages taken. The O/Mn ratio, which is expected to be 3, varied from 2.8 to 6.2; the scatter is attributed to errors in O contents. Samples milled using steel, WC and zirconia had 1.8-2.0 wt% of Fe, 11.6-12.4 wt% of W and 1.9-2.4 wt% of Zr, respectively. Compared with the amount of contaminants detected using ICP, the Fe content of the sample milled using steel media was similar, but the W and Zr contents of samples milled by WC and zirconia jars were much higher than the values from ICP analysis. It is probable that most of the W and Zr contaminants in XRF samples existed as a second phase, arising from the milling media, which remained undissolved in aqua regia.

Neither ICP nor XRF are able to give accurate oxygen stoichiometries but both are able to detect impurities, such as Fe, W and Zr. All samples were contaminated by the milling media to some degree. Steel and zirconia gave ~2 wt% of contamination, whilst WC gave > 10 wt% contamination, probably as a second phase.

From these results, it appears that three different contamination scenarios are possible. First, contamination may occur be incorporating atoms from the milling media into the desired product phase, as judged by ICP analysis of material dissolved in aqua regia. Contamination is <2 wt% for all three milling media using reaction mixtures which have the correct overall composition to prepare Li_2MnO_3. Second, ablation of WC and zirconia milling media may occur, without incorporation into the desired product phase, as shown by the presence of an insoluble residue after reaction of the milled products with aqua regia. Third, milling of reagents in isolation can lead to severe cases of contamination, especially on milling Mn oxides alone in steel media. This is apparent from the much reduced levels of contamination on milling mixtures of Mn and Li oxides to form Li_2MnO_3. It indicates that the milling media are not

simply inert attrition mills but are able to take part in chemical reactions with the reagents. If the reactants are present in the right amounts, formation of the product provides a more rapid release of the mechanical energy created during milling and appears to be the preferred reaction pathway. However, in the absence of any possible product arising from milling individual reactants, the media themselves undergo reaction as a means to release some of the absorbed mechanical energy. Further studies are underway to optimise conditions for the preparation of contamination-free samples of Li_2MnO_3.

Table 3.5 ICP and CHNS of Li_2MnO_3 produced by zirconia, steel and WC jars

Samples Li_2MnO_3	**The ratio of Li/Mn**		**Mn and impurities (mg/kg) (1/10000 wt% = 1 mg/kg)**								
	Expected	Analysed	Li	Mn	Fe	W	Zr	Y	Hf	C	H
By steel jar	2	2.01	102122	401658	16092	52.4	26.1	< 4.1	<41.0	-	-
By WC jar	2	2.20	89537	357065	79.4	319	34.3	< 4.03	<40.3	-	0.9
By ZrO_2 jar	2	1.72	99107	412888	64.2	18.6	5013	<3.75	138	1.22	0.7

Table 3.6 XRF of Li_2MnO_3 produced by zirconia, steel and WC jars

Samples Li_2MnO_3	**The ratio of O/Mn**		**Mn and impurities (wt %)**							
	Expected	Analysed	Mn	Fe	W	Zr	Cr	Co	Si	Hf
		5.19	39.0	2.0			0.1			
By steel jar	3	5.46	37.9	1.8			0.1			
		5.16	39.2	1.8						
		4.51	37.7		11.6			0.9		
By WC jar	3	3.56	42.4		12.4			1.2		
		2.80	47.0		12.4			1.2	1.1	
		4.82	40.5			2.4				0.2
By ZrO_2 jar	3	6.20	35.0			1.9				
		4.60	41.8			2.0				0.2

3.1.1.6 Synthesis routes for disordered rock-salt Li_2MnO_3

Two routes were used to study the formation of disordered Li_2MnO_3, Figure 3.9. One involved ball-milling Li_2O_2 and MnO in steel jars for times ranging from 8 min to 10 h (a). The disordered rock-salt structure started to form after 4 h and reaction was complete after 10 h. The second route involved milling pre-reacted, ordered Li_2MnO_3 for times ranging from 8 min to 10 h (b). The intensity of the superstructure peak at ~18° had decreased significantly after only 8 min and the process of phase disorder was essentially complete after 6 h. At intermediate times, especially after 2 h, the XRD patterns showed a high level of background scatter which was reduced greatly after 6 h. For longer times, there was some evidence of possible re-emergence of the broad superstructure peak at 18°, which could indicate the formation of superstructure domains with a much smaller size; alternatively, this could indicate formation of a small amount of a spinel phase.

3.1.1.7 Heat treatment on Li_2MnO_δ produced using different reactants

The Li_2MnO_δ samples produced by tungsten carbide jars by reacting Li_2O_2 and Li_2O with three manganese oxides (Section 3.1.1.3) were subsequently heated from room temperature to 800 ℃ in steps. The XRD patterns are shown in Figures 3.10 and 3.11. Except for the sample produced from Li_2O and MnO (Figure 3.11 (a)), all samples were disordered rock-salt phase at room temperature and underwent similar phase transformation during heating. From 200 ℃, a peak emerged at 18 °, which was much broader than the other peaks, indicating the growth of very small size ordered domains within small grains of disordered rock salt structure. From 600 ℃, all peaks became sharper and additional superstructure peaks appeared attributable to the monoclinic polymorph. Finally, at 800 ℃ ordered, monoclinic Li_2MnO_3 had formed. The only samples to form single phase, monoclinic Li_2MnO_3 were those from Li_2O_2, MnO (δ=3) and Li_2O, MnO_2 (δ=3). Samples from: Li_2O_2, Mn_2O_3 (δ=3.5); Li_2O_2, MnO_2 (δ=4) and Li_2O, Mn_2O_3 (δ=2.5) gave at 800 ℃, monoclinic Li_2MnO_3 as the main phase, but many small extra peaks in the range 20–30 °.

The products of ball-milling Li_2O and MnO (δ=2) at room temperature were a mixture of unreacted Li_2O and MnO with small particle size. At 200 ℃, unreacted Li_2O started to react and form Li_2CO_3 which then decomposed at higher temperatures and disappeared by 600 ℃. At 800 ℃, monoclinic Li_2MnO_3 formed. Noticeably, the background was relatively noisier

than others. Li_2O and MnO did not react with each other during milling; instead, MnO reacted with milling media and Fe contamination was introduced, which caused a noisy background.

It is concluded that heating ball-milled Li_2MnO_δ to form monoclinic Li_2MnO_3 at high temperature was only successful when $\delta=3$. One possibility is when $\delta\neq3$, the ball-milled products with a Li:Mn ratio of 2: 1, tended to decompose during heating. Another possibility is when $\delta\neq3$, the Li:Mn ratio was not 2: 1 after milling, perhaps due to Fe contamination and it decomposed during heating. However, it is also possible that when $\delta\neq3$, the ball-milled products were not single phase but the impurities were not able to detect by XRD due to small amount, small particle size and noisy background.

A continuation study on phase-pure Li_2MnO_3 with different degrees of order, lattice parameters and particle/ domain size are presented in Chapter 4, sections 4.3.2.2 and 4.3.6.3.

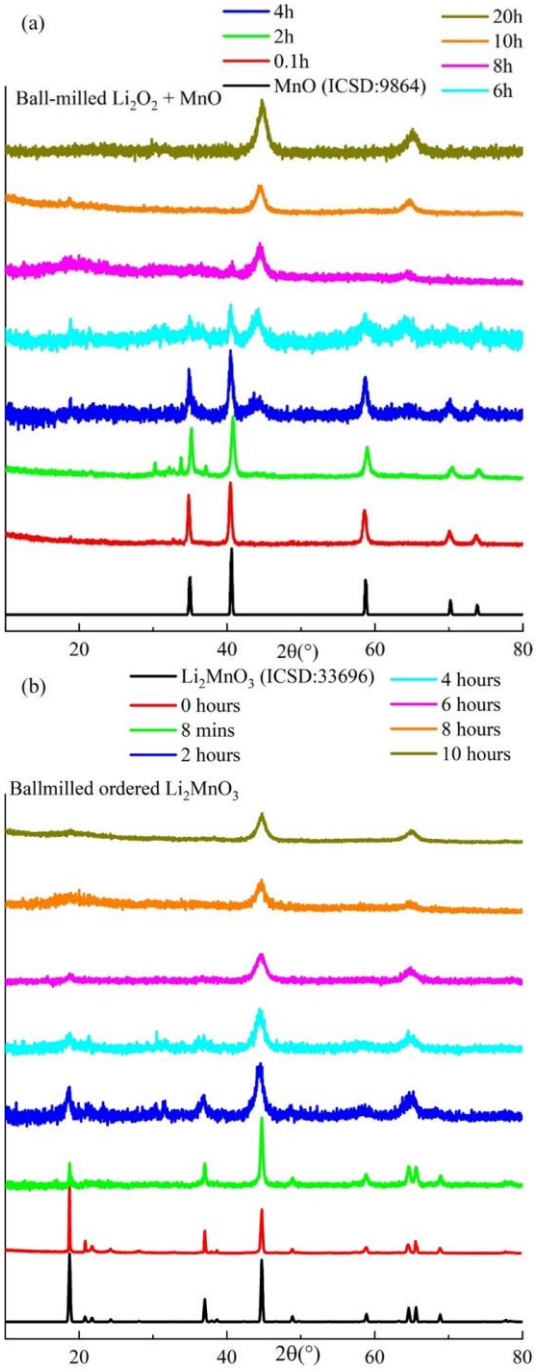

Figure 3.9 the XRD patterns of ball-milling (a) Li_2O_2 and MnO and (b) Li_2MnO_3 for different times

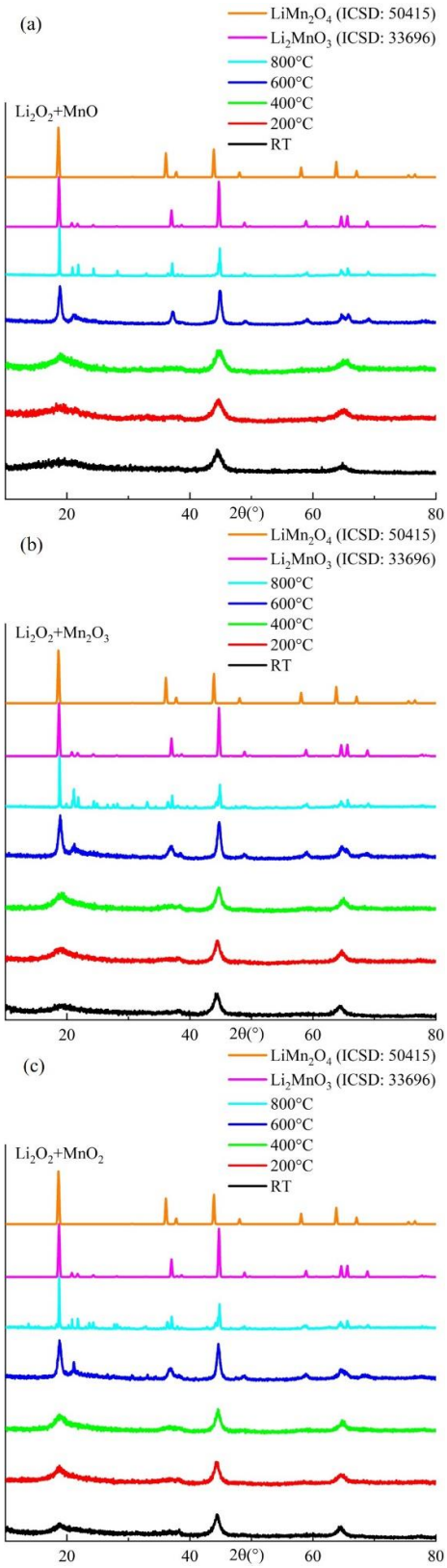

Figure 3.10 the XRD patterns of Li_2MnO_3 produced by Li_2O_2 and three Mn-O with heat treatment

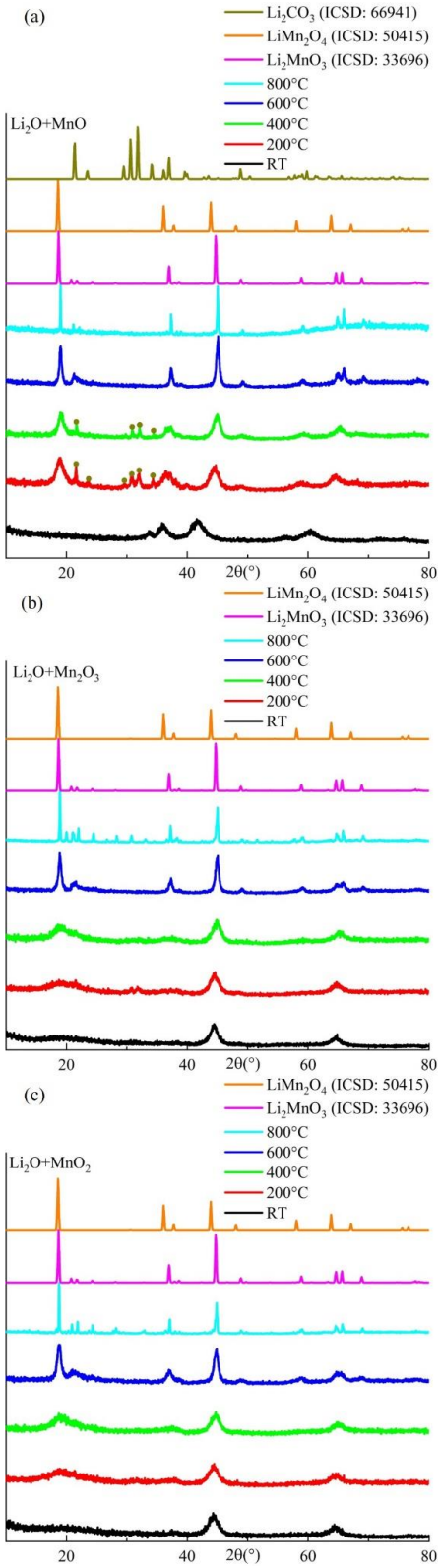

Figure 3.11 the XRD patterns of Li_2MnO_3 produced by Li_2O and three Mn-O with heat treatment

3.1.2 thermal stability of disordered Li_2MnO_3: TG results

3.1.2.1 TG of Li and Mn reactants

Figure 3.12 and 3.13 shows TG results of cycling Li_2O_2 and Li_2O over the range room temperature to 500 ℃ and MnO, Mn_2O_3 and MnO_2 from room temperature to 800 ℃. The XRD patterns recorded after TG are also shown.

Li_2O_2 had a very slow weight increase until 330 ℃, followed by a weight loss of 24.37%, which finished at ~405 ℃. After that, a small weight gain of 1.55% occurred and finished at ~455 ºC, which then was lost when heated to 500 ℃. During cooling, a small weight gain occurred and then remained constant. XRD results after TG showed the main phase changed from Li_2O_2 to Li_2O and also contained a small amount of Li_2CO_3. It appears, therefore that Li_2O_2 lost 24.37 wt% at 300-405 ℃, corresponding to 0.7 O, to form Li_2O. It may pick up CO_2 on heating, especially at 405-455 ℃, to form Li_2CO_3 and gain ~1.55 wt% corresponding to 0.03 CO_2. Li_2O_2 is expected to lose 1 O to form Li_2O, higher than the observed value of 0.7. Further studies are required to assess the purity of Li_2O_2 (Li_2O_2, 90.0%, Sigma Aldrich) and its reactivity with the atmosphere.

Li_2O showed a slow weight gain of 2.77% on cycling between room temperature and 470 ℃ which may be due to CO_2 pick up. However, after TG, the powder had stuck to the holder and could not be extracted for XRD measurements; further studies, including chemical analysis are required to assess the purity of Li_2O.

MnO started to increase in weight on heating from 450 ℃, had increased by 9.77% at 800 ℃, Figure 3.13 and did not change on cooling.

The weight of Mn_2O_3 during heating and cooling was relatively constant within ±0.25%.

MnO_2 lost 8.56% from ~605-680 ℃, followed by a much slower weight loss of 0.35% by 800 ℃.

XRD results showed that Mn_2O_3 was the main phase in all three samples after TG, but with MnO_2, a small amount of MnO_2 remained. Conclusions are as follows: MnO gained 9.77 wt%, which corresponds to 0.61 O, compared with the expected value of 0.5 O for MnO to form Mn_2O_3. MnO_2 lost 8.56 wt%, which corresponds to 0.54 O, compared with the expected 0.5 O for MnO_2 to form Mn_2O_3. It is concluded that, as expected, Mn_2O_3 is the most stable phase at high temperatures among manganese oxides.

3.1.2.2 TG-MS of disordered Li_2MnO_3.

All disordered Li_2MnO_3 samples used in TG measurements were produced using Li_2O_2 and MnO in WC jars, except samples in section 3.1.2.3, where disordered Li_2MnO_3 produced by different reactants was studied by TG.

Figure 3.14 shows TG with the combined MS signal on heating disordered Li_2MnO_3 to 1000 ℃ at 10 ℃/min. (a) is the TG profile. From room temperature to 450 ℃, a rapid weight loss occurred, ~9.24%, followed by a constant weight plateau. From 540-780 ℃, a second, slower weight loss of ~2.18% occurred, followed by 0.2% of weight loss from 940 ℃ to 1000 ℃. MS data were recorded at the same time as the TG measurements. Four characteristic H_2O signals (m/z 17, 17.5, 18 and 18,5) showed a peak at 104 ℃, with a relatively high background over the whole range. Two broad characteristic CO_2 signals (m/z 44 and 44.5) were observed at 399 ℃ and 645 ℃. Two characteristic O_2 signals (m/z 32 and 32.5) were observed at 776 ℃ and > 966 ℃.

Combined with MS data, the rapid weight loss in TG from room temperature to 450 ℃ might be a combination of two processes, water and CO_2 loss, with two different slopes shown in red and green in Figure 3.14 (a). It is noticeable that the slope changed at ~280 ℃, where two weight loss processes were observed. Assuming the weight loss before 280 ℃ was mainly due to water loss, 5.44% (0.3 mole for each mole of Li_2MnO_3) of H_2O would have been lost up to 280 ℃. Assuming the weight loss at 280-450 ℃ was mainly CO_2 loss, 3.81% (0.9 mole for each mole of Li_2MnO_3) would have been lost. The second weight loss which started from 450 ℃, was attributed to the second CO_2 loss (2.40%, 0.05 mole) and a very slight of O_2 loss, which was too small (less than 0.01 mole) to be quantitatively analysed. The third weight loss above 900 ℃ was also less than 0.01 mole of oxygen loss.

The combined TG-MS results indicate the sample was (a) hygroscopic, (b) probably contained complex carbonates and hydroxides and (c) lost oxygen at high temperatures. The two CO_2 peaks may relate to decomposition of bicarbonate, HCO_3^- and carbonate, CO_3^{2-}, which decompose at different temperatures. Basic oxides have often been observed to react with water and CO_2 by (idealised) reactions such as:

$$O^{2-} + H_2O = 2OH^- \quad (1)$$

$$O^{2-} + CO_2 = CO_3^{2-} \quad (2)$$

$$OH^- + CO_2 = HCO_3^- \quad (3)$$

Therefore, a series of TG measurements on different disordered Li_2MnO_3 samples were done and are presented in the following sections to study factors that relate to hygroscopicity, choice of reactants, synthesis method, atmosphere and aging during storage. TG at a slower heating rate was used in order to separate possible overlapping processes.

3.1.2.3 TG-MS, TG, DTG and DSC of Li_2MnO_3

Figure 3.15 shows the results of TG and the 1st derivative, DTG, on disordered rock-salt Li_2MnO_3 produced by different reactants. Samples were produced by milling Li_2O_2 or Li_2O with three manganese oxides at room temperature (See details in 3.1.1.3). TG data was collected by heating from room temperature to 800 ℃ and cooling in air. The total weight loss for each varied from 92.4% to 95.5% among five samples. During heating, at least five stages can be observed but each sample was different: we suspect that the samples may have aged differently since common storage procedures were not used prior to TG. Thus, an initial loss below 100 ℃ attributed to water loss was not observed by all samples and one sample showed the opposite trend of an increase in weight up to 200 ℃. A variety of weight loss profiles are seen up to ~720 ℃, above which, little or no further weight loss occurred. All samples showed the same TG profile on cooling; it is likely that no weight changes occurred on cooling and instead, the slight curvature in the profiles is attributable to instrumental baseline drift.

Noticeably, there were two samples having similar DTG curves: Li_2O_2 + MnO (in black) and Li_2O + MnO_2 (in cyan), both with the δ=3. A fast water loss occurred immediately once heating started and finished ~63 to 87 ℃. A relatively slow CO_2 loss occurred between ~350-470 ℃. It was followed by another CO_2 loss process with a slower rate, which ended at ~750 ℃. The DTG of these two stochiometric Li_2MnO_3 samples not only was similar, but also consistent with the water and CO_2 loss profiles in the TG-MS results. As these two samples had the same target composition, it is possible that the hygroscopic behaviours depend on the oxygen content.

Figure 3.16 (a) gives a comparison of TG results on three samples of Li_2MnO_3 prepared by different routes: A, produced by solid state reaction to give an ordered monoclinic phase; B, produced by mechanosynthesis with a disordered rock-salt structure; C, produced by solid state reaction and subsequent ball-milling to form a disordered rock-salt phase. As can be seen, there was no obvious mass change in A during heating. However, when B was heated to 800 ℃, there were at least three stages of mass loss giving 7.8% in total, including mainly H_2O and CO_2 losses and a small amount of oxygen loss. For C, before 700 ℃, there was no obvious

weight loss, which indicates C is not as hygroscopic as B. B and C were both disordered, but B was produced using Li_2O_2 and C using Li_2CO_3. This suggests that the hygroscopicity of disordered Li_2MnO_3 might relate to the use of highly reactive Li sources, such as Li_2O or Li_2O_2, rather than the disordered structure. C had two small weight gain peaks at about 300 and 500 ℃, which probably was because the ordered phase produced by solid state reaction was oxygen-deficient and had absorbed O_2 during heating. Above 700 ℃, the weight loss profiles of B and C were similar, showing a small amount of oxygen loss.

In Figure 3.16 (b), ball-milled Li_2MnO_3 (sample B in (a)) was heated for two cycles. The time intervals between the cycles were different, which were: no interval, 1 h, 12 h and 48 h. The first cycle profiles of the four samples were generally similar to sample B, Figure16 (a), but had less water and CO_2 losses. As mentioned before, the storage conditions were not closely controlled so samples could have aged differently. Before the second cycle started, weight gains occurred during storage, which were 0 wt% for no interval, 0.53 wt% for 1 h, 1.87 wt% for 12 h and 3.24 wt% for 48 h. This indicates that ball-milled Li_2MnO_3 is very hygroscopic and the weight gain during storage is mainly absorbed water and CO_2. The absorption is reversible as the increased weight during storage is lost again in the second heating cycle and the first and second cooling curves for all samples overlap. This study suggests disordered Li_2MnO_3 should be stored in an inert atmosphere during the whole synthesis and characterisation processes or dried before using.

In Figure 3.16 (c), ball-milled Li_2MnO_3 was heated in air, N_2 and O_2, with two different heating processes: heating to 500 ℃, cooling and reheating to 500 ℃ , and heating to 800 ℃. The profiles of TG heated to 500 and 800 ℃ were similar to previous study, but heating in different atmospheres did not show an obvious trend and the difference was small (less than 0.71 wt% heated to 500 ℃ and 1.09 wt% to 800 ℃). The first possibility is that samples aged to different degrees, three homogeneous samples need to be collected for the atmosphere study in the future. Another possibility is that the weight gain is either independent of oxygen partial pressure or so sensitive to oxygen that it has already reacted even in N_2. More study is required to draw conclusions.

As concluded from TG-MS results, the weight loss at 350-470 ℃ was due to a combination of water and CO_2; data at a very slow rate, 0.5 ℃/min, were collected while the TG-MS results were collected with 10 ℃/min, to possibly separate the overlapping weight loss processes, Figure 3.16 (d). A slight weight gain, about 0.5%, below 70 ℃, attributed to water uptake, was followed by three slopes below 400 ℃, which might be attributed to: (a) 0.99 wt% water loss; (b) 2.91 wt% of mixed water and CO_2 loss, and (c) 2.82 wt% CO_2 loss. By 400 ℃, the H_2O and the first CO_2 loss were complete and a plateau appeared. Above 500 ℃, the second CO_2

loss, 1.99 wt% started. In summary, the water and CO_2 losses were not well separated and the profile did not show a big difference, although the heating rate was much slower, which may indicate the reaction was temperature-dependent, not time-dependent.

The XRD patterns of the sample heated to 450 ℃ and 850 ℃ (labelled in A and B) are shown next. At 450 ℃, the sample still remained a disordered rock-salt phase, but a broad ordered domain peak appeared at about 18°. At 850 ℃, an ordered phase formed ,with sharper peaks, corresponding to monoclinic Li_2MnO_3, but it still had a noisy background. Compared with the previous study on heating Li_2MnO_3, where the sample was heated at each temperature for 20 h from room temperature to 800 ℃, the ordering did not complete during heating with this slow TG rate (27 h in total). The second CO_2 loss occurred after the phase transformation from disorder to order. Full crystallization required either higher temperature or longer heating time.

3.1.2.4 TG-DSC of disordered Li_2MnO_3

Figure 3.19 shows (a) the instrumental baseline, (b) raw data for Li_2MnO_3 and (c) calibrated data for both TG and DSC (The calibration is described in section 2.3). Below 100 ℃, a rapid endothermic reaction was seen by DSC, which corresponded to the water loss in TG. There was a relatively slow, continuous endothermic drift at higher temperatures during heating which was reversible on cooling.

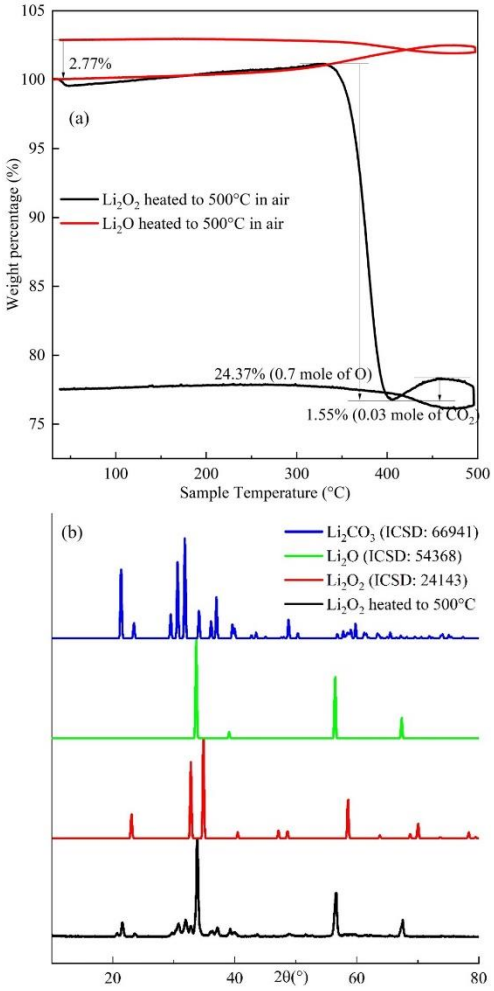

Figure 3.12 the (a) TG of Li_2O_2 and Li_2O heated to 500 °C and (b) XRD patterns of Li_2O_2 after TG.

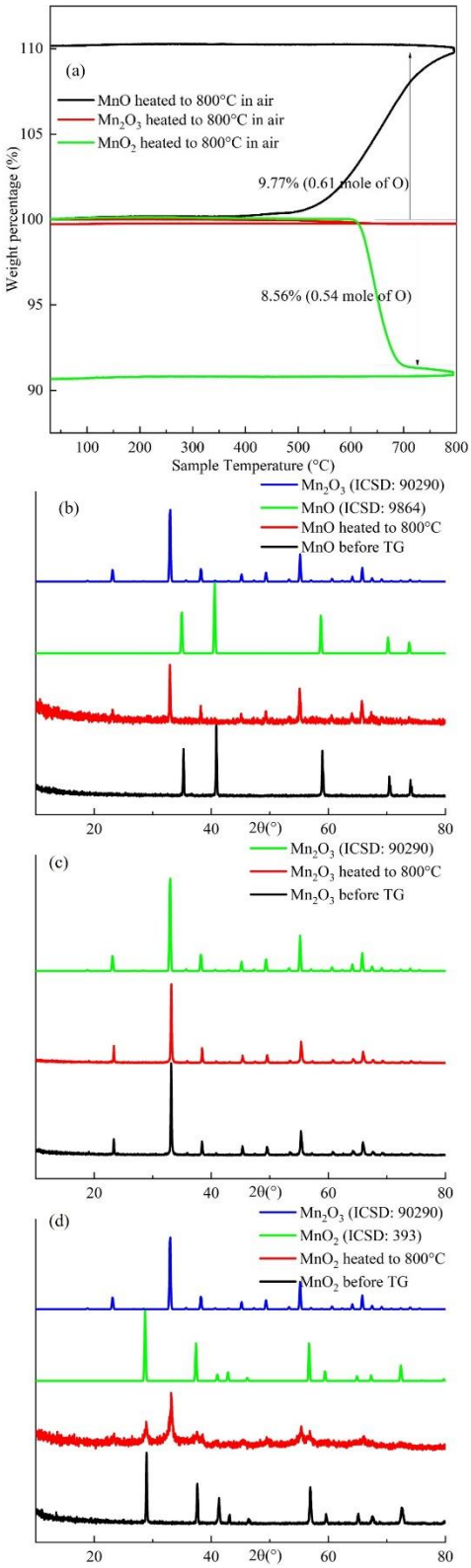

Figure 3.13 (a) the TG of MnO, Mn_2O_3 and MnO_2 heated to 800 °C and (b) to (d) XRD patterns before and after TG.

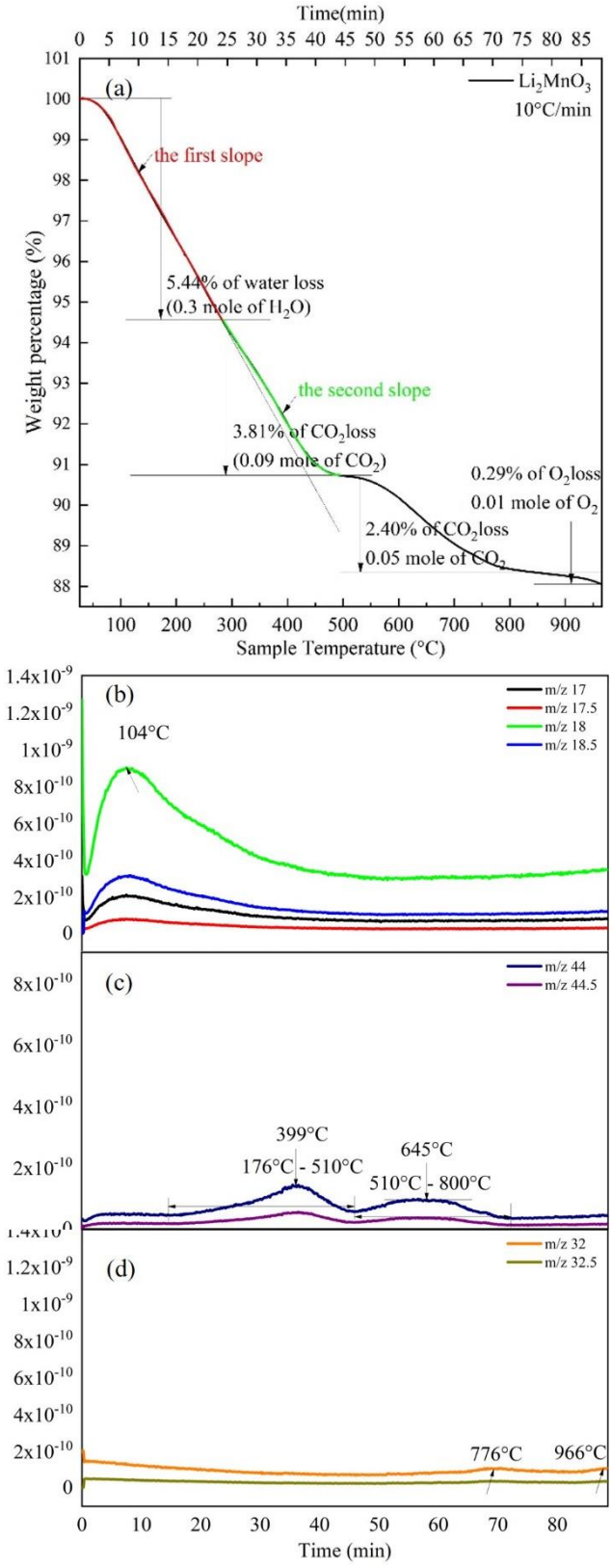

Figure 3.14 TG-MS analysis of disordered Li_2MnO_3

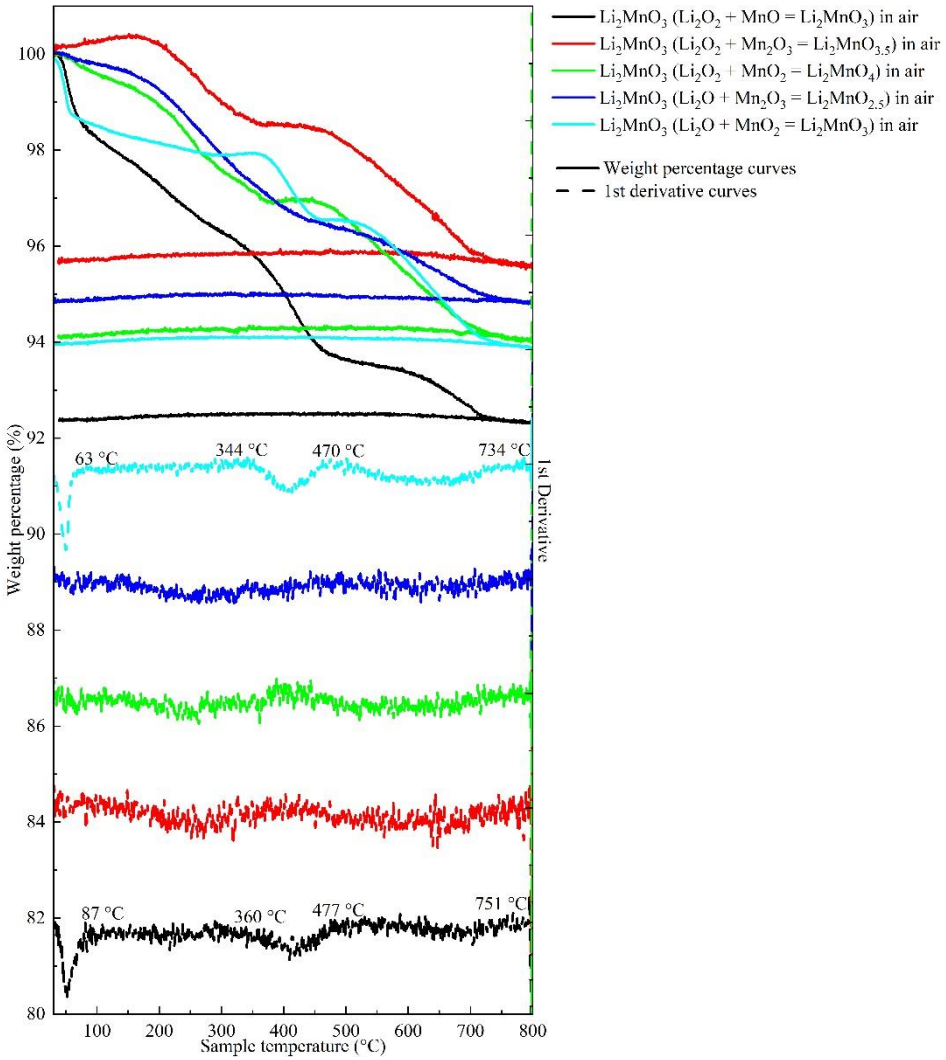

Figure 3.15 the TG patterns and DTG curves of Li_2MnO_3 produced by Li_2O_2 and Li_2O and three Mn-O with heat treatment

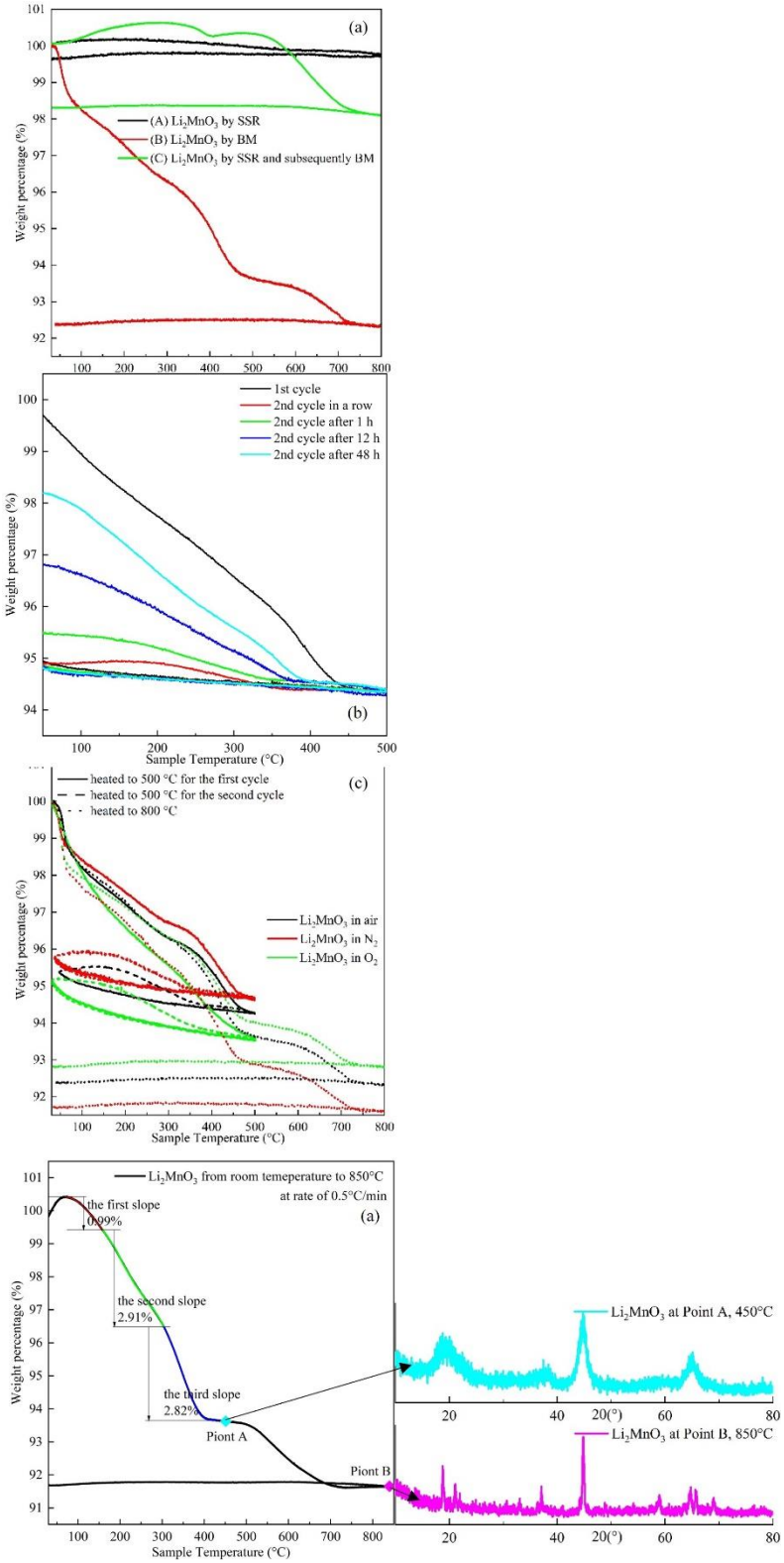

Figure 3.16 TG of Li_2MnO_3 (a) produced by different synthesis methods; (b) Li_2MnO_3 heated with different time interval, (c) heated in different atmosphere and (d) heated with a slow rate, 0.5 °C/min, and XRD patterns at Point A and B.

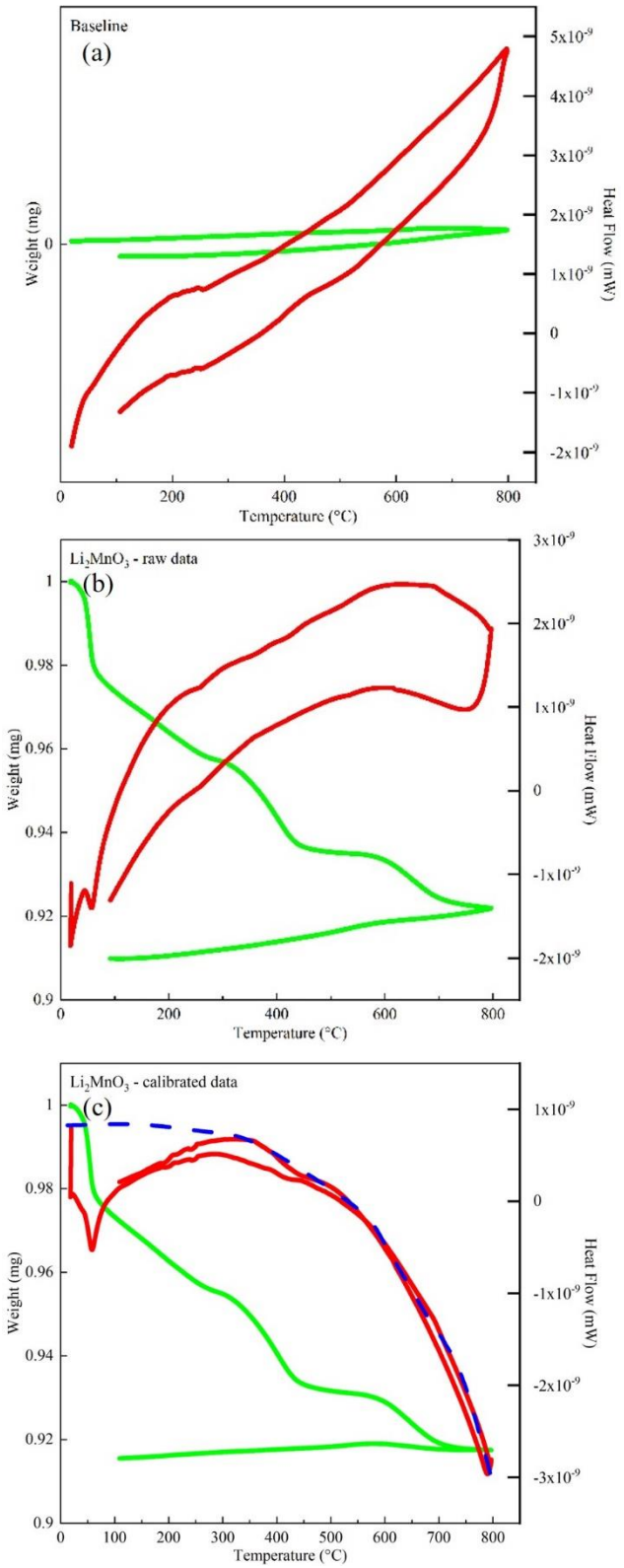

Figure 3.17 TG-DSC data Li_2MnO_3. Red and green lines represent TG and DSC results, respectively. (a) is the instrumental baseline. (b) is raw data and (c) is the extracted line, where the blue line is a possible sample baseline.

3.1.3 Characterisation of Li_2MnO_3 with different degree of ordering

3.1.3.1 Charge-discharge

The charge-discharge profiles of swagelok cells with cathodes prepared from i. disordered (room temperature), ii. partially ordered (heated at 400 ℃), iii. fully ordered (heated at 800 ℃) Li_2MnO_3 and iv. ordered Li_2MnO_3 prepared by solid state reaction were studied, Figure 3.20.

Two ordered samples, iii and iv, were run within the voltage window 2.0 to 4.8 V at rate C/10 (Figure 3.20). They both showed a plateau at about 4-4.3 V during charge and discharge. For iv, it increased rapidly to 4.8 V with a capacity of 48 mAh/g. The following cycles had similar profiles but the capacity gradually increased to about 60 mAh/g. For iii, it had a relatively obvious plateau at 4-4.3 V and eventually increased to 4.8 V with a capacity of 89 mAh/g. However, after the first cycle, the plateau became a gradually increasing slope and the capacity increased to 151 mAh/g. For both, it is noticeable that an unusual curve appeared below 2.8 V during discharge, which may indicate that the discharge voltage 2.0 V was too low and an unusual discharge reaction occurred. To avoid this, subsequent cycling tests on ordered Li_2MnO_3 were carried out within a voltage window 3.0-4.8 V.

Figure 3.21 presents the charge-discharge profiles of ball-milled Li_2MnO_3 with different degrees of order after heating. For i and ii, they did not show an obvious plateau. Their first charge cycle was unique and reached 4.8 V rapidly with capacities of 48 and 62 mAh/g, respectively. The following cycles slowly reached stable capacities of 98 and 71 mAh/g, respectively. Noticeably, in ii, the discharge capacity was about 115 mAh/g, higher than the charge capacity 71 mAh/g. For iii, it had a plateau at about 4-4.3 V. All charge and discharge profiles were similar. The first charge capacity reached 93 mAh/g and faded to 77 in the second cycle. Then the capacity gradually increased in the following cycles and reached 84 mAh/g in the seventh cycle. Comparing i and iii, their charge and discharge capacities were similar but the profiles were very different. The disordered sample presented a slope instead of a plateau.

Although Li_2MnO_3 theoretically contains only Mn^{4+} and should not be electrochemically active, all four samples were able to perform as cathodes; solid state sample iv had the lowest charge capacity, 48 mAh/g and the ball-milled samples i and iii had the highest charge capacities, about 90-100 mAh/g. The ordered samples tended to be difficult to reach the voltage as low as 2.0 V and they also presented an obvious plateau while the disordered samples presented a slope.

At this stage, we do not know whether the samples were fully oxygen stoichiometric or whether they were oxygen-deficient and the associated Mn^{3+} content was responsible for the observed capacities. It is also clear from the TG-MS results that the samples may have had significant H_2O, CO_2 contents which would have reduced the capacity values. Further work is required to resolve these questions.

3.1.3.2 XANES

Figure 3.22 shows the absorption Mn K-edge XANES spectra of Li_2MnO_3 prepared by mechanosynthesis and with subsequent heating at 200, 400, 600 and 800 ℃. The difference in peak shape and peak position was relatively small. The absorption energy values for samples at room temperature and heated to 200, 400, 600 and 800 ℃ were 6559.51, 6559.50, 6559.99, 6559.60 and 6559.31 eV, respectively. Compared with literature data [149], the Mn valence in these samples was close to 4+. Details of reference data and calibrations on experimental data are given in section 6.3.6.7. During heating, the peak shifted to higher energy, indicating the Mn valence increased slightly at 400 ℃ and then shifted back, indicating Mn valence reduced to its initial value at higher temperature. It is possible that disordered Li_2MnO_3 was non-stoichiometric at room temperature and absorbed oxygen during heating, accompanied with the oxidation of Mn^{3+}. At higher temperature, it was often observed to form $Li_2MnO_{3-\delta}$, with slight oxygen non-stoichiometry [52], which was accompanied by a reduction from Mn^{4+} to Mn^{3+}.

Table 3.7 Density of disordered rock-salt Li_2MnO_3 heated at different temperature

Samples	**Density(g/cm^3)**
At room temperauture	3.7984
At 500°C	4.0560
At 800°C	4.1809

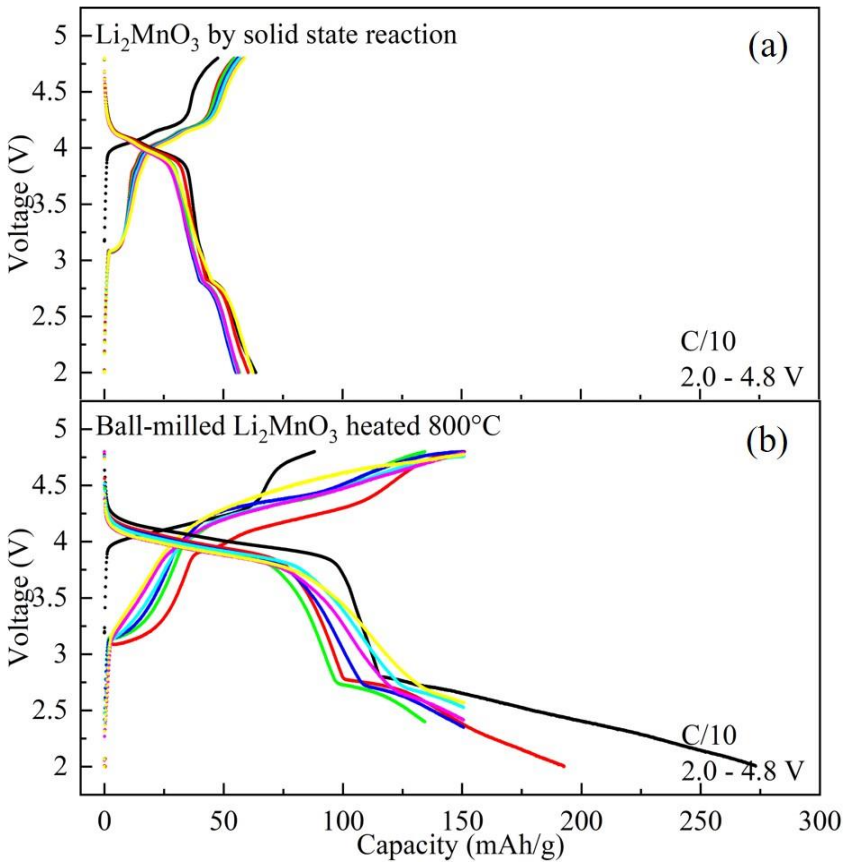

Figure 3.18 Voltage profiles and capacity retention of cathodes prepared by the ordered Li_2MnO_3, produced by (a) the solid state reaction and (b) mechanosynthesis and subsequent heating at 800 °C, respectively.

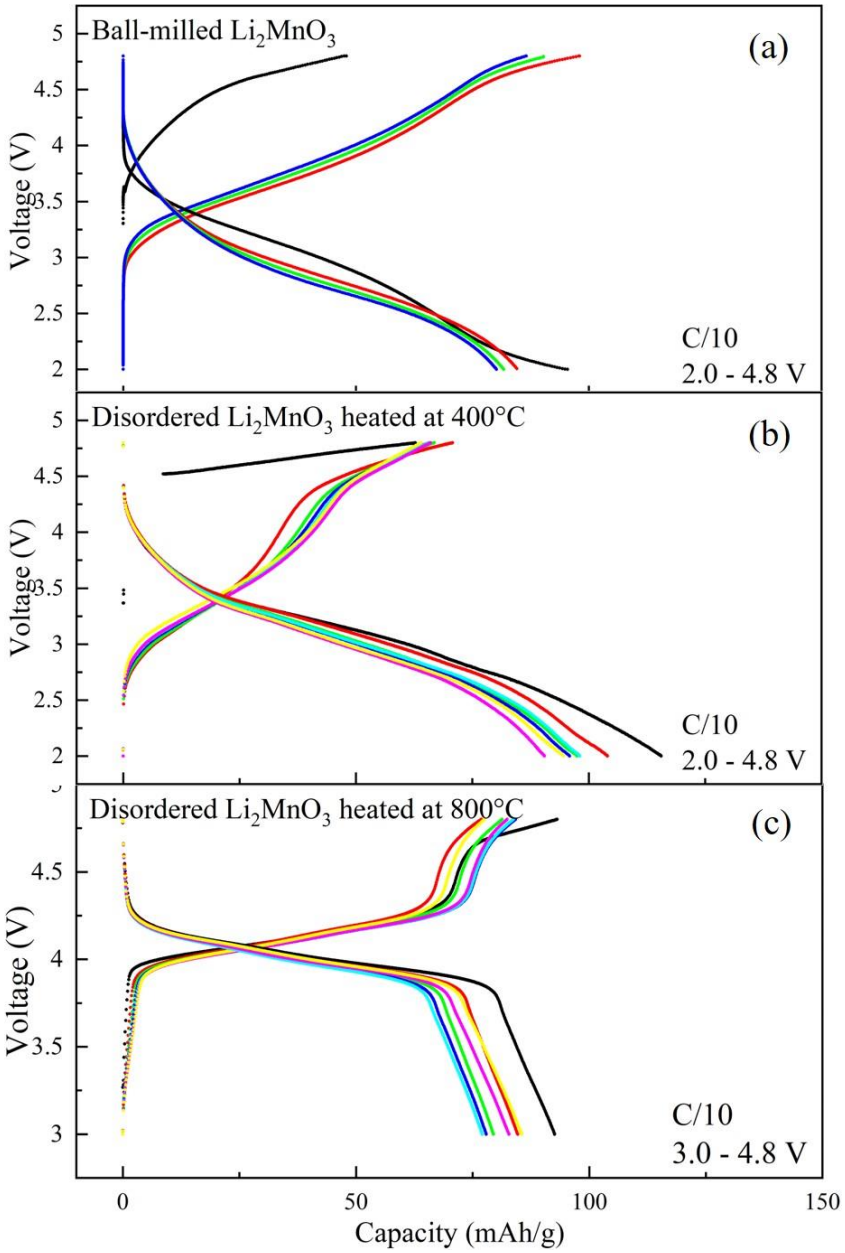

Figure 3.19 Voltage profiles and capacity retention of cathodes, prepared by Li_2MnO_3 with different order degree, cycled at C/10. (a) was the disordered Li_2MnO_3 at room temperature at 2.0 – 4.8 V; (b) was the disordered Li_2MnO_3 heated at 400 °C at 2.0 – 4.8 V, and (c) was the disordered Li_2MnO_3 heated at 800°C at 3.0 – 4.8 V.

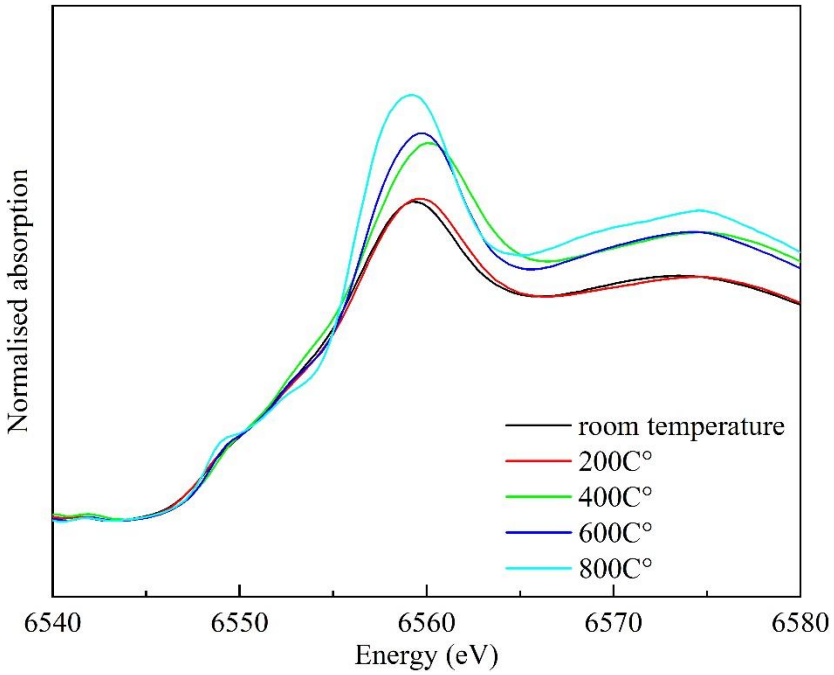

Figure 3.20 Mn K-edge XANES spectra of Li_2MnO_3 heated at different temperatures

3.1.3.3 Impedance spectroscopy

Five Li_2MnO_3 samples were prepared as pellets by: i. solid state reaction; Figure 3.23, ii. ball-milling and subsequent heating at 850 ℃ for 12 h, Figure 3.24; iii. ball-milling and subsequent heating at 850 ℃ for 48 h, Figure 3.25; iv. ball-milling and subsequent quenching from 1000 ℃, Figure 3.26; and v. ball-milling and subsequent heating at 500 ℃ for 12 h, Figure 3.27.

A typical impedance dataset of each sample is shown and a combined Arrhenius plot of conductivity values in Figure 3.28. Data are presented in four different complementary formats. In (a), the Z^* plot shows a broad semicircle, the radius of which corresponds to the sample resistance. For i, at low frequency, a poorly defined tail is seen which may represent an impedance at the sample-electrode interface. For ii and iii, the tail is barely seen, while iv and v show a relatively clear tail, especially iv showing a second semicircle.

In (b), the C' plot shows the onset of a plateau around 10^{-12} F cm^{-1} at high frequency, indicating a bulk component. For i, there was a second plateau at slightly lower frequency which was poorly-defined with a capacitance around 10^{-11} F cm^{-1}, indicating a grain boundary or possibly, a small volume fraction second phase. For i, iv and v, the capacitance value was as high as 10^{-5} F cm^{-1} at low frequency and high temperature, indicating the compound had some ionic conductivity and therefore, was a mixed conductor. For ii and iii, the capacitance value was 10^{-7} F cm^{-1} at low frequency, which may be a capacitance of surface layer or interface between sample and electrode.

The Y' spectroscopic plot, (c) shows a frequency-independent plateau over a wide range which represents the total conductivity. At high frequencies, a dispersion to higher conductivities is observed, which may relate to Jonscher's power law behaviour.

For i, the combined Z'' and M'' plot (d) shows that Z'' peak and M'' peaks approximately overlap at medium-high frequency, indicating that the M'' peak and the associated Z'' peak corresponded to the bulk impedance response. This confirms that the semicircle in the Z* plot and the Y' plateau were bulk values. For i and iii, the Z" and M" overlapped, indicating they were electrically homogeneous. However, for ii, iv and v, the Z" and M" was separated by 1-2 decades of frequency, which indicates a degree of electrical inhomogeneity. For i and ii, another peak appeared in M'' at higher frequency, indicating another component may exist, which has high conductivity.

The conductivity and activation energies are shown in the Arrhenius plot. i and iii were the most resistive, which were produced by solid state reaction and sintered at high temperature

for 48 h. Most of the Mn^{3+} might have been oxidised under these conditions and the amount of Mn^{3+} was therefore low. i, ii and iii had two slopes, which may present an extrinsic conductivity at low temperature and intrinsic conductivity at high temperature. At low temperature, the dominating conductor was possibly ionic, attributed to the effect of dopants, while at high temperature, the dominating conductor was electronic, thermally generated electrons and/or holes. iv and v had a single slope, which was produced by quenching from 1000 ℃ and heating at 500 ℃. In this case, a significant amount of Mn^{3+} possibly remained leading to mixed ionic and electronic conductivity.

In order to study the effect of atmosphere, sample v was measured under different atmosphere. The total resistance was largest in O_2 and smallest in N_2, maybe a n-type conductor, but the trend was not reversible. Sample v was heated at 400 ℃ for different time, the conductivity varied. After heated for 340 mins, it became more resistant, might indicating an aging.

3.2 Conclusions and future work

The effect of mechanosynthesis on reactants has been studied. Li_2O_2, Li_2O, LiF and Li_2CO_3 did not have phase change before and after milling, but particle size was reduced. On the other hand, the particle size of $LiOH{\cdot}H_2O$ and $LiCH_3COO{\cdot}2H_2O$ did not change but they might have preferred orientation before and after milling. In steel jars, each ball-milled Li reactants contained < 3% contamination, mainly Fe. However, ball-milled manganese oxides were highly contaminated by three different milling media. Amorphous structure was formed and Mn valence retained in tungsten carbide jars, whilst using zirconia and especially steel jars, Mn^{4+} was reduced to form either Mn_2O_3 or a spinel phase. As Fe and Zr is chemically and structurally similar to Mn, the high contamination in steel jars (> 40%) and zirconia jars (> 20%) might be introduced by direct reactions between samples and media. Future work should be aimed to obtain the particle size and do quantitative chemical analysis before and after milling.

Disordered rock-salt Li_2MnO_δ ($2.5 \leq \delta \leq 4$) were produced by Li_2O_2 with MnO, Mn_2O_3 and MnO_2 and Li_2O with Mn_2O_3 and MnO_2. With suitable manganese oxides, both Li_2O_2 and L_2O may be used to produce Li_2MnO_3. It is possible that O_2^{2-} works as an oxidising agent but O^{2-} does not give redox reaction, so no reaction occurred when Li_2O and MnO were ball-milled. Other Li reactants, such as $LiCH_3COO$, Li_2CO_3 and $LiOH{\cdot}H_2O$, did not effectively react. Disordered Li_2MnO_3 was also successfully produced by ball-milling ordered monoclinic Li_2MnO_3. During heating, disordered Li_2MnO_3 first formed an ordered superstructure domain with much smaller size and finally transformed to single phase ordered monoclinic Li_2MnO_3. When $\delta \neq 3$, the high temperature phases had complex impurities, not single phase Li_2MnO_3.

Although manganese oxides were highly contaminated when ball-milled separately, ball-milled Li_2MnO_3 products only obtained < 2% Fe, < 3% Zr and < 13% W contamination when produced in three different milling media, respectively. Ablation occurred in tungsten carbide and zirconia jars, which did not incorporate into the product, whilst in steel jars, incorporation from jars into products occurred. Future work can be considered to optimise synthesis conditions in order to produce Li_2MnO_3 with less contamination.

Ball-milled Li_2MnO_3 was very hygroscopic and contained complex hydroxides and carbonates, which decomposed at ~100 ℃ (as water) and ~400 ℃ and 650 ℃ (as CO_2), respectively. Oxygen loss occurred at ~750 ℃. This indicates ball-milled products should be synthesised and stored in an inert atmosphere. The hygroscopic behaviours may depend on oxygen content in $Li_2MnO_{3-\delta}$.

The average Mn valence in disordered Li_2MnO_3 were close to 4+, but disordered Li_2MnO_3 was still electrochemically active and had a higher charge capacity, 70-100 mAh/g, than ordered Li_2MnO_3, 50-60 mAh/g. The conductivity of disordered Li_2MnO_3 was a mixture of ionic and electronic conductor, and disordered Li_2MnO_3 was more conductive than the ordered one polymorph, which may indicate the present of Mn^{3+}. During heating, disordered Li_2MnO_3 formed ordered domains with much smaller than the grain size and Mn valence slightly increased. At high temperature, Mn valence slightly decreased again, and an ordered Li_2MnO_3 finally formed with oxygen non stoichiometry. Future work could aim to determine oxygen stoichiometry, whether it varied with reaction conditions and the mechanism of the redox reaction as cathodes.

3.3 References

[52] D. Pasero, V. McLaren, S. De Souza, and A. R. West, “Oxygen nonstoichiometry in Li2MnO3: An alternative explanation for its anomalous electrochemical activity,” *Chem. Mater.*, vol. 17, no. 2, pp. 345–348, 2005, doi: 10.1021/cm040186r.

[149] B. Y. R. D. Shannon, M. H, N. H. Baur, O. H. Gibbs, M. Eu, and V. Cu, “Revised Effective Ionic Radii and Systematic Studies of Interatomie Distances in Halides and Chaleogenides Central Research and Development Department , Experimental Station , E . L Du Pont de Nemours The effective ionic radii of Shannon & Prewitt [Acta ,” 1976.

Appendix A for Chapter 3: Impedance data

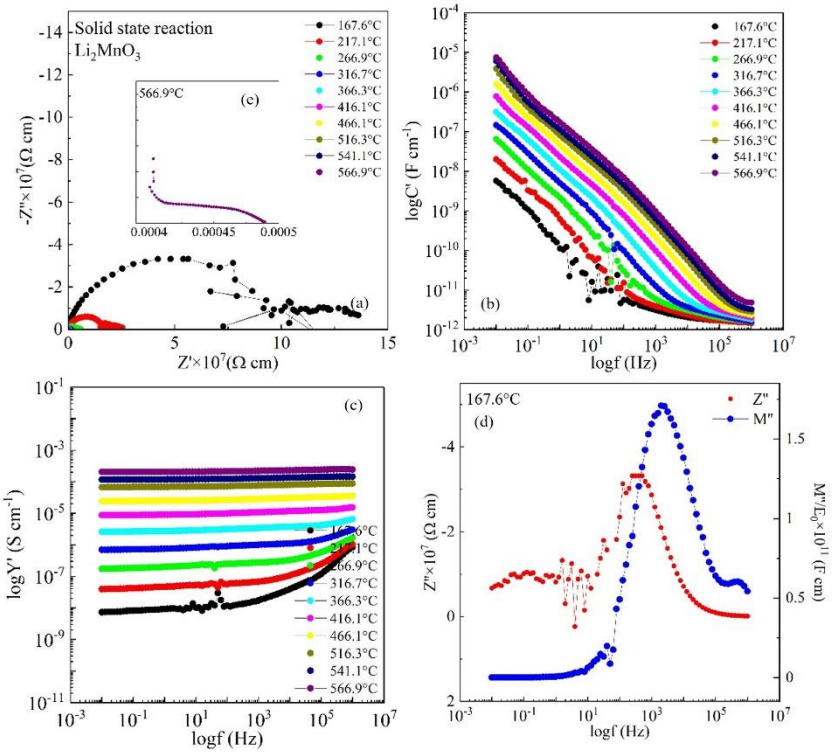

Figure 3.21 the impedance dataset for solid state Li_2MnO_3

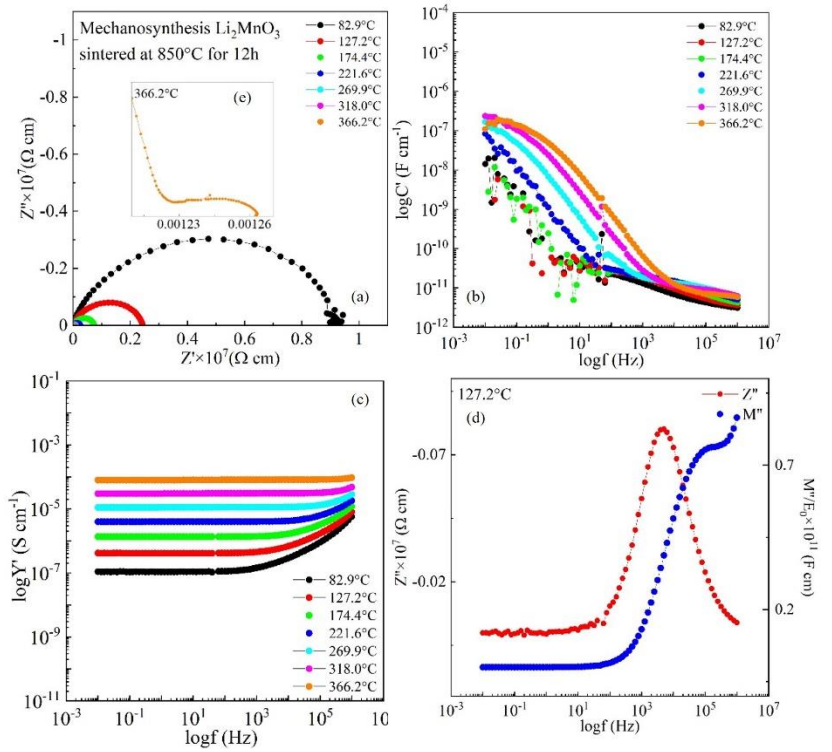

Figure 3.22 the impedance dataset for ball-milled Li_2MnO_3 sintered at 850 °C for 12 h

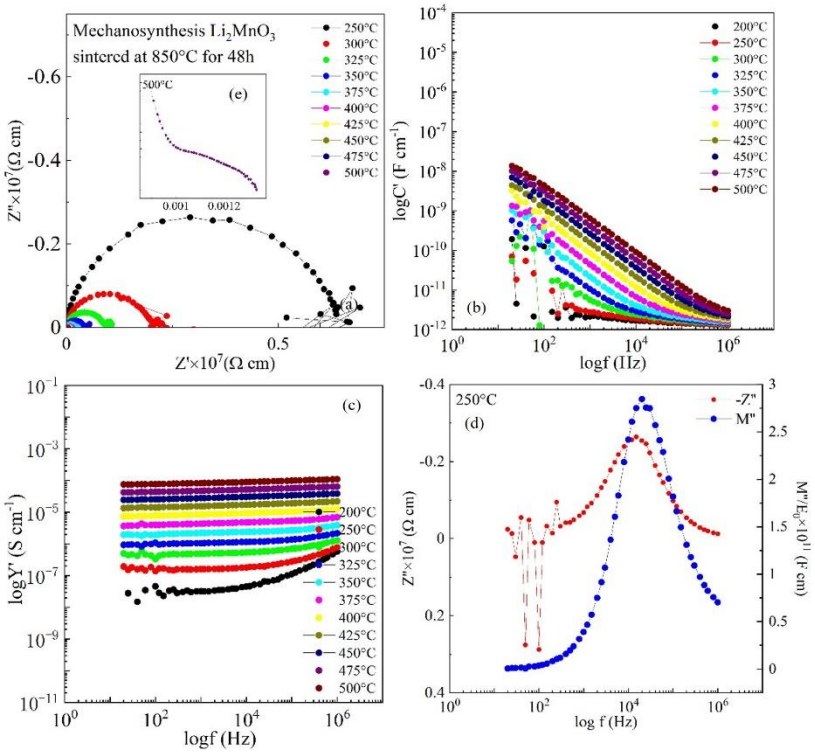

Figure 3.23 the impedance dataset for ball-milled Li_2MnO_3 sintered at 850 °C for 48 h

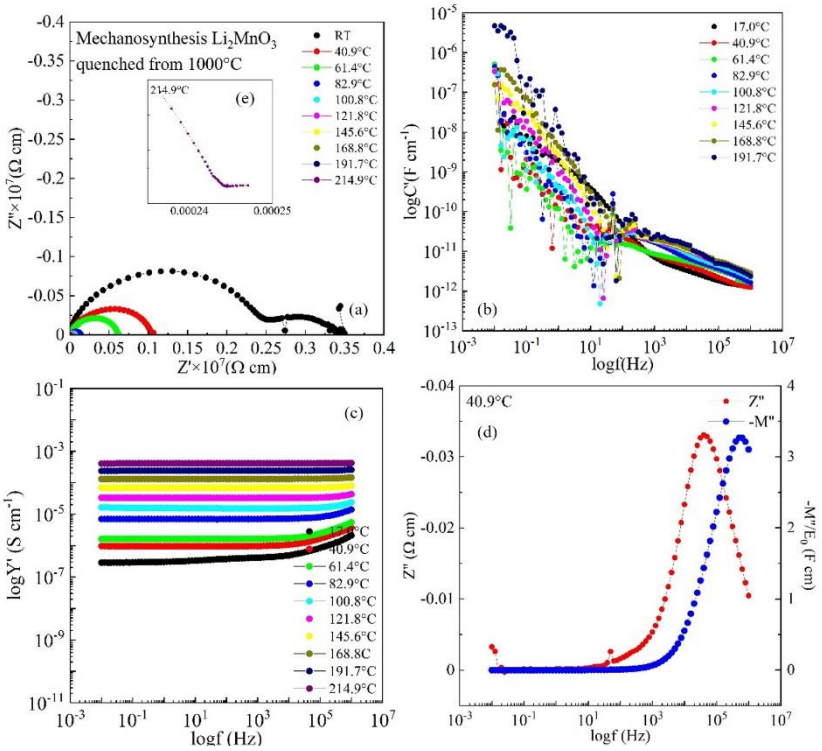

Figure 3.24 the impedance dataset for ball-milled Li_2MnO_3 quenched at 1000 °C

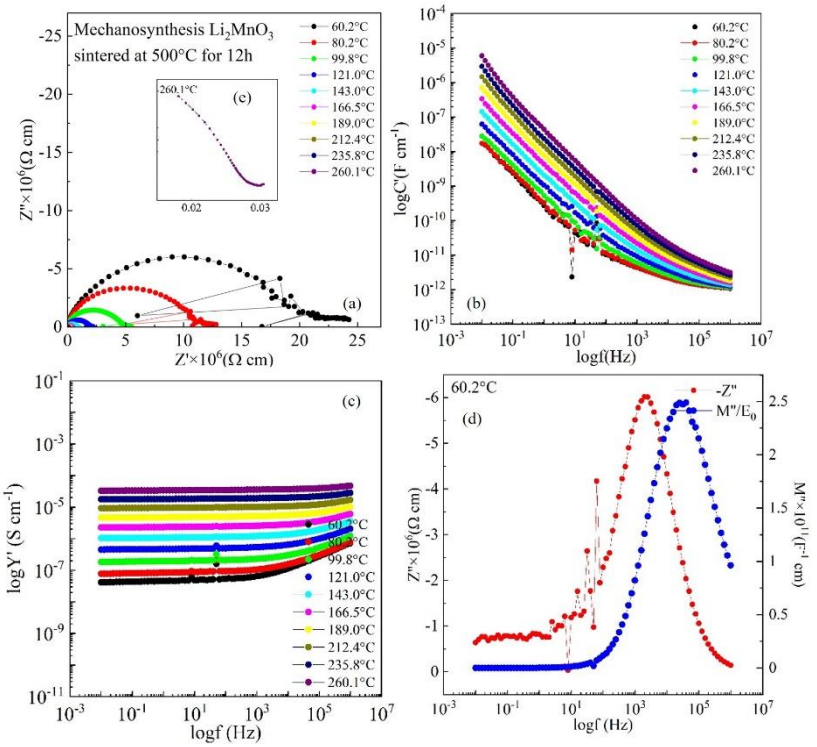

Figure 3.25 the impedance dataset for ball-milled Li_2MnO_3 sintered at 500 °C for 12h

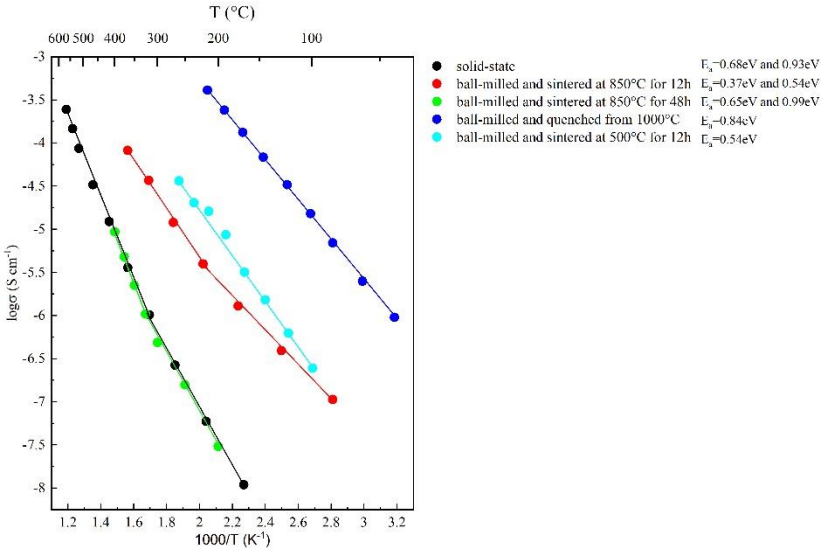

Figure 3.26 The Arrhenius plot of Li_2MnO_3

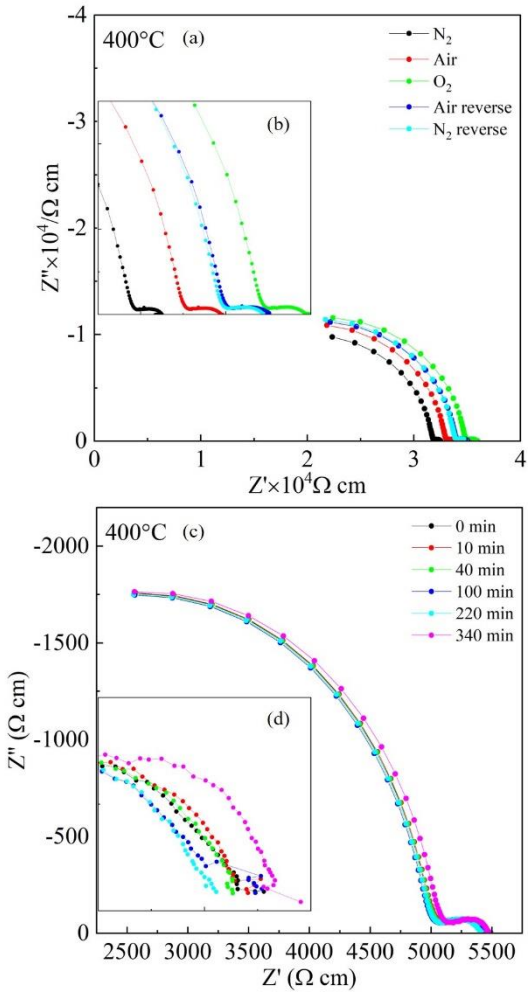

Figure 3.27 the impedance dataset for ball-milled Li_2MnO_3 (a) under different atmosphere (b) heated for different time

Chapter 4 F-Li_2MnO_3

4.1 Results and discussion

4.1.1 Four doping mechanisms

In F-doped Li_2MnO_3, fluorine substitutes for oxygen and in order to achieve charge compensation, four possible doping mechanisms are considered:

1. Electronic compensation:

$$Mn^{4+} + O^{2-} \rightarrow Mn^{3+} + F^{-} \quad (1)$$

O^{2-} is partially replaced by F^- and initially, charge is balanced by reducing Mn^{4+} to Mn^{3+} with general formula $Li_2Mn^{4+}_{1-x}Mn^{3+}_xO_{3-x}F_x$ and limiting composition, $Li_2Mn^{3+}O_2F$. The Li:Mn ratio remains as 2:1 and, assuming the rock salt stoichiometry is retained, there are no vacancies created on either cation or anion sub-lattices. Further substitution is possible in principle with reduction of Mn^{3+} to Mn^{2+} and limiting composition, $Li_2Mn^{2+}OF_2$.

2. Lithium vacancy:

$$Li^{+} + O^{2-} \rightarrow F^{-} \quad (2)$$

O^{2-} is partially replaced by F^-, and charge is balanced by leaving out Li^+. The general formula is $Li_{2-x}MnO_{3-x}F_x$, with limiting composition, $MnOF_2$. The Mn valence is 4+ but this mechanism leads to a cation-deficient rock-salt stoichiometry.

3. Double doping:

$$Mn^{4+} + 3O^{2-} \rightarrow Li^{+} + 3F^{-} \quad (3)$$

O^{2-} is partially replaced by F^- and charge is balanced by replacing Mn^{4+} with Li^+. This mechanism retains the rock salt stoichiometry with substitution on both cation and anion sublattices and Mn stays as 4+ in the general formula $Li_{2+x}Mn_{1-x}O_{3-3x}F_{3x}$. However, disorder on both sublattices would be required for the solid solution to extend as far as the limiting composition LiF.

4. Manganese vacancy:

$$Mn^{4+} + 4O^{2-} \rightarrow 4F^{-} \quad (4)$$

O^{2-} is partially replaced by F^- and charge is balanced by leaving out some Mn^{4+} giving a cation-deficient rock salt stoichiometry. The general formula is $Li_2Mn_{1-x}O_{3-4x}F_{4x}$, with limiting composition, Li_8MnF_{12}.

The quaternary system Li-Mn-O-F is shown as a compositional pyramid in Figure 4.1, together with the location of possible solid solutions in two ternary sections, Li_2MnO_3-MnO-LiF in Figure 4.2 (a), and Li_2MnO_3-MnO_2-LiF in Figure 4.2 (b). Compositions according to these four possible doping mechanisms were prepared by both solid state reaction and mechanosynthesis; results are given in sections 4.1.2-4.1.5.

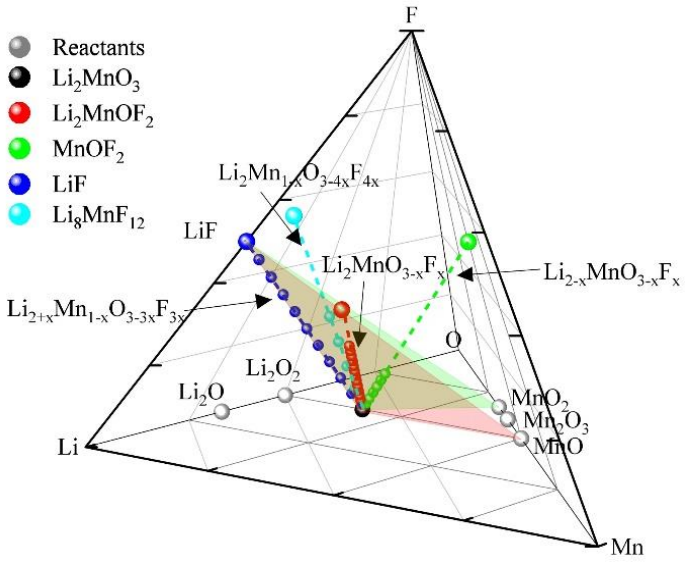

Figure 4.1 the quaternary system Li-Mn-O-F

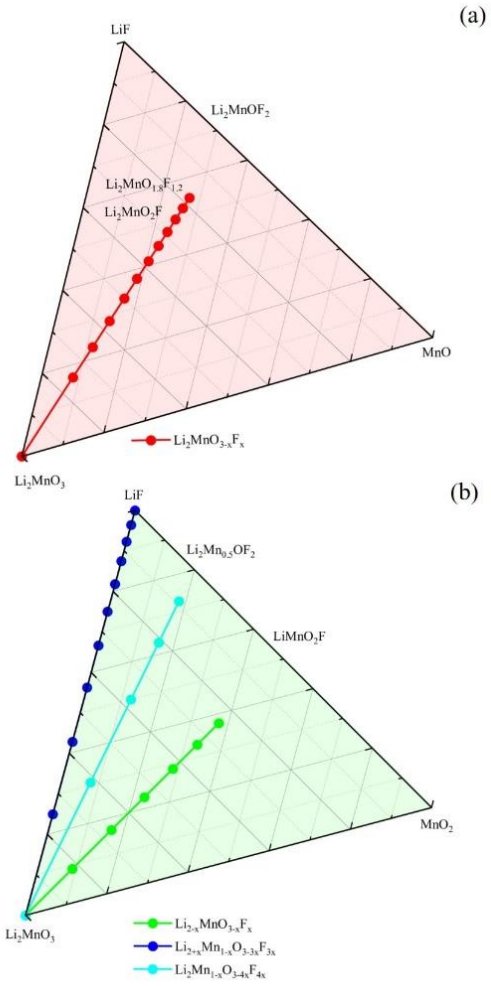

Figure 4.2 the ternary diagrams (a) Li_2MnO_3-MnO-LiF and (b) Li_2MnO_3-MnO_2-LiF

4.1.2 Mechanism 1 (M1) : electronic compensation, $Li_2MnO_{3-x}F_x$

4.1.2.1 $Li_2MnO_{3-x}F_x$ produced by solid state reaction

Samples with composition $Li_2MnO_{3-x}F_x$, x=0, 0.1…and 0.5 were prepared by solid state reaction, at 850 ℃ for 12 h, Figure 4.3. For x=0-0.2, single phase products were produced and appeared to be a solid solution based on monoclinic Li_2MnO_3. For $x \geq 0.3$, a second phase $LiMn_2O_4$ appeared and its amount increased with F content, indicating that the solid solution limit of monoclinic $Li_2MnO_{3-x}F_x$ was less than x=0.3.

Lattice parameters are summarised in Figure 4.4, using data collected from the MoPSD diffractometer. All solid-state samples correspond to an ordered monoclinic structure, using the space group $C2/m$. Lattice parameters a and β increased while c decreased. b had some scatter and might be constant. Errors were large, especially in c. XRF analysis shows that these samples had no detectable fluorine content, Table 4.1. This indicates the probable loss of fluoride at the high temperatures used in synthesis. Alternatively, fluoride doping does not lead to a wide range of thermally stable Li_2MnO_3 solid solution but instead, F may be incorporated into the $LiMn_2O_4$ secondary phase. Further study on possibility of synthesis of high temperature materials may be considered.

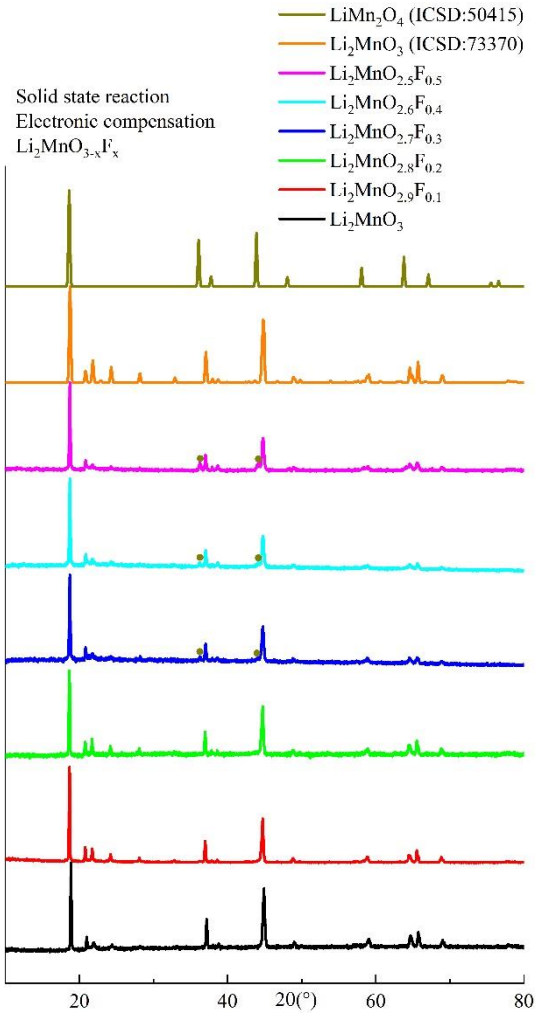

Figure 4.3 the XRD results of $Li_2MnO_{3-x}F_x$ by solid-state reaction

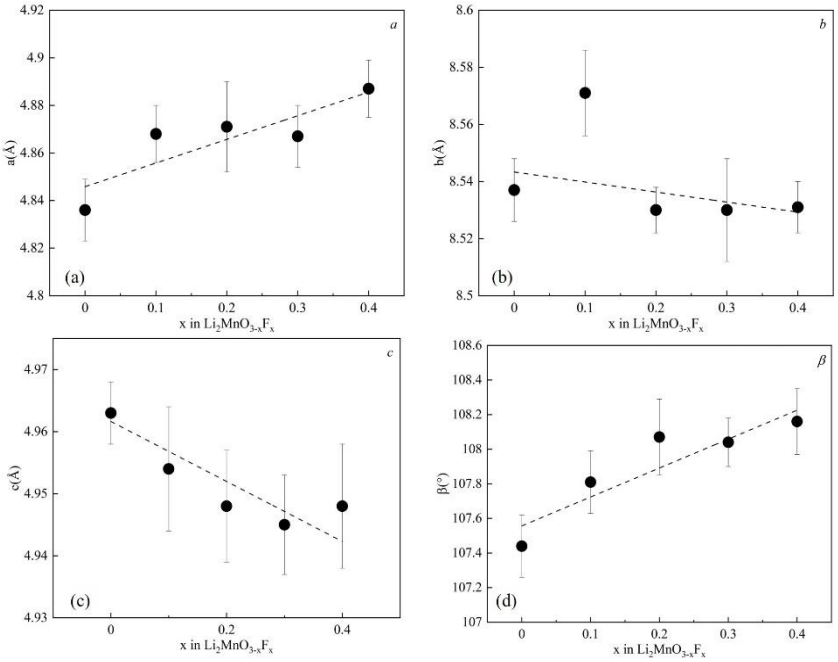

Figure 4.4 Lattice parameter of $Li_2MnO_{3-x}F_x$ produced by solid state reaction

Table 4.1 XRF data of $Li_2MnO_{3-x}F_x$ produced by solid state reaction.

Samples	**The ratio of O/Mn**	
	Expected	Practical
Li_2MnO_3	3	4.16 4.23 3.87
$Li_2MnO_{2.9}F_{0.1}$	2.9	3.89 3.53 4.30
$Li_2MnO_{2.8}F_{0.2}$	2.8	5.26 3.81 4.04
Note: No F was detected.		

4.1.2.2 $Li_2MnO_{3-x}F_x$ produced by mechanosynthesis and heated at 500 and 600 ℃

Samples in the range x=0 to 1.6 were prepared by mechanosynthesis, Figure 4.5. For $x \leq 1.4$, a disordered rock-salt phase formed, indexed using the cubic space group $Fm\bar{3}m$. When x > 1.4, extra peaks appeared. For x=1.6, two very broad extra peaks appeared around 30-40°, which may be attributed to one of the spinels $LiMn_2O_4$ or $Li_4Mn_5O_{12}$ and/or to LiF. Also, a small amount of Mn_2O_3 appeared with a relatively sharp peak, seen in the expanded region (b). The cubic lattice parameter increased approximately linearly with x over the entire composition range, $0 \leq x \leq 1.1$, from about 4.07 Å to 4.11 Å with the errors ±0.004 Å, Figure 4.6, consistent with the formation of a homogeneous, F-doped solid solution and with a substitution mechanism involving gradual reduction of Mn^{4+} to the larger Mn^{3+} and Mn^{2+} ions.

The thermal stability of ball-milled $Li_2MnO_{3-x}F_x$ was studied by heating samples at (a, b) 500 ℃ and (c, d, e) 600 ℃ for 20 h in air, Figure 4.7. Several changes were seen. First, peaks associated with the disordered rock salt subcell at 500 and 600 ℃, became sharper, indicating grain growth, Figures 4.5, 4.7 and 4.26. Grain size results (see more in section 4.1.6.2) which show temperature-dependent grain growth are summarised for a series of compositions in Table 4.5 and 4.6.

Second, a broad peak appeared at 18°, indicating either the formation of superstructure domains within grains of the rock salt structure whose size was much smaller than that of the grains themselves, or the formation of nuclei of a spinel such as $LiMn_2O_4$. Further details are shown in the expanded region 35-40° for 500 ℃ (b) and regions 17-21° and 36-40° for 600 ℃ in (d) and (e). The peak at 37.4°, attributed to (111) in the rock-salt subcell and/or to $(20\bar{1})$ in monoclinic Li_2MnO_3 moves to lower angle in x=0.2 and 0.4. At the same time, a peak appears at 36.5° whose intensity increases with x and may represent the spinel phase.

LiF appeared at high x and increased with x. It is possible that a precipitation of excess LiF occurred from the disordered rock salt solid solution. A spinel might form simultaneously. It is seen clearly at 600 ℃, that the spinel peaks growth in their intensity appears to coincide with decrease in intensity of the ordered Li_2MnO_3 peaks. LiF peaks were hardly seen at 600 ℃, except one small peak in $Li_2MnO_{1.8}F_{1.2}$. As the positions of spinel peaks at 38.2° and 44.4° overlap the peaks of LiF, it is possible that peaks of LiF are difficult to be seen when the intensity of spinel peaks increased due to its growth. Another possibility is that the amount of LiF decreased at 600 ℃ due to its recombination with part of the Li_2MnO_3 solid solution to produce a spinel, either with or without some F dopant present.

When heated at 500 ℃, the refined results, excluding the peak at 18°, show the cubic lattice parameter of the rock salt subcell does not increase with x, Figure 4.6, red line, unlike the data for the ball-milled sample without heat treatment. Therefore, there is no significant doping of Li_2MnO_3 with F at 500 ℃.

Ball-milled $Li_2MnO_{3-x}F_x$ was heated at 500 ℃ for 20 h under different atmospheres, N_2 and O_2 and results compared with those obtained in air, Figure 4.8. Similar results were obtained in all three atmospheres: grain growth occurred and either domains formed with ordered rock salt structure or secondary phase started to nucleate with a spinel structure. During heating, no obvious phase changes under different atmospheres were observed.

In summary, therefore, a range of rock salt solid solutions forms by the electronic charge compensation mechanism, which are kinetically stable but thermodynamically metastable at room temperature. On heating, these decompose by a combination of processes. First, exsolution of LiF from the solid solution may occur at the same time as small ordered domains form within the rock salt subcell. Second, with increasing x and increasing temperature, the size of the ordered domains increases but also, a spinel phase forms. This means that there is limited solubility of F in monoclinic, ordered Li_2MnO_3 at high temperatures and an electronic charge compensation mechanism associated with reduction of Mn^{4+}.

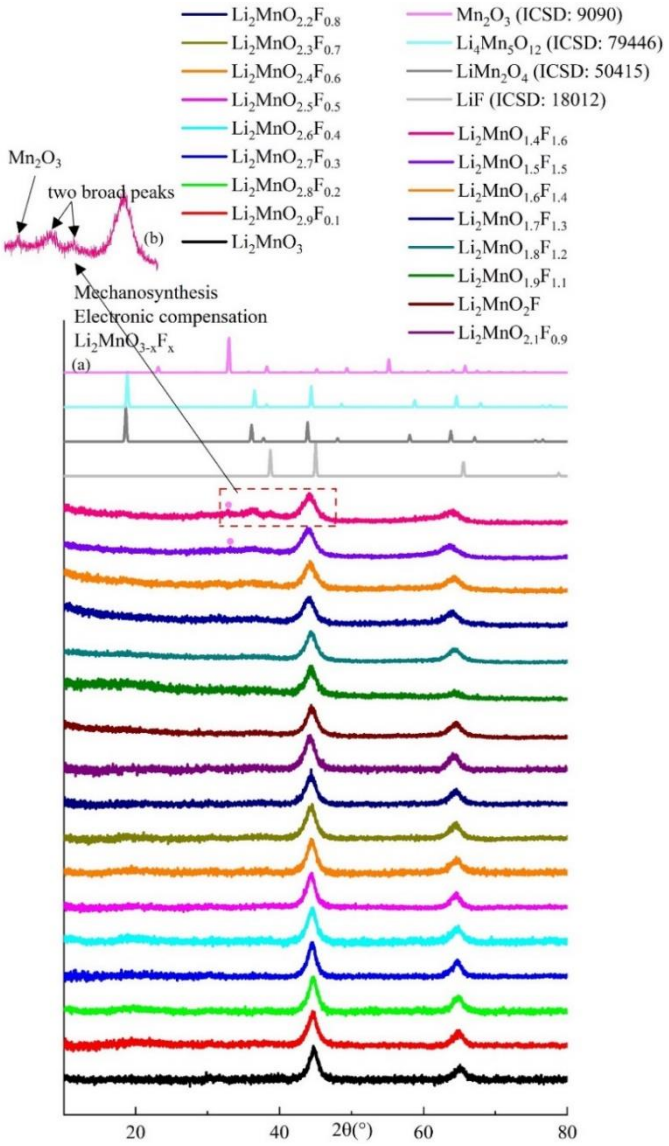

Figure 4.5 the XRD patterns of $Li_2MnO_{3-x}F_x$ by mechanosynthesis

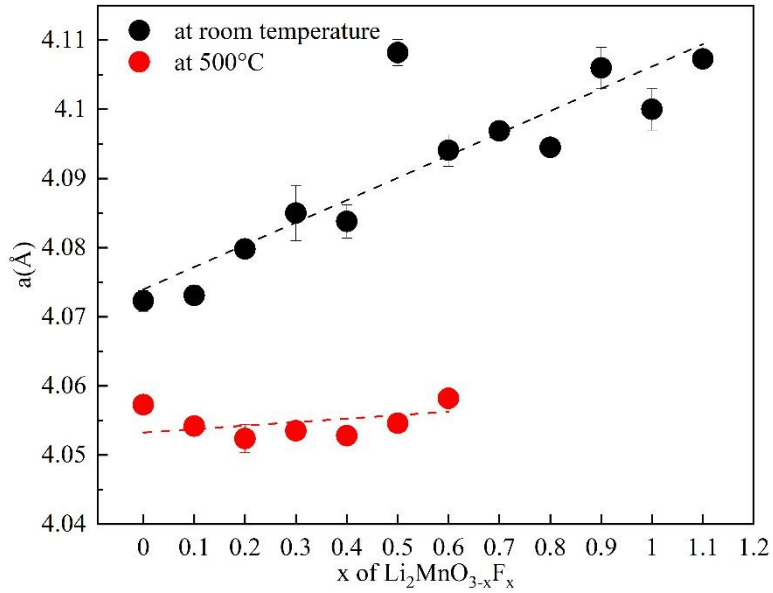

Figure 4.6 Lattice parameter of ball-milled $Li_2MnO_{3-x}F_x$ produced at room temperature and heated at 500 °C

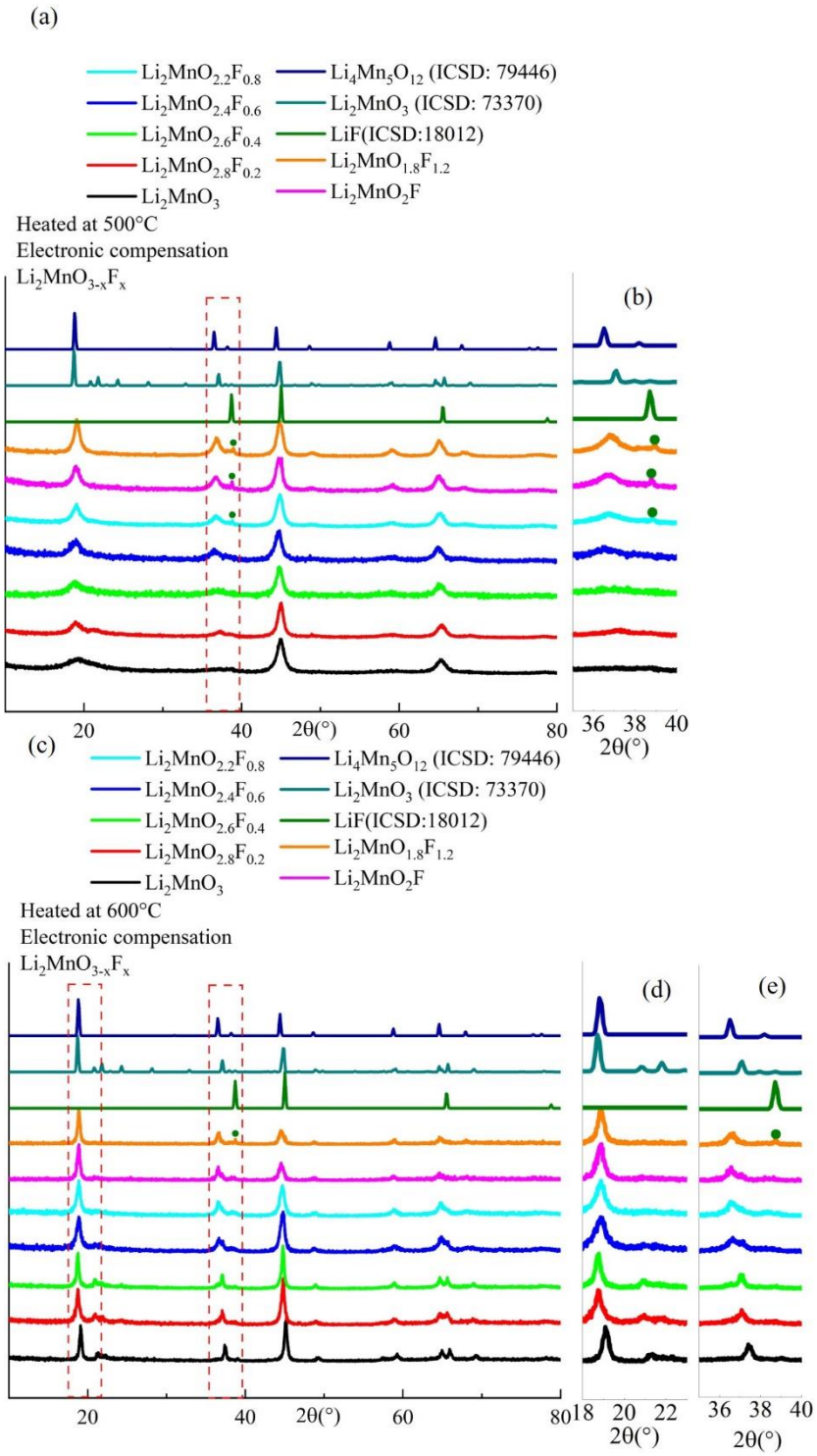

Figure 4.7 the XRD patterns of $Li_2MnO_{3-x}F_x$ by mechanosynthesis (a) heated at 500 °C and (c) 600 °C. (b) shows the magnified view of the area highlighted in (a) and (d) and (e) show that in (c).

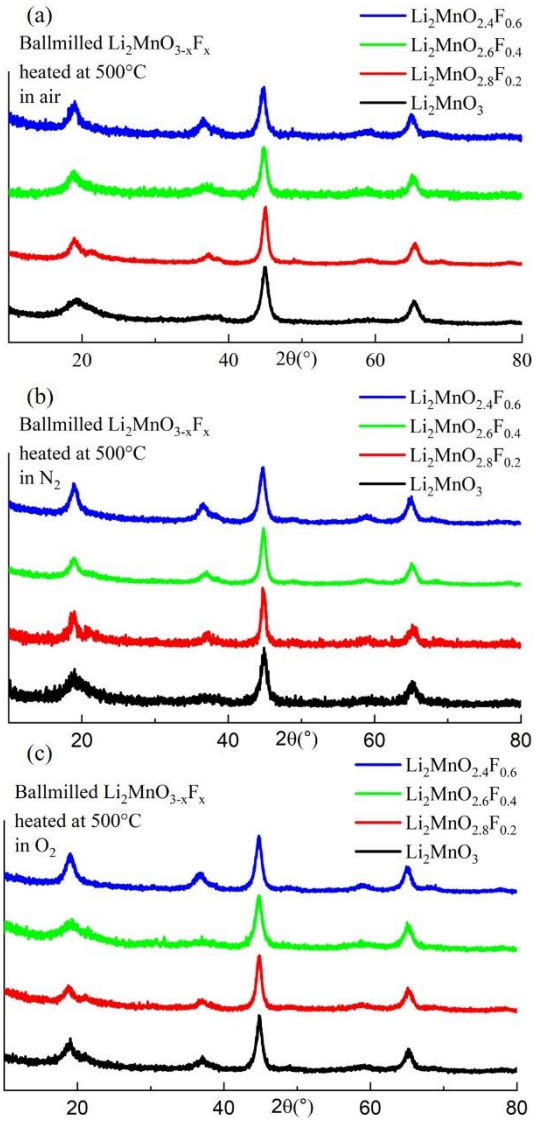

Figure 4.8 the XRD patterns of ball-milled $Li_2MnO_{3-x}F_x$ heated at 500 °C in (a) air, (b) N_2 and (c) O_2.

4.1.2.3 Fluorine content of $Li_2MnO_{3-x}F_x$ during heating

Ball-milled $Li_2MnO_{2.4}F_{0.6}$ was used to study the stability of F content by XRF analysis. Due to the low fluorescence yield of F K X-ray, the accuracy of data is poor. Therefore, for each sample, data were collected data three times and average values calculated in order to reduce the errors, shown in Figure 4.9.

Ball-milled $Li_2MnO_{2.4}F_{0.6}$ was heated in steps from 400 to 900 ℃ for 20 h at each temperature, (a). F loss did not occur below 500 ℃ but was complete by 600 ℃. The effect of time at 600 ℃ for a second sample, (b) showed a gradual decrease in F content with time, but data points showed much scatter and results are inconclusive. Some strategies to reduce F loss were tried. The effect of heating a pelleted sample covered by LiF prior to heating is shown in (c) and two powdered samples heated in Ar and N_2 in (d, e). Results show a reduction in F content at high temperatures, where the F was retained when heated up to 700 ℃ for 20 h in Ar.

A series of $Li_2MnO_{3-x}F_x$ (x=0 to 0.6) samples were heated at 700 ℃ in Ar, (f), and after 20 h, F loss did not occur under these conditions, but the practical values were consistently higher than the expected ones, which could be due to the concentration of F on the surface during heating, although errors were large. F was retained to 700 ℃ in Ar, as shown by the linear dependence of F content on x. However, XRD results show that a second phase $LiMn_2O_4$ appeared and its amount increased with F content, Figure 4.10, indicating $Li_2MnO_{3-x}F_x$ was not stable at 700℃ under Ar, although fluorine was not lost. In summary, F loss occurred in air between 500 and 600 ℃ and was dependent on the heating time length. F loss could perhaps be mitigated by strategies such as buffering with LiF and heating in inert atmospheres, N_2 and Ar, but phase transformation to a spinel occurred.

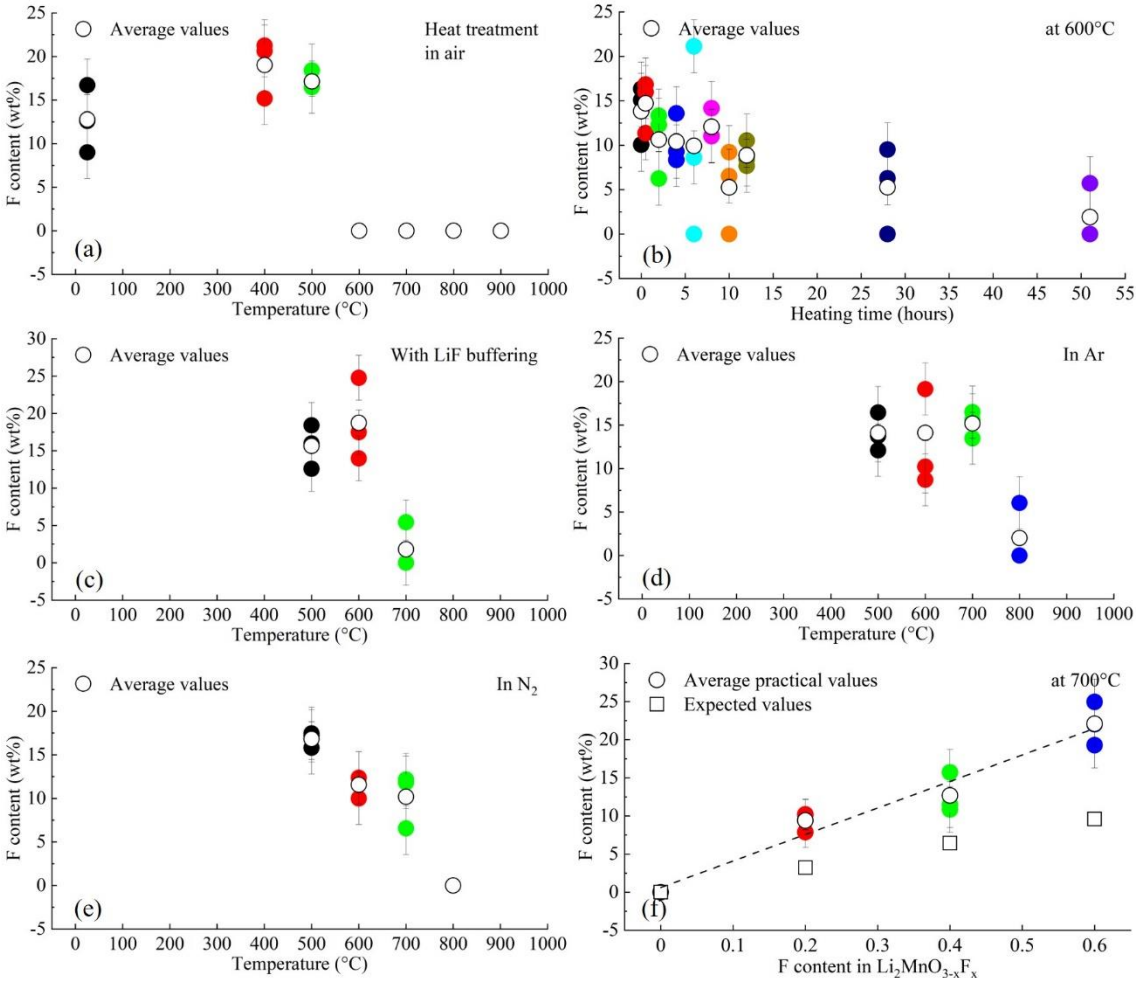

Figure 4.9 the XRF of F content of $Li_2MnO_{2.4}F_{0.6}$ (in wt %) (a) in different temperatures, (b) for different times at 600 °C, (c) in LiF buffering (c), (d) in N2, (e) in Ar, and (f) four doped samples heated in Ar at 700 °C.

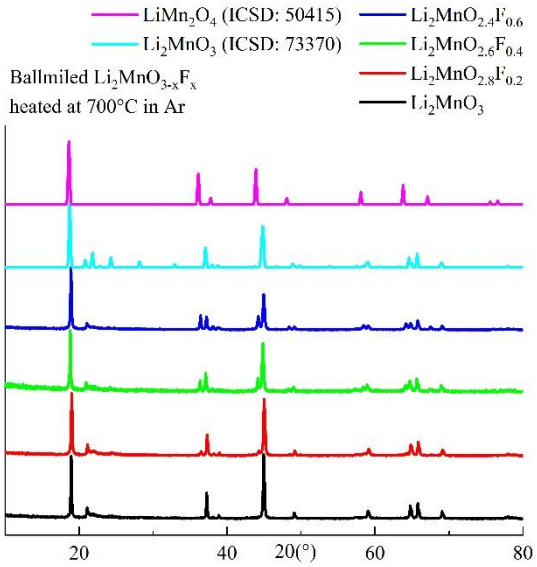

Figure 4.10 the XRD results of $Li_2MnO_{3-x}F_x$ heated at 700 °C in

4.1.2.4 $Li_2MnO_{3-x}F_x$ produced by mechanosynthesis heated at 800 and 900 ℃

Ball-milled $Li_2MnO_{3-x}F_x$ was heated in air at 800 ℃ and 900 ℃ for 20 h, Figure 4.11. At 800 ℃, for $x \leq 0.6$, samples had an ordered monoclinic structure, corresponding to Li_2MnO_3. For $x \geq 0.8$, spinel $LiMn_2O_4$ appeared. After heating at 900 ℃, no obvious spinel phase, but instead, undoped Li_2MnO_3 was observed. This may be explained by the well-documented observation that $LiMn_2O_4$ is not thermally stable > 715 ℃ [150].

Lattice parameters are summarised in Figure 4.12. Samples heated at 800 ℃ were indexed as monoclinic using the space group $C2/m$. Doped samples had larger lattice parameters *a, c* and β than the undoped one. *b* slightly increased with F content. At 900 ℃, *a, b and c* show little change and β slightly increased with F content. Similar to the solid state samples, F loss may affect the lattice parameters due to uncertainty in the F and O content and Mn valence, so it is difficult to draw conclusions.

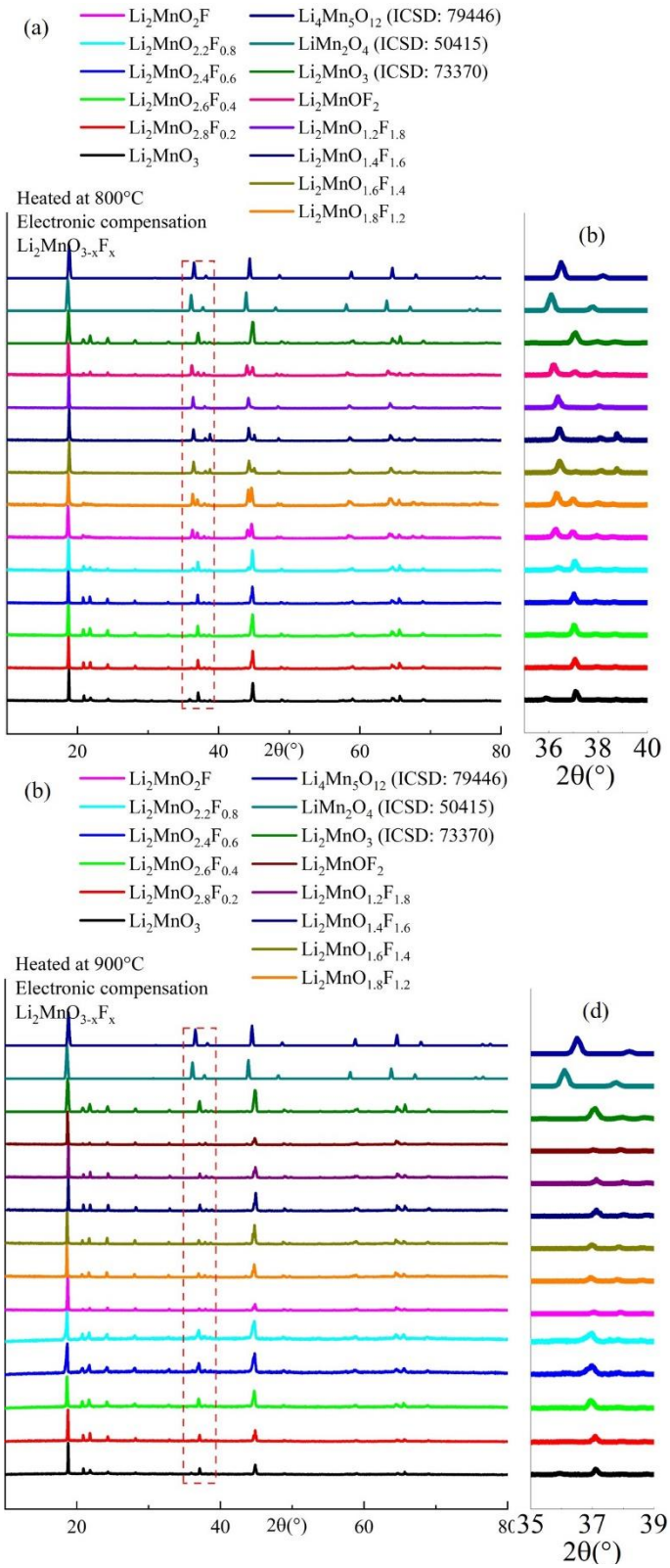

Figure 4.11 the XRD patterns of $Li_2MnO_{3-x}F_x$ by mechanosynthesis heated at (a) 800 °C and (c) 900 °C. (b) and (d) show the magnified view of the area highlighted in (a) and (c), respectively.

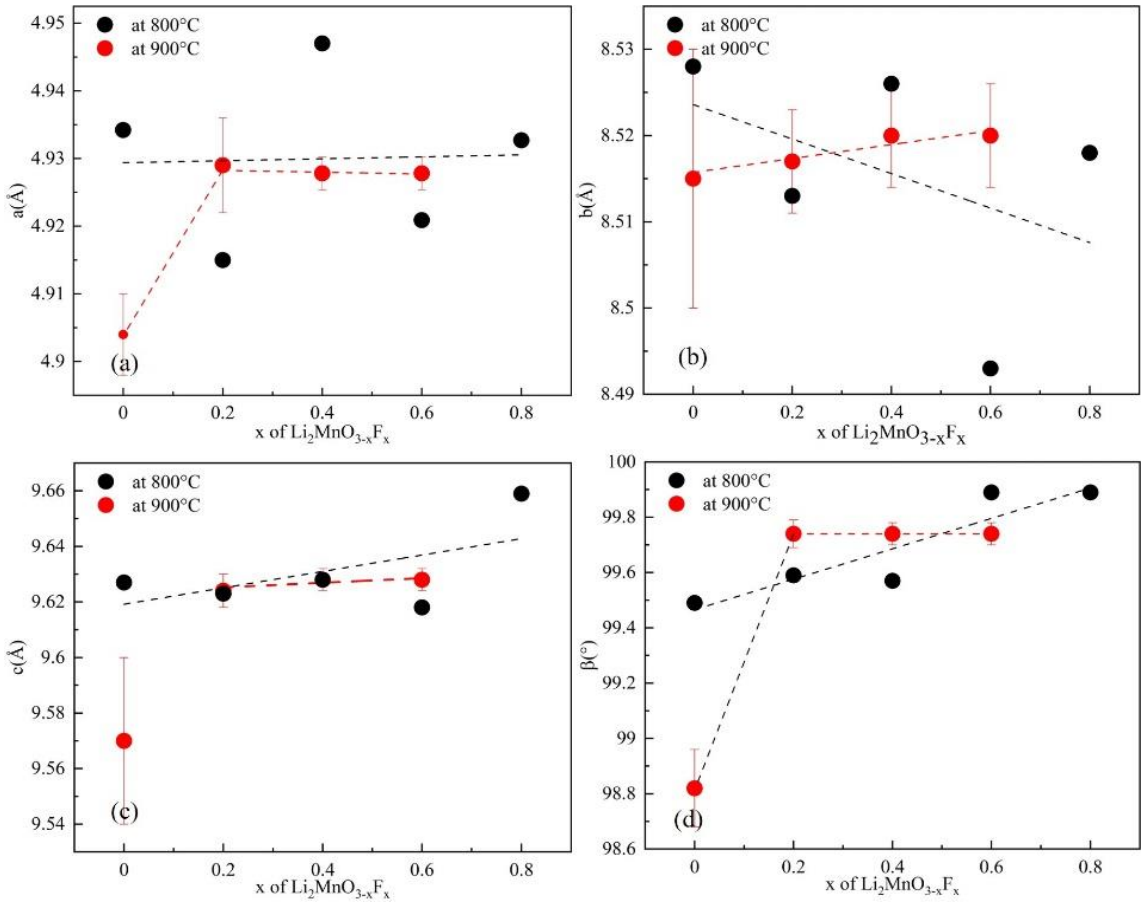

Figure 4.12 Lattice parameter of ball-milled $Li_2MnO_{3-x}F_x$ heated at 800 °C and 900 °C

4.1.2.5 $Li_2MnO_{3-x}F_x$ produced by mechanosynthesis using different Mn sources

$Li_2MnO_{3-x}F_x$ was synthesised using Li_2O_2 with MnO (Figure 4.13 (a)) and Mn_2O_3 (Figure 4.13 (b)). Using MnO, samples x=0.2 to 1.2 had a disordered rock-salt phase. With higher fluorine content, longer milling time was required to form a single phase disordered rock-salt. Using Mn_2O_3, a disordered rock-salt phase formed from x=0.2 to 1.0. For x=1.2, Mn_2O_3 remained after 40 h milling.

It would be expected that, for x > 1, manganese is partially reduced to Mn^{2+}. In order for this to occur using Mn_2O_3 as a reagent, some reduction is necessary and presumably, could require Li_2O_2 to act as a reducing agent, by means of the reaction,

$$O_2^{2-} = O_2 + 2e^- \quad (5)$$

Since Mn_2O_3 remains after mechanosynthesis for x=1.2, this reduction reaction, in air, appears to be unlikely in present circumstances. Besides that, the reactivity of Mn_2O_3 in mechanosynthesis may be less than that of either MnO or MnO_2. Two alternative reactions using Li_2O_2 are first, disproportionation,

$$O_2^{2-} = O^{2-} + \frac{1}{2}O_2 \quad (6)$$

This would not involve any change in Mn valence state. Second, oxidation according to:

$$O_2^{2-} + 2e^- = 2O^{2-} \quad (7)$$

It remains to be seen whether reactions (6) and/or (7) are the principal modes of reaction of Li_2O_2 towards Mn oxides.

4.1.2.6 Li_2MnO_2F produced by mechanosynthesis using different Li and Mn sources

Li_2MnO_2F was synthesised using LiF and (A) Li_2O + Mn_2O_3; (B) Li_2O + MnO_2; (C) Li_2O + MnO + MnO_2; (D) Li_2O_2 + MnO; (E) Li_2O_2 + Mn_2O_3; and (F) Li_2O_2 + MnO_2, Figure 4.14. After 20 h milling, all samples had a disordered rock-salt phase, except the ones with MnO_2, (B) and (F). MnO_2 remained after 20 h milling. The reaction mixtures for B and F contained more oxygen than needed to form Li_2MnO_2F and loss of excess oxygen may be a rate-limiting step in the reaction.

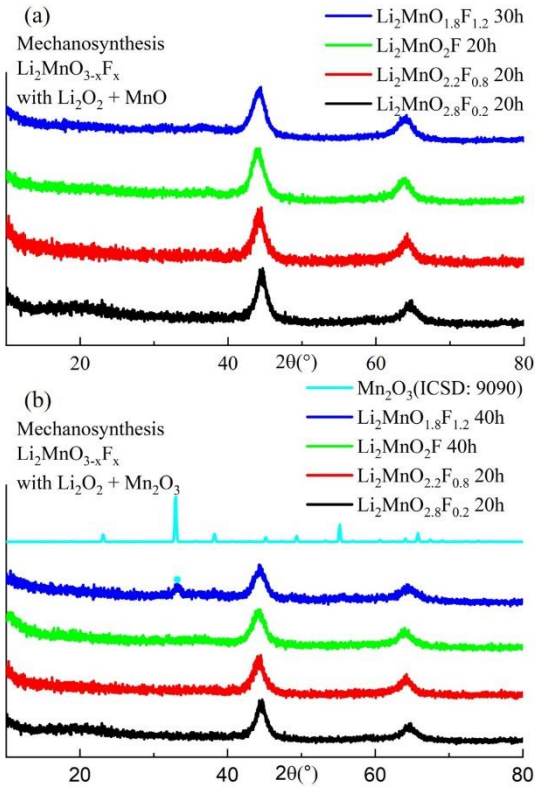

Figure 4.13 the XRD patterns of $Li_2MnO_{3-x}F_x$ produced by mechanosynthesis using (a) Li_2O and MnO and (b) Mn_2O_3 respectively

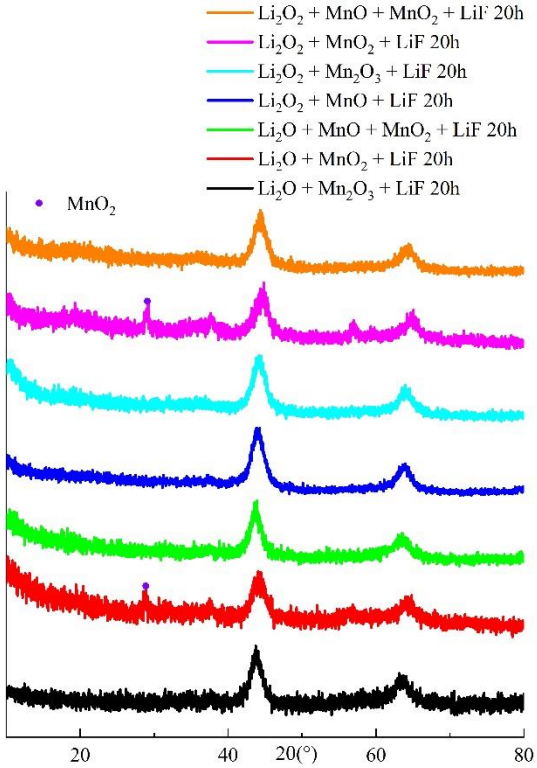

Figure 4.14 the XRD patterns of Li_2MnO_2F produced by mechanosynthesis using different Li and Mn sources

4.1.3 Mechanism two (M2) : lithium vacancy $Li_{2-x}MnO_{3-x}F_x$

4.1.3.1 $Li_{2-x}MnO_{3-x}F_x$ produced by solid state reaction

Samples with compositions $Li_{2-x}MnO_{3-x}F_x$, x=0, 0.1, 0.2 and 0.5 were produced by solid state reaction, at 850 ℃ for 12 h, Figure 4.15. Single phase products have formed for x=0 and 0.1, corresponding to monoclinic Li_2MnO_3. For $x \geq 0.2$, a second phase $LiMn_2O_4$ appeared and the amount of $LiMn_2O_4$ increased with F content, indicating the solid solution limit of $Li_{2-x}MnO_{3-x}F_x$ was less than x=0.2.

4.1.3.2 $Li_{2-x}MnO_{3-x}F_x$ produced by mechanosynthesis

Samples with compositions $Li_{2-x}MnO_{3-x}F_x$, x=0 to 0.8 were prepared by mechanosynthesis, Figure 4.16. For $x \leq 0.6$, a disordered rock-salt phase formed. For $x \geq 0.7$, a peak appeared at around 36° which may correspond to (311) of spinel. A second phase Mn_2O_3 formed which may be oxidised from the reactant MnO. The solid solution limit was lower than 0.6.

Lattice parameter *a* is shown in Figure 4.17, redline. The results show so much scatter that no conclusions can be drawn.

Ball-milled $Li_{2-x}MnO_{3-x}F_x$ was heated at 500 ℃ for 20 h, Figure 4.18. With increasing F content, samples gave an ordered spinel $LiMn_2O_4$, instead of Li_2MnO_3. For $x \geq 0.2$, a small amount of LiF phase appeared.

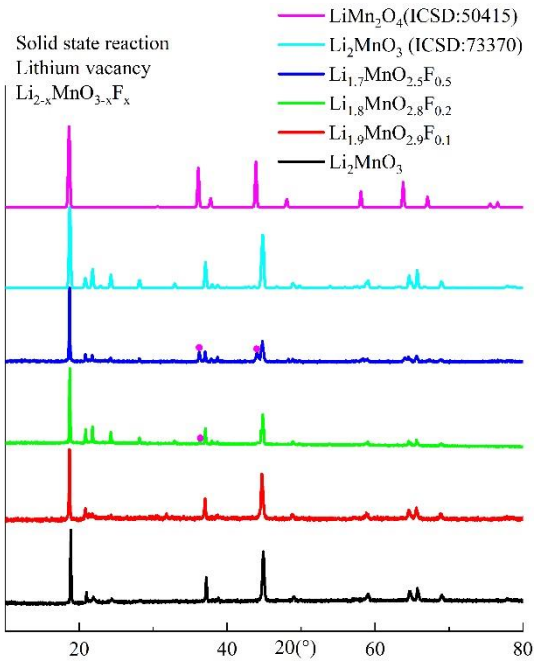

Figure 4.15 the XRD results of $Li_{2-x}MnO_{3-x}F_x$ by solid-state reaction

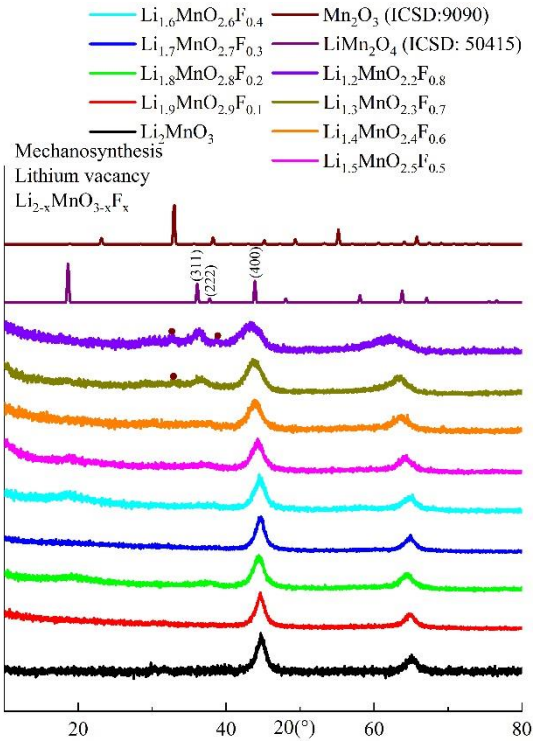

Figure 4.16 the XRD patterns of $Li_{2-x}MnO_{3-x}F_x$ by mechanosynthesis

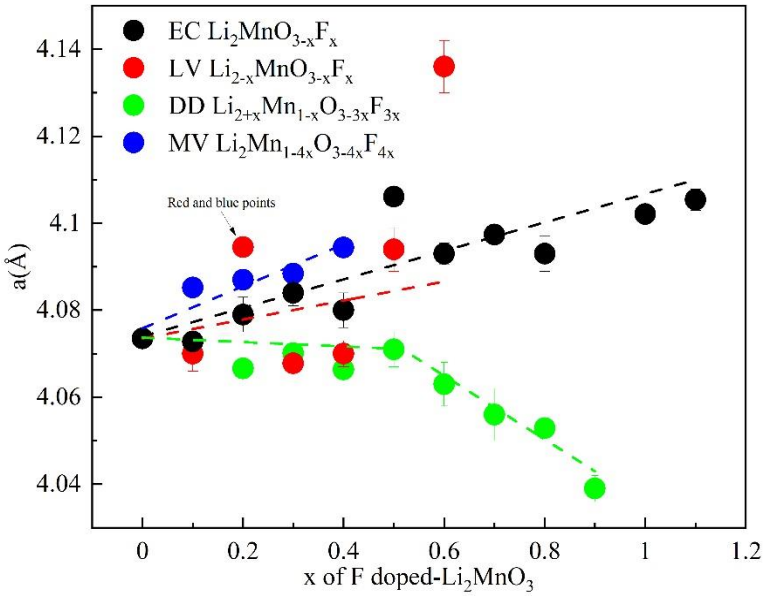

Figure 4.17 Lattice parameter of ball-milled F doped Li_2MnO_3 produced at room temperature with four different doping mechanisms

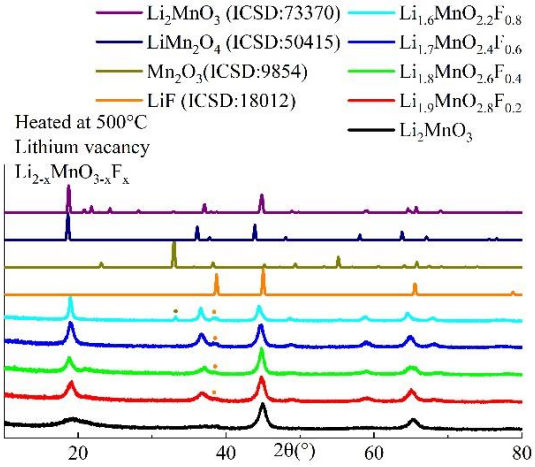

Figure 4.18 the XRD patterns of $Li_{2-x}MnO_{3-x}F_x$ by mechanosynthesis heated at 500 °C

4.1.4 Mechanism three (M3) : double doping $Li_{2+x}Mn_{1-x}O_{3-3x}F_{3x}$

4.1.4.1 $Li_{2+x}Mn_{1-x}O_{3-3x}F_{3x}$ produced by solid state reaction

Samples with compositions $Li_{2+x}Mn_{1-x}O_{3-3x}F_{3x}$, x=0, 0.1 and 0.2 were prepared by solid state reaction, at 850 ℃ for 12 h, Figure 4.19. From x=0.1, LiF second phase appeared and its amount increased with F content. The solid solution limit of monoclinic $Li_{2+x}Mn_{1-x}O_{3-x}F_x$ was less than 0.1.

4.1.4.2 $Li_{2+x}Mn_{1-x}O_{3-3x}F_{3x}$ produced by mechanosynthesis

Results shown in Figure 4.20 indicate a single phase rock solid solution for $0 \leq x \leq 0.6$. At higher x, the (111) peak is observed with increasing intensity. This could represent either continuation of the single phase rock solid solution to cover the entire compositional range $0 \leq x \leq 2$ or the existence of a two phase region of two rock salt phases with $x \approx 0.6$ and x=1 (i.e., LiF).

Lattice parameter *a* is shown in Figure 4.17, green line; *a* is almost constant at small x but decreases approximately linearly at high x. One interpretation of these results is that a continuous solid solution with no change in *a* forms at low x. The limit of the solid solution was $x \leq 0.5$ and when $x > 0.5$, a second phase, LiF appeared. As both of F doped Li_2MnO_3 and LiF had rock-salt phases, overlapping on (111) peak, at high x, the *a* values represent the average of the mixture of $x \approx 0.5$ and LiF. Another possibility is that the solid solution formed in the whole range but lattice parameter has been largely affected by contaminations and storage conditions of samples, so further work to collect results with less scatter is needed.

Ball-milled $Li_{2+x}MnO_{3-3x}F_{3x}$ was heated at 500 ℃ for 20 h, Figure 4.21. Peaks became sharper, indicating grain growth. For undoped Li_2MnO_3, a broad superstructure peak of small domain appeared at 18° but was not present in F-doped samples. F doping may facilitate local disordering and ball-milled samples of low x remained stable to at least 500 ℃.

4.1.5 Mechanism four (M4) : manganese vacancy $Li_2Mn_{1-x}O_{3-4x}F_{4x}$

4.1.5.1 $Li_2Mn_{1-x}O_{3-4x}F_{4x}$ produced by solid state reaction

Samples with compositions $Li_2Mn_{1-x}O_{3-4x}F_{4x}$, x=0, 0.1, 0.2 and 0.3 were prepared by solid state reaction, synthesised at 850 ℃ for 12 h, Figure 4.22. From x=0.1, a second phase LiF appeared and another second phase $LiMn_2O_4$ appeared from x=0.3. The solid solution limit of $Li_2Mn_{1-x}O_{3-4x}F_{4x}$ was less than 0.1.

4.1.5.2 $Li_2Mn_{1-x}O_{3-4x}F_{4x}$ produced by mechanosynthesis

Samples with compositions $Li_2Mn_{1-x}O_{3-4x}F_{4x}$, x=0-0.5 were prepared by mechanosynthesis, Figure 4.23. A single phase rock-salt solid solution with $0 \leq x \leq 0.3$ was produced. After that, the products were a mixture of two of reactants, LiF and MnO. Noticeably, for x=0.2 and 0.3, the background was noisier, which indicates very disordered, semi-amorphous products.

Lattice parameter *a* is shown in Figure 4.17, blue line.

Ball-milled $Li_2Mn_{1-x}O_{3-4x}F_{4x}$ was heated at 500 ℃ for 20 h, Figure 4.24. From x=0.2, a spinel phase formed which corresponds to $LiMn_2O_4$ and a second phase LiF appeared. Similar to M2, it may either be unreacted LiF which was undetectable at room temperature or the product of decomposition of disordered phase.

The XRD results of synthesis by solid state reaction and mechanosynthesis give the following conclusions: First, extensive F-doped Li_2MnO_3 solid solutions were not produced by any of the four mechanisms using high temperature solid state reaction. Second, by mechanosynthesis, a disordered rock-salt phase formed in a wide range of solid solutions with all four doping mechanisms. Except M3, double doping, samples with the other three mechanisms were metastable and formed ordered monoclinic or spinel during heating. For the samples without rock-salt stoichiometry, it was more difficult to achieve high F doping and they tended to form $LiMn_2O_4$ instead of Li_2MnO_3 during heating.

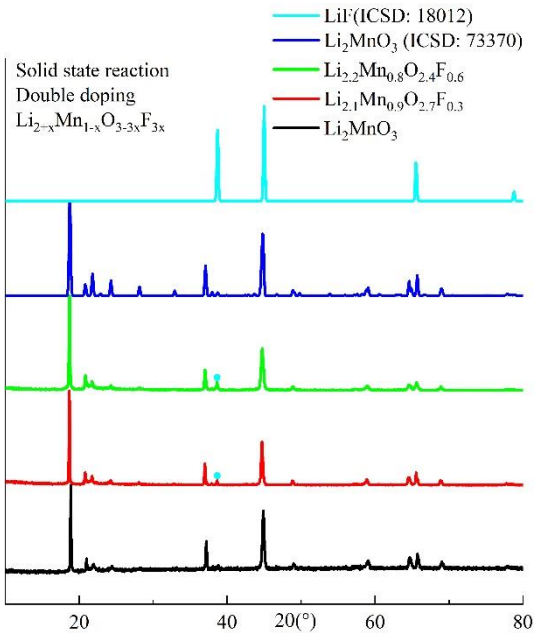

Figure 4.19 the XRD results of $Li_{2+x}Mn_{1-x}O_{3-x}F_x$ by solid-state reaction

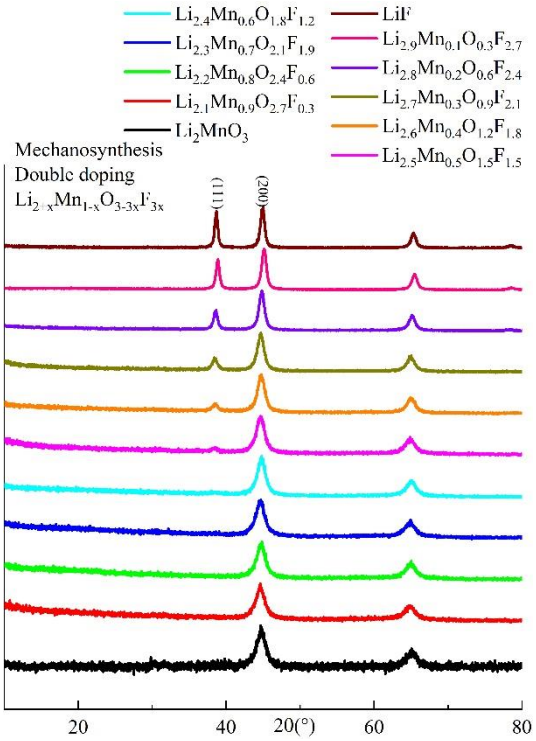

Figure 4.20 the XRD patterns of $Li_{2+x}Mn_{1-x}O_{3-3x}F_{3x}$ by mechanosynthesis

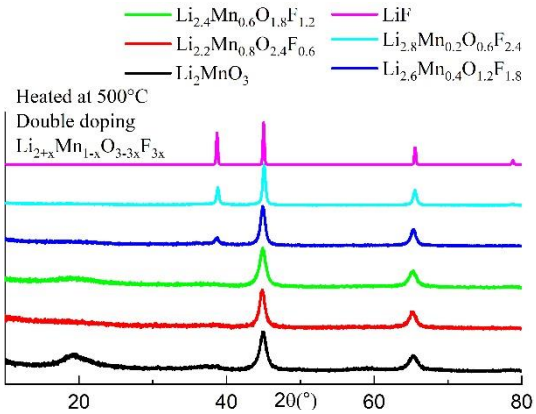

Figure 4.21 the XRD patterns of $Li_{2+x}Mn_{1-x}O_{3-3x}F_{3x}$ by mechanosynthesis heated at 500 °C

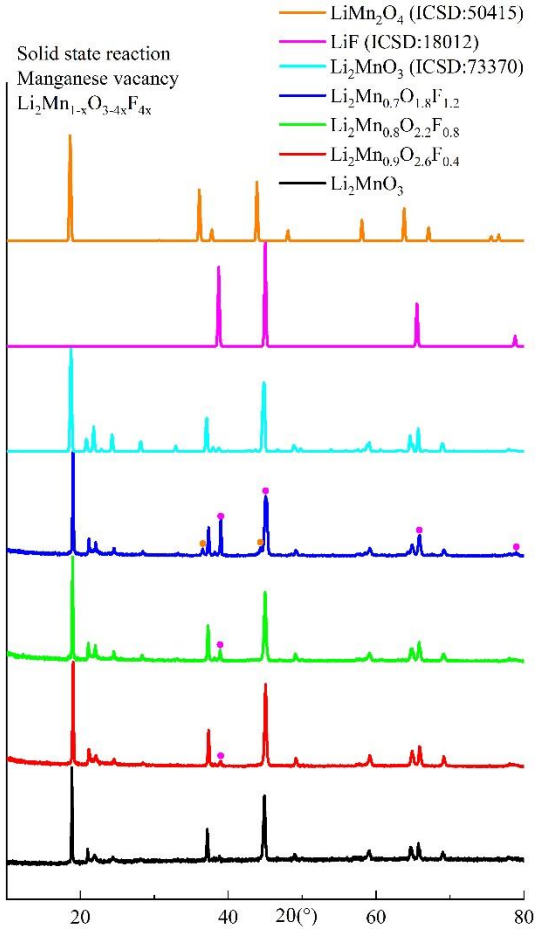

Figure 4.22 the XRD results of $Li_2Mn_{1-x}O_{3-4x}F_{4x}$ by solid-state reaction

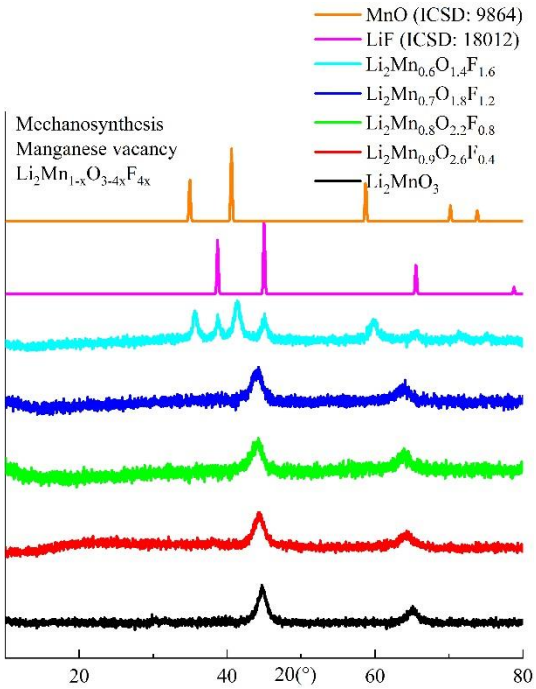

Figure 4.23 the XRD patterns of $Li_2Mn_{1-x}O_{3-4x}F_{4x}$ by mechanosynthesis

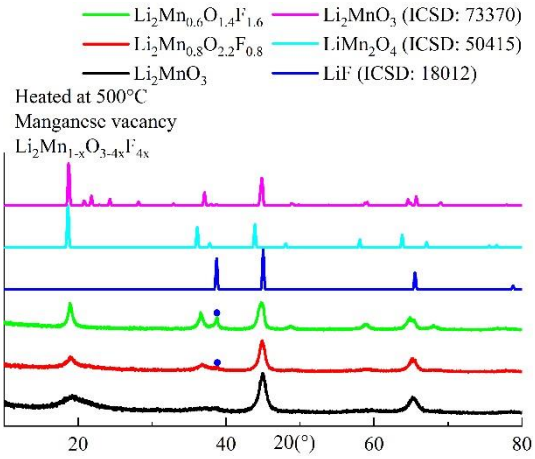

Figure 4.24 the XRD patterns of $Li_2Mn_{1-x}O_{3-4x}F_{4x}$ by mechanosynthesis heated at 500 °C

4.1.6 Characterisation of ball-milled $Li_2MnO_{3-x}F_x$

4.1.6.1 Chemical analysis of $Li_2MnO_{3-x}F_x$ using zirconia, steel and tungsten carbide jars

The chemical analysis of five ball-milled $Li_2MnO_{3-x}F_x$ samples (x=0, 0.2, 0.8, 1.0 and 1.2) was carried out by ICP and XRF; results are summarised in Table 4.2 and 4.3. Similar to the ICP results of Li_2MnO_3 (section 3.1.1.5), samples produced using steel jars dissolved completely in aqua regia but those produced with tungsten carbide and zirconia jars, only partially dissolved. The expected Li/Mn ratio is 2 and the results show that all compositions had a Li:Mn ratio close to 2 (with an error ±5%). Steel and zirconia jars gave higher levels of contamination, about 1.2-2.1 wt% Fe and about 2.0 wt% Zr, respectively, while tungsten carbide jars only gave about 0.1-0.2 wt% W.

XRF data of F-doped samples are given in Table 4.3. The O:Mn ratio data were consistently higher than expected and with much scatter in the data, Figure 4.25 (a). The detection of oxygen by XRF is reported to be limited by low fluorescence yield for oxygen K X-rays and the bremsstrahlung. Therefore, F:Mn ratio is alternatively presented and it gave less scattering but their values for three milling media are all located higher than the expected values, Figure 4.25 (b). Contaminations of samples produced by steel jars and zirconia jars were ~1.34-3.28 wt% Fe and 0.78-5.26 wt% Zr, while those of samples produced by WC jars were 2.60-12.42 wt% W.

In summary, both of ICP and XRF show that samples produced by three different milling media were contaminated, where Fe and Zr may have been introduced into the samples and WC existed as a second phase. Samples with WC jars show a much higher contamination in XRF than that in ICP, which indicates the undissolved chemicals in ICP might contain high values of W. ICP results show that the Li/Mn ratio was close to the expected values, which is a good indication that the samples did not lose F during ball-milling. On the other hand, XRF data gave much scatter, and might be with large errors, especially on oxygen.

Table 4.2 Results of the ICP analysis for ball-milled $Li_2MnO_{3-x}F_x$

Samples	**The ratio of Li:Mn**		**Li and Mn (mg/kg)**		**Impurities (mg/kg) (1 mg/kg = 1/10000 wt%)**					
	Expected	Analysed	Li	Mn	Fe	W	Zr	Co	Cr	Hf
Samples by steel										
Li_2MnO_3	2	2.01	102122	401658	16092	52.4	26			<41.0
$Li_2MnO_{2.8}F_{0.2}$	2	1.95	104387	423524	12702	<49.3	<12.3	<12.3	386	<61.7
$Li_2MnO_{2.2}F_{0.8}$	2	1.92	100101	413682	17298	<49.5	<12.4	<12.4	493	<61.9
Li_2MnO_2F	2	2.00	103297	409639	20145	<52.1	<13.0	<13.0	577	<65.1
$Li_2MnO_{1.8}F_{1.2}$	2	1.98	102578	409382	21049	<51.5	<12.9	<12.9	846	<64.4
Samples by WC										
Li_2MnO_3	2	2.20	99107	357065	79.4	319	34.3			<40.3
$Li_2MnO_{2.8}F_{0.2}$	2	1.95	100184	407595	<17.0	1895	<11.3	2599	<22.6	<56.5
$Li_2MnO_{2.2}F_{0.8}$	2	1.90	94761	393727	<17.4	1187	<11.6	5056	<23.2	<58.0
Li_2MnO_2F	2	2.05	105706	408103	<17.4	1922	<11.6	1948	<23.2	<58.0
$Li_2MnO_{1.8}F_{1.2}$	2	1.99	98981	392848	<18.6	2314	<12.4	3375	<24.8	<62.0
Sample by ZrO2										
Li_2MnO_3	2	1.72	89537	412888	64.2	18.6	5013			138
Li_2MnO_2F	2	1.95	101085	409651	<17.5	<46.7	19825	<11.7	<23.4	429

Table 4.3 Results of the XRF for ball-milled $Li_2MnO_{3-x}F_x$

Samples Li2MnO3	**The ratio of O:Mn**		**The ratio of F:Mn**		**Mn, O and F (wt%)**			**Impurities (wt%)**		
By steel jars	Expected	Analysed	Expected	Analysed	Mn	O	F	Fe	W	Zr
		5.19		0	38.981	58.92	0	1.99		
Li_2MnO_3	3	5.46	0	0	37.886	60.219	0	1.82		
		5.16		0	39.211	58.961	0	1.83		
		4.51		0.54	43.514	46.727	8.093	1.43		
$Li_2MnO_{2.8}F_{0.2}$	2.8	3.56	0.2	0.62	37.032	53.197	7.919	1.34		
		2.8		0	48.114	49.711	0	1.72		
		4.51		1.54	36.228	42.395	19.345	1.83		
$Li_2MnO_{2.2}F_{0.8}$	2.2	3.56	0.8	1	45.659	36.342	15.724	2.18		
		2.8		1.43	39.188	39.276	19.429	2.07		
		4.51		2.1	38.452	30.856	27.909	2.62		
Li_2MnO_2F	2	3.56	1	1.13	49.955	27.251	19.517	3.28		
		2.8		1.5	41.763	33.774	21.608	2.86		
		4.82		1.65	43.11	28.87	24.671	2.86		
$Li_2MnO_{1.8}F_{1.2}$	1.8	6.2	1.2	2.08	38.045	30.931	27.391	2.29		
		4.6		2.13	42.541	23.282	31.388	2.67		
By WC jars	Expected	Analysed	Expected	Analysed	Expected		Analysed	Fe	W	Zr
Li_2MnO_3	3	4.51	0	0	37.663	49.491	0	0.15	11.57	

		3.56		0	42.426	44.003	0			12.37
		2.72		0	46.981	37.253	0			12.42
		3.57		0	44.505	46.271	0			8.69
$Li_2MnO_{2.8}F_{0.2}$	2.8	4.04	0.2	0.38	39.756	46.751	5.231			7.6
		4.2		0.47	38.841	47.467	6.271			6.8
		2.96		1.11	42.747	36.799	16.337			3.74
$Li_2MnO_{2.2}F_{0.8}$	2.2	3.42	0.8	1.35	38.852	38.714	18.129			3.65
		4.18		1.06	37.447	45.629	13.693			3
		2.97		1.37	41.256	35.738	19.515			3.26
Li_2MnO_2F	2	2.29	1	1.38	45.292	30.206	21.656			2.6
		2.7		1.96	39.371	30.957	26.686			2.81
		3.3		1.8	36.708	35.266	22.806			4.79
$Li_2MnO_{1.8}F_{1.2}$	1.8	3.39	1.2	1.76	36.57	36.148	22.304			4.6
		2.05		1.38	45.183	26.985	21.526			5.71

By zirconia jars	Expected	Analysed	Expected	Analysed	Expected		Analysed	Fe	W	Zr
		4.82		0	40.532	56.864	0			2.44
Li_2MnO_3	3	6.2	0	0	34.968	63.135	0			1.9
		4.6		0	41.796	56.017	0			1.98
		4.84		0	39.556	55.783	0			4.23
$Li_2MnO_{2.8}F_{0.2}$	2.8	5.33	0.2	0.41	35.683	55.427	5.113			3.54
		4.66		0	40.437	54.917	0			4.5
$Li_2MnO_{2.2}F_{0.8}$	2.2	4.1	0.8	1.94	34.578	41.242	23.224			0.77
		3.97		1.39	37.573	43.441	18.058			0.93

		4.24		2.01	33.876	41.825	23.52	0.78
		3.79		1.99	34.703	38.344	23.831	2.58
Li_2MnO_2F	2	5.13	1	1.52	32.341	48.33	17.011	2.26
		3.02		1.84	38.545	33.925	24.582	2.87
		4.44		2.98	28.902	37.369	29.774	3.72
$Li_2MnO_{1.8}F_{1.2}$	1.8	3.41	1.2	3.06	30.99	30.742	32.758	5.26
		4		2.32	31.97	37.225	25.616	4.53

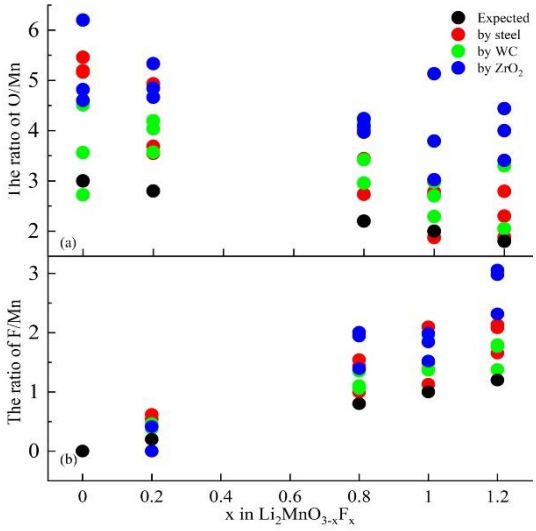

Figure 4.25 (a) the ratio of O/Mn, (b) F/Mn and (c) F/O obtained from XRF of ball-milled $Li_2MnO_{3-x}F_x$ produced by steel, WC and zirconia jars.

4.1.6.2 Grain and domain size broadening of $Li_2MnO_{3-x}F_x$ at room temperature and 500 ℃

The rock-salt structure is in a face centered cubic unit cell. Based on this, theoretical densities of ball-milled $Li_2MnO_{3-x}F_x$ at room temperature are calculated and shown together with the measured densities, Table 4.4. Theoretically, the density increases with x from 3.5754 to 3.6661 g/cm^3. By measurement, undoped Li_2MnO_3 had a density of 3.7984 g/cm^3 while the doped samples had lower densities, about 3.6362-3.6783 g/cm^3. Except Li_2MnO_2F, all samples had a slightly higher measured value than the expected, indicating that either the unit mass is higher or the unit volume is lower than the expected. As discussed in section 4.1.6.1, when samples were produced in steel jars, they were contaminated by ≤ 3 wt% of Fe, which may slightly increase the average unit mass.

The particle sizes and the XRD patterns of $Li_2MnO_{3-x}F_x$ at room temperature are shown in Table 4.5 and Figure 4.26 (a), collected by Mo PSD mixed with silicon standard. The Scherrer formula was used to calculate the particle size from the additional line broadening compared with line widths of a silicon standard. The peaks around 20° shifted to the left with the increase of F content, indicating an increased *a*. Particle sizes of four samples show a decrease with the increase of F content from about 83 Å to about 56 Å. At 500 ℃, samples still had a disordered rock-salt structure but with sharper peaks. Ordered domains appeared at around 8.5° with much broader peaks. The particle sizes and domain sizes at 500 ℃ calculated with the Scherrer equation are summarised in Table 4.6 and XRD patterns are in Figure 4.26 (b). Particle sizes decreased from about 95 Å to about 80 Å with increasing F content. Domain sizes varied from 23 Å to 39 Å and did not show an obvious trend. Peak positions of main phase remained at 20.12° but those of domains slightly shifted from 8.68° to 8.52°, indicating an increase of lattice parameter of domains.

The particle sizes of F doped Li_2MnO_3 with M2, M3 and M4 are summarised in Table 4.7 to 4.9 and XRD patterns in Figure 4.27. F doped samples with M2, lithium vacancy and M4, manganese vacancy, had smaller particle size than undoped one. For M3, double doping, F doped samples had smaller particle sizes than the undoped one, except x=0.8, $Li_{2.8}Mn_{0.2}O_{0.6}F_{2.4}$, which shows a particle size of 105.32 Å. As mentioned in 4.1.4.2, this may indicate the possibility that when x > 0.5, the product was a mixture of x=0.5 and LiF, so at x=0.8, it might be a mixture of x=0.5 and LiF, where the latter was better crystalised and had a large grain size.

Table 4.4 Densities of ball-milled $Li_2MnO_{3-x}F_x$ (M1) at room temperature

Sample	Theoretical density	Measured density
Li_2MnO_3	3.5754 g/cm³	3.7984 g/cm³
$Li_2MnO_{2.8}F_{0.2}$	3.5895 g/cm³	3.6592 g/cm³
$Li_2MnO_{2.2}F_{0.8}$	3.6318 g/cm³	3.6783 g/cm³
Li_2MnO_2F	3.6459 g/cm³	3.6362 g/cm³
$Li_2MnO_{1.8}F_{1.2}$	3.6661 g/cm³	3.6741 g/cm³

Table 4.5 the particle size broadening of the ball-milled $Li_2MnO_{3-x}F_x$ (M1) at room temperature

Formula	2θ (°)	Crystallite size (Å)
Li_2MnO_3	20.02	83.08
$Li_2MnO_{2.8}F_{0.2}$	20.00	92.13
$Li_2MnO_{2.6}F_{0.4}$	19.97	73.01
$Li_2MnO_{2.4}F_{0.6}$	19.88	56.25

Table 4.6 Particle and domain size broadening of ball-milled $Li_2MnO_{3-x}F_x$ (M1) at 500 °C

Formula	2θ(°)	Crystallite size (Å)	2θ (°)	Domain size (Å)
Li_2MnO_3	20.12	94.66	8.68	31.23
$Li_2MnO_{2.8}F_{0.2}$	20.12	91.09	8.68	22.93
$Li_2MnO_{2.6}F_{0.4}$	20.15	86.18	8.53	24.76
$Li_2MnO_{2.4}F_{0.6}$	20.12	79.67	8.52	38.91

Table 4.7 the particle size broadening of the ball-milled $Li_{2-x}MnO_{3-x}F_x$ (M2) at room temperature

Formula	2θ (°)	Crystallite size (Å)
Li_2MnO_3	20.02	83.08
$Li_{1.8}MnO_{2.8}F_{0.2}$	19.93	54.34
$Li_{1.6}MnO_{2.6}F_{0.4}$	20.56	58.98
$Li_{1.4}MnO_{2.4}F_{0.6}$	19.84	43.02

Table 4.8 the particle size broadening of the ball-milled $Li_{2+x}Mn_{1-x}O_{3-3x}F_{3x}$ (M3) at room temperature

Formula	2θ (°)	Crystallite size (Å)
Li_2MnO_3	20.02	83.08
$Li_{2.2}Mn_{0.8}O_{2.4}F_{0.6}$	20.10	72.12
$Li_{2.4}Mn_{0.6}O_{1.8}F_{1.2}$	20.07	69.01
$Li_{2.6}Mn_{0.4}O_{1.2}F_{1.8}$	20.80	76.23
$Li_{2.8}Mn_{0.2}O_{0.6}F_{2.4}$	20.19	105.32

Table 4.9 the particle size broadening of the ball-milled $Li_2Mn_{1-x}O_{3-4x}F_{4x}$ (M4) at room temperature

Formula	2θ (°)	Crystallite size (Å)
Li_2MnO_3	20.02	83.08
$Li_2Mn_{0.9}O_{2.6}F_{0.4}$	19.99	63.63
$Li_2Mn_{0.8}O_{2.2}F_{0.8}$	20.00	62.17
$Li_2Mn_{0.7}O_{1.8}F_{1.2}$	19.98	64.52
$Li_2Mn_{0.6}O_{1.4}F_{1.6}$	19.97	60.73

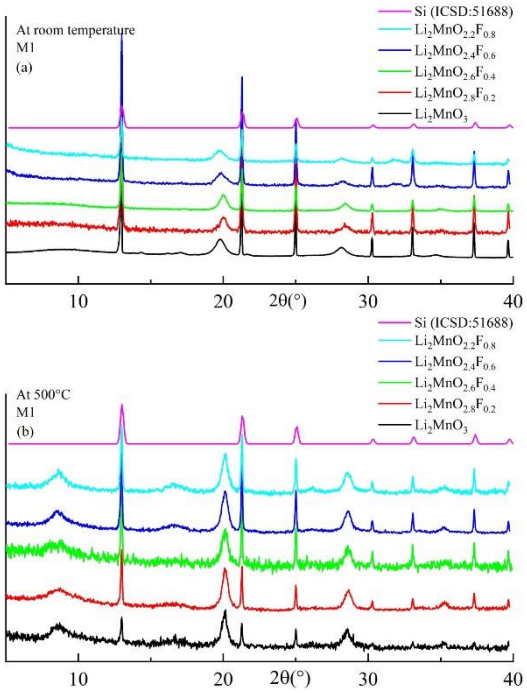

Figure 4.26 the XRD patterns by Mo PSD of $Li_2MnO_{3-x}F_x$ at room temperature

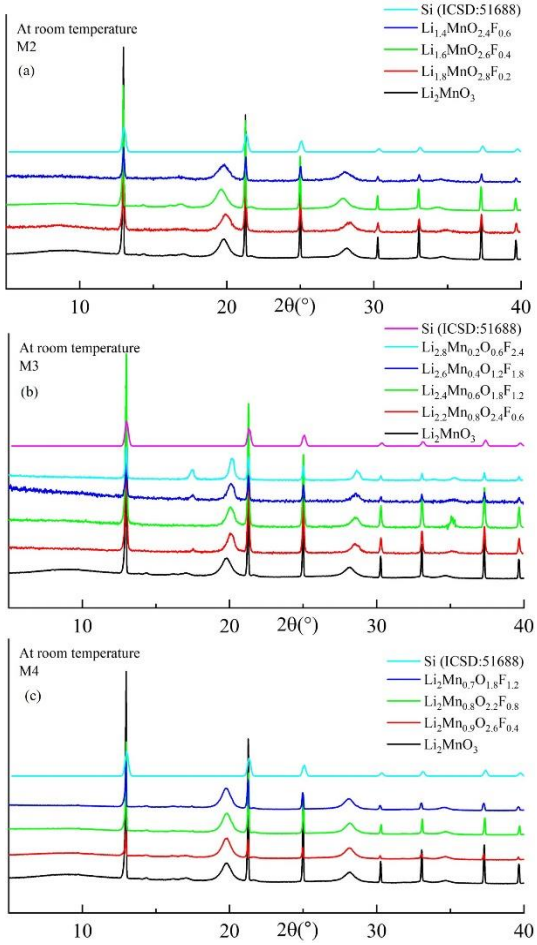

Figure 4.27 the XRD patterns by Mo PSD of $Li_{2-x}MnO_{3-x}F_x$, $Li_{2+x}Mn_{1-x}O_{3-3x}F_{3x}$, and $Li_2Mn_{1-x}O_{3-4x}F_{4x}$ at room temperature.

4.1.6.3 TG of ball-milled $Li_2MnO_{3-x}F_x$

Figure 4.28 shows the TG and DTG profiles on heating and cooling in air of ball-milled samples of $Li_2MnO_{3-x}F_x$, x=0, 0.2…, 1.2. The TG profiles changed systematically with x. Sample x=0 showed the largest overall weight loss, ~7.5 % in up to four overlapping stages; none of the weight loss was regained on cooling. Sample x=1 showed very little overall change in weight but with evidence of both weight loss and subsequent weight gain at intermediate temperatures. Sample x=1.2 was similar to x=1.0 but with greater weight gain and a net overall increase in weight of 1-1.5 % which was retained on cooling.

A more detailed study on samples of x=0, Chapter 3, showed an initial weight loss below 100 ℃ that was attributed to loss of water. This was followed by loss at higher temperature of a combination of more tightly held water and CO_2. A similar interpretation may be used for the results of F-doped compositions. The initial rapid loss of water is less clear with increasing F content and may not occur at all for x=1.0 and 1.2. For x=0.2, a gradual weight loss occurs and is essentially complete by 600 ℃. For x=0.8, a constant weight plateau is seen above ~300 ℃, but gradual weight loss recommences at higher temperature and continues to 800 ℃; the weight loss above 500 ℃ is recovered on cooling. Sample x=1.0 shows a small weight loss below 300 ℃ but a gradual gain in weight occurs at higher temperature that reaches a maximum at 500 ℃. Above ~650 ℃, a gradual weight loss occurs which is regained on subsequent cooling. Sample x=1.2 shows a similar profile to x=1.0 but with a greater increase in weight between 300 and 500 ℃.

TG results for Li_2MnO_2F, x=1.0, measured in three different atmospheres are shown in Figure 4.29 (a). No obvious differences are seen in the three atmospheres, and their profiles were similar. An XRD pattern recorded after the TG cycle in air is shown in (c). It corresponds to a mixture of ordered Li_2MnO_3 and $LiMn_2O_4$ spinel phases which means that the sample probably lost Li at some stage during either synthesis or the TG cycle. Further work is required to determine whether Li is lost as Li_2O of LiF.

In order to understand better the reasons for the different weight loss/gain effects shown in Figure 4.28, a sample of Li_2MnO_2F was analysed with four successive heat/cool cycles, Figure 4.29(b). First, it was cycled between room temperature and 270 ℃. Weight loss attributed to water loss occurred on heating and was not recovered on the short timescales used during cooling. The second cycle was run from room temperature to 480 ℃. No obvious water loss occurred in this cycle, but 0.42% increase in weight started from 310 ℃ and levelled off at 445 ℃. This is attributed to oxygen uptake by the sample, which continued during the first part of subsequent cooling, above 300 ℃. In the third cycle, no significant weight change occurred

below 435 ℃, at which temperature, weight loss started and continued up to 800 ℃, with some evidence of an inflection around 600 ℃. The weight lost was partly recovered on cooling. The fourth cycle had similar profile to the third one, but again, the weight lost was only partly recovered on cooling. The XRD result recorded after four cycles is shown in (c), showing a mixture of ordered Li_2MnO_3 and $LiMn_2O_4$ spinel phases.

Evolved gas analysis, EGA is required to understand better the reasons for the weight changes that are seen, but the following initial observations may be made, based on TG-MS results for Li_2MnO_3 reported in section 3.1.2.2. First, undoped Li_2MnO_3 shows a significant amount of adsorbed water, as shown by weight loss below 100 ℃, but this decreases with increasing F content. Second, undoped Li_2MnO_3 and samples with small F content show some chemically bonded water together, possibly with some carbonate species, as shown by weight losses at higher temperature. Further work is required to separate and quantify the weight losses associated with H_2O and CO_2. Third, samples x=1.0 and especially, 1.2 showed a weight gain at intermediate temperatures that is attributed to oxygen uptake and probably involves oxidation of Mn^{2+} which is expected to be present for samples with $x > 1$. Fourth, samples with higher x: 1.0 and 1.2, show weight loss above ~650 ℃ that is at least partially reversible on cooling and is attributed to change in oxygen content associated with variation in Mn oxidation state. The lack of full reversibility over heat/cool cycles at higher temperature is may be associated with irreversible loss of Li, as discussed above.

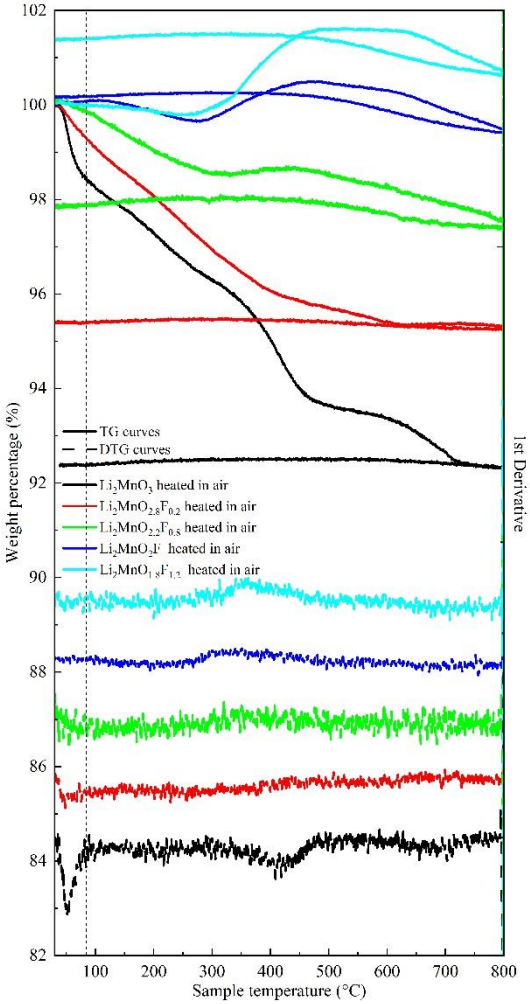

Figure 4.28 the TG profiles of ball-milled $Li_2MnO_{3-x}F_x$

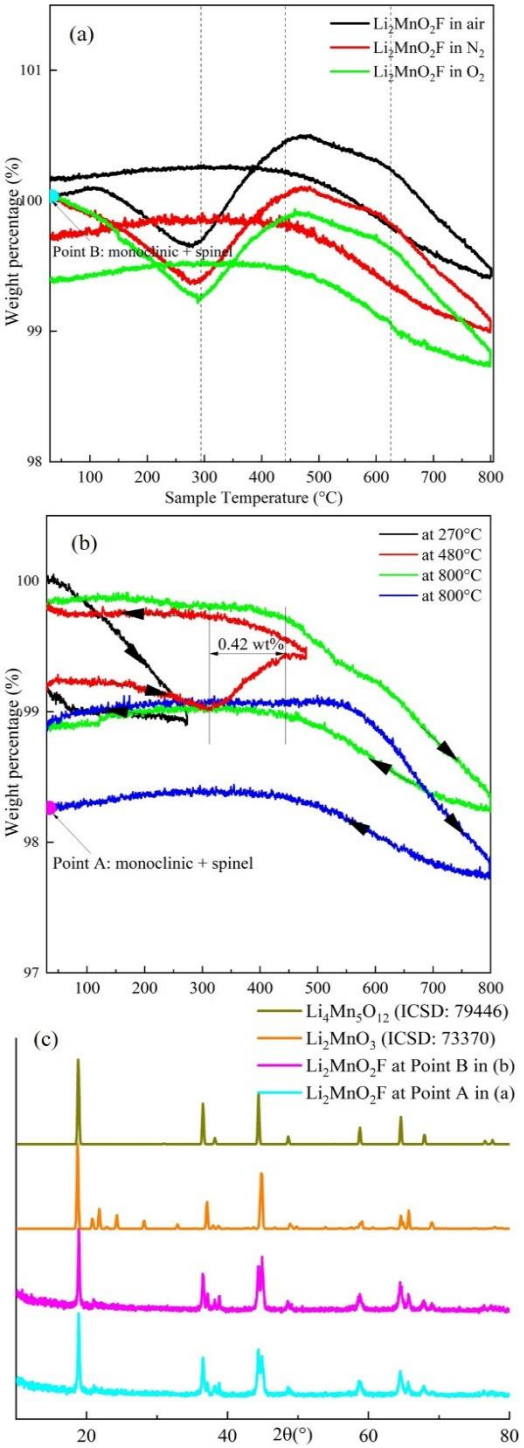

Figure 4.29 the TG profiles of ball-milled Li_2MnO_2F (a) in air, N_2 and O_2, (b) heated for 4 cycles at different temperatures and (c) the XRD patterns of Li_2MnO_2F after TG

4.1.6.4 SEM and TEM on $Li_2MnO_{3-x}F_x$

SEM images of ball-milled Li_2MnO_3 and $Li_2MnO_{2.4}F_{0.6}$ at room temperature and 500 ℃ are shown in Figure 4.30. They were all in nanosize. F-doped sample had a smaller particle size than the undoped one. Heated samples had greater particle sizes. As can be seen, particles formed large, agglomerated clusters and individual particles were difficult to separate. The cluster size for Li_2MnO_3 was ~4250 Å at room temperature and ~6500 Å at 500 ℃, for $Li_2MnO_{2.4}F_{0.6}$ was ~3500 Å at room temperature and 3750 Å at 500 ℃. In section 4.1.6.2, particle size was estimated based XRD line broadening, where the particle size for Li_2MnO_3 was ~83 Å at room temperature and ~95 Å at 500 ℃, for $Li_2MnO_{2.4}F_{0.6}$ was ~56 Å at room temperature and 80 Å at 500 ℃, suggesting that decades of particles may have clustered together and the particle size is much smaller than the ‘particles’ seen from SEM images.

Figure 4.31 is high-angle annular dark field (HAADF) images. Similar to SEM images, they show the particles in nanosize and large clusters. TEM images of ball-milled Li_2MnO_2F are shown in Figure 4.32 (a) and (b) and EEL maps of F, O and Mn are shown in Figure 4.32 (c), (d) and (e), respectively. They indicate a homogeneous distribution of elements on the surface and bulk. But the distribution of fluorine can be distinguished into F-rich and F-poor zones, which may indicate a variation in F concentration on the particle surface.

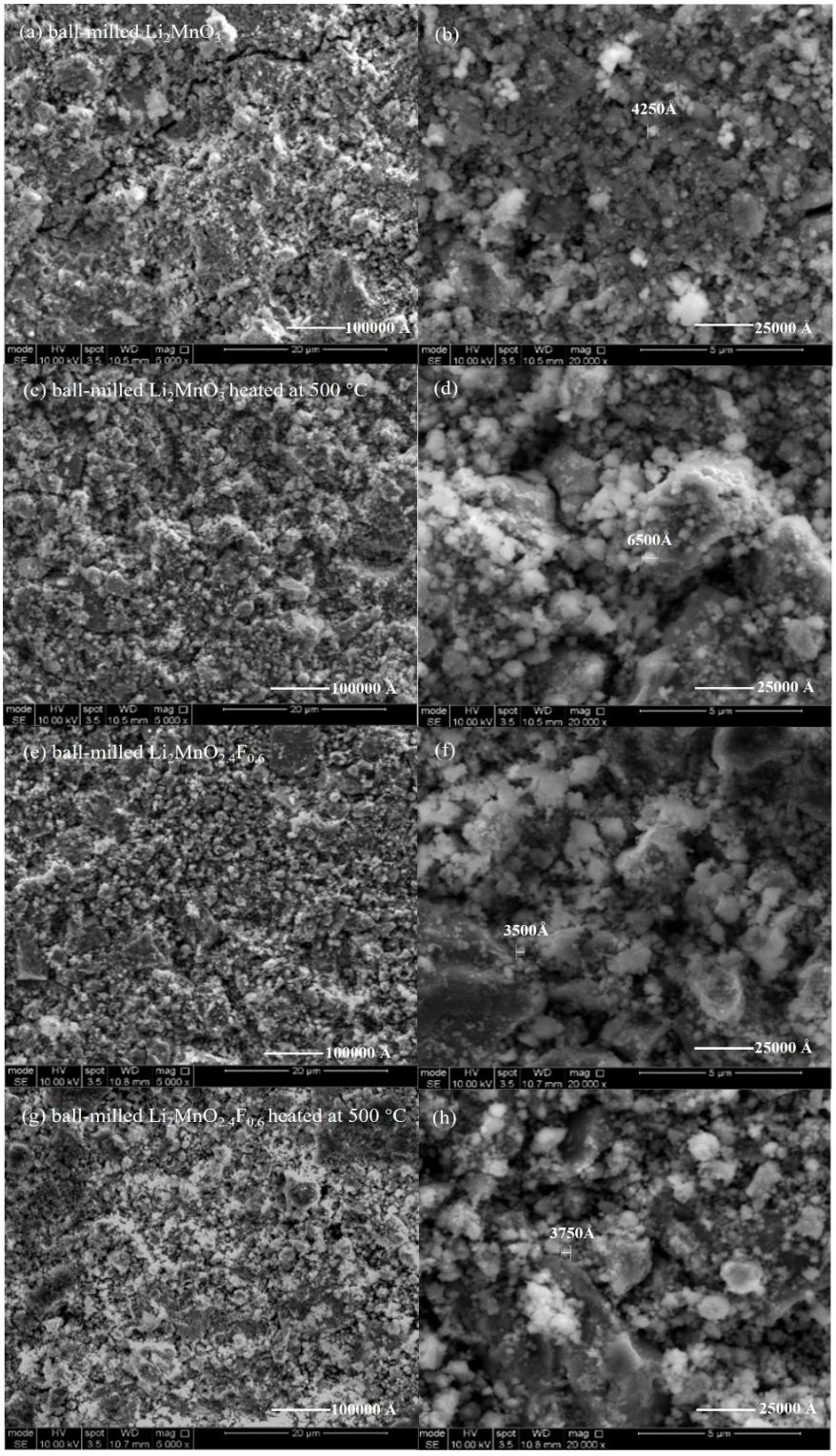

Figure 4.30 SEM images of Li_2MnO_3 at (a) and (b) room temperature and (c) and (d) 500 °C and $Li_2MnO_{2.4}F_{0.6}$ at (e) and (f) room temperature and (g) and (h) 500 °C

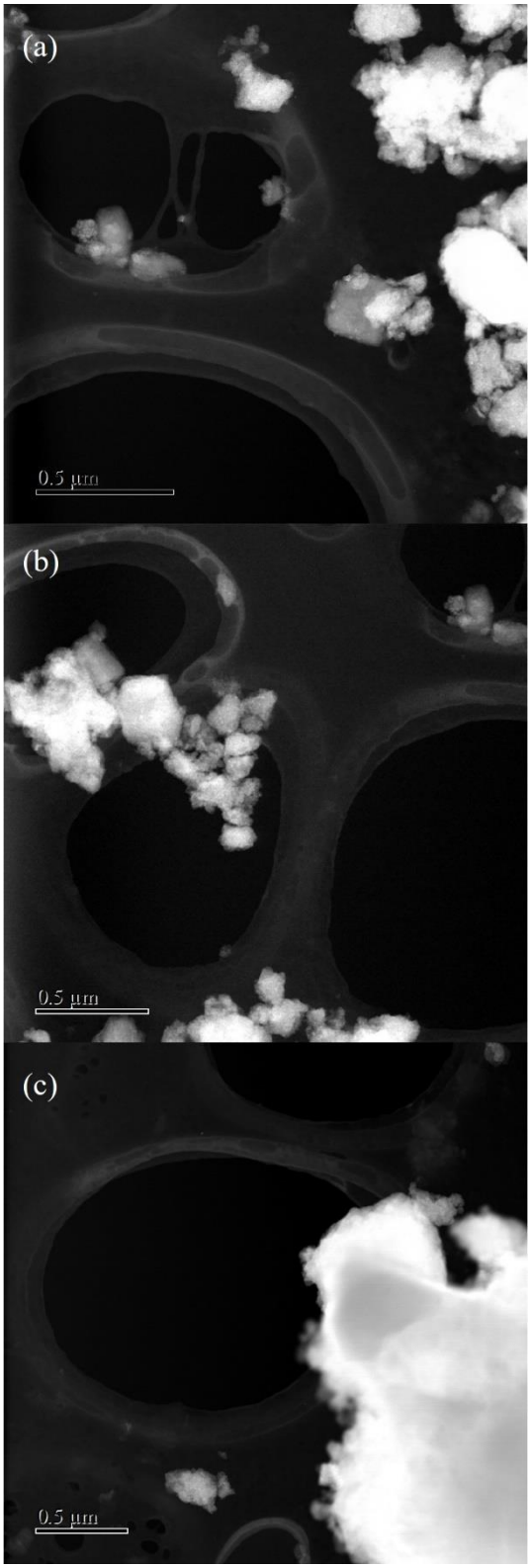

Figure 4.31 HAADF images of Li_2MnO_2F

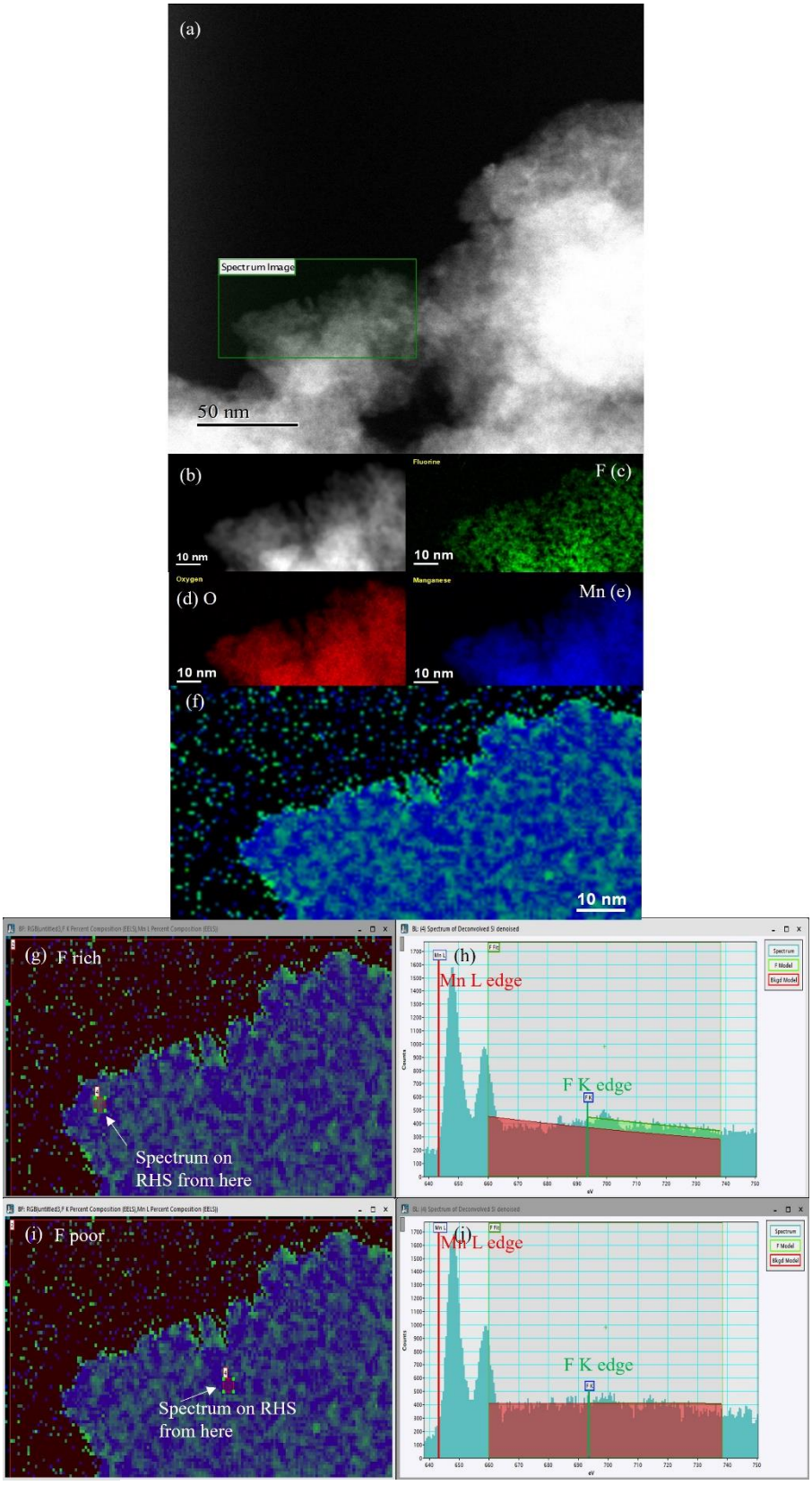

Figure 4.32 (a) and (b) TEM images, (c) to (e) EELS maps and (f) to (j) F K-edge and Mn L-edge maps

4.1.6.5 XANES on $Li_2MnO_{3-x}F_x$

Figure 4.33 shows the absorption Mn K-edge of (a) standards: MnO, Mn_2O_3 and MnO_2 and (b) literature data for a wide range of standards with different local structures reported by Sylvain Grangeon [151]. The calibration curves are shown in (c). The absorption energy values for the measured standards, MnO, Mn_2O_3 and MnO_2 were 6552.67 eV, 6556.78 eV and 6558.16 eV, respectively. For the reported standards, the average absorption energy values for Mn^{2+}, Mn^{3+} and Mn^{4+} were 6551.45 eV, 6558.23 eV and 6560.20 eV , respectively, although it can be seen that the edge shapes varied with different chemicals' structures, which makes the quantitative analysis difficult. However, the practical absorption energy values of $Li_2MnO_{3-x}F_x$ were all higher than those of the measured standards, Figure 4.34 and 4.35. One possibility is all of F doped samples contained Mn ions with valence higher than 4+, which is unlikely for Mn chemicals in air. Another possibility is that F doped samples might have considerably different local structure from that of the measured standards, which makes using the measured standards to do quantitative analysis difficult. Therefore, the following data are calibrated using the average values of reported standards.

Mn K edge XANES data are shown in Fig 33 for (a) three standards, MnO, MnO_2 and Mn_2O_3 measured here, (b) a compilation of literature data on standards and (c) a calibration graph obtained from data shown in (a) and (b). The data in (a) show edges with considerable structure which makes it difficult to assign values to the absorption edges; possibly the samples used were not fully homogeneous or stoichiometric. The data in (b) appear to be somewhat better, although some of the data for MnO_2, in particular, show two components to the absorption edge. For both sets of data, the calibration graph (c) shows a significant increase in energy between Mn^{2+} and Mn^{3+} and a smaller increase, especially for the literature data, between Mn^{3+} and Mn^{4+}.

Figure 4.34 shows experimental data for ball-milled $Li_2MnO_{3-x}F_x$. The results show decreasing Mn valence with increasing F content; using literature-based calibration data, valences appear to be in the range Mn^{4+} to Mn^{3+}, which is expected for an electronic charge balance mechanism on replacing O^{2-} by F^-. The value for Li_2MnO_3 may indicate that the sample used was not fully oxygen-stoichiometric. Also, the edges show structure, especially for compositions with high F content, which may indicate that different oxidation states of Mn are represented in the spectra and are not combined into an average oxidation state. This could be the case if the materials are hopping electron conductors in which the Mn d electrons are localised on individual cations.

Figure 4.35 gave the XANES data which were obtained on (a-c) $Li_2MnO_{2.8}F_{0.2}$ and (d-f) Li_2MnO_2F during their charge and discharge. In both cases, the Mn valence increased during charge and decreased during discharge, which indicates a reversible Mn^{3+}/Mn^{4+} redox reaction during cycling. In Li_2MnO_2F, similarly, the Mn valence increased from 3.00+ to 3.83+ during charge and decreased from 4.00+ to 3.12+ during discharge, which presented an almost complete cycling process between Mn^{4+} and Mn^{3+}. However, a similar change in shape of the edges occurs during cycling of both samples, from an edge with two clear components in the discharged state to a single edge in the charged state. This makes it difficult to make quantitative assignments of the edge data to Mn valences.

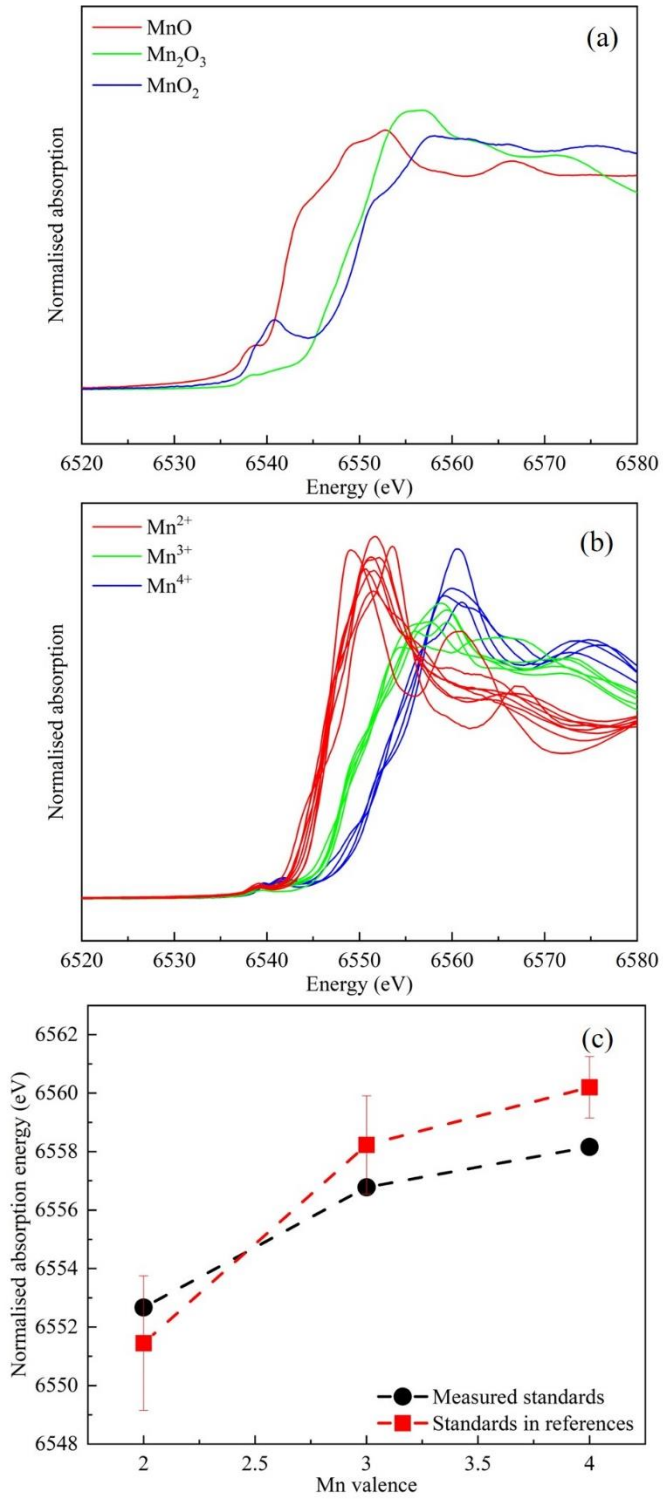

Figure 4.33 (a) Mn K-edge XANES spectra of measured standards and (b) references; (c) Calibration curves of Mn K-edge absorption energy of measured standards MnO, Mn_2O_3 and MnO_2 and references in literature.

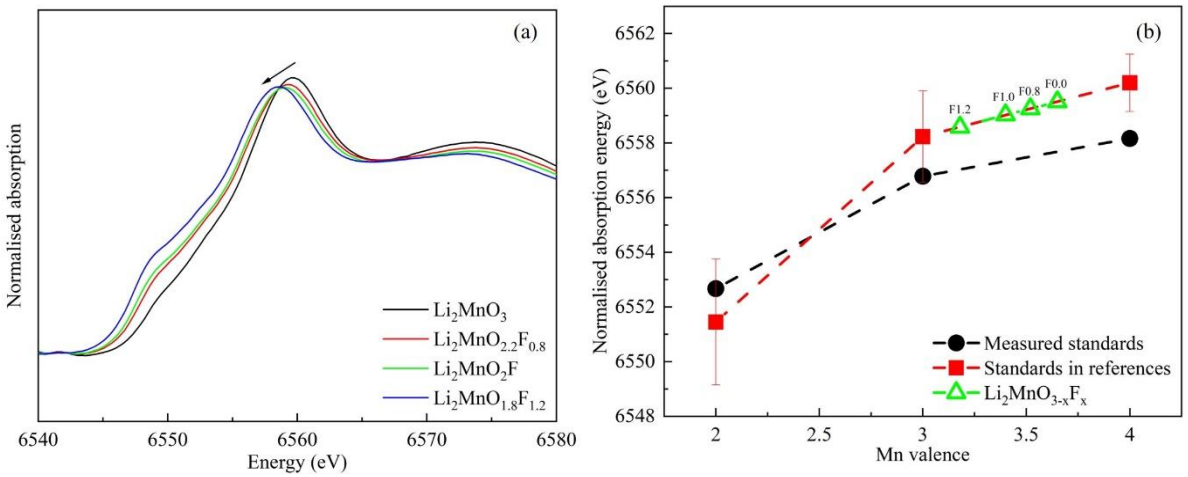

Figure 4.34 (a) Mn K-edge XANES spectra of $Li_2MnO_{3-x}F_x$ and (b) Calibration curves

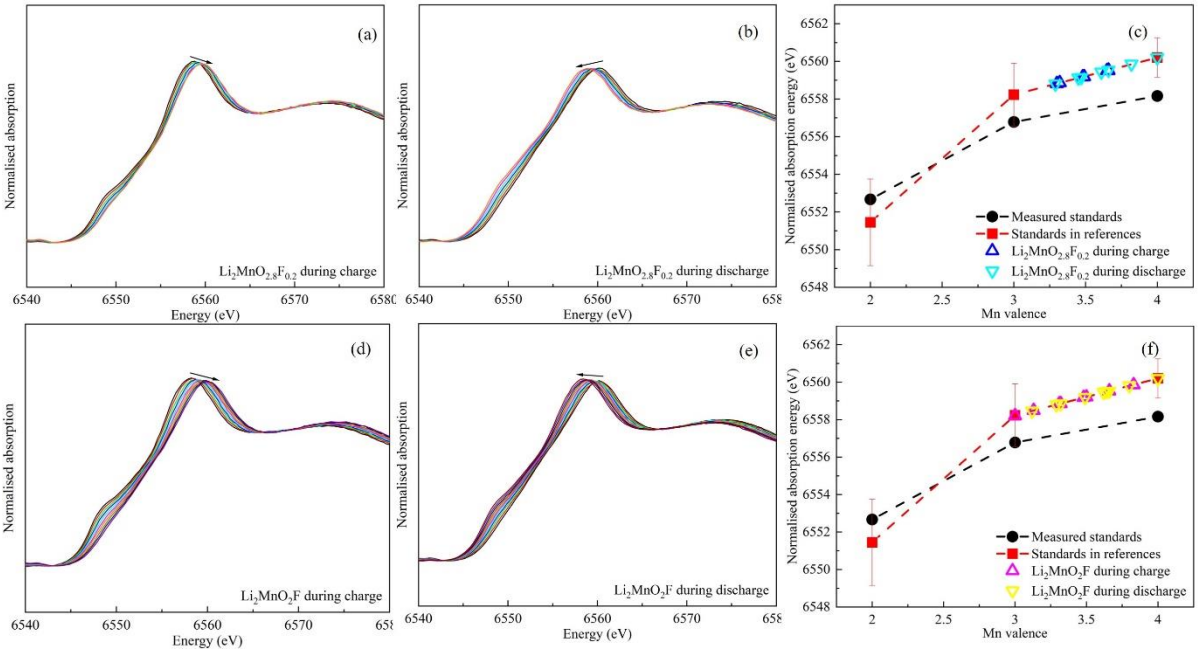

Figure 4.35 Mn K-edge XANES and calibration curves of (a) to (c) $Li_2MnO_{2.8}F_{0.2}$ and (d) to (f) Li_2MnO_2F during charge and discharge.

4.1.6.6 Charge-discharge of $Li_2MnO_{3-x}F_x$ cathode

The charge-discharge profiles of swagelok cells with cathodes prepared from ball-milled Li_2MnO_3, $Li_2MnO_{2.8}F_{0.2}$, Li_2MnO_2F and $Li_2MnO_{1.8}F_{1.2}$ are shown in Figure 4.36, within the voltage window 2.0 to 4.8 V and the rate of C/10. None of the samples showed a plateau during charge or discharge. For Li_2MnO_3 on the first charge, the profile increased rapidly to 4.5V with a capacity of 47 mAh/g. Similarly, for the other compositions, the first charge was different to subsequent cycles. Capacities then increased to 125 mAh/g for x=0.2 and 150-160 mAh/g for x=1.0 and 1.2. Li_2MnO_2F had the best performance over three cycles, with charge capacities from 215 to 163 mAh/g and discharge capacities from 168 to 146 mAh/g.

The increase in capacity observed with increasing x, especially for x=1.0, is attributed to the expected increase in concentration of redox-active Mn^{3+}. The reason for the non-zero capacity of undoped Li_2MnO_3 is unclear since stoichiometric Li_2MnO_3 containing Mn^{4+} is expected to have zero capacity. One possibility is that the sample prepared by ball-milling was oxygen-deficient $Li_2MnO_{3-\delta}$ and had an Mn^{3+} content and associated charge capacity that depended on the value of δ. Further work is required to confirm these results, understand the anomalous behaviour during first charge, study the possible influence on charge-discharge capacities of synthesis routes to Li_2MnO_3, including the choice of reactants, the effects of possible water and carbonate contents in the ball-milled products and subsequent heat treatments.

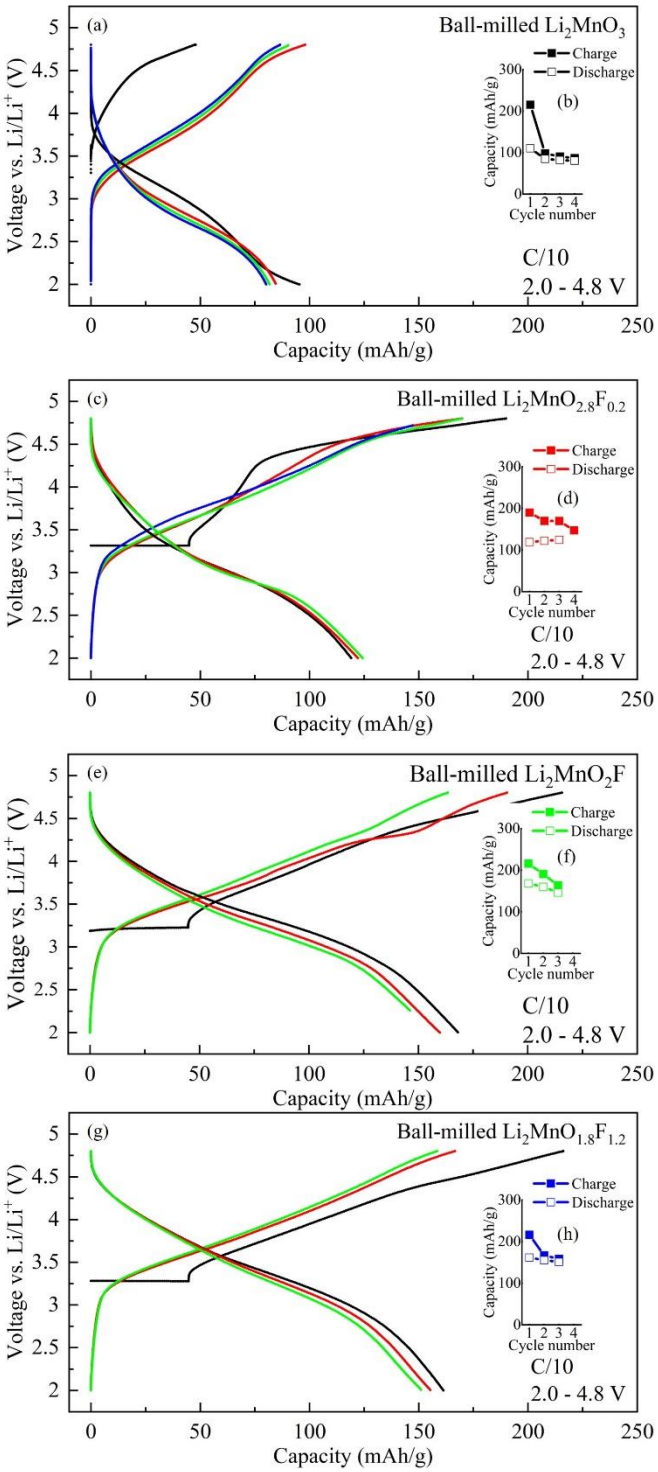

Figure 4.36 Voltage profiles of $Li_2MnO_{3-x}F_x$ between 2.0 and 4.8 V and C/10 at room temperature. (a) and (b) Li_2MnO_3; (c) and (d) $Li_2MnO_{2.8}F_{0.2}$; (e) and (f) Li_2MnO_2F and (g) and (h) $Li_2MnO_{1.8}F_{1.2}$.

4.1.7 Impedance spectroscopy on ball-milled F-Li_2MnO_3

A typical impedance dataset of ball-milled $Li_2MnO_{2.4}F_{0.6}$ is shown in Figure 4.37. Measurements were carried out from room temperature to 250 ℃. Data are presented in four different complementary formats for each sample. In (a), the Z* plot shows a broad, asymmetric semicircle, the radius of which corresponds to the sample resistance. At 56.2 ℃, the resistance was about 1.04×10^7 Ω cm. At low frequency, a poorly defined tail is seen which probably represents an impedance at the sample-electrode interface. The C' plot, (b) shows the onset of a plateau around 10^{-12} F cm^{-1} at high frequency, indicating a bulk component. A second, poorly-resolved plateau at slightly lower frequency with a capacitance around 10^{-11} F cm^{-1} indicates a grain boundary or possibly, a small volume fraction second phase, which also corresponds to the low frequency part of the broad semicircle in the Z* plot. The capacitance value was as high as 10^{-5} F cm^{-1} at low frequency and high temperature, indicating the compound had some ionic conductivity and therefore, was a mixed conductor. The Y' spectroscopic plot, (c) shows a frequency-independent plateau over the range $1x10^{-4}$ to $6x10^{-8}$ S cm^{-1} which represents the total conductivity of the sample. At high frequencies, a dispersion to higher conductivities is observed, which may relate to Jonscher's power law behaviour. The combined Z'' and M'' plot at 38.8 ℃ (d) shows that Z'' peak and M'' peaks overlap approximately at high frequency, indicating that the M'' peak, and therefore, the associated Z'' peak, was the bulk peak. This confirms that the semicircle in the Z* plot and the Y' plateau were bulk values. The separation of the Z" and M" maxima by 1-2 decades of frequency indicates a degree of electrical inhomogeneity, perhaps associated with incomplete sintering of the sample.

Impedance data sets for a wide range of undoped and F-doped samples, prepared either by ball milling (all four doping mechanisms) or high temperature solid state reaction (M1) are shown in Figures 4.38-4.42. A detailed description of each is not given since there are many similarities. All show a bulk response with some degree of sample inhomogeneity and possibly, a small grain boundary impedance. The sample-electrode responses are not well-defined, indicating a possible contribution of both ionic and electronic conductivity; this is supported by C' data, with values as high as 10^{-5} Fcm^{-1} at lowest frequencies which indicate a double layer series capacitance and the possible onset of electrochemical reactions.

Arrhenius plots of the total conductivities of all samples are shown in Figure 4.43. A wide range of conductivity values and activation energies are seen. The most resistive samples are Li_2MnO_3 and F-doped Li_2MnO_3 prepared by solid state reaction. The very low conductivities, 10^{-7}-10^{-6} Scm^{-1} at 300 ℃, are consistent with stoichiometric phases that have no Li vacancies

and no mixed valency of Mn. This supports the earlier conclusion that there was no significant doping of Li_2MnO_3 by solid state reaction. The ball milled samples made according to M3 also have very low conductivities, even though they are nanoparticles with a disordered rock salt structure. M3 involves double substitution without vacancies on either cation or anion sublattices and, again, no mixed valence of Mn. For the other three mechanisms, undoped samples always had a relatively low conductivity, but they did not give an increasing trend with F content. Future work can be conducted to synthesise and measure samples at a lower temperature to retain the properties of the original samples.

4.2 Conclusions and future work

This chapter studied four different doping mechanisms in F-doped Li_2MnO_3 and focused on Mechanism 1, electronic compensation, as it was the only mechanism where theoretically Mn^{3+} or Mn^{2+} were produced by reduction of Mn^{4+} to make Mn^{3+}/Mn^{4+} redox reaction possible to occur as cathodes. It is also the only mechanism which has a fixed Li:Mn ratio. The other three doping mechanisms are lithium vacancy, double doping and manganese vacancy, where Li:Mn ratio varies and vacancies in cation and/or anion sites are created.

By solid state reaction in all four doping mechanisms, there was no evidence that F doping was successful or solid solution has been produced, as no detectable F was in samples and lattice parameters did not change linearly. F loss might occur during synthesis or F might have been incorporated into a second phase, such as $LiMn_2O_4$.

By mechanosynthesis, a disordered rock-salt F-doped Li_2MnO_3 solid solution formed in a wide range using all of the four mechanisms. For M1, a disordered rock-salt phase formed when $0 \leq x \leq 1.4$. Lattice parameter increased approximately linearly, indicating this doping mechanism gave reduction of Mn^{4+} to Mn^{3+} or Mn^{2+}. For M2 and M4, the solid solution limit was $x < 0.7$ and $x \leq 0.3$, respectively. For M4, lattice parameter increased linearly with x and for M2, lattice parameter might increase but scattered much more significantly.

The disordered samples produced by M1, M2 and M4 were all kinetically stable but thermodynamically metastable. During heating, disordered rock-salt phase had a grain growth, accompanied with either the formation of ordered domains with much smaller size, or the nucleation of a spinel structure. At higher temperature, it transformed to ordered Li_2MnO_3 with a second phase $LiMn_2O_4$ and/or LiF. Fluorine loss occurred when $\geq$ 500 °C, and it was dependent on the heating time length.

For M3, the solid solution limit was either $x \leq 0.6$, with second phase LiF, or $0 \leq x \leq 2$ (when x=2, the composition was LiF). Compositions with M3 had good thermal stability and remained disordered rock-salt structure at least to 500 °C. As lattice parameter of four mechanisms generally scattered, future work needs to be done considering the hygroscopicity on chemical analysis and lattice parameter, such as whether wet/dry samples had different lattice parameter and whether Li/Mn/O/F ratio varies with hygroscopicity.

In mechanosynthesis, it is essential to use suitable reactants which provide a stoichiometric oxygen amount and give the required oxidising/reducing environment for Mn, i.e., providing Mn^{3+} for $Li_2MnO_{3-x}F_x$, $1 < x < 2$, and Mn^{2+} for $Li_2MnO_{3-x}F_x$, $x > 2$. For compositions with higher F, it might require longer milling time to produce single phase. Future work can be

aimed to study whether applying oxidising/reducing atmosphere during milling can affect products.

Three milling media, steel, tungsten carbide and zirconia were used and they all gave corresponding contaminations, Fe, W and zirconia, respectively. Steel and zirconia jars incorporated high level contaminations of into the ball-milled samples, whilst tungsten carbide mainly existed as a second phase and incorporated low level of contaminations into the samples.

Ball-milled $Li_2MnO_{3-x}F_x$ were in nanosize, < 100 Å. They tended to agglomerate clusters and clusters were in nanosize too. They were too small to be observed individually by electron microscopy. EEL maps show that Mn, O and F distributed homogeneously.

Ball-milled $Li_2MnO_{3-x}F_x$ was not as hygroscopic as ball-milled Li_2MnO_3. When heating $Li_2MnO_{3-x}F_x$ samples, the amount of water loss decreased with the increase of F content. F doping may mitigate the absorption of H_2O and CO_2. Future work on TG-MS is required to better understand the reason of weight changes.

$Li_2MnO_{3-x}F_x$ samples had a higher capacity and conductivity than that of Li_2MnO_3. Ball-milled Li_2MnO_3 only had a first charge capacity of 47 mAh/g, but Li_2MnO_2F 215 mAh/g. The Mn valence reversibly increased and decreased during charge and discharge, almost between 4+ and 3+. All ball-milled samples had a mixed ionic and electronic conductor. F-doped samples show a degree of electrical inhomogeneity. Except M3, all F doped samples had a higher conductivity than the undoped, but did not show a clear trend of increase with F content. In M3, doped samples had lower conductivity than the undoped.

4.3 References

[150] M. M. Thackeray, M. F. Mansuetto, and C. S. Johnson, “Thermal stability of Li4Mn5O12 electrodes for lithium batteries,” *J. Solid State Chem.*, vol. 125, no. 2, pp. 274–277, 1996, doi: 10.1006/jssc.1996.0297.

[151] A. Manceau, M. A. Marcus, and S. Grangeon, “Determination of Mn valence states in mixed-valent manganates by XANES spectroscopy,” *Am. Mineral.*, vol. 97, no. 5–6, pp. 816–827, 2012, doi: 10.2138/am.2012.3903.

Appendix A for Chapter 4: Impedance data

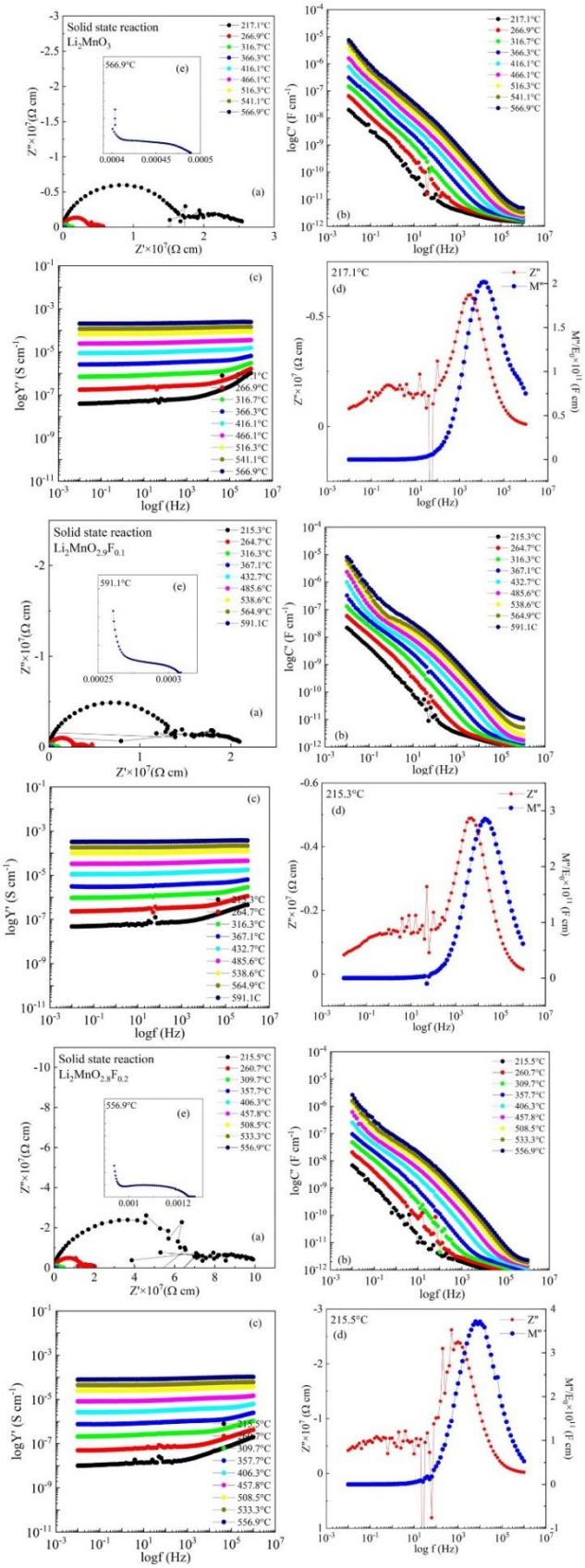

Figure 4.38 the impedance datasets for solid-state $Li_2MnO_{3-x}F_x$

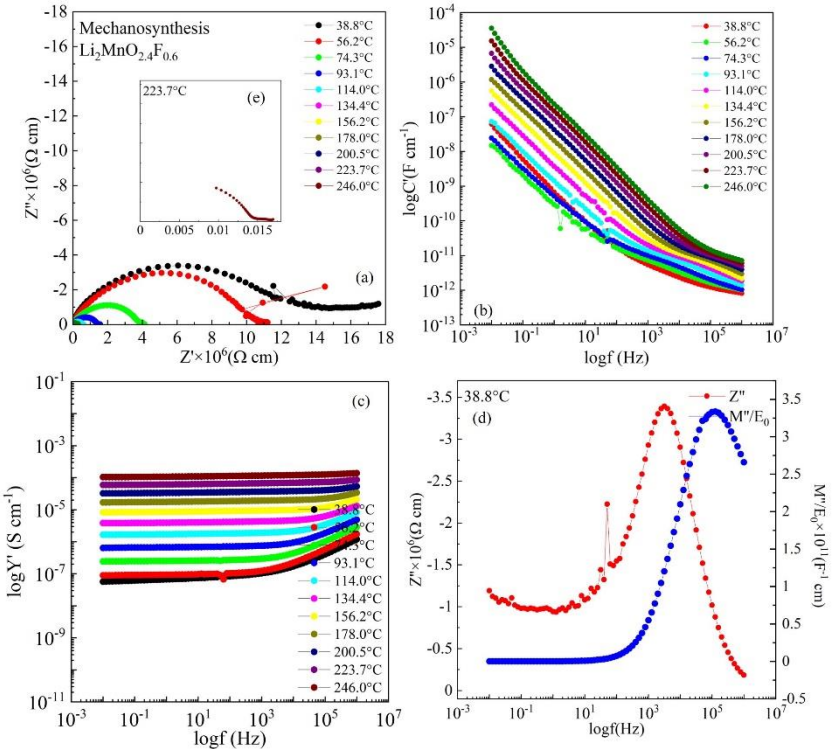

Figure 4.37 the impedance dataset for ball-milled $Li_2MnO_{2.4}F_{0.6}$

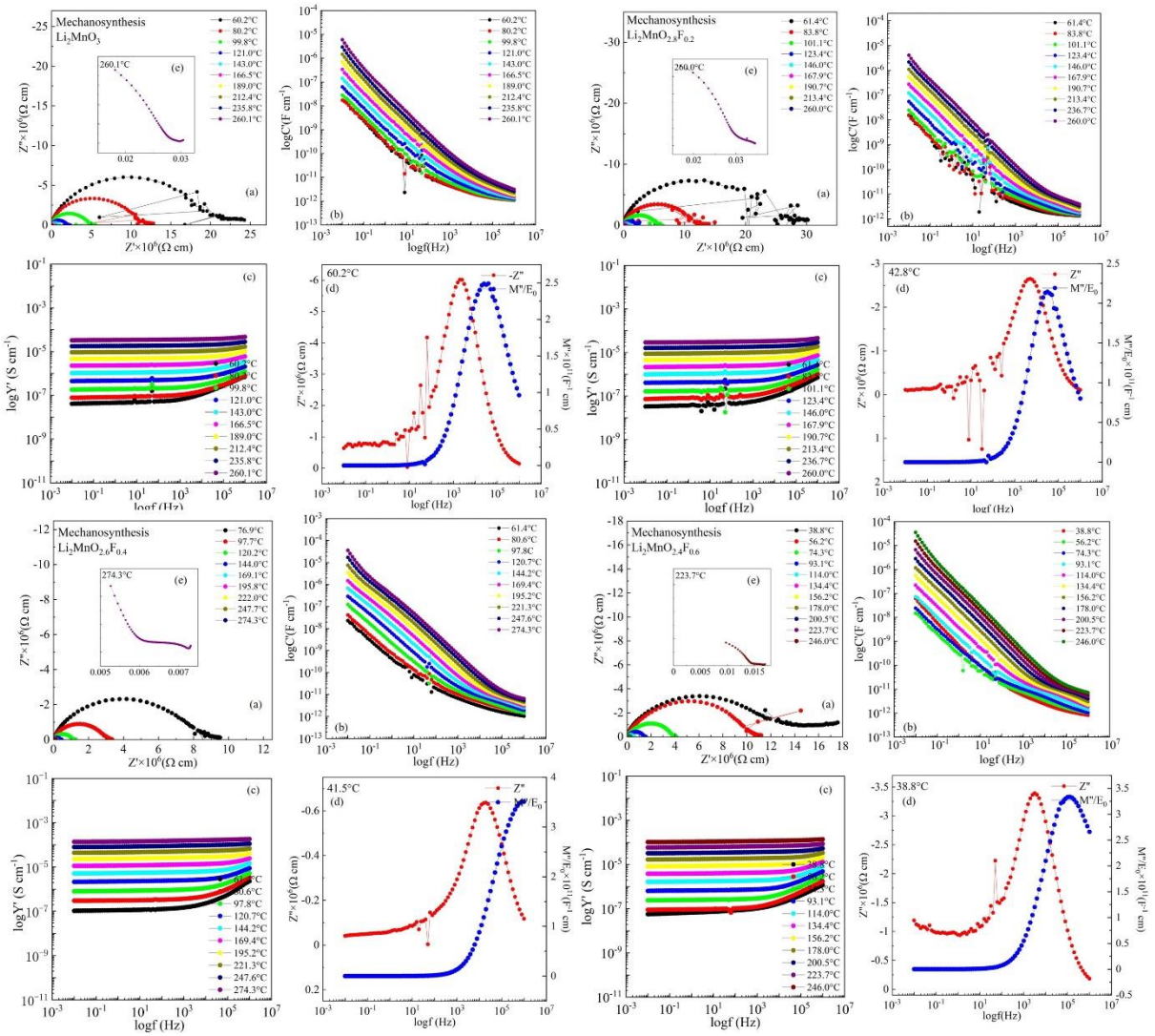

Figure 4.39 the impedance datasets for ball-milled $Li_2MnO_{3-x}F_x$

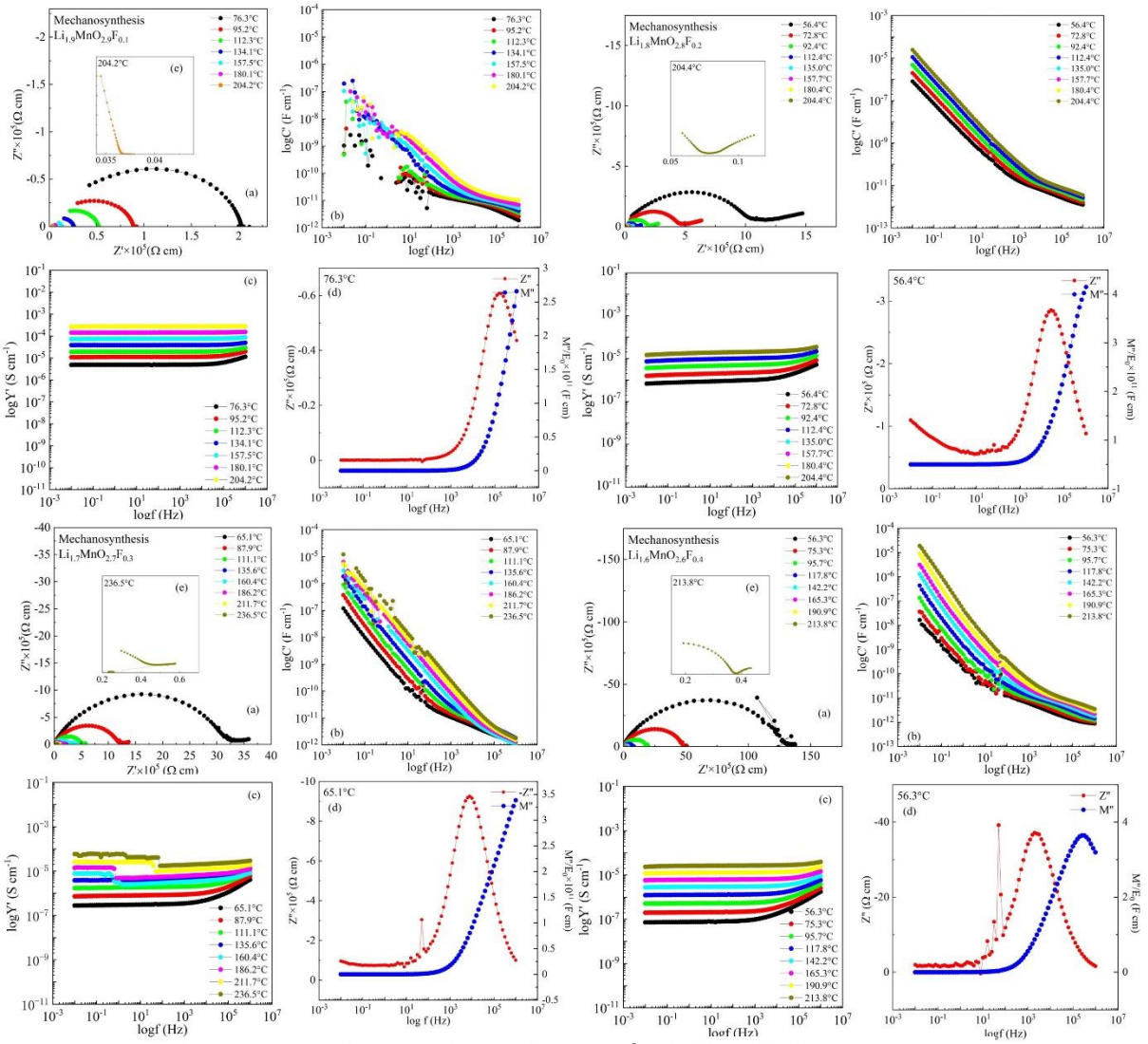

Figure 4.40 the impedance datasets for ball-milled $Li_{2-x}MnO_{3-x}F_x$

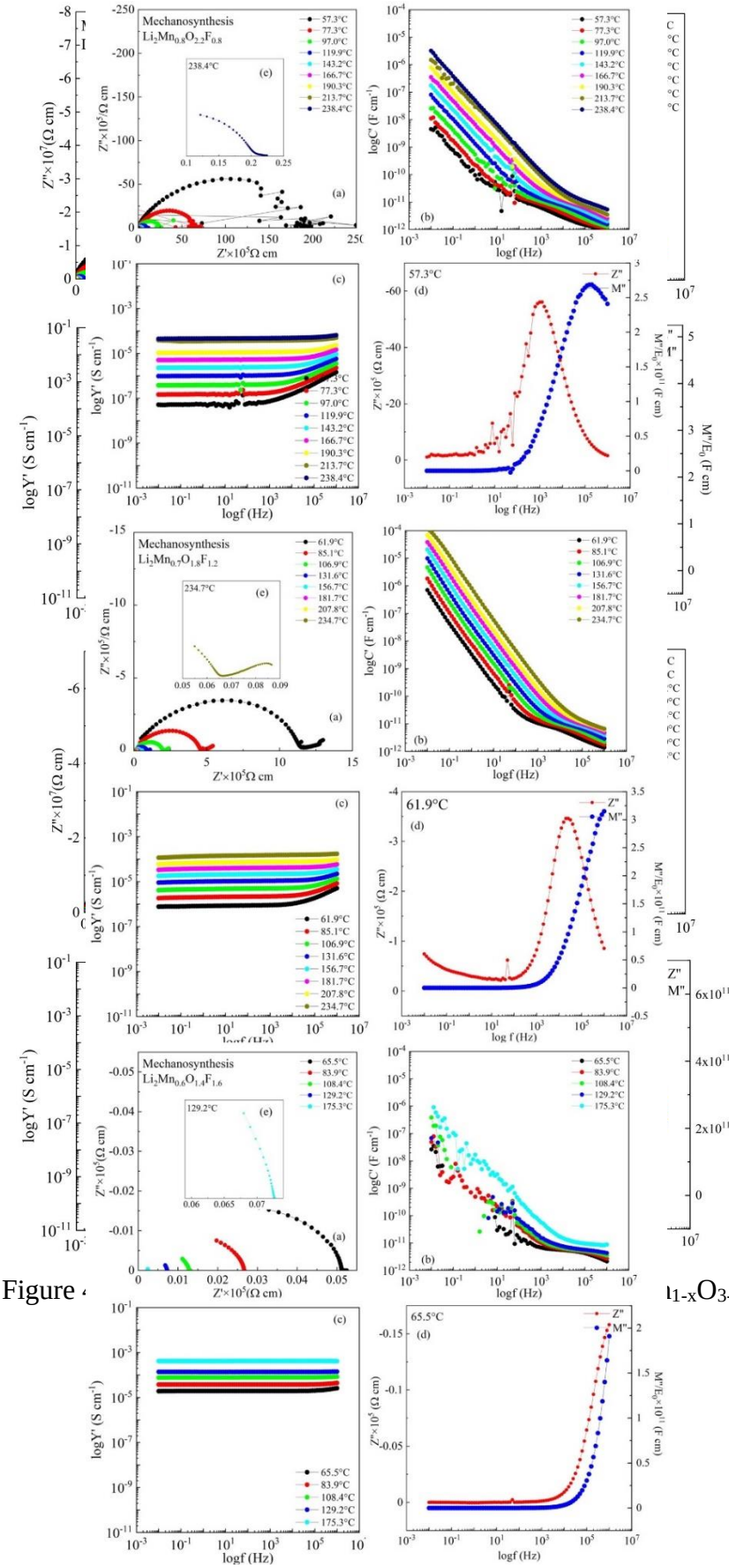

Figure 4.42 the impedance datasets for ball-milled $Li_2Mn_{1-x}O_{3-4x}F_{4x}$

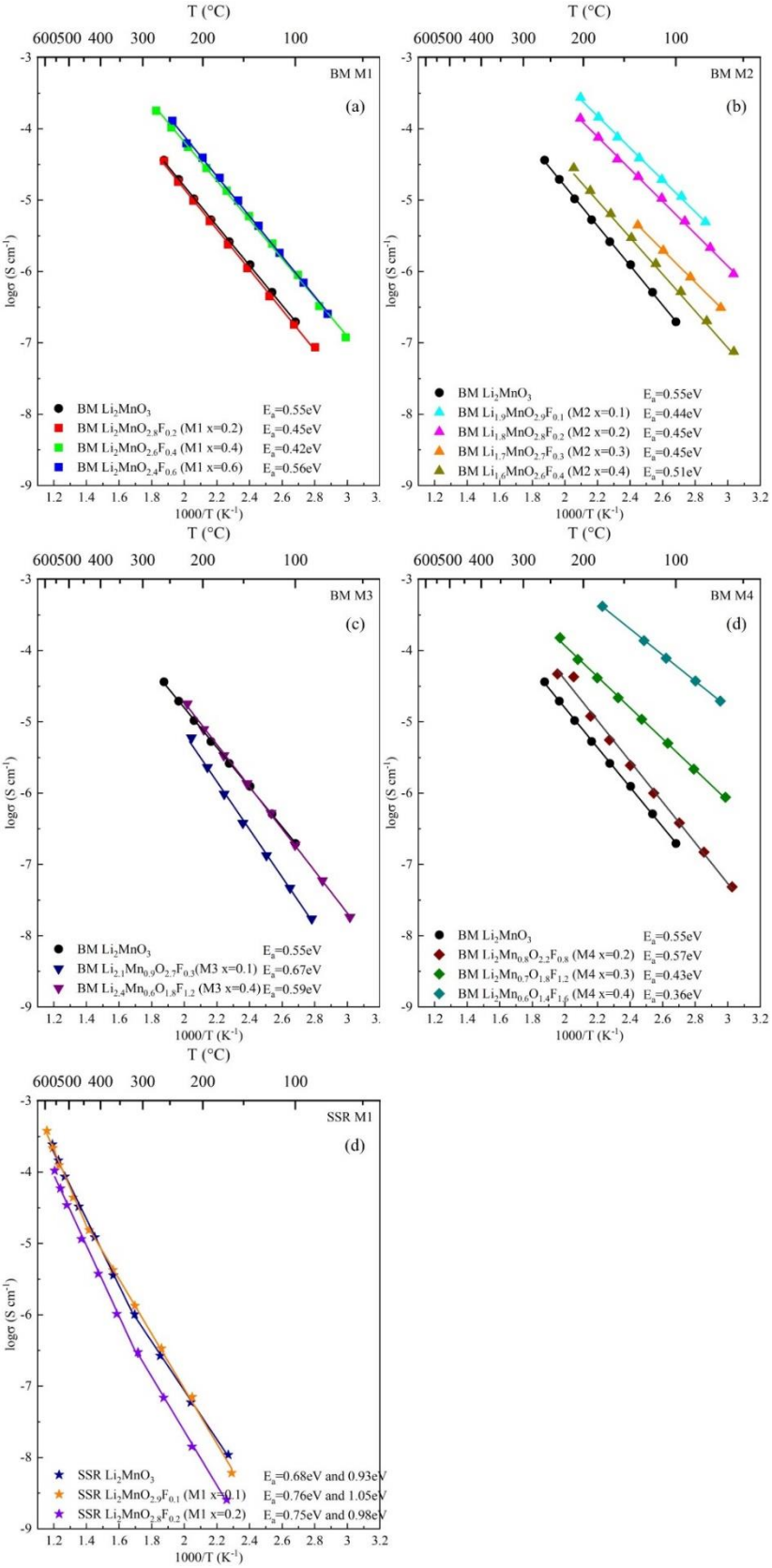

Figure 4.43 The Arrhenius plot of ball-milled F-doped Li_2MnO_3

Appendix B for Chapter 4: Refined results

Refined results on solid state Li_2MnO_3, and ball-milled $Li_2MnO_{3-x}F_x$ (x=0.0, 0.2, 0.4, 0.6, 0.8) at room temperature and 500°C

Solid state x=0.0

2Theta window: 0.1
Symmetry: Monoclinic_B C
Spacegroup: C 2/m (No. 12)

Initial cell parameters:	Refined cell parameters:
Cell_A: 4.0584	Cell_A: 4.0584(7)
Cell_B: 8.5280	Cell_B: 8.528(3)
Cell_C: 9.6360	Cell_C: 9.636(3)
Cell_Beta: 99.620	Cell_Beta: 99.62(3)
	Cell_Volume: 400.25(20)

Number of single indexed lines: 12
Number of unindexed lines: 0
Final 2Theta window: 0.03

N	2Th[obs]	H	K	L	2Th[calc]	obs-calc	Int.	d[obs]	d[calc]
1	20.127	2	0	0	20.131	-0.0041	100	2.0296	2.0292
2	28.626	2	2	0	28.62	0.0067	61.4	1.4345	1.4349
3	35.238	2	2	2	35.241	-0.0031	29.9	1.1717	1.1716
4	11.073	1	1	1	11.088	-0.0143	13.3	3.6758	3.6711
		-1							
5	16.806		3	1	16.805	0.0017	42.5	2.4268	2.4271
6	17.192	0	0	4	17.176	0.0161	8.5	2.3728	2.375
		1	1	3	17.176	0.0159			
7	17.532	1	3	1	17.51	0.0219	10.9	2.3271	2.33
8	20.178	-1	3	3	20.177	0.0007	97.4	2.0246	2.0246
9	21.954	-2	0	4	21.947	0.0068	15	1.8625	1.8631
10	25.532	2	4	0	25.545	-0.0128	8.7	1.605	1.6042
11	26.147	-1	3	5	26.147	0.0003	20.1	1.5679	1.5679
12	28.467	3	1	2	28.47	-0.0028	29.8	1.4424	1.4423
		-2	0	6	28.472	-0.0051			
13	28.886	0	6	0	28.898	-0.0127	37.6	1.4219	1.4213
14	33.6	2	6	0	33.585	0.0154	10.2	1.227	1.2276
15	35.476	2	6	2	35.447	0.0294	17.3	1.1641	1.165
		2	4	5	35.472	0.0042	1.1642		

		-2	0	8					
16	36.066				36.072	-0.0066	10.6	1.1456	1.1454
		0	4	7	36.091	-0.0253	1.1449		
17	39.301	2	6	4	39.291	0.01	9.2	1.0546	1.0549
		-4	0	6	39.32	-0.0186	1.0541		

Average delta(2Theta) = 0.009
Maximum delta(2Theta) = 0.022 (peak 7) = 2.5* average
Figure of Merit F(17) = 10.3 (0.009, 186)
Durbin-Watson serial correlation = 2.1
Sqrt[sum(w * delta(q)^2) / (Nobs - Nvar)] = 0.0004396

Ball-milled x=0.0 at room temperature

2Theta window: 0.1
Symmetry: Cubic F
Spacegroup: F m -3 m (No. 225)

Initial cell parameters:	Refined cell parameters:
Cell_A: 4.0735	Cell_A: 4.0735(6) Cell_Volume: 67.593(18)

Number of single indexed lines: 3
Number of unindexed lines: 0
Final 2Theta window: 0.01

N	2Th[obs]	H	K	L	2Th[calc]	obs-calc	Int.	d[obs]	d[calc]
1	20.061	2	0	0	20.056	0.0053	100	2.0362	2.0367
2	28.514	2	2	0	28.512	0.0025	61.7	1.4401	1.4402
3	35.102	2	2	2	35.107	-0.005	31.4	1.1761	1.1759

Average delta(2Theta) = 0.004
Maximum delta(2Theta) = 0.005 (peak 1) = 1.2 * average
Figure of Merit F(3) = 139.7 (0.004, 5)
Durbin-Watson serial correlation = 1.308 (not significant)
Sqrt[sum(w * delta(q)^2) / (Nobs - Nvar)] = 0.0002686

Ball-milled x=0.2 at room temperature

2Theta window: 0.100
Symmetry: Cubic F
Spacegroup: F m -3 m (No. 225)

Initial cell parameters:	Refined cell parameters:
Cell_A: 4.079	Cell_A: 4.079(4) Cell_Volume: 67.84(11)

Number of single indexed lines: 3
Number of unindexed lines: 0
Final 2Theta window: 0.04

N	2Th[obs]	H	K	L	2Th[calc]	obs-calc	Int.	d[obs]	d[calc]
1	20.031	2	0	0	20.031	0	100	2.0393	2.0393
2	28.514	2	2	0	28.476	0.0387	59.2	1.4401	1.442
3	35.031	2	2	2	35.062	-0.031	32.9	1.1784	1.1774

Average delta(2Theta) = 0.023
Maximum delta(2Theta) = 0.005 (peak 1) = 1.7 * average
Figure of Merit F(3) = 25.8 (0.023, 5)
Durbin-Watson serial correlation = 2.517 (not significant)
Sqrt[sum(w * delta(q)^2) / (Nobs - Nvar)] = 0.0017188

Ball-milled x=0.4 at room temperature

2Theta window: 0.1
Symmetry: Cubic F
Spacegroup: F m -3 m (No. 225)

Initial cell parameters:	Refined cell parameters:
Cell_A: 4.08	Cell_A: 4.080(4)
	Cell_Volume: 67.93(10)

Number of single indexed lines: 3
Number of unindexed lines: 0
Final 2Theta window: 0.04

N	2Th[obs]	H	K	L	2Th[calc]	obs-calc	Int.	d[obs]	d[calc]
1	20.025	2	0	0	20.022	0.0027	100	2.0399	2.0401
2	28.428	2	2	0	28.463	-0.0353	63.6	1.4443	1.4426
3	35.074	2	2	2	35.047	0.0269	41.1	1.177	1.1779

Average delta(2Theta) = 0.022
Maximum delta(2Theta) = 0.035 (peak 2) = 1.6* average
Figure of Merit F(3) = 27.8 (0.022, 5)
Durbin-Watson serial correlation = 2.595 (not significant)
Sqrt[sum(w * delta(q)^2) / (Nobs - Nvar)] = 0.0015413

Ball-milled x=0.6 at room temperature

2Theta window: 0.1
Symmetry: Cubic F
Spacegroup: F m -3 m (No. 225)

Initial cell parameters:	Refined cell parameters:
Cell_A: 4.093	Cell_A: 4.0930(25)
	Cell_Volume: 68.57(7)

Number of single indexed lines: 3
Number of unindexed lines: 0
Final 2Theta window: 0.03

N	2Th[obs]	H	K	L	2Th[calc]	obs-calc	Int.	d[obs]	d[calc]
1	19.978	2	0	0	19.959	0.0193	100	2.0446	2.0465

2	28.385	2	2	0	28.372	0.012	63	1.4465	1.4471
3	34.913	2	2	2	34.934	-0.0204	35.4	1.1822	1.1816

Average delta(2Theta) = 0.017
Maximum delta(2Theta) = 0.02 (peak 3) = 1.2* average
Figure of Merit F(3) = 34.8 (0.017, 5)
Durbin-Watson serial correlation = 1.426 (not significant)
Sqrt[sum(w * delta(q)^2) / (Nobs - Nvar)] = 0.0010597

Ball-milled x=0.8 at room temperature

2Theta window: 0.1
Symmetry: Cubic F
Spacegroup: F m -3 m (No. 225)

Initial cell parameters:	Refined cell parameters:
Cell_A: 4.093	Cell_A: 4.093(4)
	Cell_Volume: 68.55(12)

Number of single indexed lines: 3
Number of unindexed lines: 0
Final 2Theta window: 0.05

N	2Th[obs]	H	K	L	2Th[calc]	obs-calc	Int.	d[obs]	d[calc]
1	19.942	2	0	0	19.961	-0.0192	100	2.0483	2.0463
2	28.416	2	2	0	28.375	0.0404	63.9	1.445	1.447
3	34.916	2	2	2	34.937	-0.0216	38.9	1.1822	1.1814

Average delta(2Theta) = 0.027
Maximum delta(2Theta) = 0.04 (peak 2) = 1.5* average
Figure of Merit F(3) = 22.2 (0.027, 5)
Durbin-Watson serial correlation = 2.939
Sqrt[sum(w * delta(q)^2) / (Nobs - Nvar)] = 0.0017218

Ball-milled x=0.0 at 500°C

2Theta window: 0.1
Symmetry: Cubic F
Spacegroup: F m -3 m (No. 225)

Initial cell parameters:	Refined cell parameters:
Cell_A: 4.0572	Cell_A: 4.0572(19)
	Cell_Volume: 66.78(6)

Number of single indexed lines: 3
Number of unindexed lines: 0
Final 2Theta window: 0.02

N	2Th[obs]	H	K	L	2Th[calc]	obs-calc	Int.	d[obs]	d[calc]
1	20.147	2	0	0	20.137	0.0103	100	2.0275	2.0286
2	28.643	2	2	0	28.629	0.0141	60.3	1.4337	1.4344
3	35.236	2	2	2	35.253	-0.017	43.1	1.1717	1.1712

Average delta(2Theta) = 0.014
Maximum delta(2Theta) = 0.17 (peak 3) = 1.2* average
Figure of Merit F(3) = 43.5 (0.014, 5)
Durbin-Watson serial correlation = 1.841
Sqrt[sum(w * delta(q)^2) / (Nobs - Nvar)] = 0.00084575

Ball-milled x=0.2 at 500°C

2Theta window: 0.1
Symmetry: Cubic F
Spacegroup: F m -3 m (No. 225)

Initial cell parameters:	Refined cell parameters:
Cell_A: 4.0513	Cell_A: 4.0513(22)
	Cell_Volume: 66.49(6)

Number of single indexed lines: 3
Number of unindexed lines: 0
Final 2Theta window: 0.03

N	2Th[obs]	H	K	L	2Th[calc]	obs-calc	Int.	d[obs]	d[calc]
1	20.145	2	0	0	20.167	-0.0222	100	2.0278	2.0256
2	28.666	2	2	0	28.671	-0.0053	49.5	1.4326	1.4323
3	35.322	2	2	2	35.306	0.0167	25	1.169	1.1695

Average delta(2Theta) = 0.015
Maximum delta(2Theta) = 0.022 (peak 1) = 1.5* average
Figure of Merit F(3) = 40.8 (0.015, 5)
Durbin-Watson serial correlation = 1.105
Sqrt[sum(w * delta(q)^2) / (Nobs - Nvar)] = 0.00098079

Ball-milled x=0.4 at 500°C

2Theta window: 0.1
Symmetry: Cubic F
Spacegroup: F m -3 m (No. 225)

Initial cell parameters:	Refined cell parameters:
Cell_A: 4.0508	Cell_A: 4.0508(24)
	Cell_Volume: 66.47(7)

Number of single indexed lines: 3
Number of unindexed lines: 0
Final 2Theta window: 0.03

N	2Th[obs]	H	K	L	2Th[calc]	obs-calc	Int.	d[obs]	d[calc]
1	20.151	2	0	0	20.169	-0.0179	100	2.0272	2.0254
2	28.662	2	2	0	28.675	-0.0131	55.5	1.4328	1.4322
3	35.331	2	2	2	35.31	0.0206	27.2	1.1687	1.1694

Average delta(2Theta) = 0.017
Maximum delta(2Theta) = 0.021 (peak 3) = 1.2* average
Figure of Merit F(3) = 34.8 (0.017, 5)
Durbin-Watson serial correlation = 1.509
Sqrt[sum(w * delta(q)^2) / (Nobs - Nvar)] = 0.0010516

Ball-milled x=0.6 at 500°C

2Theta window: 0.1
Symmetry: Cubic F
Spacegroup: F m -3 m (No. 225)

Initial cell parameters:	Refined cell parameters:
Cell_A: 4.0584	Cell_A: 4.0584(7)
	Cell_Volume: 66.846(19)

Number of single indexed lines: 3
Number of unindexed lines: 0
Final 2Theta window: 0.01

N	2Th[obs]	H	K	L	2Th[calc]	obs-calc	Int.	d[obs]	d[calc]
1	20.127	2	0	0	20.131	-0.0041	100	2.0296	2.0292
2	28.626	2	2	0	28.62	0.0067	61.4	1.4345	1.4349
3	35.238	2	2	2	35.241	-0.0031	29.9	1.1717	1.1716

Average delta(2Theta) = 0.005
Maximum delta(2Theta) = 0.007 (peak 2) = 1.4* average
Figure of Merit F(3) = 128.8 (0.005, 5)
Durbin-Watson serial correlation = 2.992
Sqrt[sum(w * delta(q)^2) / (Nobs - Nvar)] = 0.0002946

Chapter 5 Li-Mn-O family

5.1 Results and discussion

5.1.1 Synthesis of $LiMn_2O_4$ and $LiMnO_2$

5.1.1.1 Synthesis of $LiMn_2O_4$ by solid-state reaction

Li_2CO_3 and MnO_2 were used as reactants to prepare $LiMn_2O_4$ by solid-state reaction. The mixture was heated in air at 150 °C for 2 h and then at 600 °C for 6 h. The final synthesis temperature was 850 °C for 12 h in air. The product appeared to be single phase and corresponds to $LiMn_2O_4$, Figure 5.1 (a). When the mixture was heated in N_2 (b) with the same synthesis process, instead of $LiMn_2O_4$, the product was mainly $LiMnO_2$ with a small amount of $LiMn_2O_4$ and unknown phase.

5.1.1.2 Synthesis of $LiMn_2O_4$ by mechanosynthesis

Li_2O_2 and MnO were used as reactants to prepare $LiMn_2O_4$ by mechanosynthesis. The mixture was ball-milled at 350 rpm for up to 14 h, Figure 5.2. A disordered phase started to appear after 2 h milling. After 6 h, the reactants had completely reacted and a disordered phase appeared. However, it had a high and noisy background and it was possibly amorphous. After 8 h milling, an ordered phase formed which corresponds to spinel $LiMn_2O_4$, with a very broad peak and noisy background. A second phase, Mn_2O_3, may have started to form at 4 h but appeared obviously after 12 h. The possible reason of Mn_2O_3 formation may be the decomposition of metastable phase or oxidation of the reactant, MnO. Noticeably, reactants did not provide enough oxygen for spinel $LiMn_2O$, but for rock-salt $LiMn_2O_3$. Further study with proper reactants needs to be carried out.

5.1.1.3 Heat treatment on ball-milled $LiMn_2O_4$

$LiMn_2O_4$ after 14 h milling was heated from room temperature to 600 °C, Figure 5.3. With heating, the spinel phase peaks started to get sharp and coexisted with the second phase Mn_2O_3. From 600 °C, the amount of Mn_2O_3 significantly reduced, indicating a reaction with the main phase. The ordered phase at 600 °C still correspond to spinel, which may suggest that the Li:Mn ratio of the ball-milled spinel phase was higher than 1:2, perhaps $Li_4Mn_5O_{12}$.

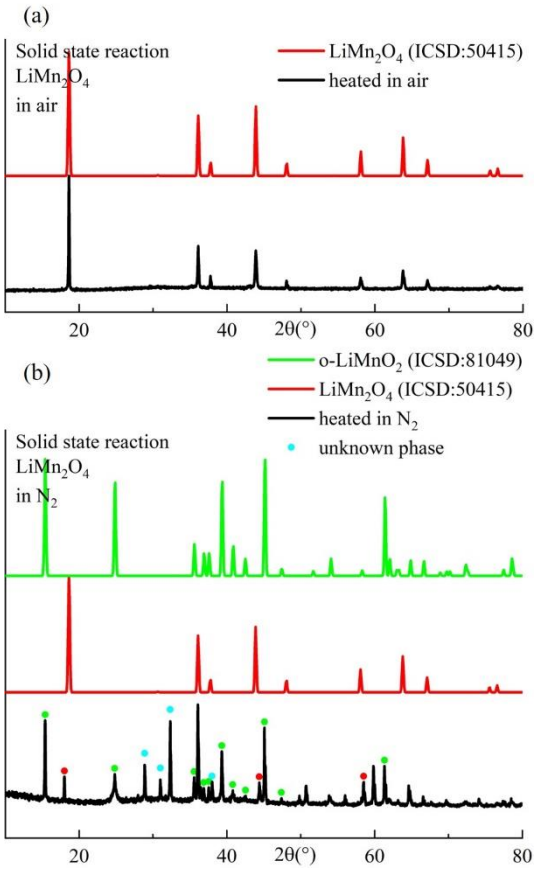

Figure 5.1 the XRD patterns of $LiMn_2O_4$ produced by solid state reaction (a) in air and (b) in N_2

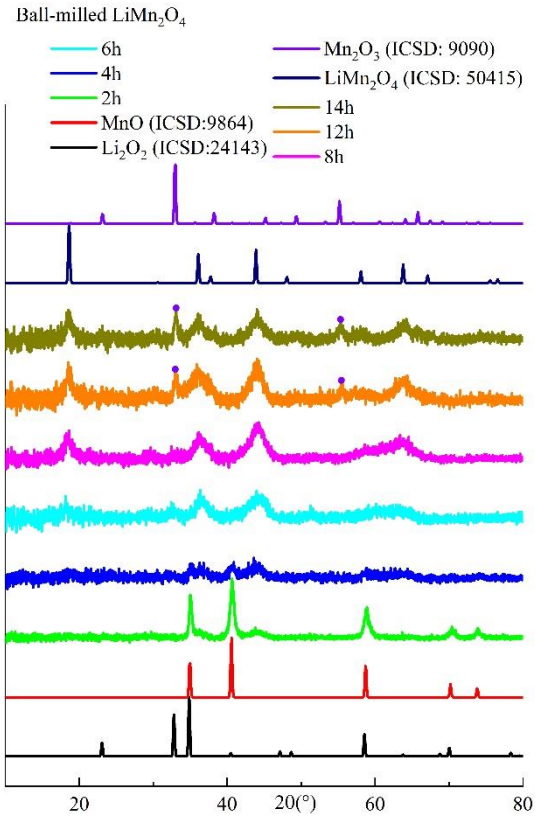

Figure 5.2 the XRD patterns of $LiMn_2O_4$ produced by mechanosynthesis

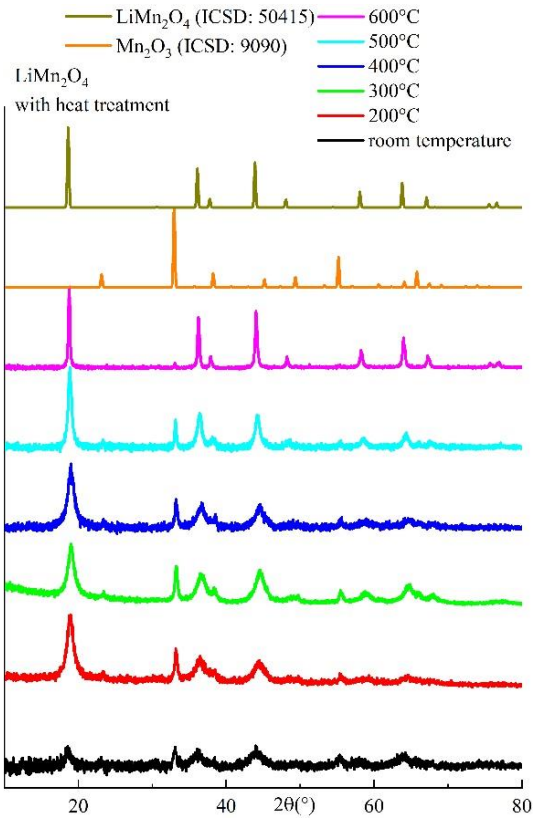

Figure 5.3 the XRD patterns of heat treatment on ball-milled $LiMn_2O_4$

5.1.1.4 Synthesis of $LiMnO_2$ by solid-state reaction

Li_2CO_3 and MnO_2 were used as reactants to prepare $LiMnO_2$ by solid-state reaction. The mixture was heated in N_2 at 150 °C for 2 h and then at 600 °C for 6 h. The final synthesis temperature was 850 °C for 12 h. The product appeared to be single phase and correspond to $LiMnO_2$, shown in Figure 5.4 (a). When the mixture was heated in air (b) with the same synthesis processes, instead of $LiMnO_2$, the products were a mixture of Li_2MnO_3 and $LiMn_2O_4$.

5.1.1.5 Synthesis of $LiMnO_2$ by mechanosynthesis

Li_2O_2 and MnO were used as reactants to prepare $LiMnO_2$ by mechanosynthesis. The mixture was ball-milled at 350 rpm up to 10 h, Figure 5.5. After 2 h, the MnO lines broaden and broad peaks of a second rock-salt phase appeared. After 4 h milling, the reactants had completely reacted and a disordered structure was formed. A very broad domain peak around 18° appeared, indicating an ordered domain formed with a much smaller size. With longer milling time, the intensity of the domain peak increased and finally an ordered phase formed, which however, does not correspond to $LiMnO_2$. Considering the Li/Mn ratio in the starting materials was 1:1, it may correspond to spinel $Li_4Mn_5O_{12}$ or a rhombohedral structure, like $LiCoO_2$.

5.1.1.6 Heat treatment on ball-milled $LiMnO_2$

$LiMnO_2$ after 10 h milling was heated from room temperature to 700 °C, Figure 5.6. With heating, the spinel phase peaks started to get sharp. From 600 °C, a second phase Li_2MnO_3 appeared. It is possible that the ball-milled products were a mixture of Mn-rich phase, such as $Li_4Mn_5O_{12}$ or $LiMn_2O_4$ and Li-rich phase, such as Li_2MnO_3.

It can be concluded that by solid state reaction, $LiMn_2O_4$ was successfully synthesised in air whilst $LiMnO_2$ was only successfully synthesised in N_2. By mechanosynthesis, single phase $LiMn_2O_4$ was not successfully synthesised. When the target product was $LiMnO_2$, a metastable disordered rock-salt phase appeared to form and with longer milling time, a phase such as a spinel and a rock-salt layered structure with small ordered domains.

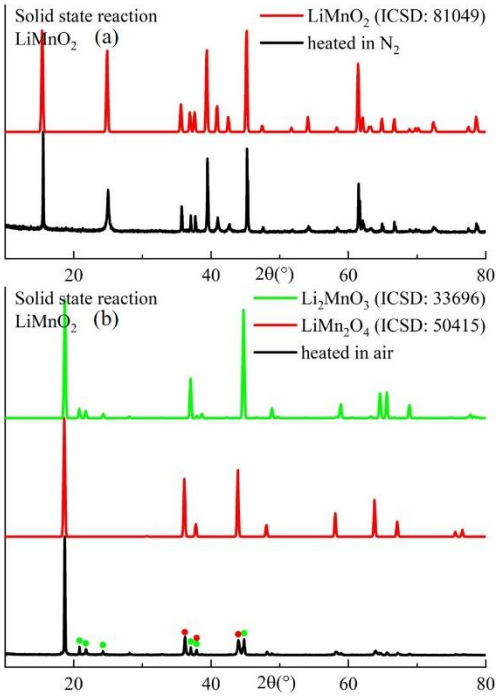

Figure 5.4 the XRD patterns of $LiMnO_2$ produced by solid state reaction (a) in N_2 and (b) in air

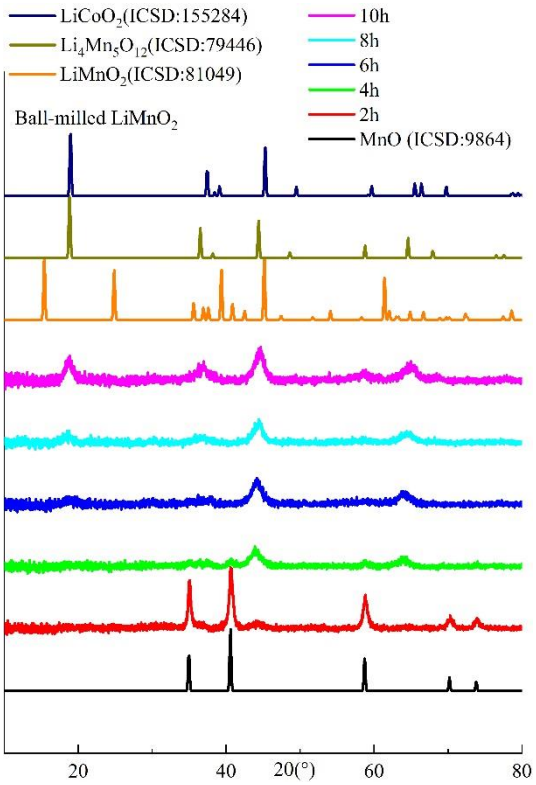

Figure 5.5 the XRD patterns of $LiMnO_2$ produced by mechanosynthesis

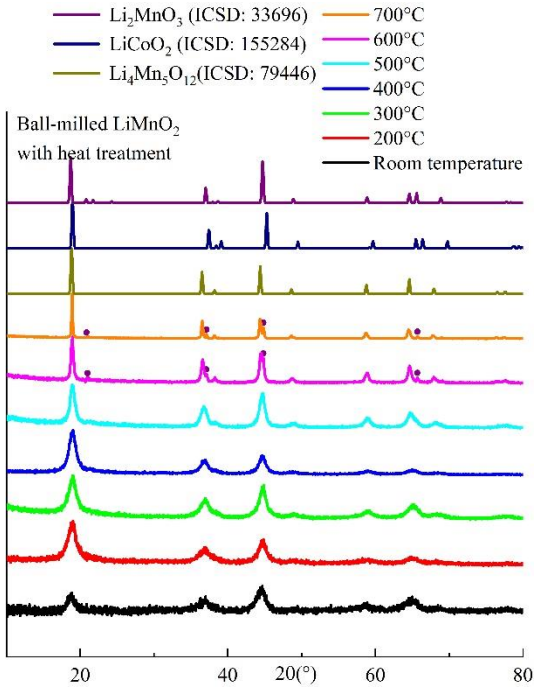

Figure 5.6 the XRD patterns of heat treatment on ball-milled $LiMnO_2$

5.1.2 Synthesis of $Li_4Mn_5O_\delta$

5.1.2.1 Synthesis of $Li_4Mn_5O_{12}$ by solid state reaction

Li_2CO_3 and MnO_2 were used as reactants to prepare $Li_4Mn_5O_{12}$ by solid-state reaction, Figure 5.7. As $Li_4Mn_5O_{12}$ is not stable at high temperature, it was synthesised at 500 °C for 36 h. By comparing the peak position of the highest peak around 19°, the main phase was the most likely to be $Li_4Mn_5O_{12}$. However, a small amount of Li_2MnO_3 formed. Also, a small amount of reactants, Li_2CO_3 and MnO_2 were still observed at 500 °C. Li_2CO_3 might not be able to completely decompose at 500 °C, so other Li possible sources were considered.

5.1.2.2 Synthesis of $Li_4Mn_5O_{12}$ by pre-ballmilling and solid state reaction

$LiOH{\cdot}H_2O$ was used as the Li source and mixed with MnO_2. Before heating, 2 h ball-milling at 350 rpm was introduced to assist the solid state reaction. Then the mixtures were heated at 600 °C for 12 h in air. By comparing the peak around 45°, the product was possible to be a mixture of $Li_4Mn_5O_{12}$ and a slight amount of second phase, Li_2MnO_3, Figure 5.8.

5.1.2.3 Synthesis of $Li_4Mn_5O_\delta$ by mechanosynthesis

Two samples were produced by mechanosynthesis at 350 rpm for 10 h using different Li and Mn sources: (A) Li_2O_2 and MnO and (B) Li_2O and MnO_2. The XRD patterns are shown in Figure 5.9(a). A, starting with a cation: anion ratio of 1:1, gave a disordered rock-salt phase, whilst B, starting with a cation: anion ratio of 3:4, gave a spinel phase. This suggests that in mechanosynthesis, it is possible to produce compositions with a fixed cation A and cation B ratio but different oxygen stoichiometry, which may be affected by starting materials and not change during milling.

To further study the variability of oxygen stoichiometry and the effect of different reactants, the following samples were produced by mechanosynthesis: i. Li_2O_2 with three manganese oxides were ball-milled with the same process: (A) Li_2O_2 and MnO, (C) Li_2O_2 and Mn_2O_3 and (D) Li_2O_2 and MnO_2, Figure 5.9 (b); ii, Li_2O with two manganese oxides were also ball-milled with the same process: (B) Li_2O and MnO_2, and (E) Li_2O, MnO and Mn_2O_3, Figure 5.9 (c). Among them, A and E had a Li:Mn:O ratio of 4:5:9, B, C and D had 4:5:12, 4:5:11.5 and 4:5:14, respectively. The results show that A and E, the ratio of cation: anion was 1:1, gave a disordered rock-salt phase and the others, the ratio of cation: anion was or close to 3:4, gave a spinel phase.

A, C and D gives $Li_4Mn_5O_9$, $Li_4Mn_5O_{11.5}$ and $Li_4Mn_5O_{14}$ when Li_2O_2 may react with MnO, Mn_2O_3 and MnO_2 respectively:

$$2Li_2O_2 + 5Mn^{2+}O = Li_4Mn^{2+}Mn_4^{3+}O_9 \quad (1)$$

$$2Li_2O_2 + \frac{5}{2}Mn_2^{3+}O_3 = Li_4Mn_5^{4+}O_{11.5} \quad (2)$$

$$2Li_2O_2 + 5Mn^{4+}O_2 = Li_4Mn_5^{4+}O_{14} = Li_4Mn_5^{4+}O_{12} + O_2 \quad (3)$$

As mentioned in 3.3.1.3, peroxide ion can act as an oxidising or reducing agent, or undergo a disproportionation, the final product may depend on Mn sources. A may not pick up enough oxygen and only gives $Li_4Mn_5O_9$ but C contained enough oxygen and gives $Li_4Mn_5O_{11.5}$. For D, as Mn is unlikely to be oxidised to higher than 4+, $\delta \leq 12$. D contains too much oxygen so O_2 may be released.

B and E used Li_2O and give $Li_4Mn_5O_{12}$ and $Li_4Mn_5O_9$, respectively. Li_2O gave no redox reaction and Mn valence is not affected:

$$2Li_2O + 5Mn^{4+}O_2 = Li_4Mn_5^{4+}O_{12} \quad (4)$$

$$2Li_2O + Mn^{2+}O + 2Mn_2^{3+}O_3 = Li_4Mn^{2+}Mn_4^{3+}O_9 \quad (5)$$

As conclusion, mechanosynthesis may be able to produce $Li_4Mn_5O_\delta$ with different oxygen content, which depends on reactants. The cation and anion ratio can be 1:1 or 3:4, which gave disordered rock-salt phase or spinel phase, respectively.

5.1.2.4 Heat treatment of ball-milled $Li_4Mn_5O_\delta$

In Figure 5.10, ball-milled rock-salt E(a) and spinel B(b) were heated up to 550 °C. E had a disordered rock-salt phase at room temperature and transformed to spinel at 400 °C, corresponding to $Li_4Mn_5O_{12}$. At higher temperatures, the peaks became sharper, indicating a grain growth. B had an ordered spinel phase at room temperature. When it was heated, no phase change occurred and the peaks became sharper, which indicates a grain growth. Up to 550 °C, no phase decomposition was observed in either sample.

To study the stability of $Li_4Mn_5O_{12}$ phase, B was heated from room temperature to 700 °C, Figure 5.11. Initially, the XRD patterns had broad peaks and noisy background, which was improved with increased temperature. At 600 and 700 °C, it showed extra small extra peaks attributed to the presence of monoclinic Li_2MnO_3. This indicates that decomposition may occur ≥ 600 °C and continued at higher temperatures. The possible decomposition products were Li_2MnO_3 and a more Mn-rich spinel, probably $LiMn_2O_4$.

5.1.2.5 TG analysis of ball-milled $Li_4Mn_5O_\delta$

Figure 5.12 shows a comparison of TG results of ball-milled (a) $Li_4Mn_5O_9$ and (b) $Li_4Mn_5O_{12}$ heated to 800 °C for two cycles. $Li_4Mn_5O_9$ (a), produced by Li_2O_2 and MnO, had a 0.89 wt% of weight increase at about 270-360 °C. It was followed by a 0.98 wt% of weight loss. At 450-510 °C, there was another slow and slight weight gain, followed by a slight weight loss at 510-580 °C. After 600 °C, a slow weight loss occurred and continued up to 800 °C, in which 0.94 wt% of weight loss was reversible during cooling and reheating.

$Li_4Mn_5O_{12}$ (b), produced by Li_2O and MnO_2, had a very similar TG profile with the ball-milled Li_2MnO_3 in 3.3.2. Assuming the weight loss process of $Li_4Mn_5O_{12}$ is similar to that of Li_2MnO_3, water and CO_2 loss may also have occurred in similar temperature ranges. Before 200 °C, a 1.49 wt% of water loss occurred. At 200-300 °C and 300-400 °C, two weight loss

processes occurred with different rate, which might be decomposition of two different species of carbonates and release of CO_2. After 600 °C, a slow weight loss occurred and continued to 800 °C. Like $Li_4Mn_5O_9$, this weight loss was partially reversible during cooing and heating in the second cycle and might relate to oxygen loss and uptake.

The TG profiles of $Li_4Mn_5O_9$ and $Li_4Mn_5O_{12}$ show a big difference on the first cycle at low temperature. $Li_4Mn_5O_9$ generally had a smaller weight change during heating and cooling and did not have an obvious water loss before 200 °C, which may indicate it was less hygroscopic than $Li_4Mn_5O_{12}$. From 5.1.2.3, Figure 5.10, when heated to 400 °C, $Li_4Mn_5O_9$ has already transformed to $Li_4Mn_5O_{12}$, indicating $Li_4Mn_5O_9$ picks oxygen during heating. Therefore, the weight gain in $Li_4Mn_5O_9$ at 270-360 °C may relate to this phase transformation. Also, the profiles after 360 °C for two samples were similar, indicating two samples mainly contained $Li_4Mn_5O_{12}$. Their XRD patterns after TG is shown in Figure 5.13. A spinel presented as the main phase and Li_2MnO_3 as the second phase in both samples, indicating the $Li_4Mn_5O_{12}$ phase had decomposed during TG. The weight loss at high temperature might be a combination of oxygen loss from $LiMn_2O_4$ and Li_2MnO_3. The standard TG profile of $LiMn_2O_4$ may be collected in future.

To further study the thermal stability and phase transformation of $Li_4Mn_5O_9$ during heating, TG in different atmospheres was recorded, Figure 5.14 (a). No obvious difference was observed in the different atmospheres. In (b), data recorded between room temperature and 450 °C. The weight increased before 395 °C and started losing after that. During cooling, a slight of weight was gained which was lost when it was heated again. Above 450 °C, another weight gain occurred, which was also lost during cooling. In (c), the sample was heated to 800 °C followed by a 2 h dwell. Similar to the previous results, it experienced two weight gain and loss processes were observed, with peaks at 395 and 642 °C. At 800 °C, no weight change occurred during the 2 h dwell. During cooling, the slow weight gain occurred, the amount of which was close to the second weight loss during heating.

As can be seen, the weight change profiles were complex with several features but the profiles and trends of weight change were very similar. The first weight gain in $Li_4Mn_5O_9$, with a peak at 395 °C, is most likely to be the phase transformation from $Li_4Mn_5O_9$ to $Li_4Mn_5O_{12}$, accompanied by oxygen absorption. The second weight gain had a peak at 640 °C, where $Li_4Mn_5O_{12}$ might have started to decompose. This weight change was reversible and might relate to the oxygen content of $LiMn_2O_4$ and Li_2MnO_3 at high temperature. More work is needed to understand the changes observed during TG.

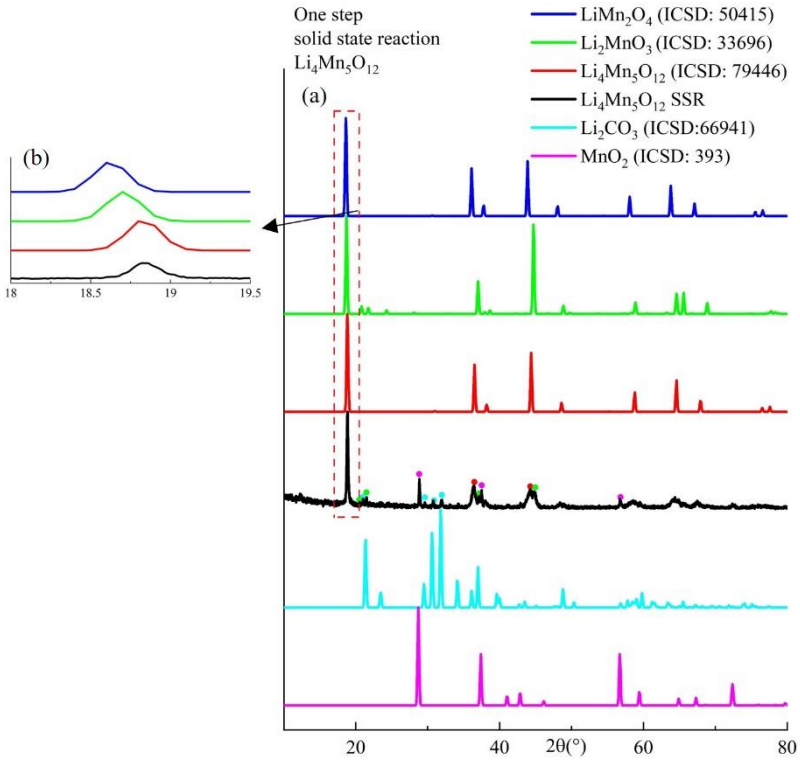

Figure 5.7 the XRD patterns of $Li_4Mn_5O_{12}$ by solid state reaction

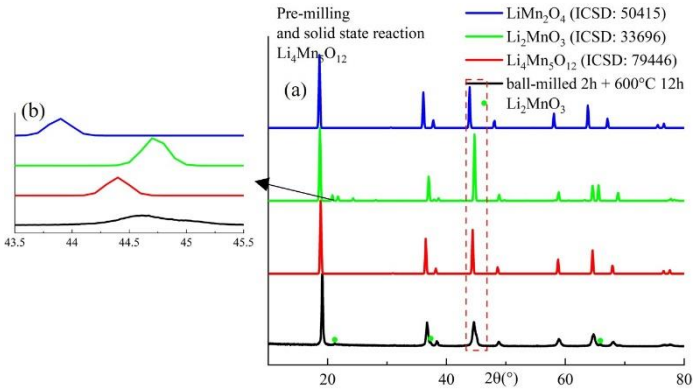

Figure 5.8 the XRD patterns of $Li_4Mn_5O_{12}$ by pre-milling and subsequent solid state reaction

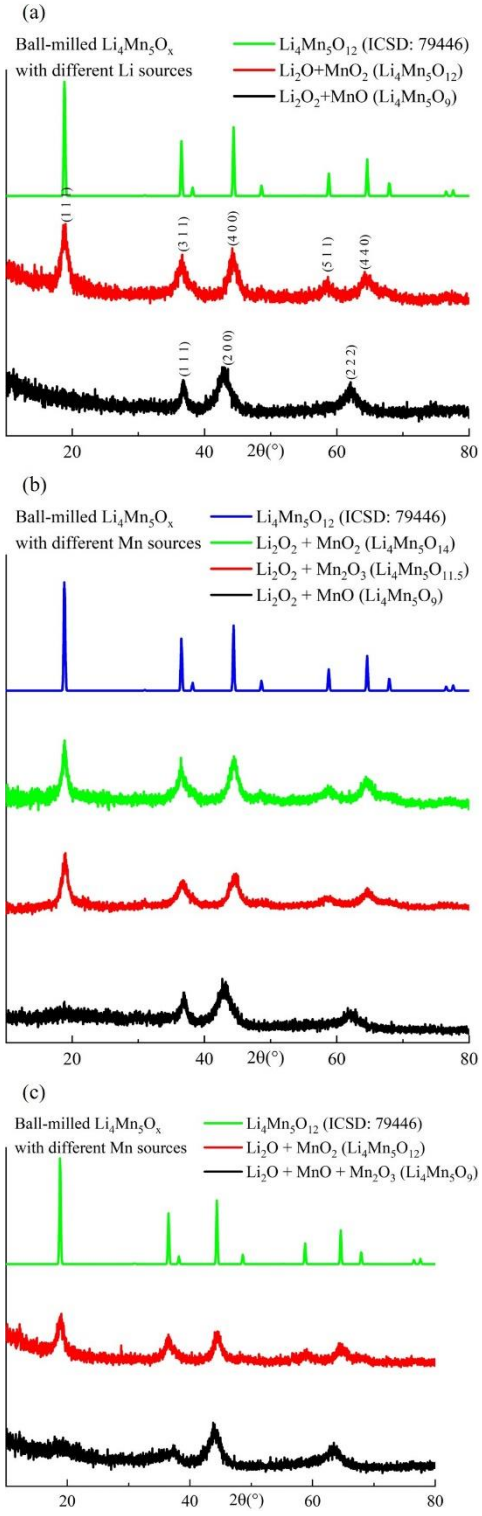

Figure 5.9 the XRD patterns of $Li_4Mn_5O_{12}$ produced by mechanosynthesis using (a) different Li sources, (b) Li_2O_2 with different Mn sources and (c) Li_2O with different Mn sources

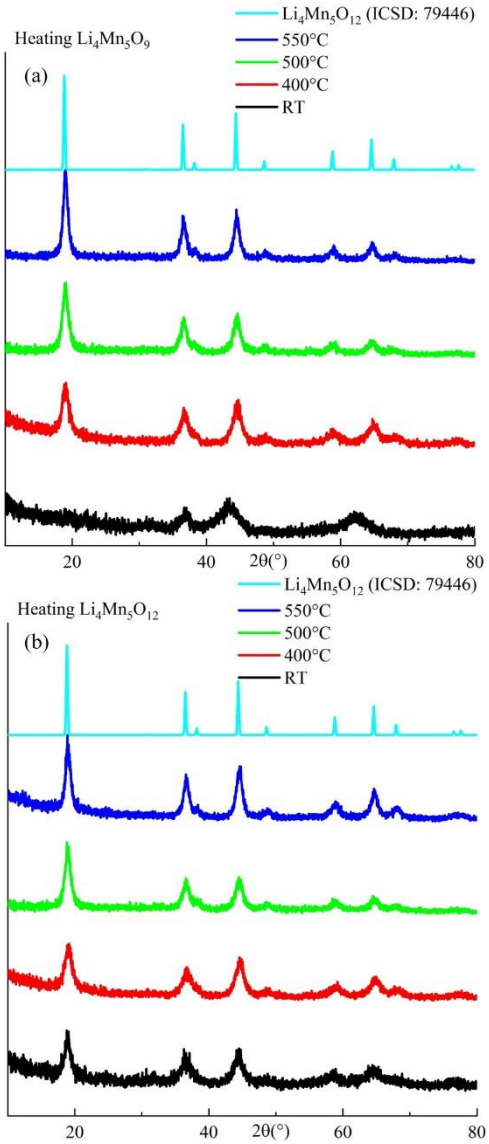

Figure 5.10 the XRD patterns of ball-milled (a) $Li_4Mn_5O_9$ and (b) $Li_4Mn_5O_{12}$ heated from room temperature to 550 °C.

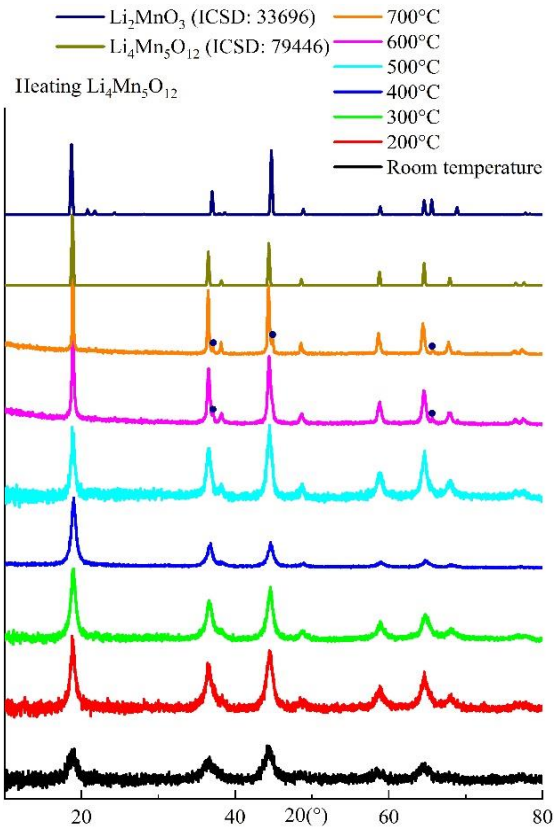

Figure 5.11 the XRD patterns of ball-milled $Li_4Mn_5O_{12}$ heated up to 700 °C

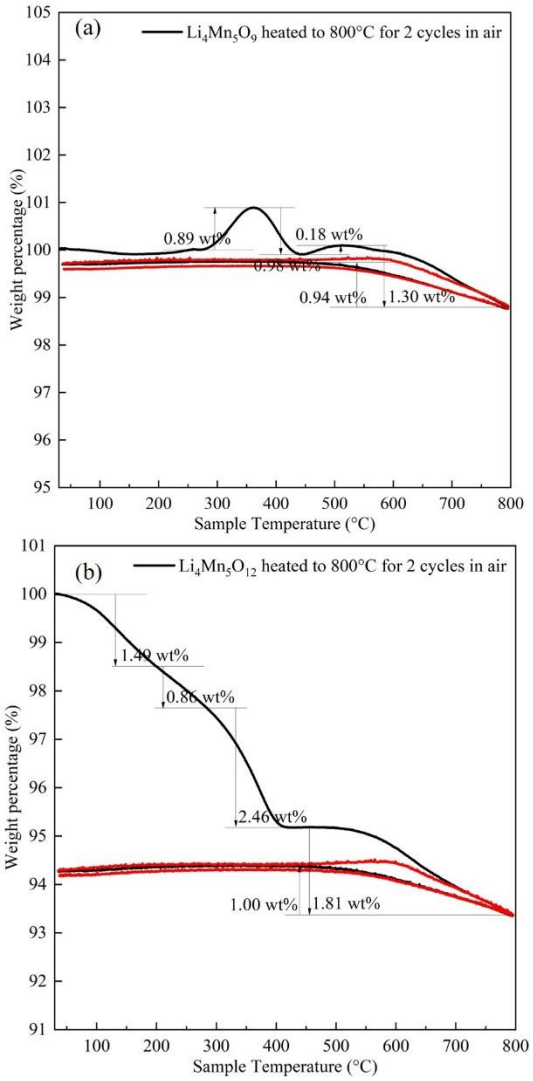

Figure 5.12 TG of (a) $Li_4Mn_5O_9$ and (b) $Li_4Mn_5O_{12}$ heated to 800 °C for 2 cycles

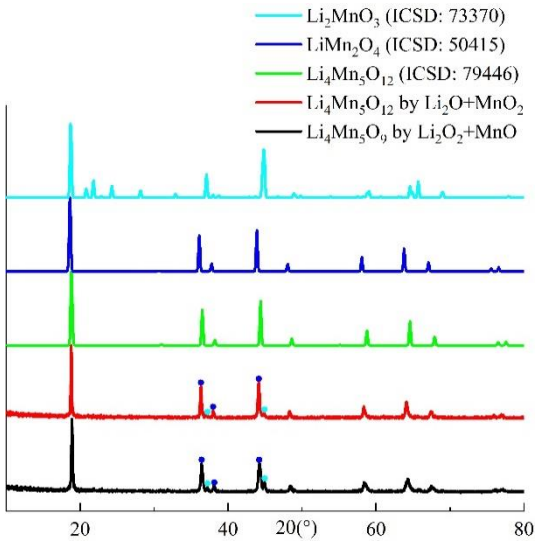

Figure 5.13 the XRD patterns of $Li_4Mn_5O_9$ and $Li_4Mn_5O_{12}$ after TG

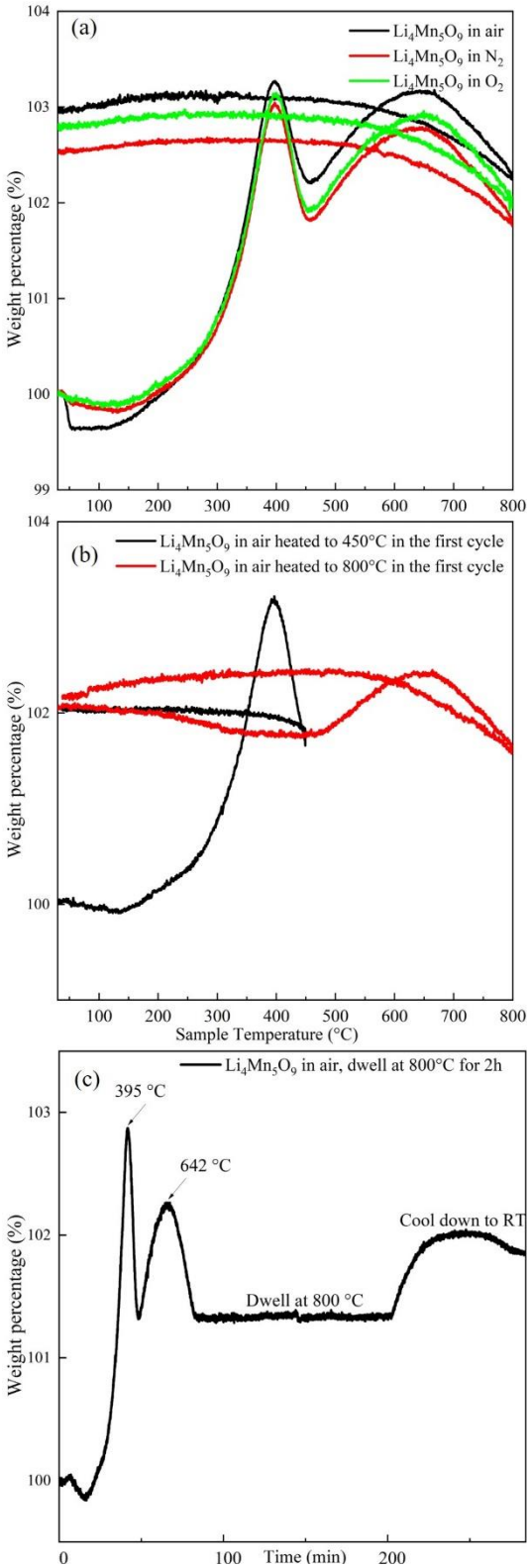

Figure 5.14 TG of $Li_4Mn_5O_9$ (a) under different atmospheres, (b) heated to 450 °C in the first cycle and 800 °C in the second cycle and (c) heated to 800 °C and dwelled for 2 h and cooled.

5.1.3 Lithium manganese oxides in a rock-salt and spinel join

The previous experiments on $Li_4Mn_5O_\delta$ show that when the cation: anion ratio is 1:1, the sample gives a disordered rock-salt phase. When the cation: anion ratio is 3:4, the sample gives a spinel phase. This provides an exploration space for the synthesis of either a rock-salt or spinel phase by mechanosynthesis, using different reactants to vary the oxygen content in final products.

The Li-Mn-O system is shown as a compositional triangle in Figure 5.15 (a). with a possible rock-salt join and spinel join (in b). Using different Mn-O reactants, the possible compositions produced using Li_2O are given in the orange area and using Li_2O_2 in the purple area. The dashed overlap triangle of the orange and purple area is enlarged in (b), where the target compounds are marked. Some preliminary results on XRD and TG are shown below.

5.1.3.1 Li-Mn-O compositions on the rock-salt join

Five compositions on the rock-salt join were prepared by mechanosynthesis, with general formula $Li_xMn_{1-x}O$ (x=0.667, 0.6, 0.5, 0.444, and 0.333). Li_2O was used as the Li source and Mn sources MnO, Mn_2O_3 and MnO_2 were chosen based on the Mn valence in the target compositions. The Mn valence in target compounds and the reactants used are summarised in Table 5.1. All samples formed a disordered rock-salt phase, Figure 5.16. The intensity of (111) peak increased with decrease of Li:Mn ratio. Among those, $LiMn_2O_3$ had a noisier background, which might be caused by high Mn content. It is also possible that some amorphous materials formed during milling. Due to the equipment shutdown and time limit, further study has not been done, such as lattice parameter, thermal stability and chemical analysis. Another Li reactant, Li_2O_2, can be tried for mechanosynthesis in the future.

TG analysis of these five samples is shown in Figure 5.17. The total weight changes for Li_2MnO_3, $Li_3Mn_2O_5$, $LiMnO_2$, $Li_4Mn_5O_9$ and $LiMn_2O_3$ were -6.09. -1.14, 1.36, 3.32 and 6.05 wt%, respectively. The first weight change stage occurred before 350 °C, which might be a combination of water loss, CO_2 release or absorption and O_2 release and especially O_2 absorption. An quick O_2 absorption, the amount of which increased with Mn/Li ratio, might have occurred at 300-350 °C, accompanied with phase change from disordered to ordered, which indicates thermal instability of those disordered rock-salt products. Another relatively slow weight gain occurred at ~500 °, which might be absorption of CO_2 and formation of Li-

$_2CO_3$, which then decomposed at a slightly higher temperature. Over 700 °C, all samples had a weight loss, possibly O_2 loss. Noticeably, except Li_2MnO_3, the water loss for other compounds was not obvious, which might be because they were not as hygroscopic as Li_2MnO_3. More study on TG is required, such as the species released and absorbed during heating, and XRD of samples after TG.

5.1.3.2 Li-Mn-O in a spinel join

Four compounds in the spinel join were prepared by mechanosynthesis, with general formula $Li_xMn_{3-x}O_4$ (x=0.333, 0.667, 1, and 1.333). The Mn valence in target compounds and the reactants are summarised in Table 5.2. No phase pure spinel was produced. Figure 5.18 (a) shows four samples' XRD patterns and (b) to (e) shows each XRD pattern analysis. For $Li_4Mn_5O_{12}$ (b), after 10 h milling, MnO_2 has not completely reacted. After 20 h milling, a spinel phase was formed but the intensity was low and peaks were broad, indicating an amorphous phase. After 30 h milling, Mn_2O_3 formed, which might be the product of decomposition of the spinel. For $LiMn_2O_4$ (c), after 10 h milling, a spinel with very broad peak and noisy background formed. For $Li_2Mn_7O_{12}$ (d), a spinel phase formed but with a second phase Mn_2O_3 after 10 h milling. For $LiMn_8O_{12}$ (e), after 10 h milling, a spinel phase formed, with second phases, Mn_2O_3 and MnO_2.

In summary, it is possible to use mechanosynthesis to produce a wide range of phase pure disordered rock-salt Li-Mn-O phases. For the spinel join, although a spinel phase was also possible to form, it tends to form an amorphous phase with unreacted manganese oxides.

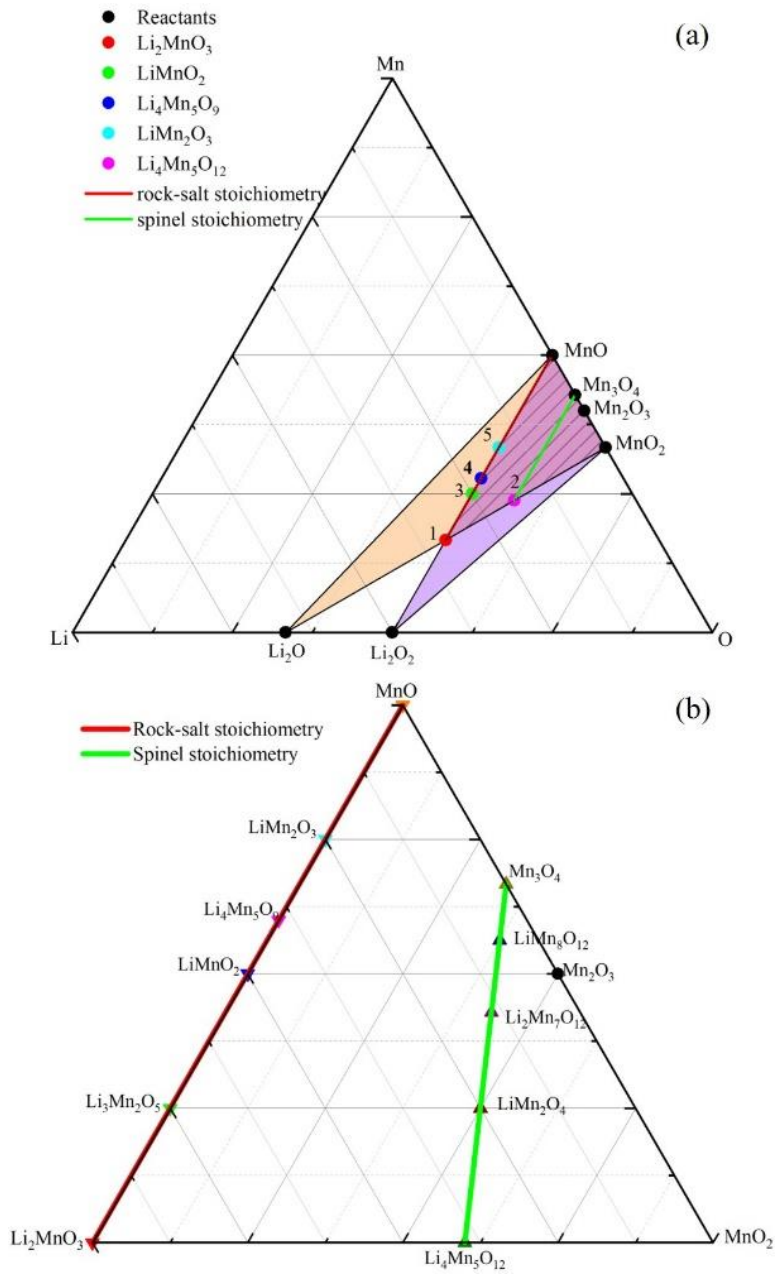

Figure 5.15 (a) the ternary diagram of Li-Mn-O, where the red line is a rock-salt join, and the green area is a spinel join. The orange area is possibly to be prepared using Li_2O and the purple area is using Li_2O_2. The overlapping area is enlarged in (b).

Table 5.1 The Mn valence and reactants of the compounds in the rock-salt join

The target compound	$Li_2Mn^{4+}O_3$	$Li_3Mn^{3+}Mn^{4+}O_5$	$LiMn^{3+}O_2$	$Li_4Mn^{2+}Mn_4{}^{3+}O_9$	$LiMn^{2+}Mn^{3+}O_3$
Reactants	Li_2O, MnO_2	Li_2O, Mn_2O_3, MnO_2	Li_2O, Mn_2O_3	Li_2O, MnO, Mn_2O_3	Li_2O, MnO, Mn_2O_3

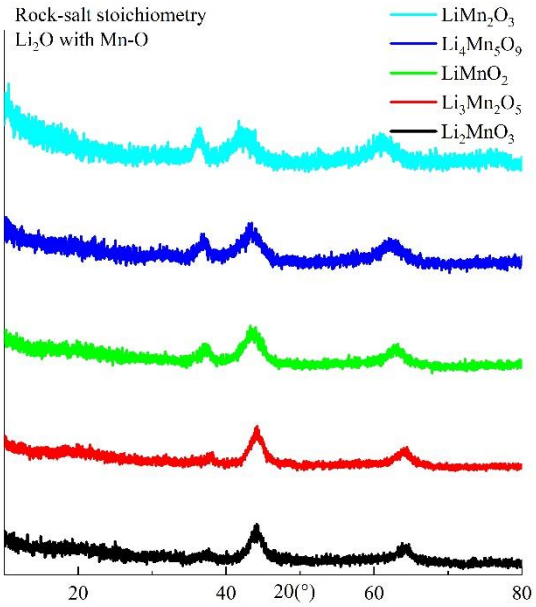

Figure 5.16 the XRD patterns of Li-Mn-O in a rock-salt join

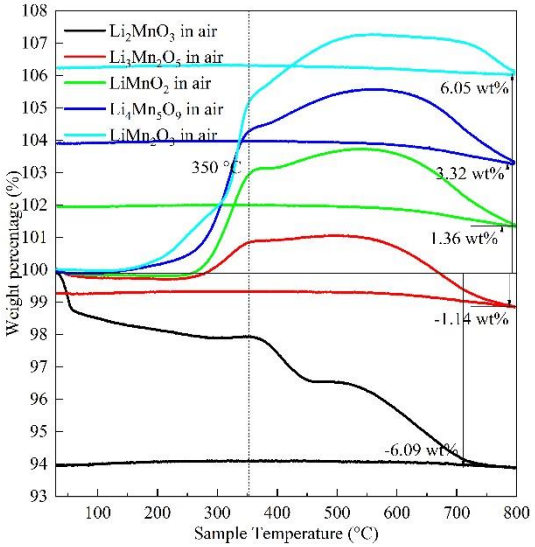

Figure 5.17 TG of Li-Mn-O in a rock-salt join

Table 5.2 The Mn valence and reactants of the compounds in the spinel join

The target compound	$Li_4Mn_5^{4+}O_{12}$	$LiMn^{3+}Mn^{4+}O_4$	$Li_2\ Mn_6^{3+}Mn^{4+}O_{12}$	$LiMn^{2+}Mn_7^{3+}O_{12}$
Reactants	Li_2O, MnO_2	Li_2O, Mn_2O_3, MnO_2	Li_2O, Mn_2O_3, MnO_2	Li_2O, MnO, Mn_2O_3

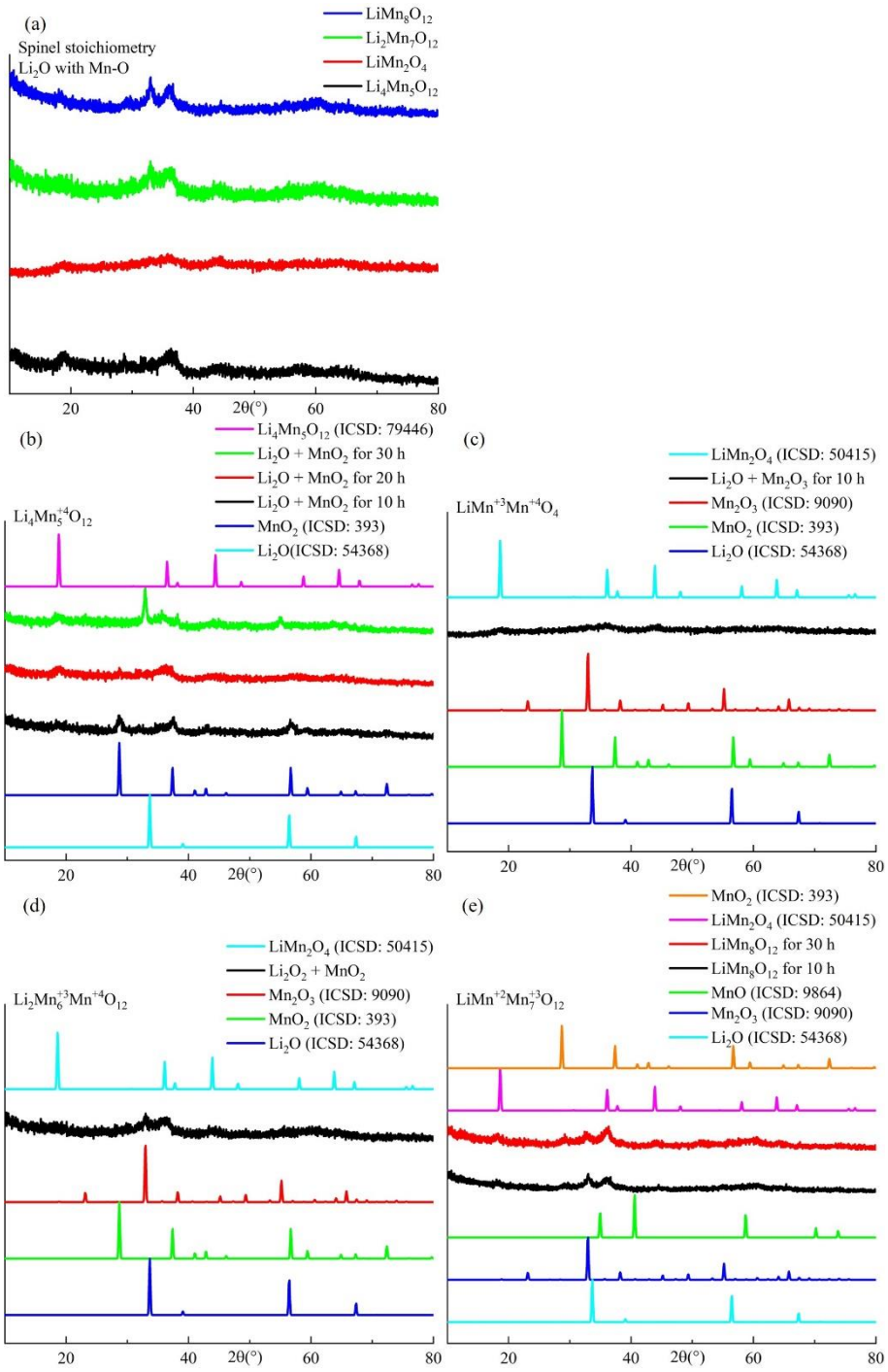

Figure 5.18 the XRD patterns of Li-Mn-O in a spinel join

5.2 Conclusions and future work

Using Li_2CO_3 and MnO_2 for solid state synthesis, $LiMn_2O_4$ was produced at 850 °C for 12 h in air, and $LiMnO_2$ was produced at 850 °C for 12 h in N_2. $Li_4Mn_5O_{12}$ were not successfully produced by one-step solid state reaction at 500 °C. To facilitate the reaction, pre-milling was introduced, and Li source, $LiOH \cdot H_2O$, was used. At 600 °C, one of the spinels, $LiMn_2O_4$ or $Li_4Mn_5O_{12}$, was produced but with a slight amount of Li_2MnO_3.

By mechanosynthesis, with a target composition $LiMn_2O_4$, spinel phase directly formed after ball-milling, but a second phase Mn_2O_3 appeared with prolonged time. For $LiMnO_2$, disordered rock-salt phase formed after short-time milling. An ordered spinel phase formed with longer milling time, probably $Li_4Mn_5O_{12}$. $Li_4Mn_5O_\delta$, ($9 \leq \delta \leq 14$), was produced using different Li and Mn sources. When $\delta=9$, with a cation:anion ratio of 1:1, disordered rock-salt phase was produced. When $11.5 \leq \delta \leq 14$, with a cation:anion ratio of 3:4 or nearly 3:4, spinel phase was produced. When heated to 400 °C, the disordered sample transformed to spinel phase, corresponding to $Li_4Mn_5O_{12}$, with an oxygen absorption at ~390 °C. All samples started to decompose ≥ 700 °C to Li_2MnO_3 and $LiMn_2O_4$, accompanied by oxygen loss. Future work on TG-MS can confirm those oxygen behaviours.

Following the study on $Li_4Mn_5O_\delta$, two series of Li-Mn-O compositions were produced with a cation:anion ratio of 1:1 and 3:4. A wide range of single-phase disordered rock-salt compositions, with the cation:anion ratio of 1:1, were successfully produced. The intensity of (111) peak increased with decrease of Li:Mn ratio. Samples with lower Li:Mn ratio were less hygroscopic. Future work should aim on the lattice parameter, chemical analysis and TG-MS. However, compositions, with the cation:anion ratio of 3:4, gave an amorphous product with Mn_2O_3 as a second phase.

Chapter 6 Li-TM-O

6.1 Results

6.1.1 Li-Nb-O-F: pure and doped Li_3NbO_4

The quaternary system Li-Nb-O-F is shown as a compositional pyramid in Figure 6.1 (a) with a ternary section Li_2O-Nb_2O_5-LiF of the quaternary system in Figure 6.1 (b).

6.1.1.1 Synthesis of F-doped and pure Li_3NbO_4 by solid state reaction

Single phase Li_3NbO_4 was successfully produced using reactants Li_2CO_3 and Nb_2O_5 by solid state reaction at 900 °C for 24 h. The XRD results are shown in Figure 6.2.

Possible mechanisms to dope Li_3NbO_4 with F were considered. Since oxygen and fluorine have different ionic charges, any doping mechanism would require additional changes to achieve charge compensation. It is assumed that niobium retains its pentavalent state for synthesis reactions in air and therefore, a combination of ionic substitution, vacancy and interstitial creation were considered as possible components of the doping mechanisms. Substitution of O by F with Li vacancy creation was considered with the general formula $Li_{3-x}NbO_{4-x}F_x$. When x=0.1 and 0.2, Li_3NbO_4 formed with $LiNbO_3$ as a second phase. No unreacted LiF was observed in the products. The solid solution limit of $Li_{3-x}NbO_{4-x}F_x$ produced by solid state reaction was therefore $x < 0.1$. It was considered unlikely that charge compensation could be achieved by creation of F interstitials and therefore, mechanosynthesis was attempted as an alternative, low temperature synthesis route.

6.1.1.2 Synthesis of Li_3NbO_4 and Li_2NbO_3F by mechanosynthesis

Li_3NbO_4 with a disordered rock-salt structure was produced using Li_2O_2 and Nb_2O_5 by mechanosynthesis at 350 rpm for 20 h. Steel jars were always used as the milling media in Chapter 6, except in 6.1.2.4, where TiO_2 were milled by steel and WC jars to compare the contaminations caused by different milling media. The XRD result is shown in Figure 6.3. Heat treatment of the disordered sample from room temperature to 800 ℃ gave the results shown in Figure 6.4. Disordered Li_3NbO_4 was stable until 400 ℃. Above 400 ℃, it decomposed to ordered Li_3NbO_4 and $LiNbO_3$, indicating that Li loss may occur at some stage, either during synthesis or subsequent decomposition. This was an unexpected result since Li_3NbO_4 can be prepared by solid state reaction at 800 ℃ with little evidence of oxygen loss. Further work to understand this result is required.

Mechanosynthesis of compositions $Li_{3-x}NbO_{4-x}F_x$ was tried using Li_2O_2, Nb_2O_5 and LiF. When x=1, Li_2NbO_3F did not form a disordered rock-salt phase, Figure 6.5. Instead, $LiNbO_3$ formed as the main product with a small amount of LiF. This result is further discussed in section 6.2.

6.1.1.3 Synthesis of Li_3NbO_4-LiF solid solutions with rock salt stoichiometry

Possible formation of a solid solution on the join Li_3NbO_4-LiF was considered, in which the overall cation:anion ratio was 1:1. Compositions with general formula $Li_3NbO_4 \cdot xLiF$: x=1, 2, 3 were prepared. Results are shown in Figure 6.6. All products had a disordered rock-salt structure and the (111) peak intensity decreased with increasing x. Results of heat treatment from room temperature to 800 ℃ are shown in Figure 6.7. No phase change occurred during heating but XRD peaks became sharper, indicating grain growth. XRF results on the F content of samples after heat treatment are shown in Figure 6.8 and Table 6.1. There was no evidence of fluorine loss for temperatures up to 800 ℃. It appears, therefore, that a thermodynamically stable rock salt solid solution with disorder on both cation and anion sub-lattices forms on the join Li_3NbO_4-LiF.

6.1.1.4 TGA of disordered rock salt Li-Nb-O materials

The TG profiles of Li_3NbO_4 and $Li_3NbO_4 \cdot xLiF$ are shown in Figure 6.9 (a). Generally, their weight loss profiles are similar with three main weight loss stages during heating but the amount of weight loss was very composition-dependent and decreased with increasing F content. The first weight loss was from room temperature to about 250 ℃ and may be due to water loss. From 280℃ to 580 ℃, a second weight loss occurred which may relate to CO_2 release and/or tightly bonded water. Above about 700 ℃, a continual gradual weight loss occurred, which may be another reaction that releases CO_2 or oxygen loss. None of the samples regained any weight during cooling.

A possible additional contribution to the weight loss profiles is that Li loss may occur during TG. The XRD result of undoped Li_3NbO_4 after TG, Figure 6.9 (b), showed the formation of a second phase $LiNbO_3$, which is evidence for significant lithium loss accompanied with transformation of the disordered rock salt structure to ordered Li_3NbO_4. It appears from the heat treatment results, Figure 6.4, that the thermal stability of undoped Li_3NbO_4 and doped materials are different. Li_3NbO_4 undergoes an ordering transformation and/or decomposition around 400 ℃, Figure 6.4, whereas the disordered rock-salt structure of the doped materials is stable to at least 800 ℃, Figure 6.7.

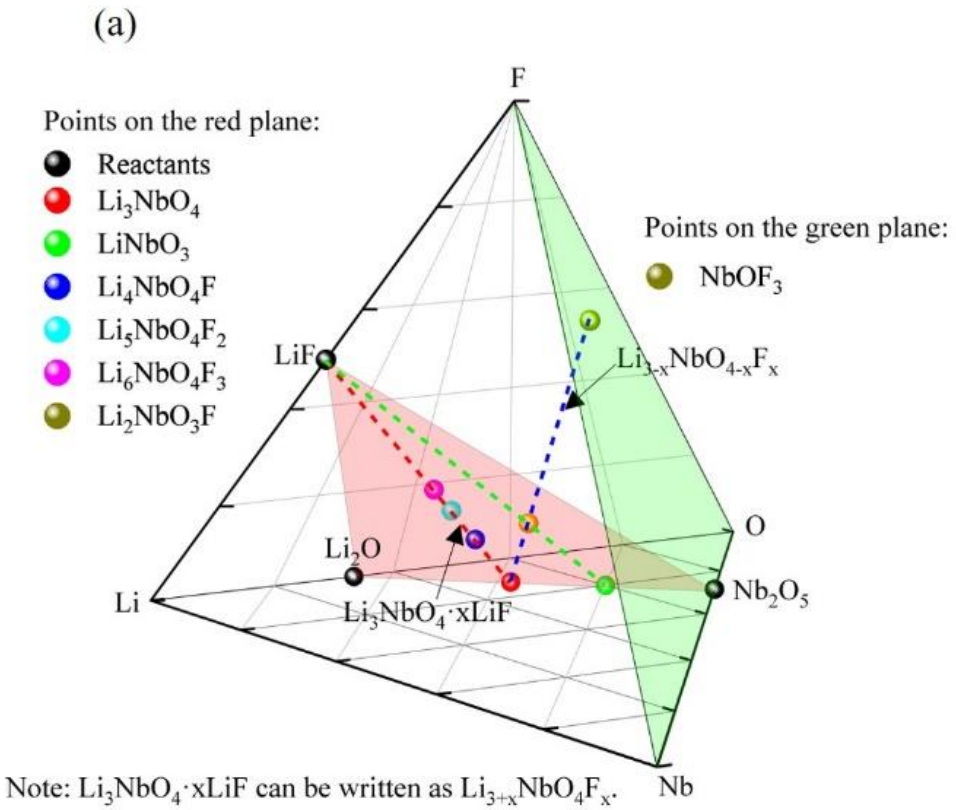

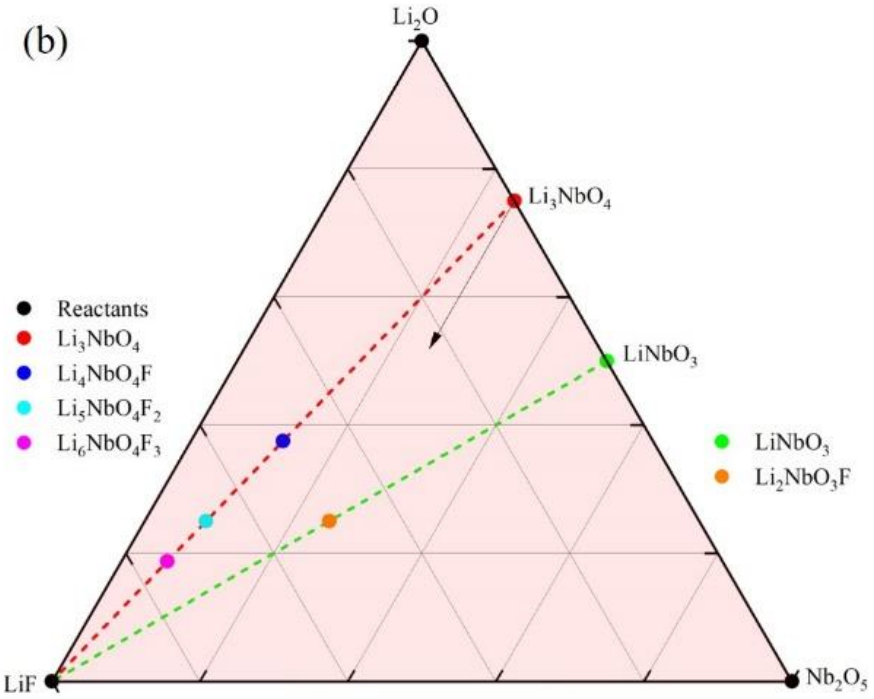

Figure 6.1 the quaternary system Li-Nb-O-F and a ternary section of Li_2O-Nb_2O_5-LiF

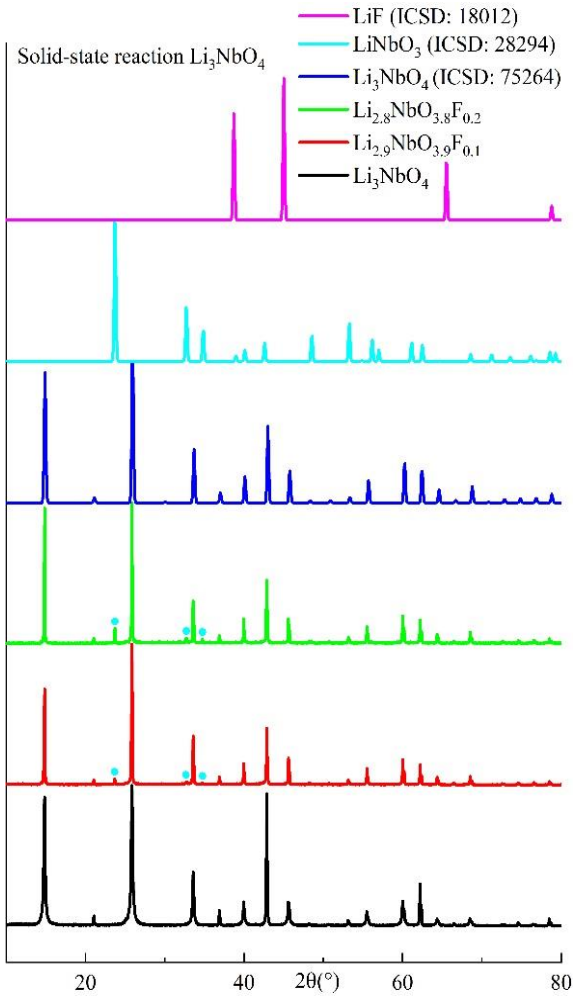

Figure 6.2 the XRD patterns of F doped and pure Li_3NbO_4 produced by solid state

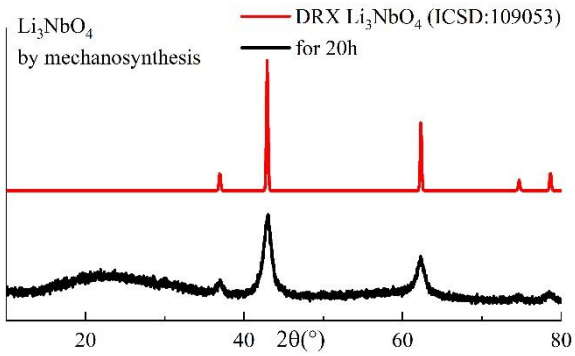

Figure 6.3 the XRD patterns of Li_3NbO_4 produced by mechanosynthesis

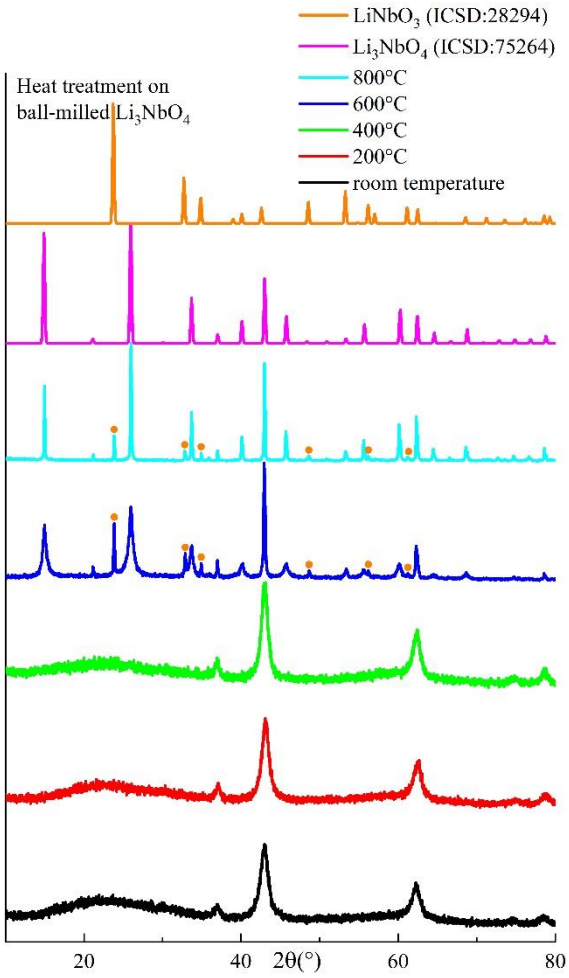

Figure 6.4 the XRD patterns the heat treatment on disordered Li_3NbO_4 from room temperature to 800 °C

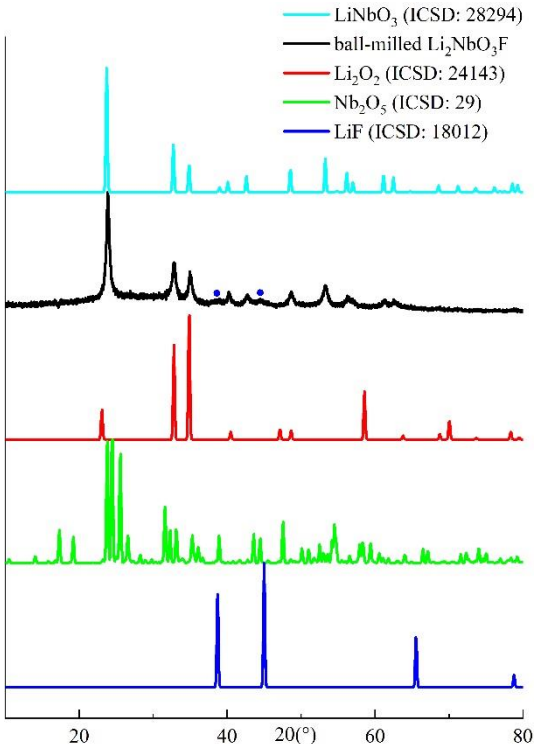

Figure 6.5 the XRD patterns of Li_2NbO_3F produced by mechanosynthesis

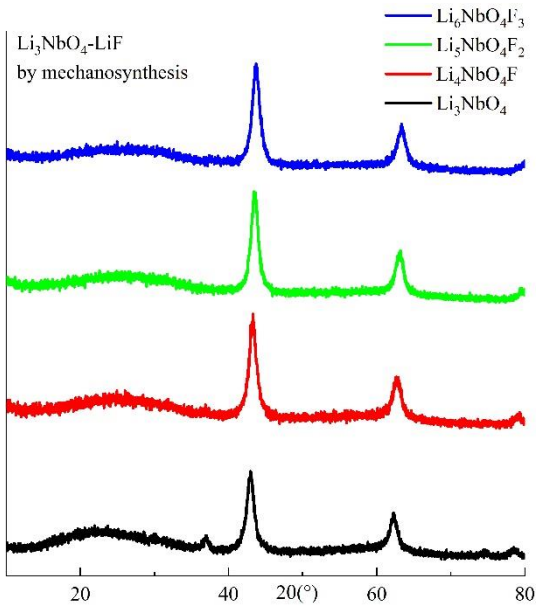

Figure 6.6 the XRD patterns of Li_3NbO_4-LiF solid solution of produced by mechanosynthesis

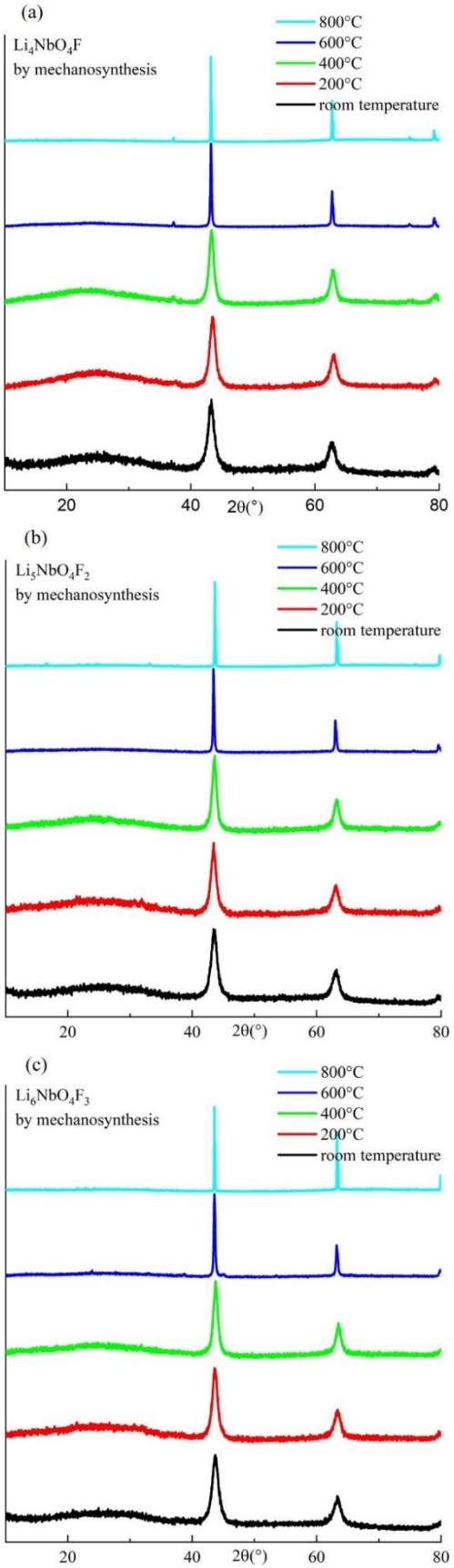

Figure 6.7 the XRD patterns of Li_3NbO_4-LiF solid solution of with subsequent heat treatment

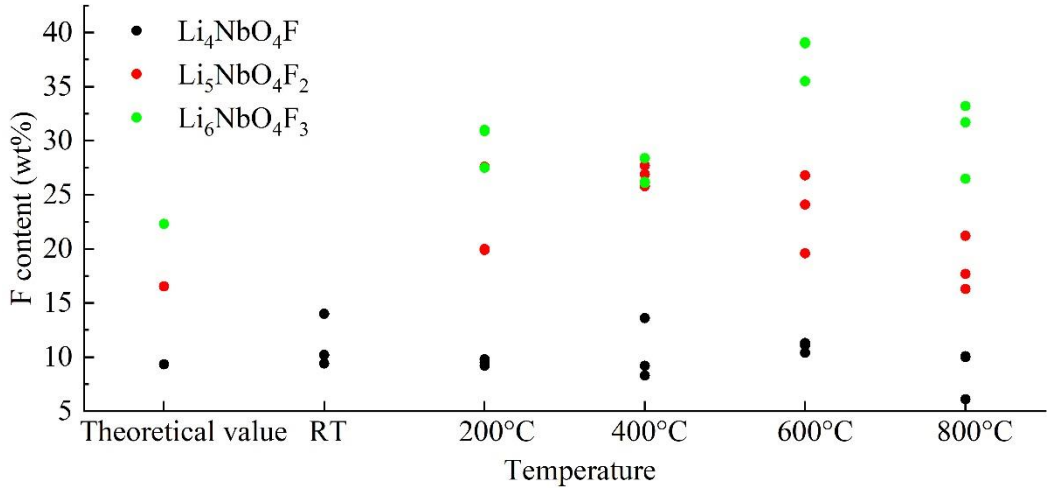

Figure 6.8 XRF of F contents in Li_3NbO_4-LiF solid solution

Table 6.1 XRF of Li_3NbO_4-LiF solid solution (units: wt%)

Li_4NbO_4F	**Theo**	**RT**			**200 °C**			**400 °C**			**600 °C**			**800 °C**		
Nb	45.6	44.6	54.1	39.6	46.0	46.2	47.4	57.7	58.2	49.3	42.0	51.3	48.6	50.9	45.3	48.0
O	31.4	43.2	34.3	45.1	42.8	42.2	41.3	32.0	30.4	35.2	45.7	35.4	38.5	34.6	44.1	37.6
F	9.33	10.2	9.4	14.0	9.2	9.8	9.5	8.3	9.2	13.6	10.4	11.3	11.1	10.0	6.1	10.0
Fe	0	1.5	1.4	1.0	1.3	1.3	1.3	1.4	1.6	1.3	1.2	1.5	1.3	3.4	3.3	3.4
$Li_5NbO_4F_2$		**RT**			**200 °C**			**400 °C**			**600 °C**			**800°C**		
Nb	40.5	-	-	-	44.2	34.1	53.0	34.5	38.1	37.5	49.1	49.9	40.4	42.9	36.4	47.4
O	27.9	-	-	-	34.2	37.6	25.4	38.2	33.7	33.7	25.1	21.6	38.3	37.7	44.4	28.8
F	16.5	-	-	-	20.0	27.6	19.9	25.8	26.9	27.2	24.1	26.8	19.6	16.3	17.1	21.2
Fe	0	-	-	-	1.5	1.0	1.6	1.1	1.2	1.4	1.6	1.7	1.5	2.5	1.8	2.5
$Li_6NbO_4F_3$		**RT**			**200 °C**			**400 °C**			**600°C**			**800°C**		
Nb	36.4	-	-	-	37.3	34.7	31.3	35.8	69.3	36.1	33.9	29.6	34.9	38.1	40.0	34.3
O	25	-	-	-	30.3	36.4	36.4	36.9		36.3	29.2	30.3	24.3	34.1	26.8	31.3
F	22.3	-	-	-	31.0	27.5	30.9	26.2	28.4	26.1	35.5	39.1	39.0	26.5	31.7	33.2
Fe	0	-	-	-	1.2	1.2	1.2	1.0	2.0	1.2	1.2	0.9	1.2	1.2	1.4	1.1

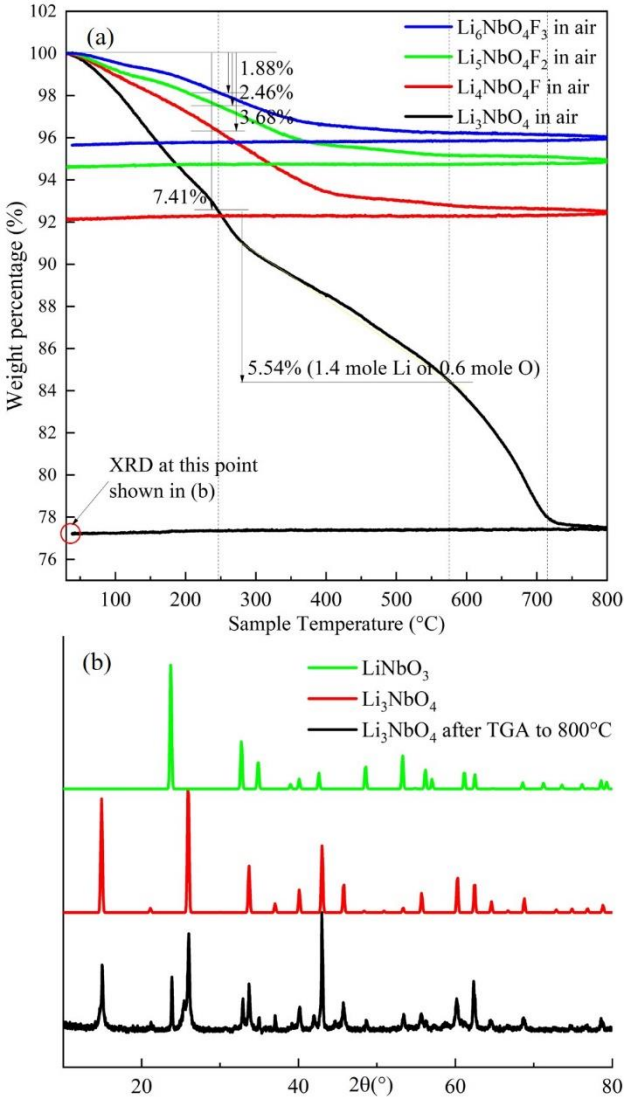

Figure 6.9 (a) TG of Li_3NbO_4 and F doped Li_3NbO_4 produced by mechanosynthesis in air; and (b) XRD of Li_3NbO_4 after TG

6.1.2 Li-Ti-O

The quaternary system Li-Ti-O-F is shown as a compositional pyramid in Figure 6.10 (a) with a ternary section, Li_2O-TiO_2-LiF in Figure 6.10 (b) and the ternary face, Li-Ti-O in Figure 6.10 (c).

6.1.2.1 Synthesis of $LiTiO_2$ with different reactants by mechanosynthesis

Preparation of $LiTiO_2$ was attempted by mechanosynthesis of three samples using different reactants: A: Li_2O_2 and TiO; B: Li_2O and Ti_2O_3; C: Li_2O_2 and TiO_2; results are shown in Figure 6.11. After 20 h milling, samples A and B formed a disordered rock-salt phase. For sample C, after 20 h milling, a disordered rock salt phase formed but a small amount of unreacted TiO_2 remained. After 60 h milling, a disordered rock salt phase formed with very broad peaks, but its composition was uncertain due to extensive contamination from the milling media, such as spinel Li-Ti-Fe-O.

Results of heating A, B, and C from room temperature to 800 ℃ are shown in Figure 6.12. All samples transformed from a disordered rock salt structure to a spinel structure with broad XRD lines at 400 ℃. At 600 and 800 ℃, the lines became narrow indicating grain growth of the spinel structure and the patterns corresponded approximately to that of $Li_4Ti_5O_{12}$, but also to an Fe-containing spinel, consistent with Fe contamination from the milling media.

The interpretation of these results is that a disordered rock salt phase forms initially as the main phase by mechanosynthesis of all three samples. Their compositions are not known; they could range from $LiTiO_2$ containing Ti^{3+}, especially for A and B, to Li_2TiO_3 containing Ti^{4+} for C, together with some Fe^{2+} or Fe^{3+} arising from contamination. On heating in air at 400 ℃, samples picked up oxygen to convert to a spinel stoichiometry, driven by the oxidation of Ti^{3+} to Ti^{4+}. Further discussion on suitable reactants for $LiTiO_2$ is continued in section 6.2.

6.1.2.2 Synthesis of Li_2TiO_3 and Li_2TiO_2F

Li_2TiO_3 with a disordered rock structure was prepared by mechanosynthesis using Li_2O_2 anTiO_2, Figure 6.13 (a). After 20 h milling, a small amount of TiO_2 remained but after 40 h,

reaction appeared to be complete. XRD results of heating disordered Li_2TiO_3 from room temperature to 800 ℃ are shown in Figure 6.13 (b). A broad superstructure peak appeared at 400 ℃ and ordered Li_2TiO_3 at 600 ℃.

Mechanosynthesis of F-doped Li_2TiO_3 with stoichiometry $Li_2Ti_{1-x}^{4+}Ti_x^{3+}O_{3-x}F_x$, x=1 ($Li_2Ti^{3+}O_2F$) was attempted using two groups of reactants: D: Li_2O_2, TiO_2 and LiF; E: Li_2O, Ti_2O_3 and LiF. Results, Figure 6.14, show that both samples formed a disordered rock salt phase after 40 h milling but with a small amount of unreacted titanium oxide that remained with longer milling time.

6.1.2.3 Synthesis of solid solution Li_2TiO_3·xLiF

The possible formation of solid solution on the join Li_2TiO_3-LiF by mechanosynthesis was attempted. Compositions Li_2TiO_3·xLiF (can be written as $Li_{2+x}TiO_3F_x$) were studied with x=1 and 2 using Li_2O, TiO_2 and LiF reactants. For both compositions, a disordered rock-salt phase formed after 40 h milling which was stable up to 800 ℃, Figure 6.15.

6.1.2.4 Synthesis of $Li_4Ti_5O_9$ and $Li_4Ti_5O_{12}$ and ball-milling on TiO_2

Different lithium sources and titanium sources were used to produce $Li_4Ti_5O_\delta$ by mechanosynthesis. The rock-salt stoichiometry $Li_4Ti_5O_9$ was milled using Li_2O, TiO and Ti_2O_3. The spinel stoichiometry $Li_4Ti_5O_{12}$ was milled using Li_2O_2 and TiO_2. XRD results are shown in Figure 6.16. Using Li_2O, TiO and Ti_2O_3, a disordered rock-salt phase formed after 20 h milling. But it is assumed to contain a second phase due to the unusual shape of the broad main peak at ~43 degree. With longer milling time, an unidentified phase labelled T appeared. Using Li_2O_2 and TiO_2, a disordered rock-salt phase formed, but some TiO_2 retained unreacted. With longer milling time, phase T appeared.

This phase T may be produced due to the abrasion between sample materials and milling media. Therefore, to study abrasive effect on titanium system, TiO_2 was ball-milled in steel and WC jars separately, Figure 6.17. After 20 h milling in a steel jar, the product of ball-milled TiO_2 matched phase T. XRF on ball-milled TiO_2 showed this sample contained 27-40 wt% of Fe contamination. After 20 h milling in a WC jar, the product of ball-milled TiO_2 remained as the rutile phase but a second phase WC appeared. XRF on the WC jar-milled sample is required.

6.1.2.5 TGA of solid solution $LiTiO_2$, Li_2TiO_3, Li_2TiO_3·xLiF, and Li_2TiO_2F

Figure 6.18 (a) shows the TG profiles of $LiTiO_2$ and Li_2TiO_3. The total weight loss of $LiTiO_2$ was only 4% but that of Li_2TiO_3 was 15%. There were four weight loss stages during heating. The first one was before 145 ℃, related to water. The water loss in $LiTiO_2$ was only about 1% but in Li_2TiO_3 was about 6%. From 145 ℃ to 355 ℃, the second weight loss occurred, which might be a mixture of water loss and CO_2 release. From 355 ℃ to 600 ℃, $LiTiO_2$ did not lose much weight. It is possible that $LiTiO_2$ had little CO_2 absorption. Most weight loss before 355 ℃ was free water and combined water, with different loss rates. For Li_2TiO_3, a 4% of weight loss occurred in the same process, which may be CO_2 release. They both had a small amount of weight loss after 700 ℃, which may be oxygen loss.

Figure 6.18 (b) is a comparison of TG profiles of Li_2TiO_3 and Li_2TiO_2F. Three weight loss stages were: first, a water loss from room temperature to 140 ℃; second, possibly a mixture of water loss and CO_2 release from 140 ℃ to 550 ℃; and third, a small continual oxygen loss at high temperatures. Generally, they had similar profiles but Li_2TiO_3 lost about 15% weight and Li_2TiO_2F only lost 10%.

Figure 6.18(c) is the TG profiles of solid solution Li_2TiO_3·xLiF. With LiF, doped samples only had less than 4% of weight loss, while the undoped Li_2TiO_3 lost 15%. The weight loss processes can be divided into three stages: first, before 175 ℃, a water loss occurred, 5% for Li_2TiO_3 and less than 0.4% for F doped ones; second, a mixture of water and CO_2 loss, from 175 ℃ to 635 ℃, 10% for Li_2TiO_3 and less than 1% for F doped ones; and third, a continual gradual oxygen loss occurred, about 0.3%, for three samples.

These TG results show a clear variation on the hygroscopicity of different samples; the most hygroscopic appears to be disordered Li_2TiO_3 and the least are similarly structured, disordered rock salt materials with the highest F content. Similar results have been seen in F doped Li_2MnO_3 (Chapter 4) and F doped Li_3NbO_4 (section 6.1.1.4). These TG results will be summarised and discussed in section 6.2.

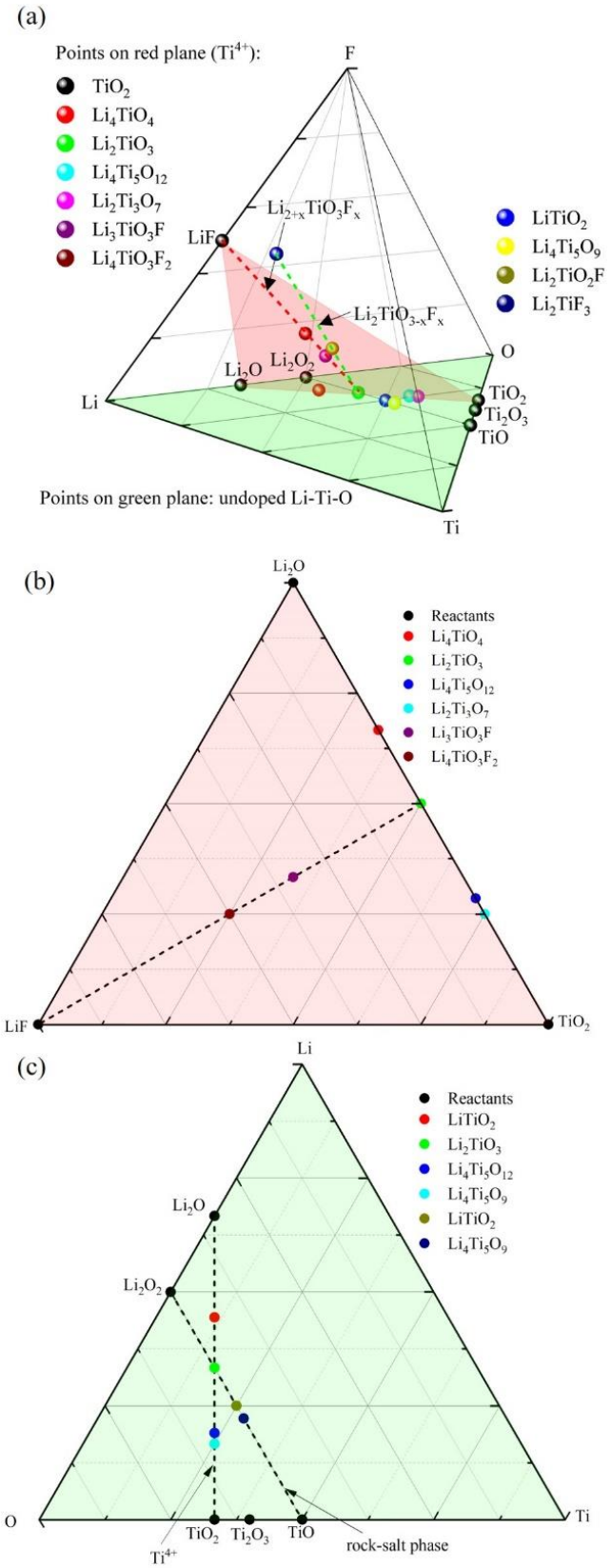

Figure 6.10 The quaternary system Li-Ti-O-F and a ternary section of Li_2O-TiO_2-LiF and Li-Ti-O

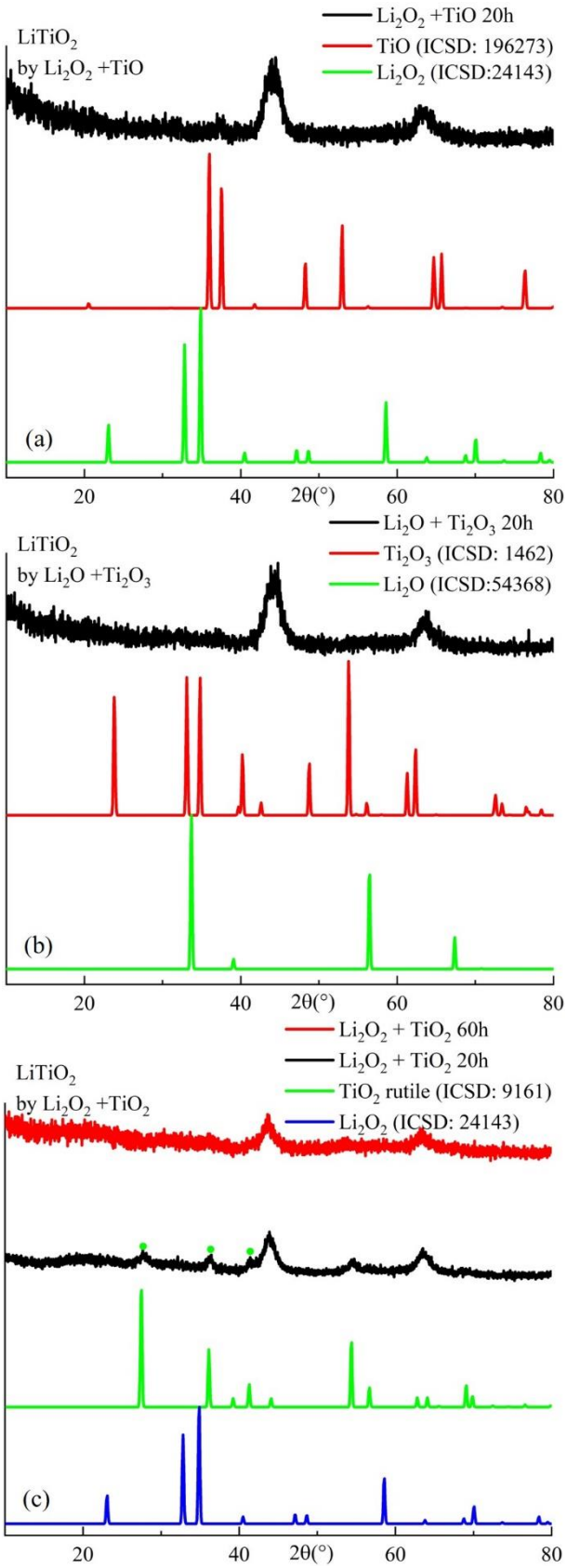

Figure 6.11 the XRD patterns of $LiTiO_2$, starting with different reactants, produced by mechanosynthesis

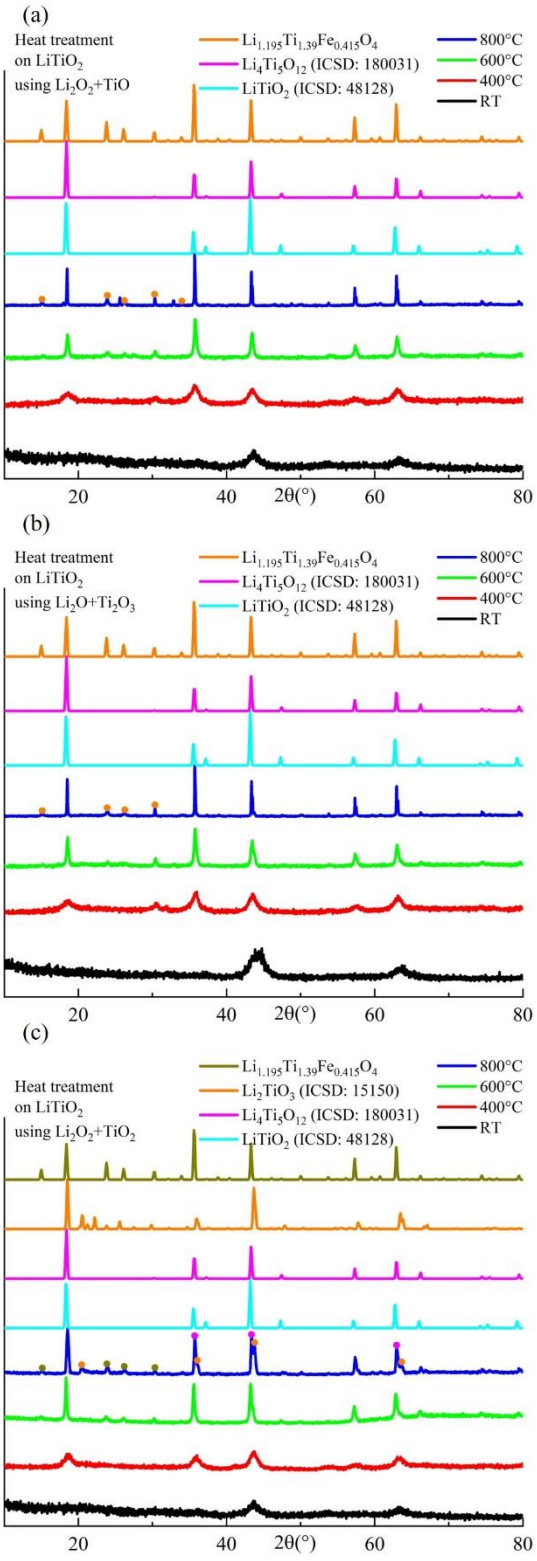

Figure 6.12 the XRD patterns of disordered $LiTiO_2$ starting with different reactants, with heat treatment from room temperature to 800 °C

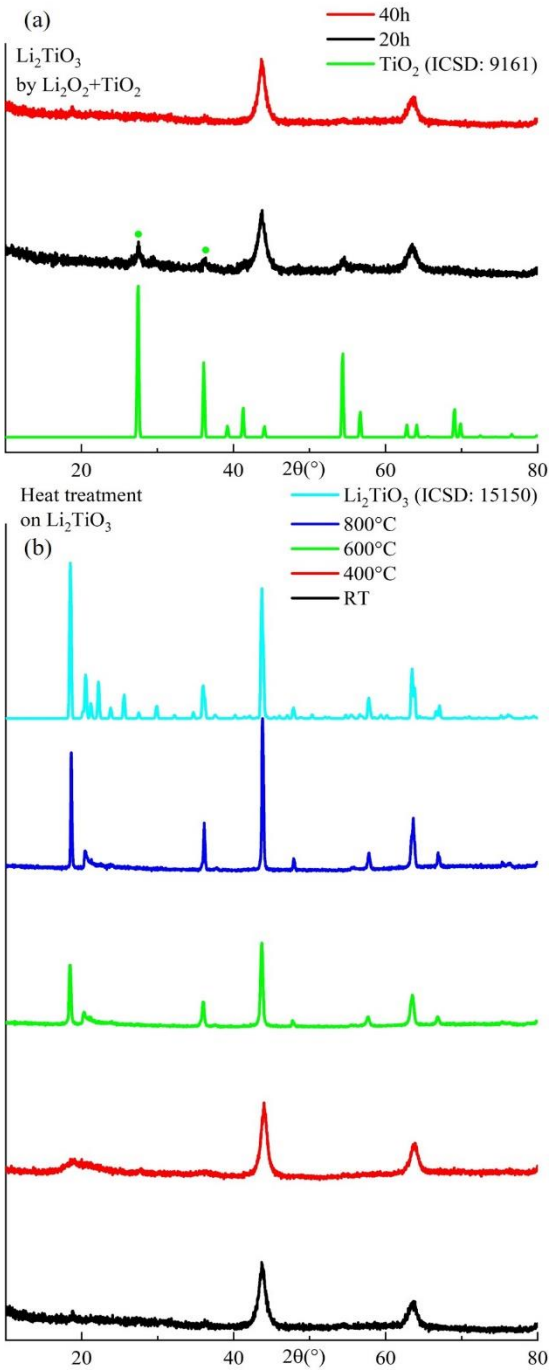

Figure 6.13 the XRD patterns of Li_2TiO_3 produced by mechanosynthesis and then heated to 800 °C

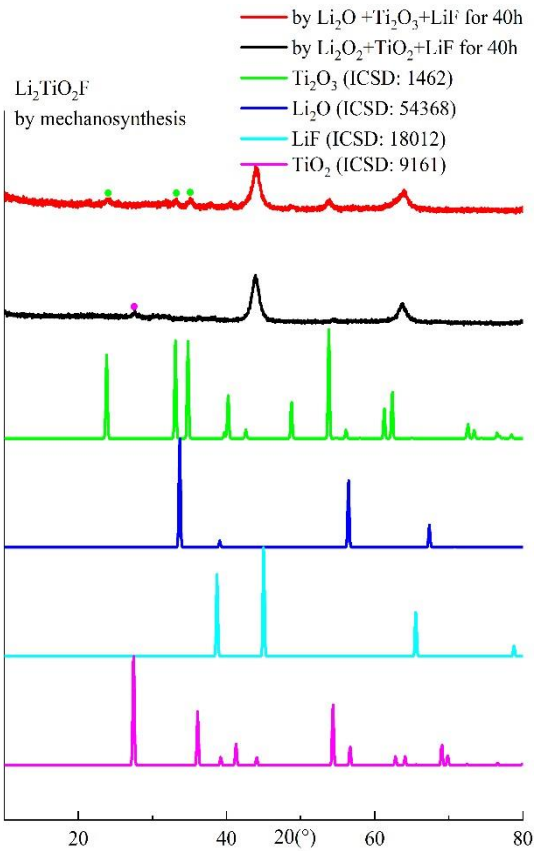

Figure 6.14 the XRD patterns of the XRD patterns of Li_2TiO_2F produced by mechanosynthesis

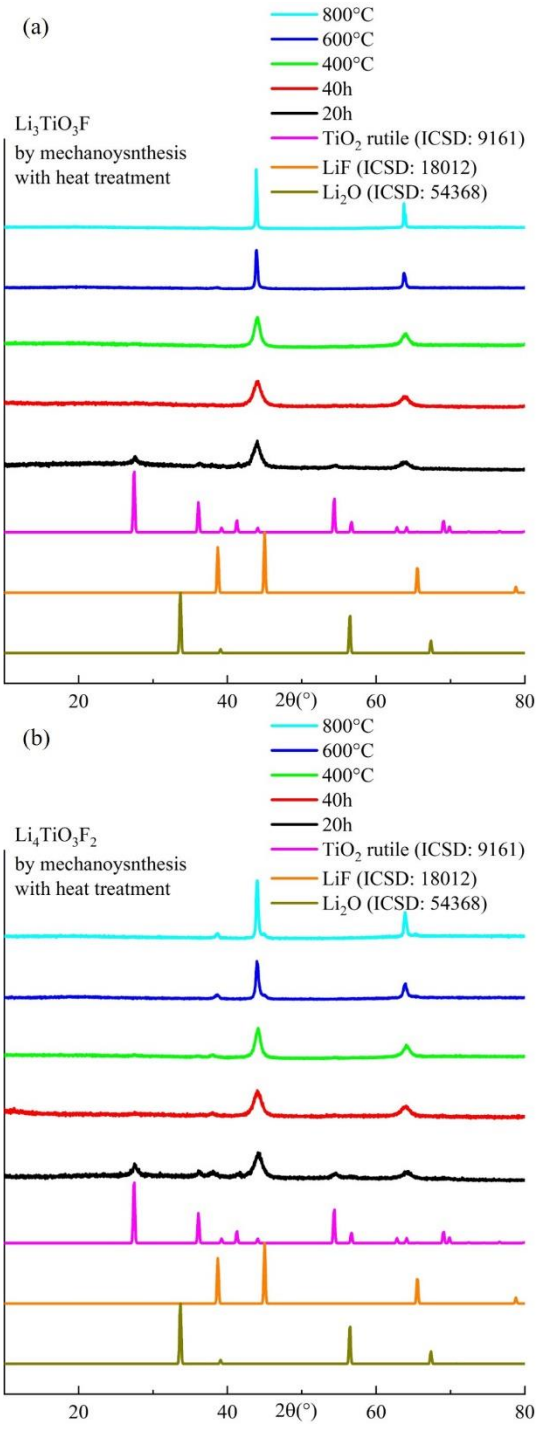

Figure 6.15 the XRD patterns of solid solution Li_2TiO_3-LiF produced by mechanosynthesis and subsequent heat treatment

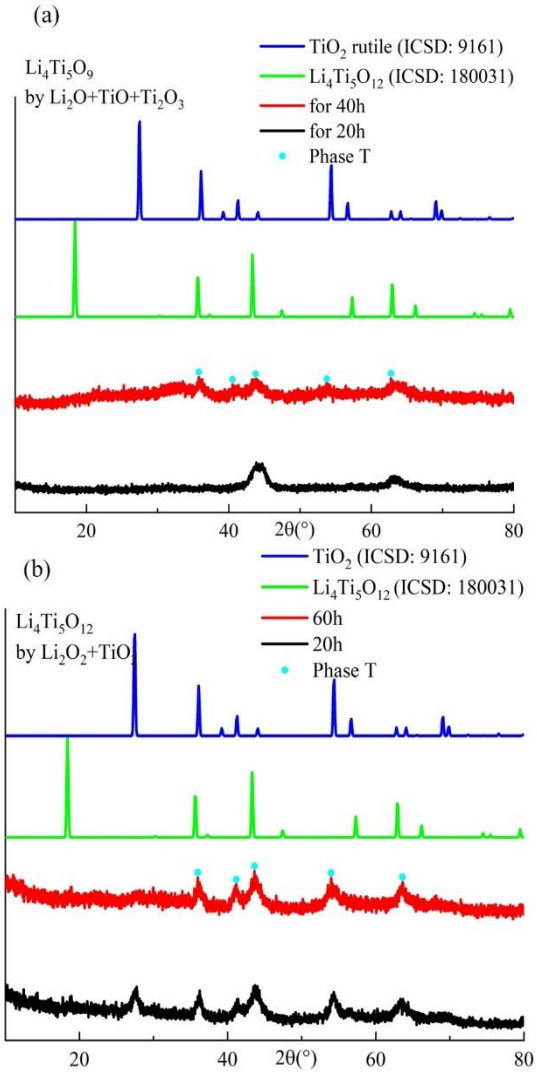

Figure 6.16 the XRD patterns of Li-Ti-O produced by mechanosynthesis

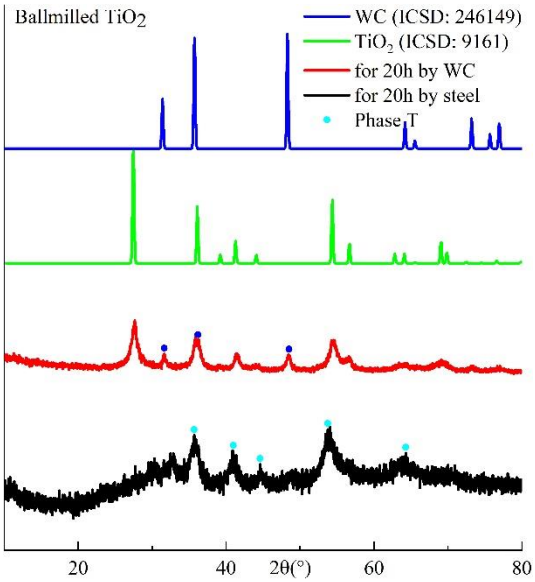

Figure 6.17 the XRD patterns of ball-milled TiO_2 by steel and WC jars

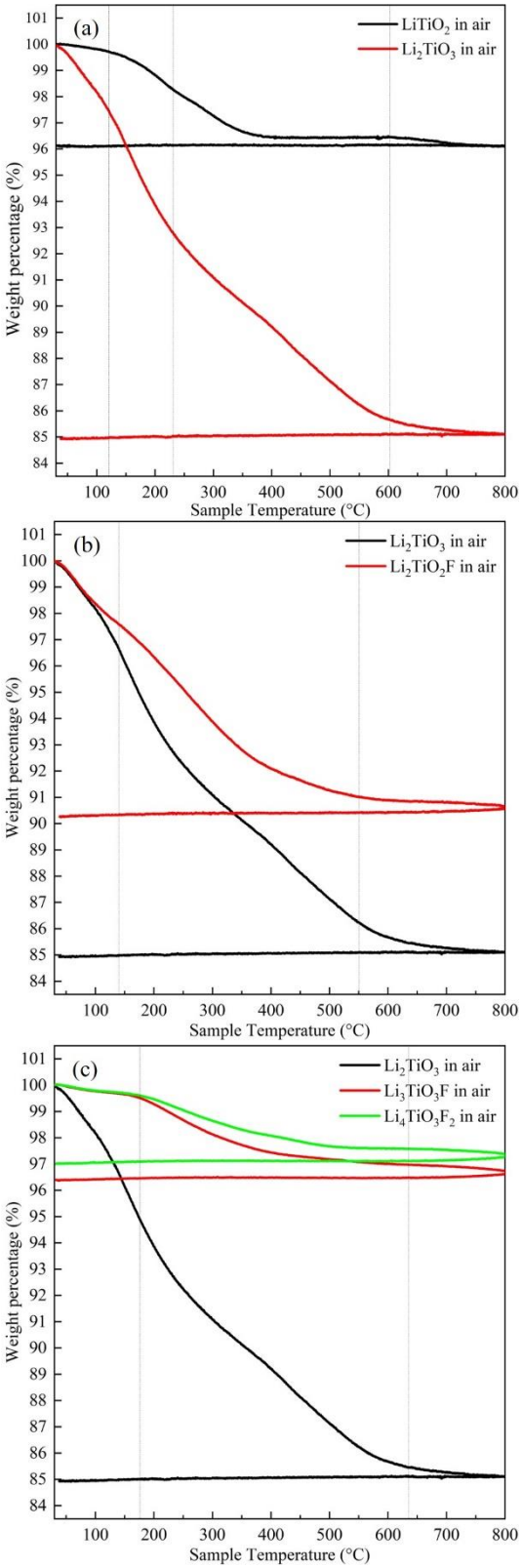

Figure 6.18 TG of disordered Li-Ti-O produced by mechanosynthesis

6.1.3 XRD and TGA of $LiAlO_2$ produced by mechanosynthesis

$LiAlO_2$ was synthesised using Li_2O_2 and Al_2O_3 by mechanosynthesis. Figure 6.19 (a) shows the XRD of ball-milled $LiAlO_2$ with subsequent heat treatment. After 20 h milling, a disordered rock salt phase formed but unreacted Al_2O_3 remained. After 60 h milling, a single phase disordered rock-salt phase was produced. When heated to 600 ℃, a very broad superlattice peak appeared at about 18° and it transformed to the α-$LiAlO_2$. At higher temperature, γ-phase $LiAlO_2$ appeared with a tetragonal structure (See more discussion on the polymorphisms of $LiAlO_2$ in section 6.2). The TG profile is shown in Figure 6.19 (b). A gradual weight loss of 10% occurred from room temperature to 490 ℃ and a followed slow weight loss of 1.2% continued to 800 ℃. The first weight loss process may be the release of H_2O and CO_2. The second process after 490 ℃ may be a mixture of CO_2 and O loss.

6.1.4 XRD and TGA of $LiFeO_2$ produced by mechanosynthesis

$LiFeO_2$ was synthesised using Li_2O_2 and Fe_2O_3 by mechanosynthesis. Figure 6.20 (a) is the XRD of ball-milled $LiFeO_2$ with subsequent heat treatment. After 20 h milling, the single phase disordered rock-salt α-$LiFeO_2$ formed. During heating, α-$LiFeO_2$ formed at 400 ℃ with a second phase $LiFe_5O_8$. Rock-salt α-$LiFeO_2$ transformed to tetragonal γ-phase at 600 ℃, and transformed back to rock-salt at 800 ℃. $LiFe_5O_8$ impurity remained up to 800 ℃. In TG profile, Figure 6.20 (b), about 4.5% weight loss gradually occurred from room temperature to 490 ℃ and about 0.3% weight loss occurred from 590 ℃ to 720 ℃. The first process may be the release of H_2O and CO_2 and the second one may be oxygen loss. (See more discussion about the polymorphisms of $LiFeO_2$ in section 6.2)

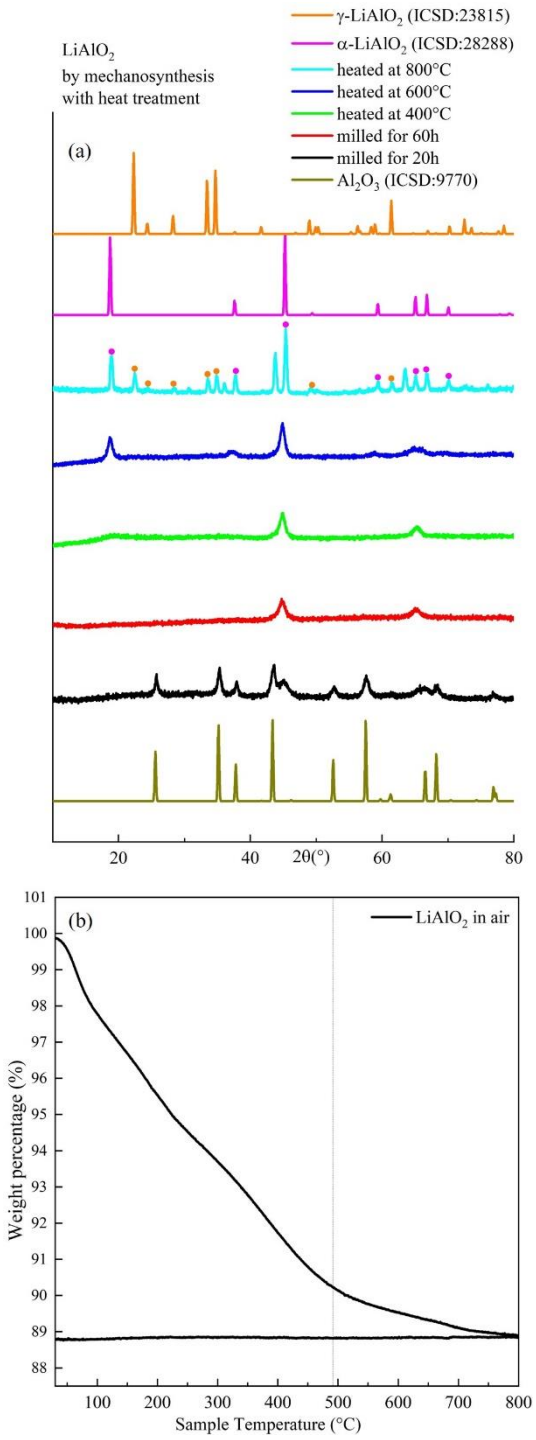

Figure 6.19 the XRD patterns and TG of $LiAlO_2$ produced by mechanosynthesis

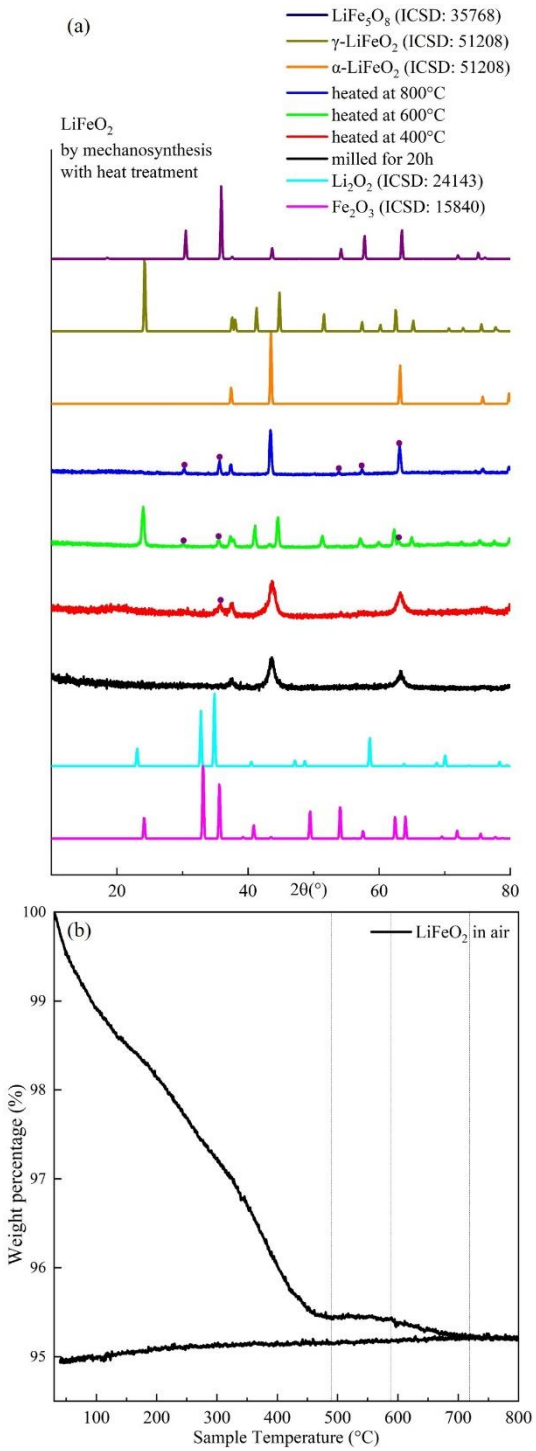

Figure 6.20 the XRD patterns and TG of $LiFeO_2$ produced by mechanosynthesis

6.1.5 Synthesis of ordered $LiCoO_2$ by mechanosynthesis and subsequent heat treatment

$LiCoO_2$ was produced by two groups of different reactants: F: Li_2O_2 + CoO; G: Li_2O_2 + Co_3O_4. Ordered $LiCoO_2$ formed after 20 h and 10 h milling, respectively. The XRD patterns (Figure 6.21) showed very broad peaks with noisy background, indicating that it had a small particle size or amorphous phase. With heat treatment, broad peaks started to sharpen, indicating grain growth (Figure 6.22).

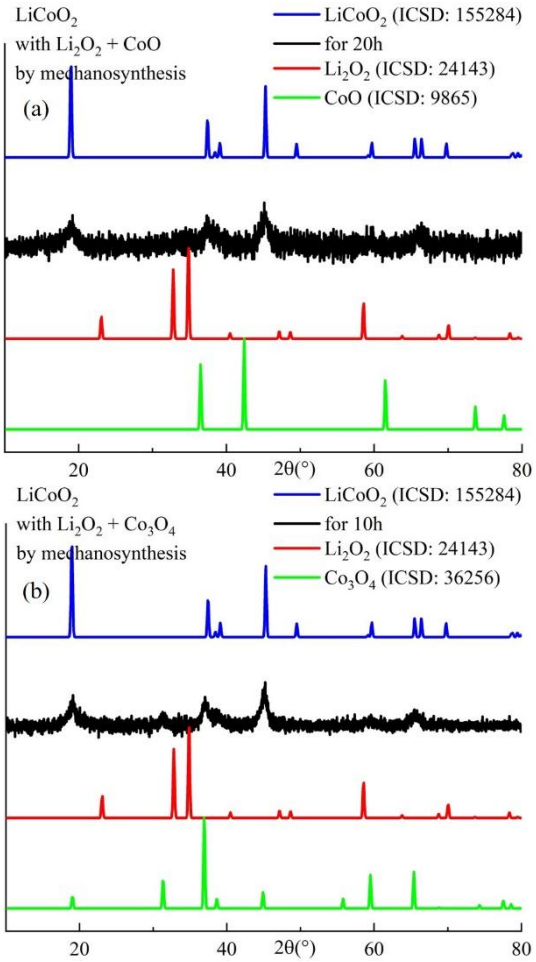

Figure 6.21 the XRD patterns of $LiCoO_2$ produced with different reactants by mechanosynthesis

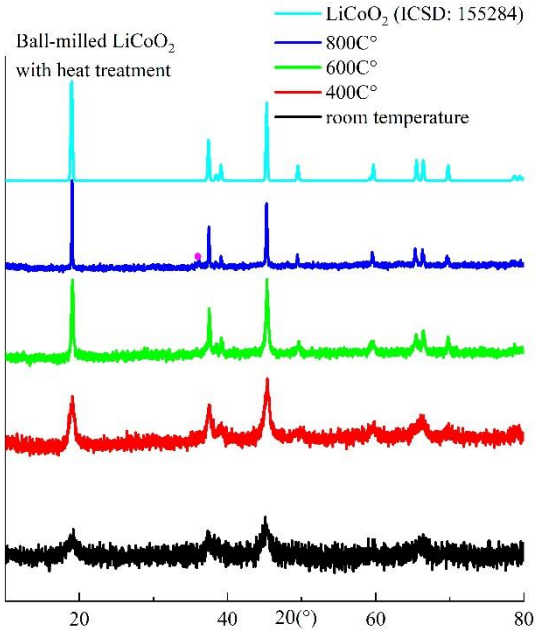

Figure 6.22 the XRD patterns of ball-milled $LiCoO_2$ with heat treatment

6.1.6 Synthesis of ordered Li-V-O by mechanosynthesis

6.1.6.1 Synthesis of $LiVO_3$ and Li_3VO_4 by mechanosynthesis and subsequent heat treatment

$LiVO_3$ and Li_3VO_4 were produced using Li_2O_2 and V_2O_5 by mechanosynthesis, shown in Figure 6.23. Ordered $LiVO_3$ and Li_3VO_4 formed, respectively, with a small particle size. With heat treatment, particle size increased. No obvious second phase appeared during heating. $LiVO_3$ was further studied using different reactants: H: Li_2O_2 + V_2O_5 (Figure 6.23 (a)); I: Li_2O_2+V_2O_3 (Figure 6.24 (a)) and J: Li_2O+V_2O_3 (Figure 6.24 (b)). H formed an ordered $LiVO_3$ phase. The main phase of I was ordered $LiVO_3$ with a small amount of Li_3VO_4 and LiV_2O_5, which may indicate that the $LiVO_3$ had decomposed during milling. J formed $LiVO_3$ with V_2O_3 as the second phase. The XRD pattern of J had very noisy background and broad peaks, indicating an amorphous phase. At about 51°, a small peak may be a disordered rock-salt phase (in red box).

V_2O_3 may be more reactive than V_2O_5 but neither of them is a suitable vanadium source to produce a disordered rock-salt phase of either $LiVO_3$ or Li_3VO_4. Ball-milling gave ordered products and $LiVO_3$ was not stable but decomposed with longer milling time.

6.1.6.2 Synthesis of Li_2VO_3 and Li_2VO_2F by mechanosynthesis

Undoped F doped Li_2VO_3 with the stoichiometry $Li_2VO_{3-x}F_x$ was prepared. Using Li_2O_2 and V_2O_5 to produce Li_2VO_3 gave a mixture of $LiVO_3$ and Li_3VO_4 (Figure 6.25 (a)). Using Li_2O_2, V_2O_5, LiF to product Li_2VO_2F gave a mixture of $LiVO_3$ and LiF (Figure 6.25 (b)). No disordered rock-salt phase of Li-V-O was produced by mechanosynthesis.

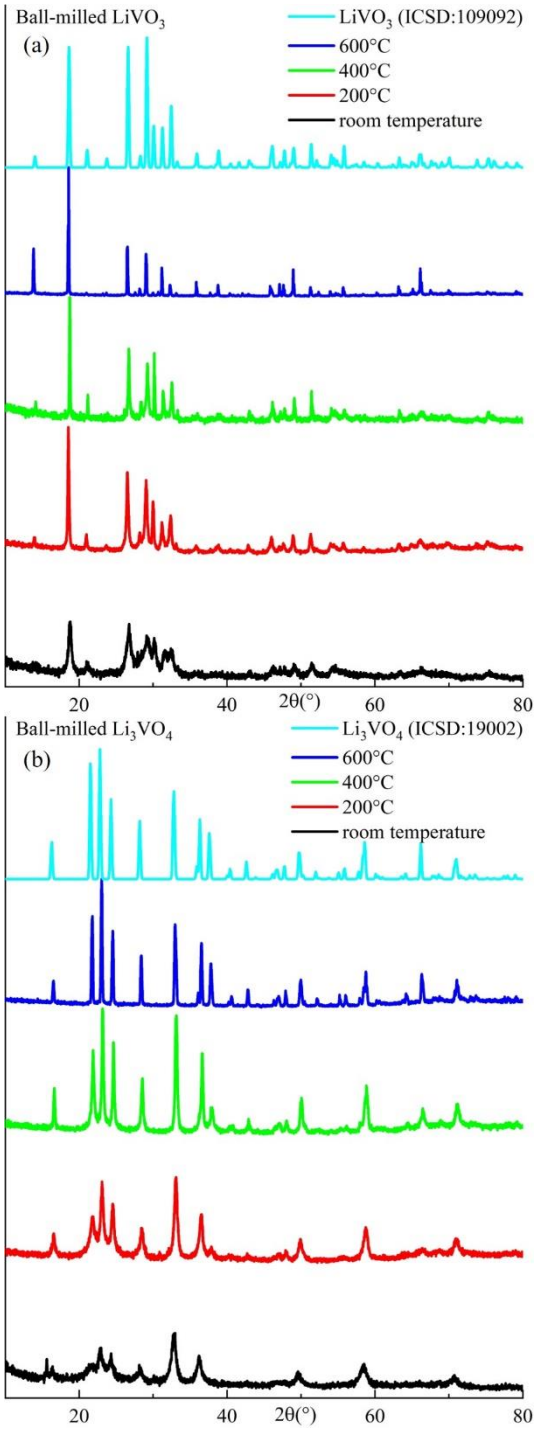

Figure 6.23 the XRD patterns of $LiVO_3$ and Li_3VO_4 produced by mechanosynthesis and subsequent heat treatment

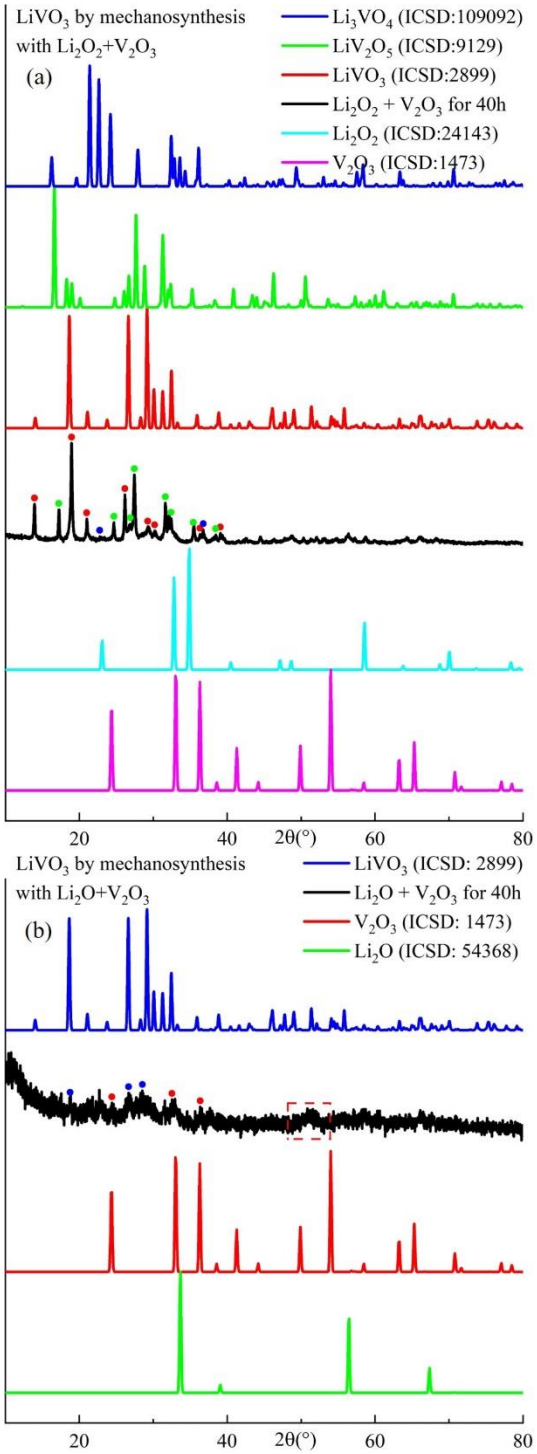

Figure 6.24 the XRD patterns of $LiVO_3$ with different reactants by mechanosynthesis

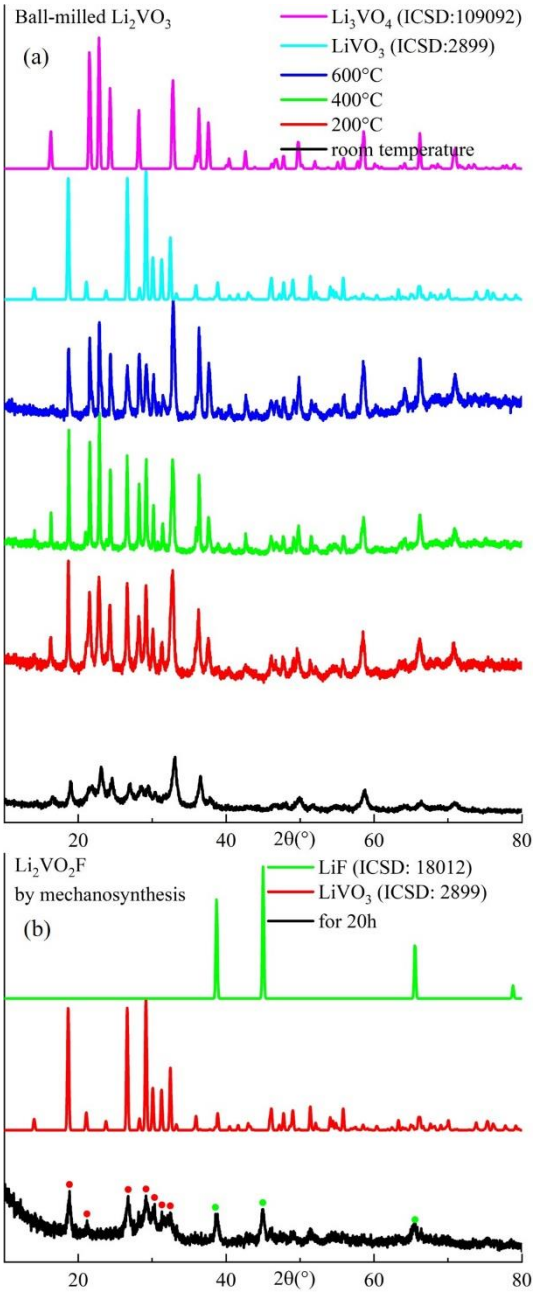

Figure 6.25 the XRD patterns of ball-milled Li_2VO_3 and Li_2VO_2F produced by mechanosynthesis

6.1.7 Li-Ni-O

6.1.7.1 Synthesis of $LiNiO_2$ and $Li_{0.9}Ni_{1.1}O_2$ by solid state reaction

Single phase $LiNiO_2$ and $Li_{0.9}Ni_{1.1}O_2$ were produced by solid state reaction using reactants $LiOH{\cdot}H_2O$ and NiO, shown in Figure 6.26. At 600 ℃, Li_2CO_3 existed as the second phase and decomposed at higher temperatures. The final synthesis temperatures for $LiNiO_2$ and $Li_{0.9}Ni_{1.1}O_2$ were 750 ℃ and 700 ℃, respectively.

6.1.7.2 Synthesis of F doped and pure $LiNiO_2$ and Li_2NiO_3 by mechanosynthesis

F substitution was introduced into $LiNiO_2$ and Li_2NiO_3 and presumably accompanied by Ni reduction to achieve charge compensation, to achieve the stoichiometries $LiNiO_{2-x}F_x$ and $Li_2NiO_{3-x}F_x$, respectively. $LiNiO_2$, $LiNiO_{1.8}F_{0.2}$, Li_2NiO_3 and Li_2NiO_2F were produced by mechanosynthesis using reactants Li_2O_2, NiO and LiF, shown in Figure 6.27. All products had a disordered rock-salt phase, and the intensity of the (111) peak increased with the Li:Ni ratio. The main peaks of Li_2NiO_2F were asymmetric (in red box), which may be unreacted LiF. Lattice parameter study is required to confirm the success of doping.

6.1.7.3 Heat treatment of $LiNiO_2$ and Li_2NiO_3

Disordered $LiNiO_2$ and Li_2NiO_3 were heated from room temperature to 800 ℃ (Figure 6.28). For $LiNiO_2$, a slight amount of Li_2CO_3 formed at 400 ℃ and decomposed at 600 ℃. The main phase started to get ordered during heating and single phase ordered $LiNiO_2$ formed at 800 ℃. For Li_2NiO_3, from 400 ℃, a large amount of Li_2CO_3 formed. At 600 ℃, the ordered $LiNiO_2$ appeared and Li_2CO_3 remained. At 800 ℃, Li_2CO_3 decomposed and a single phase formed, but it corresponded to $LiNiO_2$, not Li_2NiO_3.

6.1.7.4 TGA of $LiNiO_2$, $LiNiO_{1.8}F_{0.2}$, Li_2NiO_3 and Li_2NiO_2F

The comparison of $LiNiO_2$ and Li_2NiO_3 is in Figure 6.29 (a). There were two weight loss processes before 200 ℃, which could be related to two types of water, free water and combined water, such as hydrates. These water weight losses appeared in all Li-Ni-O samples in Figure 6.29 (a), (b), (c) and (d). Below 200 ℃. Li_2NiO_3 had 10% of water loss while $LiNiO_2$ only had 4%. For $LiNiO_2$, from 425 ℃, a slow weight gain occurred until about 750 ℃. After 750 ℃, a slight weight loss might be due to oxygen loss. For Li_2NiO_3, a slow weight gain occurred from 310 ℃. At 475 ℃, a weight loss occurred, which did not occur in $LiNiO_2$. At 750 ℃, a slight weight loss might be oxygen loss. XRD results (see in 6.1.3.3) showed that a large amount of Li_2CO_3 formed in Li_2NiO_3 when heated to 400 ℃, but that in $LiNiO_2$ was minimal. Li_2CO_3 in Li_2NiO_3 decomposed between 600 ℃ to 800 ℃. Therefore, in TG, it is possible that Li_2NiO_3 may react with CO_2 to form Li_2CO_3 after 310 ℃ and Li_2CO_3 decomposed from 475 ℃. Li_2NiO_3 may be more sensitive than $LiNiO_2$ to water and CO_2.

The comparison of Li_2NiO_3 and Li_2NiO_2F is shown in Figure 6.29 (b). The F doped sample had much less weight loss before 200 ℃, which indicating the F dopant mitigates the water absorption. They both had the CO_2 absorption peaks at 470 ℃ and 520 ℃, respectively. There was a weight loss after 520 ℃ from Li_2NiO_2F, which could be a mixture of CO_2 loss and F loss. With F doping, oxygen deficiency had been mitigated. In Figure 6.29 (c), $LiNiO_{1.8}F_{0.2}$ had a slight F loss at high temperature. Heat treatment of Li_2NiO_2F and $LiNiO_{1.8}F_{0.2}$ with XRD and XRF characterisation is required to support TG analysis. In Figure 6.29 (d), Li_2NiO_3 was measured in air and N_2 atmosphere. In a N_2 atmosphere, which contain little CO_2, there was still a weight gain peak at about 500 ℃. It may indicate the high sensitivity of Li_2NiO_3 to CO_2. After 600 ℃, there was a weight loss in N_2 but no obvious weight loss in air, which indicates Li_2NiO_3 may have some oxygen absorption in air after 600 ℃. Generally, the total weight loss of Li_2NiO_3 and Li_2NiO_2F was higher than that of $LiNiO_2$ and $LiNiO_{1.8}F_{0.2}$ (the total weight loss: 5% for $LiNiO_2$, 6% for $LiNiO_{1.8}F_{0.2,}$ 9% for Li_2NiO_3, and 9% for Li_2NiO_2F).

As conclusions, first, undoped and F-doped $LiNiO_2$ and Li_2NiO_3 with a disordered rock-salt structure were produced by mechanosynthesis; second, in both solid-state samples and heat treated ball-milled samples, the formation of Li_2CO_3 were severe. Ni system may be very sensitive to CO_2.

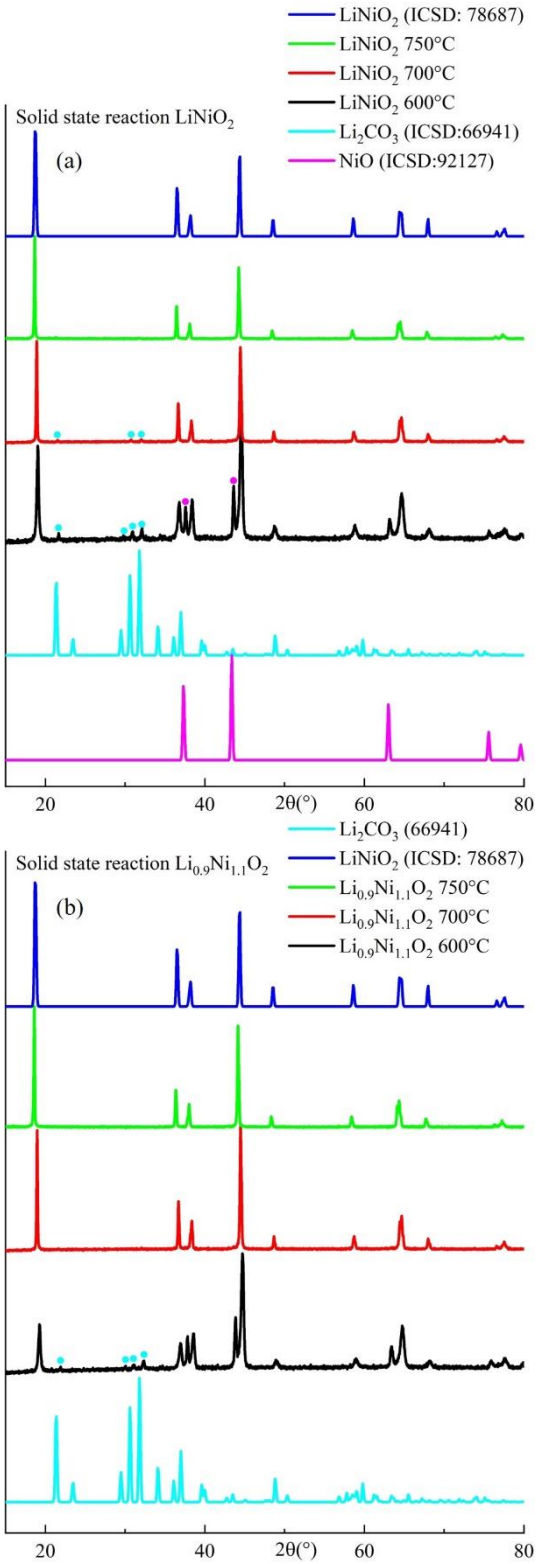

Figure 6.26 the XRD patterns of $LiNiO_2$ and $Li_{0.9}Ni_{1.1}O_2$ produced by solid state reaction

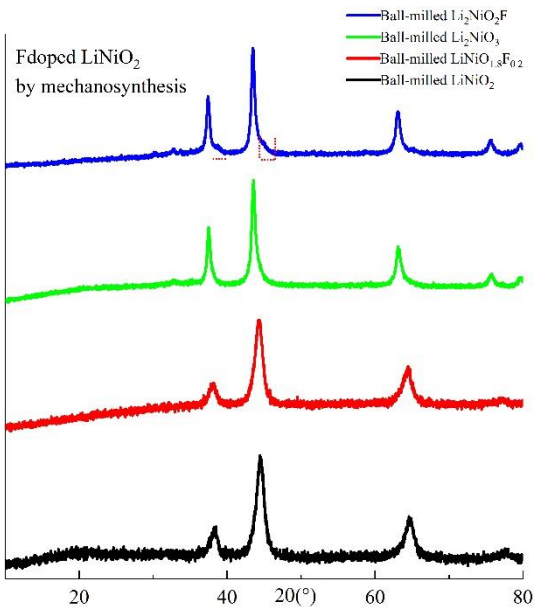

Figure 6.27 the XRD patterns of (a) $LiNiO_2$, (b) $LiNiO_{1.8}F_{0.2}$, (c) Li_2NiO_3 and (d) Li_2NiO_2F by mechanosynthesis

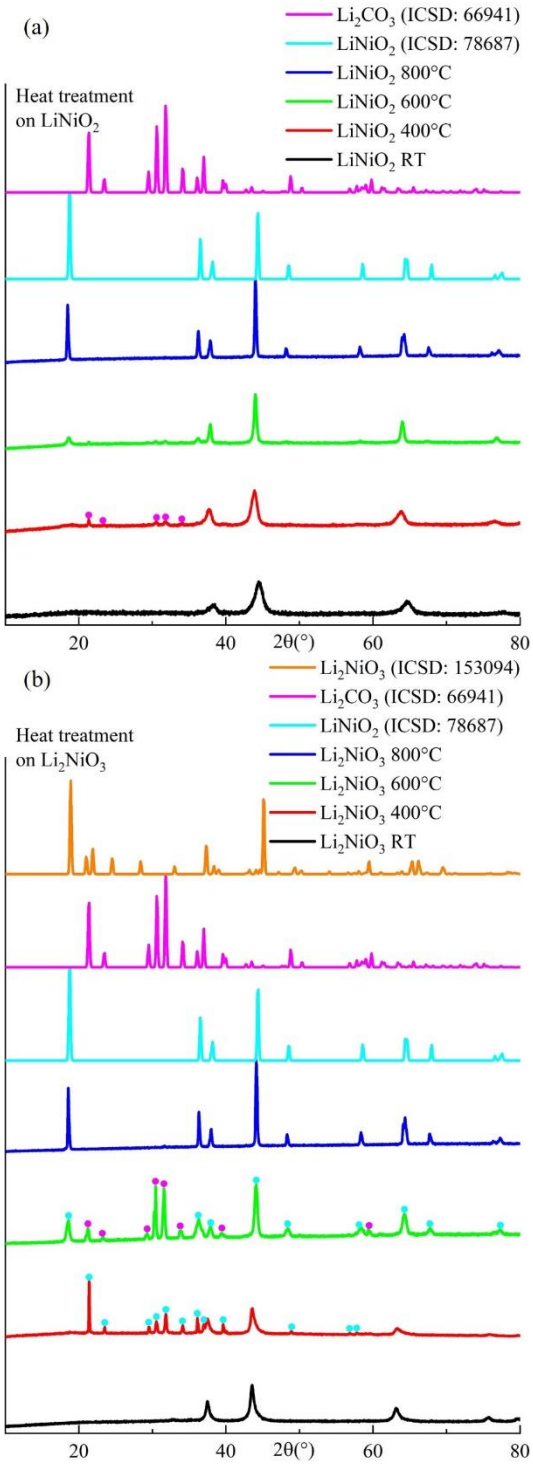

Figure 6.28 the XRD patterns of $LiNiO_2$(a) and Li_2NiO_3(b) with heat treatment

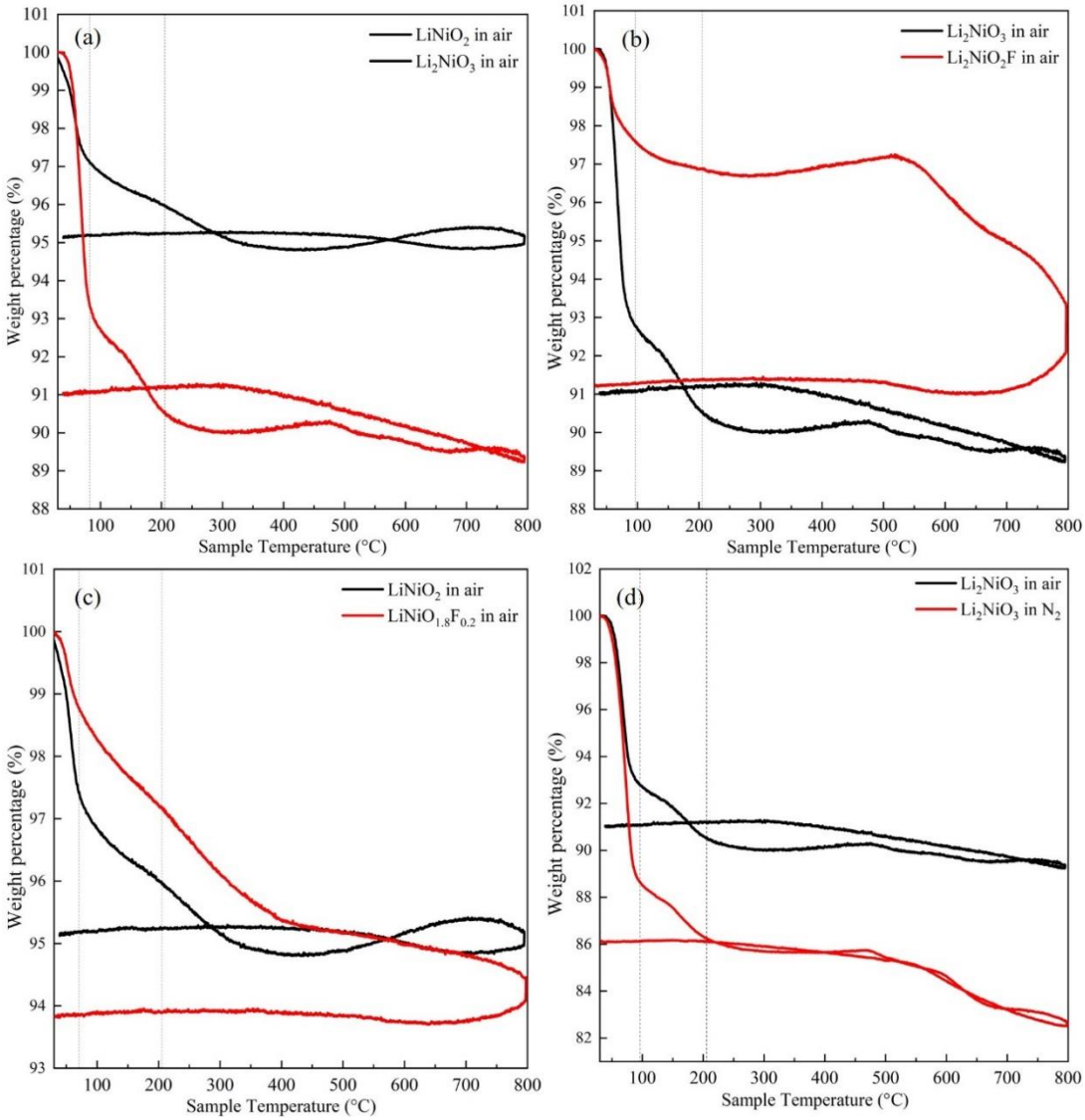

Figure 6.29 TG of (a) LiNiO and Li_2NiO_3, (b) Li_2NiO_3 in N_2 and air, (c) $LiNiO_2$ and $LiNiO_{1.8}F_{0.2}$ and (d) Li_2NiO_3 and Li_2NiO_2F

6.2 Discussion, conclusions and future work

6.2.1 Li-Nb-O

In Li-Nb-O, three main results are summarised: first, disordered rock-salt Li_3NbO_4 was successfully produced but it had a poor thermal stability. When heated to 600 ℃, a large amount of $LiNbO_3$ formed, accompanies by possibly Li loss; Second, Li_2NbO_3F did not form a disordered rock-salt phase but formed an ordered structure corresponding to $LiNbO_3$. The limit of solid solution $Li_{3-x}NbO_{4-x}F_x$ by mechanosynthesis might be < 1; Third, disordered rock-salt $Li_{3+x}NbO_4F_x$ (x=1, 2 and 3) was successfully produced, with an increased intensity of (111) peak. $Li_{3+x}NbO_4F_x$ had a good thermal stability. No phase change or F loss has been observed up to 800 ℃.

For Li_3NbO_4, single phase Li_3NbO_4 was produced by solid state reaction and mechanosynthesis, with an ordered layered and disordered rock-salt structure, respectively. The disordered rock-salt single phase Li_3NbO_4 has not been reported before. By solid state reaction, it was reported that Li_3NbO_4 formed an ordered cubic structure with the space group $I\bar{4}3m$. A cation-disordered rock-salt solid solution formed in Li_3NbO_4-based system between Li_3NbO_4 and a rock-salt phase, such as CoO [152], NiO [153] or LiF [154]. But the pure Li_3NbO_4 could not form a disordered rock-salt phase by solid state reaction. It is possible that disordered rock-salt Li_3NbO_4 is metastable and decompositions or phase transformations occur at high temperature. Mechanosynthesis, which occurs at room temperature, is a possible synthesis method and did successfully produce a disordered rock-salt Li_3NbO_4. During heating, it might decompose and formed a second phase, $LiNbO_3$. However, it is unclear why disordered Li_3NbO_3 decomposed instead of transforming ordered Li_3NbO_4, which is stable at high temperature.

The limit of solid solution $Li_{3-x}NbO_{4-x}F_x$ by solid state reaction was < 0.1. Ball-milled $Li_{3-x}NbO_{4-x}F_x$ (x=1) gave an ordered phase corresponding to $LiNbO_3$. First, Li_2NbO_3F has a cation:anion ratio of 3:4, not 1:1, which is not expected to form a rock-salt phase. This may indicate a similar conclusion as that given in previous chapters that it is important to remain the cation/anion ratio as a rock-salt stoichiometry to form a disordered rock-salt phase. Second, it is possible that Li_2NbO_3F was in the solid solution between $LiNbO_3$ and LiF. This can be understood from the phase diagram, Figure 6.1, since composition x=1 also lies on the line connecting $LiNbO_3$ and LiF which may, therefore, be an equilibrium tie line on the phase diagram. But it is still possible that solid solutions $Li_{3-x}NbO_{4-x}F_x$ may be able to form by

mechanosynthesis, but their limit is much less than x=1. Further work is required to study the solid solution possibility on the Li_3NbO_4-LiF tie and the $LiNbO_3$-LiF tie.

$Li_{3+x}NbO_4F_x$ (x=1, 2 and 3), also can be written as $Li_3NbO_4 \cdot xLiF$, were produced by mechanosynthesis. They show a good thermal stability up to 800 ℃, the possible reason of which may be that the rock-salt-structure LiF was as a stabiliser and stabilised Li_3NbO_4 at high temperature.

6.2.2 Li-Ti-O

In Li-Ti-O, the target compositions involved Ti^{3+} and Ti^{4+}. Different reactants, TiO, Ti_2O_3, TiO_2, Li_2O and Li_2O_2 have been used. Main results are summarised: first, a wide range of undoped and F-doped Li-Ti-O materials with disordered rock-salt structure forms by mechanosynthesis; second, F doping largely increases their thermal stability; third, TiO_2 may not be a suitable reactant in mechanosynthesis because it is less reactive and unlikely to form lower valence titanium on reaction with Li_2O_2 and Li_2O; fourth, contamination caused by abrasion of rutile, TiO_2 is considerable with either steel or WC milling media; fifth, attention to possible atmospheric sensitivity of ball-milled products is required.

For $LiTiO_2$, a disordered rock-salt phase formed using Li_2O_2 + TiO and Li_2O and Ti_2O_3, where the reactants possibly provided Ti^{3+}, as the target product requires. Using Li_2O_2 + TiO_2, although a disordered rock-salt phase also formed with much longer milling time, its practical composition was uncertain as an amorphous phase appeared and extensive contamination from the milling media may have been introduced. This also indicates that extra oxygen content is difficult to release in mechanosynthesis. During heating, a Li-Ti-Fe-O phase appeared in all ball-milled samples, which probably indicates that the Li-Ti-O system is sensitive to Fe contamination.

For Li_2TiO_2F, using Li_2O_2 + TiO_2 + LiF and Li_2O + Ti_2O_3 + LiF, a disordered rock salt phase formed but the reaction did not complete and a small amount of Ti-O retained unreacted. Possibly, incorporation of F into Li_2TiO_3 occurred but with a charge compensation mechanism that involved Li vacancies, instead of reduction of Ti^{4+}. The limit of $Li_2Ti_{1-x}^{4+}Ti_x^{3+}O_{3-x}F_x$ solid solution may be lower than x=1. In both cases of $LiTiO_2$ and Li_2TiO_2F , the reduction of Ti^{4+} accompany with Li_2O_2 is unlikely to occur and the reaction tends to not complete or require

longer milling time, indicating suitable reactants with required Ti valence and oxygen content are important for mechanosynthesis.

Disordered rock-salt Li_2TiO_3 and $Li_{2+x}TiO_3F_x$ (x=1 and 2) were successfully produced by mechanosynthesis. Ball-milled Li_2TiO_3, using Li_2O_2 and TiO_2, has a disordered rock-salt phase and it transformed to ordered monoclinic during heating. However, F-doped $Li_{2+x}TiO_3F_x$ (x=1 and 2) samples remained a disordered structure up to 800 ℃, demonstrating a better thermal stability.

Several solid solutions on the join of a rock-salt stoichiometry Li-TM-O and LiF were produced by mechanosynthesis with a disordered rock-salt structure, such as $Li_{3+x}NbO_4F_x$, $Li_{2+x}TiO_3F_x$ and $Li_{2+x}MnO_3F_x$ (Chapter 4). The rock-salt-structure LiF may stabilise the metastable rock-salt Li-TM-O so they show a good thermal stability at high temperatures. It was also observed that the water and CO_2 absorption in these three solid solution was much lower than the undoped sample, indicating that LiF may also mitigate samples' hygroscopic properties.

$Li_4Ti_5O_9$ and $Li_4Ti_5O_{12}$ were produced by mechanosynthesis, but they both present an unknown spinel phase, named phase T. TiO_2 was ball-milled individually, and its XRF showed samples were highly contaminated in both steel jars and WC milling media. The existence of Fe contamination was as 'as dopant' and that of W contamination as 'an impurity'. As the Li-Ti-Fe-O phase, a composition on solid solution of $Li_4Ti_5O_{12}$-$LiFe_5O_8$ [155], also appeared in other ball-milled Li-Ti-O samples, Li-Ti-O may be more sensitive to ball-milling contaminations. As a principle of choosing a suitable milling media in mechanosynthesis, the hardness and density of the milling media needs to be always higher than the ground materials to avoid forming extra contamination due to over-abrasion. The densities of milling media are 7.65 g/cm^3 for hardened steel jars and 14.3 g/cm^3 for tungsten carbide (Table 2.2), whilst the theoretical density of rutile TiO_2 is 4.13 g/cm^3 and layered $LiTiO_2$ is 3.9 g/cm^3. The density of Li-Ti-O samples is generally much lower than the milling media, and abrasion effect should be little. The reason leading to high contamination needs a better understanding. Due to the shortage of time, in Chapter 6, only XRF data on ball-milled Li-Nb-O and TiO_2 samples were collected. Further work can be aimed to carry out chemical analysis on all ball-milled samples in order to make further conclusions on contaminations caused by milling media.

6.2.3 $LiAlO_2$ and $LiFeO_2$

Disordered rock-salt $LiAlO_2$ and $LiFeO_2$ were produced by mechanosynthesis. During heating, it first transformed to α-$LiAlO_2$ and then to γ-$LiAlO_2$ at higher temperature. The disordered α-

$LiFeO_2$ transformed to γ-$LiFeO_2$ at 600 ℃, with a second phase $LiFe_5O_8$, and then back to α-$LiFeO_2$ at 800 ℃.

$LiAlO_2$ has at least five reported polymorphisms, including the tetragonal γ-phase and the orthorhombic β-phase [156], and the rhombohedral α-phase which can be synthesised from the γ-$LiAlO_2$ under high pressure, 3.5 Gpa, and temperature, 850 ℃ [157]. Compared with the density of γ-phase of 2.615 g/cm^3, α-phase had a higher density of 3.401 g/cm^3. A monoclinic phase can be produced under intermediate pressure, 18 kpa, and temperature, 420 ℃, from the β-$LiAlO_2$ [158]. In 2004, a new δ-$LiAlO_2$ was reported to be produced from shock compressed γ-$LiAlO_2$ under 48 Gpa and at ~1300 ℃, stable up to 500 ℃. It is isostructural to tetragonal γ-$LiFeO_2$, with the space group $I4_1/amd$. The refinement results suggested that it contained some disordering and defects in the lattice [159].

As for $LiFeO_2$, the α-$LiFeO_2$ has a disordered rock-salt structure, with the space group $Fm\bar{3}m$, and it is stable at least at 900 ℃ [160]. The γ-$LiFeO_2$ forms by reducing the symmetry from cubic to tetragonal by ordering Li^+ and Fe^{3+} at octahedral sites [161]. The β-$LiFeO_2$ is an intermediate phase between the α and γ phase, with the space group $C2/c$ [162]. The fourth one, layered $LiFeO_2$ has a rhombohedral structure, with the space group $R\bar{3}m$ [163], [164]. Despite polymorphisms of $LiAlO_2$ and $LiFeO_2$ have been widely studied, there is still controversy on the type of polymorphs, their stability and synthesis methods.

6.2.4 Li-Co-O and Li-V-O

In Li-Co-O and Li-V-O systems, no disordered rock-salt phase was successfully produced. Ordered $LiCoO_2$, $LiVO_3$ and Li_3VO_4 with small particle size were produced by mechanosynthesis and the particle size increased during heating. These unsuccessful results were unexpected as both $LiCoO_2$ and $LiVO_2$ can be synthesised as a layered rhombohedral phase by solid state reaction. The ratio of ionic radii of Li/TM for V is suitable but for Co is quite large (Li^+: 90 pm; V^{3+}: 78 pm; Co^{3+}: 68.5 pm. Li^+/V^{3+}=1.15; Li^+/Co^{3+}=1.31), which may cause incompatibility in the rock-salt structure.

By solid state reaction, $LiCoO_2$ can be synthesised as a layered rhombohedral structure at 900 ℃, called HT-$LiCoO_2$, whilst at 400 ℃ as a cubic spinel, called LT-$LiCoO_2$ [165]. A disordered rock-salt $Li_xCo_{1-x}O_2$ was synthesised at 1100 ℃ in a pumped vacuum [166]. It was also reported that a disordered rock-salt $Li_{0.86}V_{0.8}O_2$ was synthesised by hydrothermal method and a phase transition of $LiVO_2$ occurred from ordered to disordered during charge/discharge [109]. Based on literature, both $LiCoO_2$ and $LiVO_2$ have possibility to fit into the rock-salt

lattice with disorder on cation sites. Future work can be aimed to produce the disordered rock-salt $LiCoO_2$ and $LiVO_2$ by mechanosynthesis under proper conditions and study the limitation of the formation of disordered rock-salt phase in Li-TM-O.

6.2.5 Li-Ni-O

Ordered $LiNiO_2$ and $Li_{0.9}Ni_{1.1}O_2$ was produced by solid state reaction. Disordered rock-salt $LiNiO_2$, $LiNiO_{1.8}F_{0.2}$, Li_2NiO_3 and Li_2NiO_2F were produced by mechanosynthesis. During heating, ball-milled $LiNiO_2$ transformed to rhombohedral $LiNiO_2$, but ball-milled Li_2NiO_3 did not transformed to monoclinic Li_2NiO_3. Instead, it formed an ordered phase corresponding to $LiNiO_2$. It was reported that Li_2NiO_3 was synthesised in highly oxidising conditions. It is isostructural to Li_2MnO_3 with a monoclinic structure and shows peaks of stacking fault at about 21°. However, ball-milled Li_2NiO_3 after heat treatment showed a simpler structure like $LiNiO_2$, without stacking faults. One possibility is that Li_2NiO_3 decomposed. It may be not stable at high temperature, which has been observed in Li_2NiO_3 that a rock-salt phase with lower Li/Ni ratio appeared during charge/discharge of Li_2NiO_3 [167]. Another possibility is that when heating the disordered Li_2NiO_3, it formed a rhombohedral structure, and Li and Ni atoms in layers were still randomly located, so it would not form stacking faults or ordered domains. It was also reported that a fully Ni^{4+} was difficult to achieve and a mixed Ni^{4+} and Ni^{3+} always present in Li_2NiO_3, accompanied with the oxygen non-stoichiometry, $Li_2NiO_{3-\delta}$, $\delta < 0.135$ [ref requested]. The real composition of heated Li_2NiO_3 needs to be analysed by ICP. Lattice parameter and cation occupancy need to be studied as well. Both of solid state and ball-milled Li-Ni-O sample have some Li_2CO_3 present during heating. Possibly, Li-Ni-O system is sensitive to CO_2, so synthesis under CO_2-free atmosphere may be needed.

6.2.6 TGA

From the previous TGA-MS on Li_2MnO_3 (Chapter 3), it has been observed that ball-milled Li_2MnO_3 samples had a water loss at about 108 ℃ and two processes of CO_2 release at 413 ℃ and 628 ℃, respectively. A slight oxygen loss occurred at a high temperature, above 700 ℃. All ball-milled Li-TM-O samples in this chapter show similar TG profiles which H_2O release below 200℃ and two of CO_2 release at ~400 ℃ and ~600 ℃. At high temperature, lithium and/or oxygen loss also occurred. Similar to results from F doped Li_2MnO_3 (Chapter 4) that F

doping may mitigate the absorption of water and CO_2, in this chapter, all F-doped samples show less water and CO_2 release than the undoped during heating. Also, Li_2TMO_3 tends to lose more weight than $LiTMO_2$, which may involve oxygen loss and oxidisation of transition metal. Several factors may be involved, particularly the basicity of materials with increasing Li_2O content. Basic oxides react with water by (idealised) reactions such as:

$$O^{2-} + H_2O = 2OH^- \quad (1)$$

whereas there is no equivalent reaction with F^- ions. In addition, with increasing TM content (comparing $LiTiO_2$ and Li_2TiO_3, and $LiNiO_2$ and Li_2NiO_3), the oxygens increasingly form covalent bonds to TM. Uptake and absorption of CO_2 may arise by a similar mechanism in which basic oxide ions, together with hydroxide ions, lead to formation of stable carbonate species:

$$O^{2-} + CO_2 = CO_3^{2-} \quad (2)$$

$$OH + CO_2 = HCO_3^- \quad (3)$$

Further studies are required to confirm whether sample history, such as exposure to air prior to TG, affects the TG results. Among of Li-TM-O, Li-Ni-O had unexpected TG profiles, which may relate to CO_2 absorption peak between 400 ℃ to 600 ℃ and/or phase change due to the poor stability of both $LiNiO_2$ and Li_2NiO_3 [167]. Generally, except the conclusion on the hygroscopicity of ball-milled samples, a better understanding on TG profile in each Li-TM-O system is needed. Future work, such as TG-MS study on Li-TM-O study is required. A vacuum or argon atmosphere should be considered for storage.

6.3 References

[109] K. Ozawa *et al.*, "Structural modifications caused by electrochemical lithium extraction for two types of layered LiVO2(R-3m)," *J. Power Sources*, vol. 174, no. 2, pp. 469–472, 2007, doi: 10.1016/j.jpowsour.2007.06.100.

[152] M. Vega-Glez, M. A. Castellanos Román, and A. Huanosta-Tera, "Short range order in new rock salt type structures of the system Li 3NbO4-CoO," *Rev. Mex. Fis.*, vol. 51, no. 3, pp. 299–303, 2005.

[153] Z. Wu *et al.*, "Synthesis and electrochemical properties of cation-disordered rock-salt xLi3NbO4·(1 − x) NiO compounds for Li-ion batteries," *Int. J. Energy Res.*, vol. 45, no. 3, pp. 3966–3978, 2021, doi: 10.1002/er.6050.

[154] J. J. Bian, J. Y. Wu, and L. Wang, "Structural evolution, sintering behavior and microwave dielectric properties of (1-x)Li 3NbO 4-xLiF (0≤x≤0.9)," *J. Eur. Ceram. Soc.*, vol. 32, no. 6, pp. 1251–1259, 2012, doi: 10.1016/j.jeurceramsoc.2011.12.026.

[155] S. Scharner, W. Weppner, and P. Schmid-Beurmann, "Cation Distribution in Ordered Spinels of the Li2O-TiO2-Fe2O3System," *J. Solid State Chem.*, vol. 134, no. 1, pp. 170–181, 1997, doi: 10.1006/jssc.1997.7572.

[156] M. Marezio, "The crystal structure and anomalous dispersion of γ-LiAlO2," *Acta Crystallogr.*, vol. 19, no. 3, pp. 396–400, 1965, doi: 10.1107/s0365110x65003511.

[157] M. MAREZIO AND J. P. REMEIKA, "High-Pressure Synthesis and Crystal Structure of α-LiAlO2," *J. Chem. Phys.*, vol. 44, no. 3143, pp. 2–4, 1966.

[158] C. H. Chang and J. L. Margrave, "High-Pressure-High-Temperature Syntheses. III. Direct Syntheses of New High-Pressure Forms of LiA102 and LiGaOa and Polymorphism in LiM02 Compounds =(B, Al, Ga)," *J. Am. Chem. Soc.*, vol. 90, no. 8, pp. 2020–2022, 1967.

[159] X. Li, T. Kobayashi, F. Zhang, K. Kimoto, and T. Sekine, "A new high-pressure phase of LiAlO2," *J. Solid State Chem.*, vol. 177, no. 6, pp. 1939–1943, 2004, doi: 10.1016/j.jssc.2003.12.014.

[160] V. R. Galakhov, E. Z. Kurmaev, S. Uhlenbrock, M. Neumann, D. G. Kellerman, and V. S. Gorshkov, "Electronic structure of LiNiO2, LiFeO2 and LiCrO2: X-ray photoelectron and X-ray emission study," *Solid State Commun.*, vol. 95, no. 6, pp. 347–351, 1995, doi: 10.1016/0038-1098(95)00279-0.

[161] A. R. Armstrong, D. W. Tee, F. La Mantia, P. Novák, and P. G. Bruce, "Synthesis of tetrahedral LiFeO2 and its behavior as a cathode in rechargeable lithium batteries," *J. Am. Chem. Soc.*, vol. 130, no. 11, pp. 3554–3559, 2008, doi: 10.1021/ja077651g.

[162] M. Tabuchi, K. Ado, H. Sakaebe, C. Masquelier, H. Kageyama, and O. Nakamura, "Preparation of AFeO , (A = Li , Na) by hydrothermal method," *Solid State Ionics*, vol. 79, pp. 220–226, 1995.

[163] T. Shirane *et al.*, "Structure and physical properties of lithium iron oxide, LiFeO2, synthesized by ionic exchange reaction," *Solid State Ionics*, vol. 79, no. C, pp. 227–233,

1995, doi: 10.1016/0167-2738(95)00066-F.

[164] M. T. Kazuaki Ado, H. Kobayashi, H. Kageyama, and O. Nakamura, “Preparation of LiFeO 2 with Alpha- NaFeO2 -Type Structure Using a Mixed-Alkaline Hydrothermal Method,” *J. Electrochem. Soc.*, 1997.

[165] R. J. Gummow, M. M. Thackeray, W. I. F. David, and S. Hull, “Structure and Electrochemistry of Lithium Cobalt Oxide,” *Mater. Res. Bull.*, vol. 27, pp. 327–337, 1992.

[166] W. D. Johnston, R. R. Heikes, and D. Sestrich, “The preparation, crystallography, and magnetic properties of the LixCo(1-x)O system,” *J. Phys. Chem. Solids*, vol. 7, no. 1, pp. 1–13, 1958, doi: 10.1016/0022-3697(58)90175-6.

[167] M. Bianchini *et al.*, “From LiNiO2to Li2NiO3: Synthesis, Structures and Electrochemical Mechanisms in Li-Rich Nickel Oxides,” *Chem. Mater.*, vol. 32, no. 21, pp. 9211–9227, 2020, doi: 10.1021/acs.chemmater.0c02880.

Chapter 7 Conclusions and future work

7.1 Conclusions

7.1.1 Li-Mn-O-F rock-salt and spinel materials

The effect of ball-milling on reactants was studied. Ball-milling Li reactants in steel jars, such as Li_2O_2, Li_2O, LiF and Li_2CO_3, did not cause loss/gain of O_2 but reduced particle size. However, some Li hydrates, such as $LiOH{\cdot}H_2O$ and $LiCH_3COO{\cdot}2H_2O$, presented different structures after milling, which may be because they have preferred orientation in ball-milling. Manganese oxides underwent redox reactions during milling in steel and zirconia jars and tended to form either Mn_2O_3 or a spinel. In tungsten carbide jars, no obvious phase change occurred, but amorphous phases formed.

The possibility of contamination caused by milling media was a constant problem. All ball-milled Li reactants using steel jars were lightly contaminated although, ball-milled manganese oxides, as well as TiO_2, were highly contaminated by steel, zirconia and tungsten carbide jars, which might be the reason of phase change during milling. Ball-milled Li_2MnO_3 and F-doped Li_2MnO_3 products were also lightly contaminated by three milling media but contaminations existed in products in a different way. Steel and zirconia jars incorporated high level contamination into the ball-milled products, whilst tungsten carbide mainly existed as a second phase and incorporated low level of contamination into the products that dissolved in aqua regia.

Different Li reactants were tried to study their reactivity in mechanosynthesis. $LiCH_3COO$, Li_2CO_3 and $LiOH{\cdot}H_2O$ were not very reactive but Li_2O and Li_2O_2 were. Disordered Li_2MnO_3 was produced successfully by three routes: i. milling Li_2O_2 and MnO; ii. milling Li_2O and MnO_2 and iii. milling ordered monoclinic Li_2MnO_3. During heating, disordered Li_2MnO_3 first formed an ordered superstructure with much smaller domain size and finally transformed to monoclinic Li_2MnO_3.

A series of single phase disordered rock-salt Li_2MnO_δ ($2.5 \leq \delta \leq 4$) compositions with varied oxygen content was successfully produced using Li_2O_2 and Li_2O with MnO, Mn_2O_3 and MnO_2, although accurate oxygen contents have not been determined so far.

A wide range of disordered rock-salt F-doped Li_2MnO_3 solid solution successfully formed by mechanosynthesis using four mechanisms, including $Li_2Mn^{4+}_{1-x}Mn^{3+}_xO_{3-x}F_x$, $Li_{2-x}MnO_{3-x}F_x$, $Li_{2+x}Mn_{1-x}O_{3-3x}F_{3x}$, and $Li_2Mn_{1-x}O_{3-4x}F_{4x}$. Mechanism three, $Li_{2+x}Mn_{1-x}O_{3-3x}F_{3x}$ solid solution, had good thermal stability and remained disordered rock-salt structures at least to 500 ℃. Disordered rock-salt structures with the other three doping mechanisms of compositions were kinetically stable but thermodynamically metastable. Similar to Li_2MnO_3, during heating, they showed a grain growth, accompanied with either the formation of ordered domains with much smaller size, or the nucleation of a spinel structure. At higher temperature, it transformed to ordered Li_2MnO_3 with a second phase $LiMn_2O_4$ and/or LiF. Fluorine loss occurred ≥ 500 °C.

Ball-milled $Li_4Mn_5O_\delta$ ($9 \leq \delta \leq 14$) with different oxygen content gave two different structures, rock-salt or spinel. When $\delta=9$, with a cation:anion ratio of 1:1, disordered rock-salt phase was produced. When $11.5 \leq \delta \leq 14$, with a cation:anion ratio of 3:4 or nearly 3:4, spinel phase was produced. Again, they were not thermally stable. Ball-milled $Li_4Mn_5O_\delta$ rock-salt transformed to spinel $Li_4Mn_5O_{12}$ at ≥ 400 °C, and finally decomposed to Li_2MnO_3 and $LiMn_2O_4$ at ≥ 700 °C.

Following the study on $Li_4Mn_5O_\delta$, Li-Mn-O were produced by mechanosynthesis with either a rock-salt stoichiometry or spinel stoichiometry. However, a wide range of single phase materials only formed with rock-salt stoichiometry and structure. No single phase compositions could form with spinel stoichiometry and the products tended to form amorphous phase.

Among four doping mechanisms, only $Li_2MnO_{3-x}F_x$ solid solutions create Mn^{3+}, which provides the possible redox couple Mn^{4+}/Mn^{3+} as cathodes. Mn^{3+} has been successfully created in $Li_2MnO_{3-x}F_x$ by mechanosynthesis. $Li_2MnO_{3-x}F_x$ had a higher capacity than Li_2MnO_3. Li_2MnO_2F achieved a capacity of 215 mAh/g, whilst Li_2MnO_3 70-100 mAh/g. Ball-milled $Li_2MnO_{3-x}F_x$ presented a mixed ionic and electronic conductivity and was more conductive than Li_2MnO_3. They consisted of nano particles, < 100 Å, and the distribution of F ions was homogeneous.

7.1.2 Li-TM-O (TM=Nb, Ti, Al, Fe, Co, V, and Ni)

A wide range of Li-TM-O compositions was successfully produced with disordered rock-salt structures by mechanosynthesis, including Li_3NbO_4, $Li_{3+x}NbO_4F_x$, $LiTiO_2$, Li_2TiO_3, $Li_{2+x}TiO_3F_x$, $LiAlO_2$, $LiFeO_2$, $LiNiO_2$, $LiNiO_{1.8}F_{0.2}$, Li_2NiO_3 and Li_2NiO_2F. Most of them were metastable and underwent phase change or decomposed during heating. During heating, ball-milled Li_3NbO_4 decomposed and transformed to a mixture of ordered Li_3NbO_4 and a phase

corresponding to ordered $LiNbO_3$, indicating a severe Li loss. Also, ball-milled $LiTiO_2$ transformed to a spinel, probably $Li_4Ti_5O_{12}$, and ball-milled Li_2NiO_3 transformed to a phase corresponding to ordered $LiNiO_2$, with a possible Li loss. On the other hand, ball-milled Li_2TiO_3, $LiNiO_2$, $LiAlO_2$ and $LiFeO_2$ formed their corresponding ordered structures during heating.

Similar to Li_2MnO_3-LiF solid solution, complete ranges of Li_3NbO_4-LiF and Li_2TiO_3-LiF solid solutions were prepared and had good thermal stability. They remained rock-salt structure and experienced no F loss at high temperatures.

However, in Li-Co-O and Li-V-O systems, no disordered rock-salt phase was successfully produced. Ordered $LiCoO_2$, $LiVO_3$ and Li_3VO_4 were directly produced by mechanosynthesis with small particle size.

7.1.3 Hygroscopicity in ball-milled products

Ball-milled samples often showed high hygroscopicity and absorbed water and possible CO_2 during synthesis and/or storage. This may relate to the reaction of water and CO_2 with Li reactants, Li_2O_2 and Li_2O, which are basic oxides. Ball-milled undoped products were often more hygroscopic than F doped ones. F doping may mitigate the absorption of H_2O and CO_2. Also, ball-milled products with higher Li:TM ratio showed higher hygroscopicity, which might be again due to the greater use of Li reactants.

Due to the high hygroscopicity of ball-milled products, a vacuum or argon atmosphere should be considered for synthesis and storage.

7.2 Future work

Do chemical analysis on all ball-milled samples to confirm the real compositions, especially oxygen stoichiometry. Study whether oxygen stoichiometry will vary using different reactants when they provide ‘right’ or ‘not right’ amount of oxygen.

Look for the range where rock-salt structure can be formed in Li-TM-O-F systems by mechanosynthesis and their thermal stability.

Study the manganese valence in F doped Li_2MnO_3, with four different doping mechanisms, especially on $Li_2MnO_{3-x}F_x$, where Mn^{3+} and/or Mn^{2+} are theoretically created. For compositions with other three doping mechanisms, study whether they only contain Mn^{4+}.

Test in electrochemical cells as possible cathodes, which were prepared by F doped Li_2MnO_3 compositions: 1. test the activity of redox couple Mn^{4+}/Mn^{3+} and/or Mn^{4+}/Mn^{2+}, in $Li_2MnO_{3-x}F_x$; 2. test whether other compositions, which are theoretically only contain Mn^{4+}, are not active; 3. obtain a better understanding on their redox mechanisms as cathodes, such as whether oxygen redox exists.

Study the structure changes from ordered to disordered during heating or during charge and discharge, such as decompositions and phase change, on ball-milled meta-stable products. Study the structure and size of the short range ordered domain which has been observed during heating. Compare the local structure ordering and bonding in undoped and F doped compositions.

Optimising the synthesis and storage conditions of mechanosynthesis. As shorter milling time may introduce less contamination, possible shorter milling time to form a desirable phase needs to apply. Beside milling time, several variables, such as milling speed, the amount of milled powders and the weight ratio of balls/powders, also should be studied.

An atmosphere-controlled ball mill, Pulverisette 7 can be introduced and all experiments and characterisations should be carried out in inert atmosphere. Pulverisette 7 can apply oxidising/reducing atmosphere during milling, which can be another variable to study. Further exploration on synthesis which is highly restricted by atmosphere, such as N doping, can be tried using Pulverisette 7.